Developing nebulized spray pyrolysis as a synthesis route for energy materials: Composite electrolytes and mixed electron-proton-conductors

TECHNISCHE UNIVERSITÄT DARMSTADT

Vom Fachbereich Material-und Geowissenschaften

der Technischen Universität Darmstadt

zur Erlangung des akademischen Titels

Dr. rer.-nat.

genehmigte Dissertation von

Aamir Iqbal Waidha, M. Sc

aus Kaschmir, Indien

1. Gutachter: Prof. Dr. Wolfgang Ensinger

2. Gutachter: Prof. Dr. Oliver Clemens

Tag der Einreichung: 18.10.2021

Tag der Prüfung: 21.12.2021

Darmstadt 2021

D17

Developing NSP as a synthesis route for energy materials: Composite electrolytes and mixed electron-proton-conductors
Submitted doctoral thesis by Aamir Iqbal Waidha

1. Reviewer: Prof. Dr. Wolfgang Ensinger
2. Reviewer: Prof. Dr. Oliver Clemens

Date of submission: - 18.10.2021
Date of thesis defense: - 21.12.2021
Darmstadt

Please cite this document as:
URN: urn:nbn:de:tuda-tuprints-207737
URL: https://tuprints.ulb.tu-darmstadt.de/20773

This document is published by tuprints,
TU Darmstadt publication service
http://tuprints.ulb.tu-darmstadt.de
tuprints@ulb.tu-darmstadt.de

“The reward of the young scientist is the emotional thrill of being the first person in the history of the world to see something or to understand something. Nothing can compare with that experience.” – Cecilia Payne-Gaposchkin

Erklärungen laut Promotionsordnung

§8 Abs. 1 lit. c PromO
Ich versichere hiermit, dass die elektronische Version meiner Dissertation mit der schriftlichen Version übereinstimmt.

§8 Abs. 1 lit. d PromO
Ich versichere hiermit, dass zu einem vorherigen Zeitpunkt noch keine Promotion versucht wurde. In diesem Fall sind nähere Angaben über Zeitpunkt, Hochschule, Dissertationsthema und Ergebnis dieses Versuchs mitzuteilen.

§9 Abs. 1 PromO
Ich versichere hiermit, dass die vorliegende Dissertation selbstständig und nur unter Verwendung der angegebenen Quellen verfasst wurde.

§9 Abs. 2 PromO
Die Arbeit hat bisher noch nicht zu Prüfungszwecken gedient.

Darmstadt: - Aamir Iqbal Waidha

Zussammenfassung

Diese Arbeit befasst sich mit der Entwicklung und dem Verständnis von Komposit-Festkörperelektrolyten für Lithium-Ionen-Batterien und der Rolle von Perowskit-Materialien als bifunktionale Katalysatoren für die Sauerstoffreduktions- und Sauerstoffentwicklungsreaktion für ihre Anwendung in Brennstoffzellen und Metall-Luft-Batterien. Die Materialsynthese von Lithium-Granaten und bariumreichen Kobaltaten und Ferraten erfolgt durch vernebelte Sprühpyrolyse, die Partikelmorphologien und -größen liefert, die sich als vorteilhaft für ihren Einsatz in solchen energiebezogenen Anwendungen erweisen könnten.

Lithium-Ionen-Batterien mit Festelektrolyten sind in der Lage, die Anforderungen mobiler Fahrzeuge an eine hohe Energiedichte zu erfüllen und bieten darüber hinaus eine höhere Sicherheit. Obwohl im Laufe der Jahre eine Vielzahl verschiedener anorganischer und organischer Festelektrolyte für den Einsatz in solchen Batterien erforscht wurde, weist jeder dieser Elektrolyte inhärente Probleme auf, wie z. B. einen hohen Ladungsübergangswiderstand an der Grenzfläche zwischen Elektrode und Elektrolyt, mechanische und chemische Instabilitäten an der Grenzfläche zwischen Elektrode und Elektrolyt, eine geringere Ionenleitfähigkeit im Vergleich zu flüssigen Elektrolyten und vor allem Anfälligkeit für Feuchtigkeit. In dieser Hinsicht können Verbundelektrolyte, die eingebettete anorganische keramische Füllstoffe und ein Polymer plus Li-Ionen-Matrix enthalten, von der hohen Li-Ionen-Leitfähigkeit und dem breiten elektrochemischen Betriebsfenster der anorganischen Füllstoffe profitieren, während das Polymer gute mechanische Eigenschaften bieten kann, was zu einem geringen Grenzflächenwiderstand zwischen Elektrode und Elektrolyt führen kann. Am wichtigsten ist, dass Komposit-Elektrolyte mechanische Stabilität gegenüber metallischen Lithium-Anoden bieten können, die die "Holy grail“-Anoden für Lithium-Ionen-Batterien in festem Zustand sind.

In dieser Arbeit wurden sowohl Li-Ionen-aktive als auch inerte keramische Füllstoffe verwendet, um Komposit-Elektrolyte über einen lösungsmittelfreien Ansatz herzustellen, im Gegensatz zu konventionellen lösungsmittelbasierten Ansätzen, bei denen ein keramischer Füllstoff zunächst in einem Lösungsmittel wie Acetonitril dispergiert und dann das Li-Ionen-Salz und das Polymer hinzugefügt wurde. Andererseits, ermöglicht Kryomahlen als lösungsmittelfreier Ansatz, die Exposition empfindlicher keramischer Füllstoffe wie Granate gegenüber Feuchtigkeit zu verhindern und die Erhitzungsschritte nach der Membranherstellung zur Entfernung des Lösungsmittels zu begrenzen. Mischungen von Komposit-Elektrolyten, die von "Keramik in Polymer" bis "Polymer in Keramik" reichen, wurden untersucht, um die Rolle der Füllstoffgröße, der Füllstoffzusammensetzung und des Gewichtsanteils von Füllstoff und Polymer auf die Li-Ionen-Leitfähigkeit mit Hilfe der elektrochemischen Impedanzspektroskopie zu ermitteln. Im Allgemeinen wird festgestellt, dass die Ionenleitfähigkeit mit zunehmendem Gewichtsanteil der Keramik abnimmt und je nach Gewichtsanteil des Füllstoffs im Verhältnis zum Polymer alternative Li-Ionen-Transportpfade zugänglich werden. Es wird versucht, die Li-Ionen-Transportwege in Komposit-Elektrolyten mittels elektrochemischer Impedanzspektroskopie zu untersuchen. Die Ergebnisse zeigen, dass in polymerreichen Kompositelektrolyten die Zusammensetzung des Füllstoffs im Vergleich zur Partikelgröße und -morphologie von geringerer Bedeutung ist, während bei keramikreichen Kompositelektrolyten die intrinsische Leitfähigkeit der Keramik eine wichtige Rolle für die Ionenleitfähigkeit spielt. Darüber hinaus wird die chemische Kompatibilität der Granat/PEO-Grenzfläche mittels elektrochemischer Impedanzspektroskopie untersucht, was auf die Notwendigkeit hinweist, die chemische Stabilität dieser Grenzfläche zu verbessern, um granatreiche Kompositelektrolyte zu realisieren. Zur Verbesserung der Ionenleitfähigkeit in den

granatreichen Verbundelektrolyten wird eine neuartige Idee vorgestellt, die auf der PEO-Infiltration eines porösen, mit Aluminium dotierten Granatnetzwerks basiert, das vor dem Erhitzen behandelt wurde. Ein solches poröses Dünnschichtnetzwerk wird durch die Verwendung von Granatpulvern aus der Sprühpyrolyse und anschließendem Spin Coating hergestellt. Ein vorgewärmtes Grundgerüst würde im Prinzip die Widerstände des Li-Ionen-Transports an der Grenzfläche zwischen den Partikeln im Vergleich zu einem losen mechanischen Kontakt der Granatpartikel in den partikelbasierten Verbundelektrolyten begrenzen. Die poröse Mikrostruktur der Granatdünnschichten und die erfolgreiche Polymerinfiltration werden durch die Rasterelektronenmikroskopie bestätigt. Die Polymerinfiltration führt zu einer Leitfähigkeit von 5.3 x 10^{-7} S cm^{-1} bei 298 K, die um sechs Größenordnungen höher ist als die des ursprünglichen aluminiumdotierten Granatdünnfilms und um eine Größenordnung höher als die des partikelbasierten aluminiumdotierten Granat enthaltenden Verbundelektrolyten mit einem ähnlichen Gewichtsverhältnis von Füllstoff zu Polymer.

Die Vielseitigkeit der Pulversynthese durch vernebelte Sprühpyrolyse ermöglicht auch die Herstellung neuer bariumreicher Kobaltate und Ferrate auf Perowskit-Basis, die als bifunktionale Katalysatoren für Sauerstoffreduktions- und Sauerstoffentwicklungsreaktionen eingesetzt werden können. Die Entwicklung neuer bifunktionaler Katalysatoren ist wichtig, um die träge Kinetik der Sauerstoffreduktions- und Sauerstoffentwicklungsreaktion zu überwinden. Vernebelte Sprühpyrolyse bietet hier den Vorteil der Synthese von Nanopartikeln mit einer großen Oberfläche, die sich als vorteilhaft für die katalytische Leistung erweisen kann.

Unter Verwendung von vernebelte Sprühpyrolyse als Synthesetechnik wurden zum ersten Mal Serien von Verbindungen mit der Zusammensetzung $BaFe_{1-x}Co_xO_{3-y-\delta}(OH)_y$ synthetisiert und untersucht. Es wurde festgestellt, dass die gesamte Serie in der orthorhombischen Raumgruppe *Cmcm* kristallisiert. Iodometrische Titration und Mössbauer-Spektroskopie zeigten, dass Co in Bezug auf seinen Oxidationszustand flexibler ist und je nach Co-Gehalt im Zustand 2+/3+ vorliegt, während Fe unabhängig von der Zusammensetzung den Oxidationszustand 3+ beibehält. Impedanzstudien deuten auf eine verbesserte elektronische Leitfähigkeit hin, wenn der Co-Gehaltzunimmt. Die Leitfähigkeit der x=1 Zusammensetzung beträgt 10^{-4} S cm-1 bei 298 K und ist damit um vier Größenordnungen höher als bei der x=0 zusammensetzung. Außerdem wurde die gesamte Serie auf ihre bifunktionale katalytische Leistung bei der Sauerstoffreduktions- und Sauerstoffentwicklungsreaktion untersucht.

Um die Bedeutung von vernebelte Sprühpyrolyse für die Synthese solcher Oxid-Hydroxid-Phasen hervorzuheben, wurde versucht, ähnliche Zusammensetzungen im Festkörperverfahren zu synthetisieren. In diesem Zusammenhang wurden zwei neue Phasen gefunden, über die bisher noch nicht berichtet wurde. i) $BaCoO_{2.67}$ mit Co in gemischter 3+/4+ Oxidationsstufe und drei verschiedenen Koordinationsumgebungen, d.h. 4-, 5- und 6-fach. Diese Phase wird durch topochemische Oxidation von $BaCoO_{2.46}$ synthetisiert. Die Struktur ist isotypisch zu $BaFeO_{2.33}F_{0.33}$ und $BaFeO_{2.67}$, die beide in der monoklinen Raumgruppe $P2_1/m$ kristallisieren, welche über Gruppen-Untergruppen-Beziehungen mit der kubischen Aristotypstruktur mit der Raumgruppe *Pm*-3*m* verwandt ist. Die gemischte Valenz von Co führt zu einer elektronischen Leitfähigkeit in der Größenordnung von 10^{-4} S cm^{-1} bei 298 K, die derjenigen des x=1 Mitglieders der Serie $BaFe_{1-x}Co_xO_{3-y-\delta}(OH)_y$ ähnelt. Interessanterweise wurde festgestellt, dass die Sauerstoffreduktions- und Sauerstoffentwicklungsaktivität dieser Verbindung mit der des Benchmark-Perowskit-Katalysators $Ba_{0.5}Sr_{0.5}Co_{0.8}Fe_{0.2}O_{3-\delta}$ vergleichbar ist, was auf den intermediären Spinzustand von Co^{3+} zurückzuführen sein könnte, der zu der elektronischen Konfiguration $t_{2g}^5e_g^1$ führt. ii) Eine neue hochgradig

sauerstoffdefiziente tetragonale $BaCoO_{2+\delta}$ Phase mit quadratisch-planarer Koordination von Co^{2+} wurde zum ersten Mal synthetisiert. Die Struktur und deren magnetische und elektronische Eigenschaften werden diskutiert. Diese neue Modifikation unterscheidet sich von der bereits bekannten triklinen Modifikation von $BaCoO_2$ mit vierfacher tetraedrischer Koordination von Co^{2+}. Obwohl die Verbindung aufgrund ihrer metastabilen Beschaffenheit nicht auf ihre katalytische Aktivität hin charakterisiert werden konnte, deutet das aus den Neutronendaten gewonnene magnetische Moment (3,7 μ_B) auf einen hohen Spinzustand für Co^{2+} hin, was eine e_g Besetzung von 2 für diese Verbindung impliziert, während 1 für einen guten bifunktionalen Katalysator erwünscht ist. Interessanterweise ist dies der erste Bericht über die Hochtemperatursynthese einer solchen hochgradig sauerstoffarmen Perowskit-Phase, die traditionell über die Niedertemperatur-Hydrid-Reduktionsmethode synthetisiert wurde.

Abstract

This thesis demonstrates work related to the development and understanding of composite solid electrolytes for all-solid-state lithium-ion batteries and the role of perovskite materials as bifunctional catalyst towards oxygen reduction as well as oxygen evolution reactions for their application in fuel cells and metal-air batteries. The material synthesis of lithium garnets and barium-rich cobaltates and ferrates is carried out via nebulized spray pyrolysis which provides particle morphologies and sizes that may prove to be advantageous for their use in such energy related applications.

All-solid-state lithium-ion batteries consisting of solid electrolytes have the capability for meeting mobile high energy density storage demands as required by electric vehicles in addition to their higher safety. Although variety of different inorganic and organic solid electrolytes have been researched over the years for their application within such batteries, each of these electrolytes have inherent issues like high charge transfer resistance at the electrode/electrolyte interface, mechanical and chemical instabilities at the electrode/electrolyte interface, lower ionic conductivity compared to that of liquid electrolytes and most importantly susceptibility to moisture. In this respect, composite electrolytes comprising of embedded inorganic ceramic fillers and a polymer plus a Li salt matrix can benefit from high Li-ion conductivity and wide electrochemical operational window of the inorganic fillers whereas the polymer can provide good mechanical properties, which may result in low electrode/electrolyte interfacial resistance. Most importantly composite electrolytes may provide mechanical stability against a metallic lithium anode, which is the “holy grail anode” for all-solid-state lithium-ion batteries.

Within this thesis, both Li-ion active and inert ceramic fillers were used to prepare composite electrolytes via a solvent free approach as opposed to conventional solvent-based approaches, where a ceramic filler is first dispersed in a solvent like acetonitrile followed by the addition of Li-salt and the polymer. On the other hand, the use of cryo-milling as a solvent free approach helps in preventing the exposure of sensitive ceramic fillers like garnets to moisture as well as limiting the post membrane fabrication heating steps for solvent removal. Blends of composite electrolytes ranging from “ceramic in polymer” to “polymer in ceramic” were studied to establish the role of filler size, filler composition and filler to polymer weight fraction on the Li-ion conductivity via the use of electrochemical impedance spectroscopy. In general, the ionic conductivity is found to decrease upon the increase in ceramic weight fraction and alternative Li-ion transport pathways become accessible depending upon the filler to polymer weight fraction. An attempt is made to investigate the Li-ion transport pathways within composite electrolytes via electrochemical impedance spectroscopy. The results indicate that within polymer-rich composite electrolytes the composition of the filler is of less relevance compared to that of particle size and morphology, whereas for ceramic-rich composite electrolytes the intrinsic conductivity of the ceramic plays a significant role towards the ionic conductivity. In addition, interfacial chemical compatibility between the garnet/PEO interface is studied via electrochemical impedance spectroscopy and hints towards the need for improving the chemical stability of this interface in order to realize the garnet-rich composite electrolytes. To improve the ionic conductivity within the garnet-rich composite electrolytes, a novel idea based on PEO infiltration of pre-heat treated porous aluminum-doped garnet network is demonstrated. Such a porous thin film network is obtained via the use of as-synthesized garnet powders obtained from nebulized spray pyrolysis followed by spin coating. A pre-heat treated backbone would in principle limit the particle/particle interfacial Li-ion transport resistances compared to that of loose mechanical contact of garnet particles within the particulate-based

composite electrolytes. The porous microstructure of the garnet thin films along with the successful polymer infiltration is confirmed via scanning electron microscopy. The polymer infiltration results in a conductivity of 5.3 x 10^{-7} S cm^{-1} at 298 K which is six orders of magnitude higher than pristine aluminum-doped garnet thin film and an order of magnitude higher than the particulate based aluminum-doped garnet containing composite electrolyte with similar filler to polymer weight ratios.

The powder synthesis versatility of nebulized spray pyrolysis also allows for the preparation of new perovskite-based barium-rich cobaltates and ferrates, that can be used as bifunctional catalyst towards oxygen reduction reaction and oxygen evolution reaction. Developing new bifunctional catalyst is important to overcome sluggish kinetics of oxygen reduction reaction and oxygen evolution reaction. Herein, nebulized spray pyrolysis offers advantage of synthesizing nano-particles that offer high surface area that can prove to be beneficial towards catalytic performance.

Using nebulized spray pyrolysis as the synthesis technique series of compounds with the composition $BaFe_{1-x}Co_xO_{3-y-\delta}(OH)_y$ were synthesized and investigated for the first time. The whole series was found to crystallize in the orthorhombic space group *Cmcm*. Iodometric titration and Mössbauer spectroscopy indicated that Co is more flexible with respect to its oxidation state and is present in 2+/3+ state depending on the Co content whereas Fe was found to maintain 3+ oxidation state irrespective of the composition. Impedance studies indicate an enhanced electronic conductivity as the Co content increases with the x=1 composition demonstrating a conductivity of 10^{-4} S cm^{-1} at 298 K that is four orders of magnitude higher than the x=0 member. Further, the whole series was investigated for its bifunctional catalytic performance towards oxygen reduction reaction and oxygen evolution reaction.

To highlight the importance of nebulized spray pyrolysis towards the synthesis of such oxide hydroxide phases, attempts were made to synthesize similar compositions via solid-state route. In this context two new phases were found which had not been reported so far. i) $BaCoO_{2.67}$ with Co in mixed 3+/4+ oxidation state and occupying three different coordination environments i.e. 4-, 5- and 6-fold. This phase is synthesized via topochemical oxidation of $BaCoO_{2.46}$. The structure is found to be isotypic to $BaFeO_{2.33}F_{0.33}$ and $BaFeO_{2.67}$, both crystallizing in the monoclinic space group $P2_1/m$, which is related to the cubic aristotype structure with space group $Pm\text{-}3m$ via group-subgroup relations. The mixed valence of Co results in the electronic conductivity of an order of 10^{-4} S cm^{-1} at 298 K which similar to that of the x=1 member of the series $BaFe_{1-x}Co_xO_{3-y-\delta}(OH)_y$. Interestingly, oxygen reduction and oxygen evolution activity of this compound was found to be comparable to that of benchmark perovskite catalyst $Ba_{0.5}Sr_{0.5}Co_{0.8}Fe_{0.2}O_{3-\delta}$, which could be due to the intermediate spin state of Co^{3+} resulting in the electronic configuration of $t_{2g}^5e_g^1$. ii) A new highly oxygen deficient tetragonal $BaCoO_{2+\delta}$ phase with square planar coordination of Co^{2+} is synthesized for the first time. The structure and its magnetic and electronic properties are discussed. This new modification is different compared to already known triclinic modification of $BaCoO_2$ with four-fold tetrahedral coordination of Co^{2+}. Although the compound could not be characterized for its catalytic activity due to its metastable nature, the magnetic moment (3.7 μ_B) obtained from the neutron data suggests a high spin state for Co^{2+} which implies an e_g occupancy of 2 for this compound whereas 1 is desired for a good bifunctional catalyst. Interestingly, this is the first report on the high temperature synthesis of such highly oxygen deficient perovskite phase, which traditionally have been synthesized via the low temperature hydride reduction method.

Preface: - Personal contribution

This thesis presents a cumulative dissertation summarizing the scientific findings published in the peer-reviewed journals. The articles published have been adapted to the corporate design of TU Darmstadt. To make it easier for the reader to follow, the important parts of the supplementary information have been incorporated within the text of main chapters. Minor corrections or typos within the published articles, if found, were corrected. Other than that no changes have been made to the original publications. The publications along with the personal contribution are listed below.

1. **Compositional Dependence of Li-Ion Conductivity in Garnet Rich Composite Electrolytes for All-Solid-State Lithium-Ion Batteries – Towards Understanding the Drawbacks of Ceramic Rich Composites**
   Reprinted with permission from {A. I. Waidha, T. Ferber, M. Donzelli, N. Hosseinpourkahvaz, V. Vanita, K. Dirnberger, S. Ludwigs, R. Hausbrand, W. Jaegermann and O. Clemens, *ACS Appl Mater Interfaces*, 2021, **13**, 31111-31128.}. Copyright {2021} American Chemical Society.

The sample preparation, X-ray diffraction, impedance spectroscopy and scanning electron microscopy experiments were planned, carried out and analyzed by myself. XPS studies on the thin films and garnet thin film synthesis were carried out by Thimo Ferber and Manuel Donzelli, respectively. Niloofer Hosseinpourkahvaz contributed to impedance measurements and prepared the samples for SEM. FT-IR and Raman measurements were carried out by Vanita Vanita. Dr. Klaus Dirnberger and Prof. Sabine Ludwigs collected and evaluated the DSC data on the composite electrolytes. The funding for the project was secured by Dr. René Hausbrand, Prof. Wolfram Jaegermann and Prof. Oliver Clemens. The manuscript draft was written and composed by myself and proof read by Prof. Oliver Clemens. XPS part of this article was written by Thimo Ferber and proof read by Dr. René Hausbrand, Prof. Wolfram Jaegermann and Prof. Oliver Clemens. All authors contributed towards the discussion and feedback towards the final published article.

2. **PEO Infiltration of Porous Garnet-Type Lithium-Conducting Solid Electrolyte Thin Films**
   A. I. Waidha, V. Vanita and O. Clemens, *Ceramics*, 2021, **4**, 421-436. Reprinted under Creative Commons CC By 4.0 license.

In this article, measuring and analysis of X-ray diffraction, impedance spectroscopy and scanning electron microscopy measurements were carried out by myself. Garnet powders and thin films were prepared by Vanita Vanita and were part of her advanced research lab project. Infiltration of the films were carried out by myself. The article was written by me along with Prof. Oliver Clemens.

3. **Synthesis, Structure and Electrical Conductivity of a New Perovskite Type Barium Cobaltate $BaCoO_{1.80}(OH)_{0.86}$**
   Reproduced from Ref. A. I. Waidha, M. Lepple, K. Wissel, A. Benes, S. Wollstadt, P. R. Slater, A. D. Fortes and O. Clemens, *Dalton Trans.*, 2018, 47, 11136-11145 with permission from the Royal Society of Chemistry.

Within this publication, sample synthesis, diffraction experiments, impedance spectroscopy, energy dispersive X-ray spectroscopy, Fourier-transform infrared spectroscopy and iodometric titration were carried out and analyzed by myself. DSC measurements were carried out by Dr. Maren Lepple. Dr. Kerstin Wissel carried out the scanning electron microscopy of the samples. Dr. A. Benes measured XPS spectra. Both Prof. Peter slater and Dr. A.D. Fortes were part of neutron experiment proposal and experiments, respectively. The manuscript was written by me along with Prof. Oliver Clemens. All the co-authors proof-read the manuscript.

4. **Synthesis of Bifunctional $BaFe_{1-x}Co_xO_{3-y-\delta}(OH)_y$ Catalysts for the Oxygen Reduction Reaction and Oxygen Evolution Reaction**
   Reproduced from Ref. A. I. Waidha, L. Ni, J. Ali, M. Lepple, M. Donzelli, S. Dasgupta, S. Wollstadt, L. Alff, U. I. Kramm and O. Clemens, J. Mater. Chem. A, 2020, 8, 616-625 with permission from the Royal Society of Chemistry.

The synthesis and experiments were planned by myself. Jasim Ali carried out the powder synthesis and iodometric titrations. X-ray diffraction, impedance spectroscopy, scanning electron microscopy and Fourier-transform infrared spectroscopy were carried out by myself. Mössbauer and electrochemical measurements were carried out by Lingmei Ni and Prof. Ulrike Kramm. Lingmei Ni also provided the plots for the electrochemical data. SQUID measurements were carried out by Supratik Dasgupta and Prof. Lambert Alff. M. Donzelli carried out the XPS measurements. The manuscript was written by me followed by proof reading by Prof. Oliver Clemens and Prof. Ulrike Kramm. All co-authors contributed towards the discussion.

5. **Structural, Magnetic and Catalytic Properties of a New Vacancy Ordered Perovskite Type Barium Cobaltate $BaCoO_{2.67}$**
   A. I. Waidha, H. Khatoon Siddiqui, Y. Ikeda, M. Lepple, S. Vasala, M. Donzelli, A. D. Fortes, P. Slater, B. Grabowski, U. I. Kramm and O. Clemens, *Chemistry*, 2021, **27**, 9763-9767. Reprinted under Creative Commons CC By 4.0 license.

Sample synthesis, X-ray diffraction, impedance spectroscopy, scanning electron microscopy, energy dispersive X-ray spectroscopy and iodometric titration were carried out by myself. Computational studies were carried out by Dr. Yuji Ikeda and Prof. B. Grabowski. DSC measurements were carried out by Dr. Maren Lepple. Magnetic measurements were carried out by Dr. Sami Vasala. Humera Khatoon Siddiqui and Prof. Ulrike Kramm measured the catalytic activity of the title compound. M. Donzelli measured and analyzed the XPS spectra. Both Prof. Peter slater and Dr. A.D. Fortes were part of neutron experiment proposal and experiments, respectively. The manuscript was written by me and Prof. Oliver Clemens did the proof reading. All co-authors contributed to the discussions and graphs related to the publication.

6. **$BaCoO_{2+\delta}$: A New Highly Oxygen Deficient Perovskite-Related Phase With Unusual Co Coordination Obtained by High Temperature Reaction with Short Reaction Times**
   Reproduced from Ref. A. I. Waidha, H. Zhang, M. Lepple, S. Dasgupta, L. Alff, P. Slater, A. D. Fortes and O. Clemens, *Chemical Communications*, 2019, **55**, 2920-2923 with permission from the Royal Society of Chemistry.

The sample synthesis, X-ray diffraction, impedance spectroscopy, energy dispersive X-ray spectroscopy, iodometric titration and Raman spectroscopy were carried out and evaluated by myself. The structural solution of the title compound via coupled Rietveld analysis of X-ray and neutron powder diffraction data was done with the inputs from Prof. Oliver Clemens. DFT studies were carried out by Hongbin Zhang. Dr. Maren Lepple carried out DSC measurements. SQUID measurements were carried out by Supratik Dasgupta and Lambert Alff. The proposal for neutron diffraction experiment was written in collaboration with Prof. Peter Slater. Dr. Andreas Fortes helped with carrying out neutron experiments at ISIS facility, Didcot, UK. The manuscript was written by myself along with inputs from Prof. Oliver Clemens. All the authors proof read the manuscript and contributed towards the discussion.

Table of Content

1 Introduction

The ever increasing demand for energy due to rapid population growth and industrialization has been a major factor for our dependence on non-renewable sources of energy i.e. fossil fuels, such as coal, natural gas, petroleum etc. Although, our requirements for the energy have been met so far but this has simultaneously put a great amount of strain on our conventional sources of energy and has driven them to the point of exhaustion. Not only this, the burning of the fossil fuels has significantly contributed towards environmental pollution due to the production of greenhouse gases, which are the major cause for global climate change. A recent study by the researchers from the University of Harvard has shown that exposure to the particulate matter from the fossil fuel emissions accounts for 18% of the global deaths which related to almost one in five in 2018 [1]. Therefore, the need for transition towards greener alternatives is quite clear and evident while we still have the time.

1.1 Future energy supply and the problem of energy storage

One of the major challenges of the 21st century is the development of new renewable and clean energy sources and limiting the use of fossil fuels. This requires a well-coordinated strategy that includes everything ranging from short-term solutions to a comprehensive research of alternative energy sources and an appropriately adapted energy infrastructure. A variety of different alternate fossil fuel sources have been of interest to fulfil the future energy demand. These are hydrogen, wind, hydro, solar etc. Among these capture of radiation energy from the sun has the potential to meet all the energy requirements of the planet and indeed development of the solar cell technology has received a significant attention over the years [2]. Nevertheless, an important drawback of all these technologies is their intermittent nature. This means that these won't be available round the clock and are affected by various geological, cost, political etc. factors. For example, duration and intensity of sun light for solar cells and water flow in streams for hydro energy. Additionally, most of these renewable energy sources are suited for grid production as opposed to mobile applications like in the case of electrical vehicles. Therefore, these sources of energy require a storage system, which can store the produced energy during high availability and deliver the same during low availability. Hence, energy storage systems are essential for regulating the fluctuating energy from renewable energy sources.

Batteries are the most promising and effective candidates for energy storage and transport. Among the battery systems, lithium ion batteries (LIBs) are thought to be most promising and successful due to their high energy density, mobility, fast charging/discharging capabilities and the battery of choice for electric vehicles [3]. Nevertheless, conventional LIBs using graphite anode and a liquid electrolyte suffer from major drawbacks. Although the liquid electrolytes used in conventional LIBs offer high room temperature Li-ion conductivity (10.7 mS cm^{-1} for $LiPF_6$ in 1:1 solvent of EC/DMC), they suffer from severe drawbacks in terms of cycle life and safety [4, 5]. The commercially used liquid electrolytes are mainly solutions composed of one or more lithium salts dissolved in two or more solvents. The use of mixed solvent formulation is to meet the contradicting requirements of battery applications, which cannot be completely fulfilled by an individual solvent or a salt. Moreover, the goal is to implement metallic Li as an anode, which offers higher capacity as compared to that of graphite anode eventually resulting in high energy density LIBs. For example, Propylene carbonate (PC) attracted wide research interest due to its high dielectric constant, which describes the ability to dissolve wide range of lithium salts [5]. PC also possesses a wide liquid range, which is the difference between its

melting (224.3 K) and boiling (515 K) temperature [6]. However, Li-ion cells with metallic Li anode and PC electrolyte suffer from capacity fading, which is mainly due to the unwanted side reactions occurring at the lithium/PC interface [5]. Further, non-uniform stripping and plating of Li-ions on the lithium surface during cycling was observed, which results in the dendrite formation [5]. On the other hand, ether based electrolytes have been of interest not only due to their low viscosity and resulting high ionic conductivity but also due to their better cycling ability which prevents dendrite formation during cycling at the Li electrode [5]. However, the lithium ion cells containing these electrolytes and metallic Li anode demonstrate poor capacity retention and further results in dendrite formation at higher cycles (>100 cycles) [7]. Ethylene carbonate (EC) has comparable viscosity to that of PC and has slightly higher dielectric constant, which would favor salt dissociation. However, EC has high melting point ~309 K, therefore preventing its use as room temperature electrolyte. Nonetheless, none of the individual electrolytes possess sufficient characteristics for their use as electrolytes in high energy density LIBs. Most importantly, all these electrolytes are unstable with metallic lithium which offers an order of magnitude higher theoretical capacity (3860 mA h g^{-1}) compared to that of traditional carbon based anodes (372 mA h g^{-1}) [8, 9], therefore limiting the energy density of LIBs. Additionally, lithium hexaphosphate the most widely used Li-salt in liquid electrolytes, despite having high thermal stability in inert and dry atmospheres up to 380 K is highly reactive towards moisture or alcohols, resulting in the formation of highly acidic and corrosive hydrogen fluoride (HF) [4]. The reaction first involves the decomposition of $LiPF_6$ leading to the formation of lithium fluoride and phosphorous pentafluoride:

$$LiPF_6 \rightarrow LiF + PF_5$$

PF_5 can then further go on to react with water resulting in the formation of corrosive

$$PF_5 + H_2O \rightarrow POF_3 + 2HF$$

The formed HF can cause leaching of metal ions from the cathodes into the liquid electrolytes and cause capacity fading.

In this context, all solid state lithium ion batteries (ASSLIBs) based on a solid electrolytes (SEs) can address not only the safety concerns of the conventional liquid electrolyte based LIBs, but also enable the use of metallic lithium as an anode and high voltage cathode materials, resulting in the high energy density and long term stable batteries.

1.2 All-solid-state Li-ion batteries and composite electrolytes

All solid state batteries comprising of SEs seem to be promising due to their higher safety, energy density and cycle life compared to conventional LIBs. SE is a critical component in a solid state battery along with the electrode materials, since they determine the power density, stability and the safety of the solid state batteries. For the successful implementation of SEs in ASSLIBs, SEs must not only possess high ionic conductivity (>10^{-4} S cm^{-1}), negligible electronic conductivity (<10^{-12} S cm^{-1}) but also chemical compatibility with the electrodes and wide electrochemical window [10]. Further, replacement of the liquid electrolyte with a SE could resolve other key issues which limit the performance of the conventional LIBs like cathode dissolution, capacity fading and higher Li-ion transference numbers. The schematic representation of ASSLIB is shown in Figure 1.1.

In terms of safety, SEs enable removal of volatile and flammable carbonate based electrolytes. Overheating of the battery occurring due to battery operation or high ambient temperatures can result in series of reactions within conventional LIBs, for example $LiPF_6$ can decompose into LiF and gaseous PF_5 at temperatures above 343 K [11]. PF_5 is highly reactive with moisture,

resulting in the formation of hazardous HF. Therefore, in case the battery casing is damaged, all the toxic and flammable components can leak which can cause a great deal of bodily harm. Additionally, gas pressure above the threshold value can result in battery explosion [11, 12]. At temperatures above 473 K to 523 K, liquid electrolytes tend to react with the electrode materials ($LiCoO_2$, $LiNiO_2$, $LiMnO_2$) resulting in the formation of O_2. This can lead to energy generation of more than 2000 J g^{-1}, resulting in temperatures reaching 873 K within few minutes causing battery explosion [13, 14]. SEs on the other hand are resistant to such thermal decompositions within these temperature ranges. Although the safety data of ASSLIBs is rare, the superiority of these batteries can be inferred from the following key points. i) SEs are usually synthesized at temperatures far above 473 K, therefore these can be expected to be thermally stable up to these temperatures. ii) Safety can also be established from the fact that these batteries are operated at temperatures of about 373 K, whereas for the conventional LIBs, operation below 333 K is usually recommended. Additionally, ASSLIBs do not require a polypropylene or polyethylene separator, present in conventional LIBs with liquid electrolytes, which can melt at temperatures of 423 K and cause internal short circuiting in batteries [15].

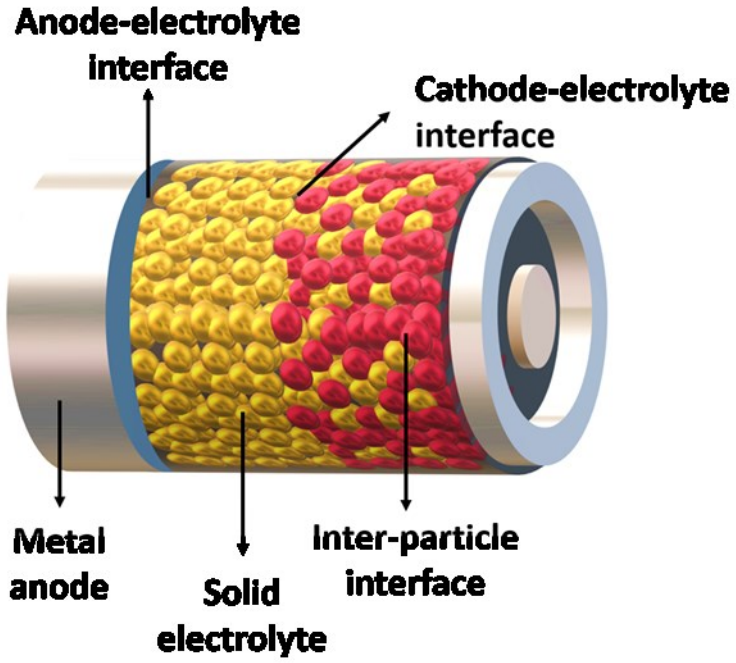

Figure 1.1: Schematic of a ASSLIB with its components and interfaces between the components.

ASSLIBs can also offer longer cycle lifetimes due to reduction of side reactions at the electrode/electrolyte interface. For example, in conventional LIBs, a stable solid electrolyte interface (SEI) is formed between the carbon anode and liquid electrolyte below 1V vs Li^+/Li, preventing further reaction [16]. However, this interface can still be damaged due to reaction with the transition metal ions which are dissolved in the liquid electrolyte due to cathode dissolution and migrate from the cathode towards the anode. Additionally, this results in the capacity loss and poor cycling ability [17, 18]. In contrast, SE not only impedes metal ion dissolution but also enables longer battery cycling life [19].

Both inorganic and organic solid electrolytes have received significant interest over the years. Among inorganic solid electrolytes, sulfide based electrolytes have demonstrated highest ionic conductivities but they are known to be highly sensitive towards moisture and unstable with Li metal anode [10, 20]. NASICON-type (e.g., $Li_{1.3}Al_{0.3}Ti_{1.7}(PO_4)_3$) materials are stable in ambient atmosphere, show wide electrochemical operational window and also high Li-ion

conductivities, but these suffer from high grain boundary resistances and are also unstable with metallic Li anode [10]. Perovskite-based electrolytes (e.g., $La_{0.57}Li_{0.29}TiO_3$) demonstrate high grain conductivity, high mechanical strength to avoid dendrite growth and wide operational window, however they suffer from high grain boundary resistance and stability issues with Li metal anode [10]. Li-containing garnets (e.g., $Li_7La_3Zr_2O_{12}$ (LLZO)) on the other hand are stable with Li-metal anode, possess high Li-ion conductivity, wide electrochemical window and high mechanical strength [10]. However, the main drawback is their high brittleness resulting in high interfacial resistances at Li/garnet interface and their sensitivity to moisture leading to the formation of decomposition products at their interfaces, i.e. Li_2CO_3 [21].

On the other hand, organic-based polymer solid electrolytes (PSE) offer flexibility, light weight and are also inexpensive. A variety of PSEs, such as polyvinylidene fluoride (PVDF), polyacrylonitrile (PAN), poly(ethyl carbonate) (PEC), poly(methyl methacrylate) (PMMA) and polyethylene oxide (PEO), have been of interest [22]. Due to their flexibility they have the ability of forming a smooth and uniform contact at the electrode/electrolyte interface, which can lower the resistances at these interfaces. From the application point of view, these polymer electrolytes should possess high Li-ion conductivity, wide electrochemical operational window, high mechanical strength, chemical/mechanical stability with electrode materials and scalability. However, similar to inorganic SE, none of the single polymer electrolyte possess all these properties. Most of the single polymer electrolytes suffer from low Li-ion conductivity (10^{-5} -10^{-7} S cm^{-1}) at room temperatures along with low Li-ion transference numbers (0.22) [23, 24]. Further, they also suffer from poor thermal and electrochemical stabilities [25].

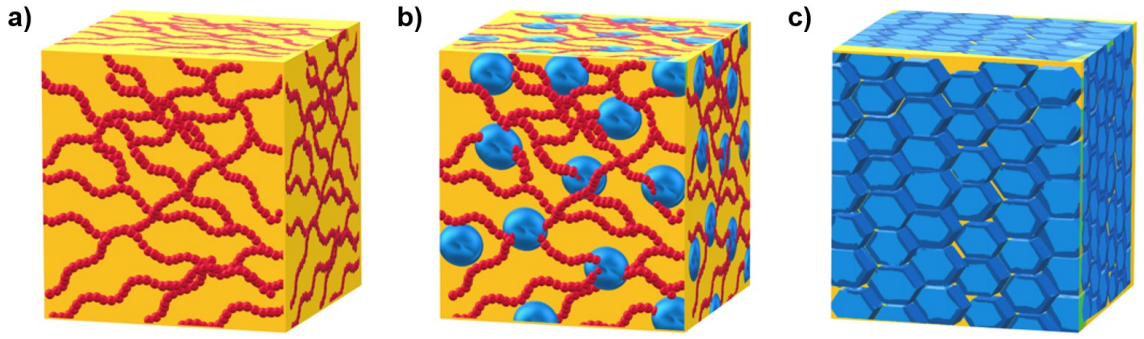

Figure 1.2: Schematic representation of a) polymer electrolytes with polymer chains, b) composite electrolytes with polymer chains and ceramic filler particles and c) well sintered ceramic electrolyte.

To overcome the inherent problems of the individual solid electrolytes, a viable solution similar to the liquid electrolytes is to combine them. The resulting composite electrolyte (CE) comprising of inorganic and organic conductors might be the ultimate solution, which benefits from the virtues of each component. For instance, the addition of polymer to a garnet electrolyte can improve the charge transfer resistance at the electrode/electrolyte interface. On the other hand, addition of inorganic electrolyte to polymer may improve its ionic conductivity, Li-ion transference number and mechanical strength. Figure 1.2 shows the representation of polymer electrolyte, composite electrolyte and ceramic electrolyte along with their properties in Table 1.1.

Table 1.1: Comparison of the properties between polymer, composite and ceramic electrolytes.

Polymer Electrolyte	Composite electrolyte (aim and hopes)	Ceramic electrolyte
Low ionic conductivity	High ionic conductivity	High ionic conductivity
Low Li-ion transference number	Transference number = 1	Transference number = 1
Flexible	Flexible	Rigid
Limited stability against Li metal	Stable against Li metal	Stable against Li metal
Compatible with volume changes	Compatible with volume changes	Not compatible

To overcome the inherent problems of the individual solid electrolytes, a viable solution similar to the liquid electrolytes is to combine them. The resulting composite electrolyte (CE) comprising of inorganic and organic conductors might be the ultimate solution, which benefits from the virtues of each component. For instance, the addition of polymer to a garnet electrolyte can improve the charge transfer resistance at the electrode/electrolyte interface. On the other hand, addition of inorganic electrolyte to polymer may improve its ionic conductivity, Li-ion transference number and mechanical strength. Figure 1.2 shows the representation of polymer electrolyte, composite electrolyte and ceramic electrolyte along with their properties in Table 1.1.

1.3 Perovskites and their importance for fuel cell materials

Although the ASSLIBs can solve the energy storage and mobile application issues, they still need to be charged, which requires energy. In this respect an on-demand renewable energy sources coupled to a energy storage device like LIB has the benefits of providing energy whenever and wherever required. In this respect fuel cells are highly desired due to their clean operation. A fuel cell is an electrochemical device that is capable of converting chemical energy into electrical energy via oxygen reduction reaction (ORR) using oxygen and hydrogen as fuel. Conversely water electrolyzer is a device which splits water into hydrogen and oxygen via hydrogen evolution reaction (HER) and oxygen evolution reaction (OER), respectively. Both ORR and OER reactions are also important for energy storage devices like metal-air batteries. For metal-air batteries, ORR takes place during the discharge cycle while OER takes place during the charging process [26]. Therefore, catalyzing both ORR and OER becomes a critical requirement for a material for its application as bifunctional catalyst in fuel cells, electrolysis cells or metal-air batteries. However, both ORR and OER are kinetically sluggish, resulting in over potentials and limiting the commercialization of these energy devices [26]. Currently, noble metal based platinum (Pt) and palladium (Pd) are the benchmark catalyst for ORR and IrO_2 and RuO_2 are the best known OER catalyst [27]. However, these materials are scarce and costly. Therefore, significant efforts are dedicated towards development of new non-noble metal bifunctional catalyst towards ORR and OER. In this respect perovskite oxides have attracted a great attention due to their unique and tunable electronic and catalytic properties [28]. Figure 1.3 illustrated the role of mixed electron proton conducting perovskite towards ORR.

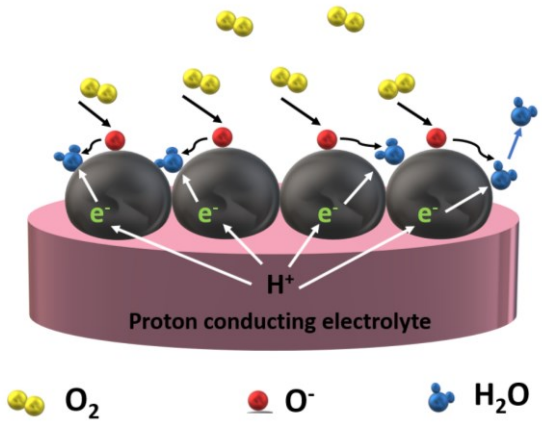

Figure 1.3: Graphic representing working concept of mixed ion conducting perovskite wherein a proton conducting perovskite is used as a cathode material and oxygen reduction reaction is taking place on the surface on the cathode particle resulting is the formation of water.

Perovskite materials have their origin dated back to 1839 when $CaTiO_3$, a mineral referred to as perovskite and named after Russian mineralogist, L. A. Perovski was discovered [29]. The perovskite crystal structure is highly flexible with respect to its cationic, anionic composition and structural defects. These consist of wide range of compositions as nearly all the metals ions can be incorporated within this structure. Among them oxide-based perovskites are widely interesting due to their application in energy conversion and storage devices ranging from solid oxide fuel cells (SOFCs), solid oxide electrolysis cells (SOECs) to metal-air batteries [26]. Via the cationic substitution or deficiency at the A/B site, perovskites with a new formula of $A'_yA_{1-y}B'_xB_{1-x}O_{3-\delta}$ can be synthesized. Due to this, their physiochemical properties can be altered, which can further allow for tuning their catalytic ORR/OER activities. The compositional and crystal structural flexibility of perovskites leads to tunable electronic properties of perovskite oxides, which in turn also tunes their various physical and chemical properties and therefore makes them an ideal candidate as bifunctional electrocatalyst for ORR and OER [27,28, 30].

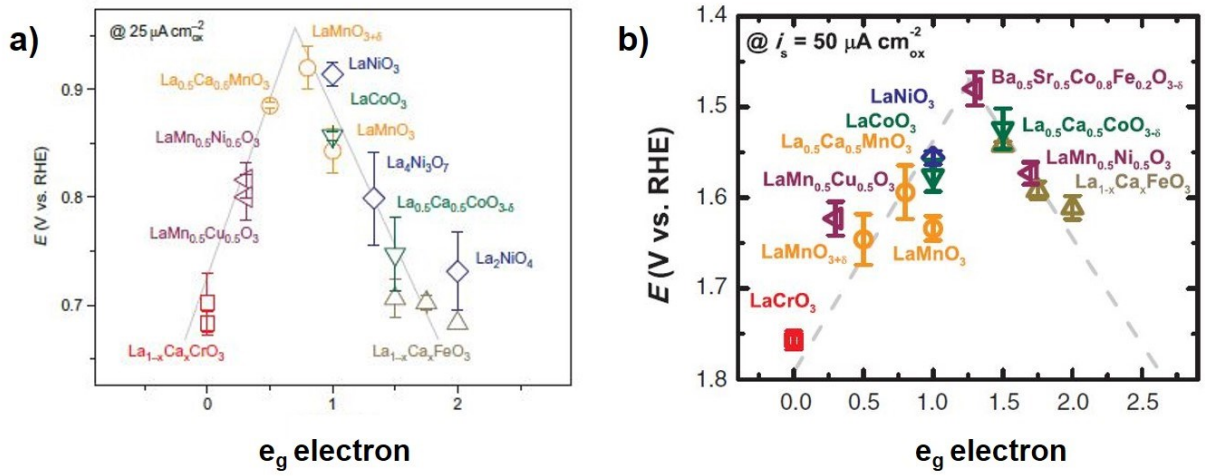

Figure 1.4: Volcano trend observed for both a) ORR (Reprinted with permission from ref.[31], Copyright 2011, Nature Publishing Group and b) OER (From [32], Reprinted with permission from AAAS) for transition metal containing perovskite oxides.

For perovskite different activity descriptors have been given in the literature in order to search for a high performance bifunctional catalyst. For example, the group of Shao-Horn et. al reported the molecular orbital principles as the activity descriptor for ORR and OER for perovskite oxides [31, 32]. The activity descriptor is associated with the filling of the e_g orbital of the B cation, which is usually a transition metal cation in the perovskite. Due to the dominance of the overlap between the e_g orbital and adsorbate compared to that of t_{2g} orbit, the electron number in the e_g orbit correlates with the binding strength of the adsorbed oxygen species to the active metal site. Hence, OER and ORR activity both are correlated to the e_g filling of the B site cation and shows a volcanic type plot, where on the both sides of the volcano lie the perovskites with little or high e_g occupancy. Perovskites with best ORR/OER performance are known to show e_g filling close to 1 as shown in Figure 1.4.

The e_g occupancy of the active B site depends on both the oxidation and the spin states. In this respect perovskites based cobaltates are interesting candidates as bifunctional catalyst for ORR and OER since both the oxidation states and spin of the Co can be tuned.

1.4 Structure of the thesis

This cumulative thesis consists of two main parts dealing with synthesis and characterization of garnet and perovskites materials via nebulized spray pyrolysis (NSP) for their use in composite electrolytes for ASSLIBs and as bifunctional catalyst, respectively. The fundamentals relevant to these two chapters are summarized in **chapter 2** where the basic concepts related to NSP, Li-ion batteries, composite electrolytes, and perovskite structure are given. Additionally, scientific and theoretical fundamentals of different characterization techniques used within this thesis are discussed.

Chapter 3 is entirely dedicated to the composite electrolytes for ASSLIBs. This chapter comprises of two publications. Before these articles are mentioned, a brief summary of the scientific findings from these two articles is presented. The first publication given in **section 3.1** deals with the characterization of composite electrolyte membranes ranging from "ceramic in polymer" to "polymer in ceramic". An in depth analysis of Li-ion transport within the composite electrolytes via impedance spectroscopy is provided. The interfacial studies are carried out to establish the stability between the individual components within the CEs. In **section 3.2,** an attempt is made to fabricate ceramic-rich CE with an aim to improve the Li-ion conductivity using a 3-dimensional Li-ion conducting porous garnet LLZO backbone. The porous garnet backbone is synthesized via the combination of NSP and spin coating followed by its infiltration with a Li-ion conducting polymer. The two publications within this chapter are

1. **3.1 Compositional Dependence of Li-ion Conductivity in Garnet Rich Composite Electrolytes for All Solid State Lithium Ion Batteries – Towards Understanding the Drawbacks of Ceramic Rich Composites**
2. **3.2 PEO Infiltration of Porous Garnet-Type Lithium-Conducting Solid Electrolyte Thin Films**

Chapter 4 is focused on different perovskite-related barium cobaltate systems and their application as bifunctional catalyst towards ORR and OER. This chapter comprises of two publications and 2 short communications, each dealing with a different composition synthesized during the course of this thesis. Before these publications are given, a summary of the scientific findings within these publications is given. This is followed by cumulative part comprising of four publications divided into four sections. **Section 4.1** is the publication related to the synthesis of the first hydrated phase $BaCoO_{1.80}(OH)_{0.86}$ within the $BaCoO_{3-\delta}$ system via NSP. The structural, electronic and magnetic properties of this system are discussed. A special emphasis is given to highlight the role of temperature on water loss and structural transitions studied via a combination of high temperature XRD and STA. **Section 4.2** deals with the synthesis of the whole series of $BaFe_{1-x}Co_xO_{3-y-\delta}(OH)_y$ via NSP. The water uptake and average oxidation as a function of Co doping is studied. The electronic and catalytic properties as a function of Co doping are presented**.** In addition to these two articles, two communications related to the side products synthesized via solid state route obtained during the course of this thesis are also given, which establishes the uniqueness of NSP in synthesizing the oxy hydroxide compounds within the barium cobaltate system. In **Section 4.3** the focus is on the topochemical oxidation of $BaCoO_{2.46}$ resulting in the synthesis of a new vacancy ordered compound with the composition of $BaCoO_{2.67}$ with charge ordering between Co^{3+} and Co^{4+}. The compound is characterized for its structure, electronic and magnetic properties. The bifunctional performance of this composition towards ORR and OER is discussed in comparison to the benchmark perovskite catalyst $Ba_{0.5}Sr_{0.5}Co_{0.8}Fe_{0.2}O_{3-\delta}$. In **Section 4.4**, the communication related to the characterization of a new metastable modification of highly anion deficient perovskite-related $BaCoO_{2+\delta}$ with interesting square planar coordination of Co^{2+} ions,

synthesized via the high temperature solid state route is given. The structural, magnetic and electronic properties of this system are discussed. Overall **chapter 4** comprises of following publications:

1. **4.1 Synthesis, structure and electrical conductivity of a new perovskite type barium cobaltate $BaCoO_{1.80}(OH)_{0.86}$**
2. **4.2 Synthesis of bifunctional $BaFe_{1-x}Co_xO_{3-y-\delta}(OH)_y$ catalysts for the oxygen reduction reaction and oxygen evolution reaction**
3. **Structural, Magnetic and Catalytic Properties of a New Vacancy Ordered Perovskite Type Barium Cobaltate $BaCoO_{2.67}$**
4. **$BaCoO_{2+\delta}$: A new highly oxygen deficient perovskite-related phase with unusual Co coordination obtained by high temperature reaction with short reaction times**

2 Fundamentals

This chapter provides a summary of the fundamentals which are relevant towards understanding the scientific findings presented in this thesis. A brief introduction to LIB is given while focusing on the SE materials for ASSLIBs. An overview of the perovskite structure is provided and the necessary properties of the perovskite type compounds, concerning their application as bifunctional catalyst for the oxygen reduction reaction and oxygen evolution reaction are briefly discussed. In addition, the working principles of variety of characterization methods used within the scope of this thesis are presented.

2.1 Nebulized spray pyrolysis

Nebulized spray pyrolysis (NSP) is a highly flexible technique for the synthesis of nano-crystalline powders and thin films with a precise control over morphology. The technique paves way for the continuous synthesis of nanomaterials which are typically synthesized in batches. The technique offers additional control over chemical composition with powders having stoichiometry identical to the precursor solution without being contaminated by impurities such as those coming from the crucibles during solid state route. Therefore, NSP is suitable for synthesizing high purity metal oxide powders as well as thin films [33].

Recently, Djenadic et al. demonstrated the use of NSP towards the synthesis of nanocrystalline LLZO and Al-doped LLZO via this method [34]. During their synthesis, they observed that the as-synthesis powders obtained are mixture of $La_2Z_2O_7$ and Li_2CO_3. Heating this powder further at 1273 K for just 1 hours resulted in the formation of the desired garnet phase. Interestingly, the pellets prepared via this method exhibited the ionic conductivity of 1.2 x 10^{-6} S cm^{-1} and 4.4 x 10^{-6} S cm^{-1} for tetragonal and cubic garnets, respectively. The observed ionic conductivity is low, especially for the cubic Al-doped LLZO garnet which has been known to exhibit the ionic conductivity of 4 x 10^{-4} S cm^{-1}, which is nearly two orders of magnitude higher than the NSP synthesized cubic Al-doped LLZO garnet. This lower ionic conductivity was attributed to the lower relative pellet density of 47-56%. For the use of inorganic ceramic electrolytes relative density of 100% is desired. The conductivity of the NSP synthesized pellet can be drastically improved by combining it to techniques like field assisted sintering technique (FAST). Botros et al. demonstrated that by combing NSP and FAST, the ionic conductivity of 0.33 mS cm^{-1} can be achieved for the Al-doped LLZO with the activation energy of 0.38 eV [35]. In comparison NSP synthesized pellets showed the activation energy of 0.49 eV. The improved conductivity was due to high relative density of pellets, i.e. 93%. Nevertheless, such porous garnets might be beneficial in composite electrolytes, where continuous 3 dimensional ceramic network can provide Li-ion conducting pathways along with the garnet/polymer interface and the polymer itself.

Similarly, compounds with perovskite structure can also be synthesized via NSP. Here, NSP offers an additional advantage of not only fast but also direct synthesis of perovskite compounds, i.e. the as-synthesized powders obtained show both the perovskite-type composition and structure as opposed to garnets where additional post synthesis heating step is required in order to obtain the desired phase. Benel et al. reported on the synthesis of $La_{0.6}Sr_{0.4}CoO_{3-\delta}$ via NSP [36]. Recently, Knöchel et al. reported on a hydrated perovskite compound $BaFeO_{2.33}OH_{0.33}$ and $BaFeO_{2.25}OH_{0.5}$, which are the water containing counterparts of $BaFeO_{2.5}$ [37]. The inclusion of protons leads to increased conductivity in the hydrated phases compared to that of water free $BaFeO_{2.5}$ due to proton conductivity. During the master thesis of the author, it was observed that water rich phase $BaCoO_{1.80}(OH)_{0.86}$ can be synthesized via

NSP and could not be synthesized via the conventional solid-state route. Interestingly, such a water-rich phases had not been previously observed within the barium cobaltate perovskite system. Further, the compound showed *ccp* arrangement of $AO_{3-\delta}$ layers, which is unusual for barium cobaltates since they are known to crystallize in hexagonal cubic packing (*hcp*) arrangement due to the large size of Ba atom. The presence of protons along with the mixed oxidation state of the B site cation can result in mixed ionic and electronic conductivity, which makes such material interesting not only for their application as proton conductors but also electrocatalyst. Therefore, this compound was further investigated for its structure and properties along with its doping during the course of this doctoral thesis. Additionally, two other compositions $BaCoO_{2+\delta}$ and $BaCOO_{2.67}$ synthesized via solid state route in the context to understand the significance of NSP process towards the synthesis of hydrated barium-rich cobalt and iron containing perovskites.

NSP was used as the primary synthesis method for the synthesis of various garnet compositions (chapter 3) and hydrated perovskites (chapter 4). In the following subsection, a brief introduction to the NSP technique, including its equipment and process will be given.

2.1.1 NSP equipment

In comparison to the traditional wet chemical synthesis methods like sol gel and hydrothermal synthesis, NSP offers continuous powder synthesis. The typical schematic diagram of NSP set-up is shown is Figure 2.1. It consists of intake system, feeding system, nebulizer chamber, pyrolytic chamber and the powder collector.

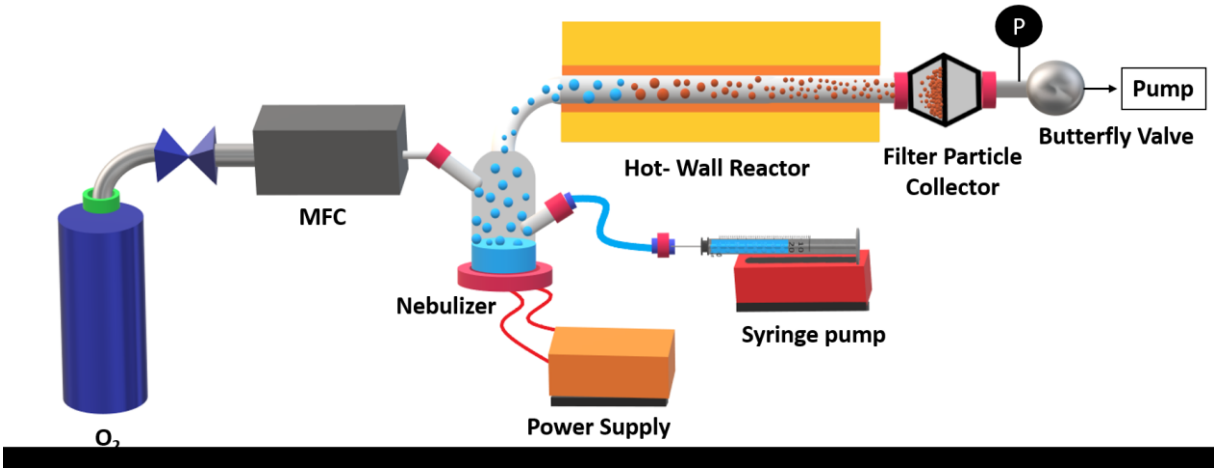

Figure 2.1: Schematics of a typical NSP set up.

i) The intake system consists of a gas system which provided continuous flow of desired gas (in this thesis O_2 and Ar were used for garnet and perovskite synthesis, respectively). The flow of gas is controlled via a controller. ii) The feeding system is used to continuously supply the precursor solution to the nebulizer chamber. Iii) Inside the nebulizer chamber, the precursor solution from the feeding system is atomized to generate tiny precursor droplets. These droplets are transferred into the pyrolytic chamber by the gas from the intake system. iv) Inside the pyrolytic chamber, usually maintained at high temperatures (above 1173 K during this thesis), the precursor droplets transform into solid particles due to the evaporation of solvent from the precursor droplets. This zone can be arranged into both horizontal and vertical arrangement. Within this thesis horizontal arrangement was utilized. The pyrolytic chamber can be further divided into multiple zones with each zone maintained at different temperature. In this thesis, single zone chamber was employed. v) The powders produced are then transferred

to the powder collector. Here, in this chamber substrates can also be used in order to deposit thin films directly [38].

2.1.2 NSP process

The NSP process refers to the formation of precursor droplets via nebulization in a nebulizer chamber. The droplets are transferred to into a reaction chamber via a carrier gas wherein each droplet undergoes physical and chemical reactions, which includes i) solvent evaporation, ii) precipitation, iii) drying and iv) sintering. The powders are finally collected on a filter paper in the collection chamber.

2.1.2.1 Nebulization

The droplet formation takes place via splitting of the precursor solution inside the nebulizer chamber via atomization. Within this thesis, the atomization was achieved via an ultrasonic nebulizer. In 1927, the process of ultrasonic atomization was discovered by Wood and Loomis. It was observed when a thin layer of liquid is subjected to perturbation via ultrasonic waves, fine droplet of the liquid at the solid liquid interface are produced. Two mechanism are usually given to understand the phenomenon.

The first theory is based on the theory of cavitation. When the liquid at the solid/liquid interface is disturbed via the ultrasonic waves microbubbles are produced as cavities due to the vibrations. The cavities break up due to the pressure difference and release energy in the process. Fine droplets are generated at the liquid surface and are ejected due to the shock waves that are produced by the cavity collapse. The second mechanism is based on the capillary wave theory, in which ultrasonic wave generated via an ultrasonic nebulizer propagates vertically perpendicular to the nebulizer surface towards the liquid surface. This results is the generation of capillary waves on the liquid surface, which consist of peak and troughs with their amplitude being dependent on the intensity of the vibrations. When the vibrations reach critical amplitude, the peaks of the capillary wave are stripped from liquid surface leading to the formation of fine droplets.

2.1.2.2 Evaporation and precipitation

Within this stage, four processes occur simultaneously, i.e. heat transfer, mass diffusion, vapor diffusion and droplet shrinkage. Upon the entry of the precursor into the pyrolytic chamber, solvent evaporation takes places from the droplet surface, diffusing into the surrounding gas. The size of the droplet decreases as the solvent evaporation takes place and the diffusion of the solute towards the center of the droplet occurs. Both, droplet surface shrinkage and solute diffusion are considered to be the important steps towards the resulting morphology of the powders. For example, if the concentration of the solute is higher near the surface of the droplet compared to that of the inner concentration, the solute precipitation first takes place on the surface of the droplet as the solute concentration increases due to the solvent evaporation. The precipitated solute results in the formation of solid spherical shell, covering the droplet surface and retards the further droplet shrinkage process. The lower concentration of the solute at the center of the droplets favors the solute precipitation on the surface where the concentration is high. This results in the formation of the hollow spherical morphology.

2.1.2.3 Particle drying and decomposition

Since the NSP process takes at high temperature (greater than 1173 K were used in this thesis), the process of drying and decomposition occur simultaneously. Since each droplet within the pyrolytic chamber are usually separated from each other and there is a low probability of them colliding with each other, each of these droplets acts as the micro-reactor,

thus preventing in the agglomeration of the particles. Both drying and decomposition process usually takes place in a single zone furnace with short length. However, sometimes additional post synthesis heat treatment may be required to obtain the desired phases. This is the case for the garnet synthesis, where additional heat treatment is required [34]. However, the sintering times are temperatures are significantly reduced compared to that of conventional solid state route where temperature higher than 1273 K and times more than 20 hours are required [39].

2.2 Lithium-ion battery

Batteries are electrochemical devices that mainly provide two functions i.e. storage and conversion of electrical energy into chemical energy and vice versa. Often the term cell is used to refer to the basic electrochemical unit [40]. Generally, batteries can be categorized into primary and secondary batteries based on their recharging capabilities. Primary batteries can be utilized only once, which means they are not rechargeable since they rely on the irreversible chemical reactions. On the other hand, secondary batteries can be repeatedly used, therefore being rechargeable. In general, batteries comprise of two electrodes, i.e. an anode (negative electrode) and a cathode (positive electrode), both separated from each other by an electronically insulating electrolyte layer. By convention, anode (eg. Li, Na, graphite) and cathode ($LiCoO_2$, $LiFePO_4$) are named based on the oxidation and reduction reactions taking place during discharge cycle, respectively. The two electrodes are connected to each other via an external circuit, allowing for the transfer of electrons. Inside the battery, the electronically insulating electrolyte not only separates the two component electrodes but also allows for the transfer of charge carrying ionic specie.

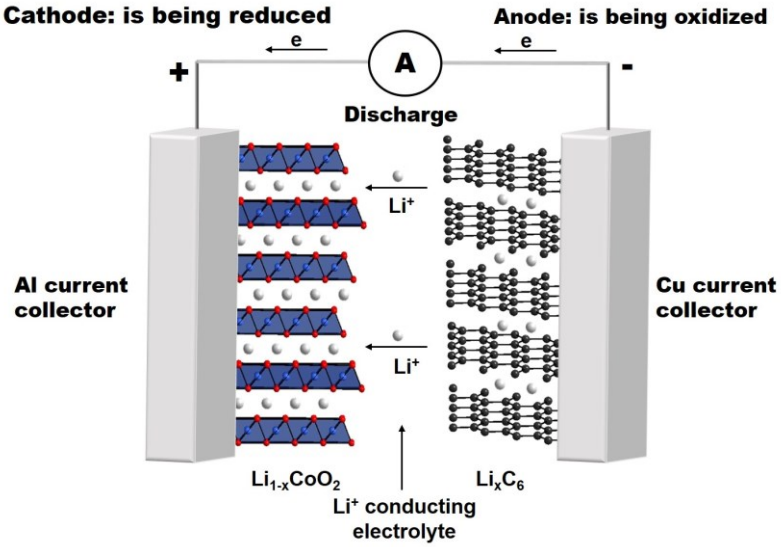

Figure 2.2: Schematics of a Li ion battery comprising of a graphite anode, $LiCoO_2$ cathode and a liquid electrolyte. The discharge cycle is being shown wherein the Li ions move from the anode towards the cathode.

The process of energy storage and conversion takes place via charging and discharging cycles. Figure 2.2 shows the schematics of a Li-ion battery comprising of a graphite anode, liquid electrolyte and $LiCoO_2$ cathode. During the charge and discharge cycle, shuttling of the Li ions between a cathode and an anode occurs, which can be represented by the following redox reaction

$$Anode: C_6 + xLi^+ + xe^- \leftrightarrow Li_xC_6$$

$$Cathode: LiCoO_2 \leftrightarrow Li_{1-x}CoO_2 + xLi^+ + xe^-$$

From the above discussion, it becomes evident that electrolyte not only acts as the pathway for the Li-ion transport between the two electrodes but also plays a major role as an electronic insulator to prevent cell short circuit. Conceptually, the electrolyte should be stable and not undergo any net chemical changes during battery operation. Therefore, in a simplified expression the electrolyte should be electrochemically stable with both the anode and cathode during the battery cycling. Due to the increasing pursuit of high energy density batteries, which require the use of highly oxidizing cathodes and more reducing anodes such as lithium metal,

a constant need of improving electrolyte stability is required. The stability of an electrolyte is quantified in volts, i.e. between its reductive and oxidative decomposition limits and is referred to as “electrochemical stability window”. Clearly, the redox potentials of the electrode materials should be within the electrochemical stability window of the electrolyte to enable a stable rechargeable battery operation. The role of electrolyte is not limited to just electrode separation, electronic insulation or electrochemical stability, but covers diverse aspects with multitude of requirements like

- High conductivity across a wide temperature range
- Chemical, electrochemical and mechanical compatibility with the electrode materials
- Cyclic stability over several thousands of cycles
- Safety
- Processability
- Environmental friendliness

Therefore, fulfilling all these requirements is necessary for the next generation high energy density, safe, portable and flexible LIBs which can be implemented for diverse applications ranging from portable electronics to grid storage to electrical vehicles.

2.2.1 All-solid-state lithium-ion batteries

With the advent of electric vehicles, the demand for high energy density batteries is at its peak. ASSLIBs can deliver both the high energy density as well as power densities compared to that of conventional LIBs. With the use of high capacity electrodes with extreme potentials and by lowering the mass/volume of inactive materials, high energy density batteries can be achieved. Solid electrolytes have large electrochemical stability window (0 V to 5.5 V vs Li^+/Li), which enables the use of high voltages cathodes like $LiNiPO_4$ [41, 42]. Not only this, SE have good electrochemical stability with the electrodes, high mechanical strength to prevent dendrite formation and can also enable the use of high capacity metallic lithium as anode (3860 $mAhg^{-1}$).

Several inorganic solid electrolytes have been explored. Initially Bates et al. [43] introduced lithium phosphorous oxynitride (LiPON). Thin film batteries using LiPON separated were shown to demonstrate thousands on cycles with Li acting as the negative electrode [44]. However, the bulk electrolyte was found to demonstrate low conductivity (2×10^{-6} S cm^{-1}) at room temperature [45]. Thio- lithium super ionic conductor (LISICON) based electrolytes on the other hand demonstrate high lithium ion conductivity and low activation energy at room temperature. This is the case for $70Li_2S\text{-}30P_2S_5$ glass ceramic with thio-LiSICON structure which exhibits Li-ion conductivity of 3.2×10^{-3} S cm^{-1} at room temperature [46, 47]. The main drawback of these type of electrolytes is their sensitivity towards humidity. Recently, Kanno et al. demonstrated that phosphorous and germanium doping into Li_3PS_4 crystal could lead to enhanced Li-ion conductivity [48]. The resulting composition $Li_{3.25}P_{0.75}Ge_{0.25}S_4$ demonstrates Li-ion conductivity of 2.2×10^{-3} S cm^{-1} at room temperature. Nevertheless, the germanium within this composition was found to get reduced at low potentials along with the sensitivity of the sulfide within the material towards moisture, resulting in the production of harmful H_2S gas [49]. Similarly, perovskite type $Li_{0.05-3x}La_{0.5+x}TiO_3$ (LLTO) exhibits high bulk Li-ion conductivity of 1×10^{-3} S cm^{-1} [50] but significantly lower overall Li-ion conductivity of ~2×10^{-5} S cm^{-1} due to high grain boundary resistance [51]. Further, LLTO is unstable with metallic Li anode which prevents its application in ASSLIB [10]. Garnets on the other hand not only demonstrate high room temperature Li-ion conductivity but also stability against Li anode [10]. However, due to their brittleness high interfacial resistance at the garnet/Li interface are observed [10].

As already mentioned in section 1.2 and from the discussion above, there is so far not a single SE which fulfils all the prerequisites for an ideal solid electrolyte for its incorporation in an ASSLIB for a large scale production. Therefore, a strategy similar to liquid electrolytes, where in two different SEs are mixed together to form a CE needs to be explored. Within the course of this thesis, CE were prepared using inorganic ceramic garnet powders and PEO. Therefore, a brief introduction to both of these components will be given in the subsequent subsections.

2.2.1.1 Garnet-type lithium ion conductors

The ideal garnets have a general formula $A_3B_2M_3O_{12}$ (A= Ca^{2+}, Mg^{2+}; B= Al^{3+}, Cr^{3+}, Ga^{3+}; M= Si^{4+} or Ge^{4+}) and crystallize in the space group *Ia*-3*d*, wherein A, B and M are eight-fold or dodecahedral, six-fold or octahedral and four-fold or tetrahedral coordinated cation sites, respectively. The Li garnets can be classified into 4 subtypes depending on the number of Li atoms per formula unit i.e. Li3, Li5, Li6 and Li7. The general formula can be given as $Li_3Ln_3Te_2O_{12}$ (Li3 phase, Ln= La^{3+}, Pr^{3+}, Y^{3+}), where in Ln and Te are six and eight fold coordinated sites and Li occupies solely the tetrahedral site. These compounds were found to demonstrate low ionic conductivities along with high activation energies implying that Li ions at the tetrahedral sites are less mobile [10]. The significant interest towards Li ion conducting garnets ($Li_5La_3M_2O_{12}$, M= Ta and Nb, Li5 phase) was generated after the report of Thangadurai et al. in which Li-ion conductivity of ~10^{-6} S cm^{-1} was achieved at 298 K [52]. Interestingly, it was also found that Ta members of these garnets were chemically stable with molten Li-metal, moisture and demonstrated wide electrochemical window [52]. After this discovery, subsequent studies focused on optimizing the ionic conductivity of the garnets via doping. Partial substitution of the La^{3+} with K^{+} and Nb^{5+} with In^{3+} were found to have an impact on the overall conductivity [10, 52, 53]. Via these doping strategies, it was found additional Li-ions can be stuffed into the garnet structure and since all these Li-ions cannot occupy the tetrahedral site, excess Li cations were found to occupy the six fold coordinated site, which were initially empty in the parent garnet structure [54]. These garnets containing more than 5 Li atoms per formula unit are referred to as Li stuffed garnets.

After their initial reports, Thangadurai et al. reported on the partial substitution of the La^{3+} site with the divalent alkaline earth cations which lead to the generation of an entirely new class of the garnet related structures ($Li_6ALa_2M_2O_{12}$, A= Ca^{2+}, Ba^{2+}, Sr^{2+}; M= Nb^{5+} or Ta^{5+}, Li6 phase). Among these, $Li_6BaLa_2Ta_2O_{12}$ was found to exhibit maximum conductivity of 4 x 10^{-5} S cm^{-1} at 295 K with the activation energy of 0.4 eV. Complete replacement of pentavalent M by a tetravalent cation like Zr^{4+} leads to the Li-rich garnet phase $Li_7La_3Zr_2O_{12}$ (LLZO) [53, 54]. In general, lithium ion conductivity is found to increase exponentially with Li ion content.

LLZO was reported by Murugan et al. and is considered to be the most attractive candidate among the Li-stuffed garnets mainly due to its high lithium ion conductivity, high lithium transference number, wide electrochemical window and most important stability with the Li metal anode [52, 53]. Despite these advantages it suffers from major drawbacks. LLZO is highly sensitive to moisture and CO_2 which leads to formation of Li_2CO_3 via an intermediate LiOH [55]. LLZO is known to crystallize in two phases: a thermodynamically stable tetragonal phase ($I4_1/acd$), which exhibits an ordered arrangement of Li-ions in the lithium sub-lattice and a cubic polymorph (*Ia*-3*d*) with disordered arrangement of Li-ions. The cubic polymorph (1.3 x 10^{-3} S cm^{-1}) is of interest due to its two orders of magnitude higher Li-ion conductivity compared to that of tetragonal LLZO (1.6 x 10^{-6} S cm^{-1}) [10, 53]. The crystal structure of cubic garnet is given in Figure 2.3. The higher ionic conductivity in the cubic LLZO is due to the disordered arrangement of Li^{+} ions over the tetrahedral (24*d*) and the two disordered octahedral sites (48*g*

and 96*h*) whereas in the tetragonal LLZO they are ordered on the tetrahedral (8*a*) and two octahedral (16*f*/32*g*) sites. The cubic phase has been known to occur at temperatures above 873 K [53]. Therefore, significant efforts have been made to stabilize the cubic phase at room temperatures. This mainly has been achieved via the substitution strategies where in doping at the different cations sites realizes the cubic phase through the reduction of overall lithium content and introduction of disorder on the lithium sub lattice [10]. The aliovalent doping with the substituent Al^{3+} or Ga^{3+} at the Li-site is an effective strategy to stabilize the cubic phase at the room temperatures [10]. However, there is still a significant debate about the site preferences (24*d* tetrahedral or 48*g*/96*h* octahedral) for Al^{3+} [56, 57]. An additional advantage of using Al^{3+} as the dopant is that it acts as a sintering aid resulting in the higher densification of the ceramic pellets with better Li-ion conductivity (6.8 x 10^{-4} S cm^{-1}) [10].

Similar stabilization effects are observed for the aliovalent doping of Li^{+} by Ga^{3+} substitution for which the Li-ion conductivity of 1.3 x 10^{-3} S cm^{-1} at 297 K has been reported [10], although the Ga^{3+} distribution within the LLZO framework was found to be difficult to determine. It has been observed that 0.2-0.24 moles of Ga or Al per formula unit are necessary to result in the structural transformation from tetragonal to cubic garnets [53, 57]. The cubic modification can also be obtained via supervalent doping on the Zr^{4+} sites (Sb^{+5}, Ta^{+5}, Nb^{+5}, Te^{+6}) [52].

Within this thesis, tetragonal as well as cubic LLZO-based garnets (Al and Ga doped LLZO) were primarily used as the ceramic fillers in the composite electrolytes.

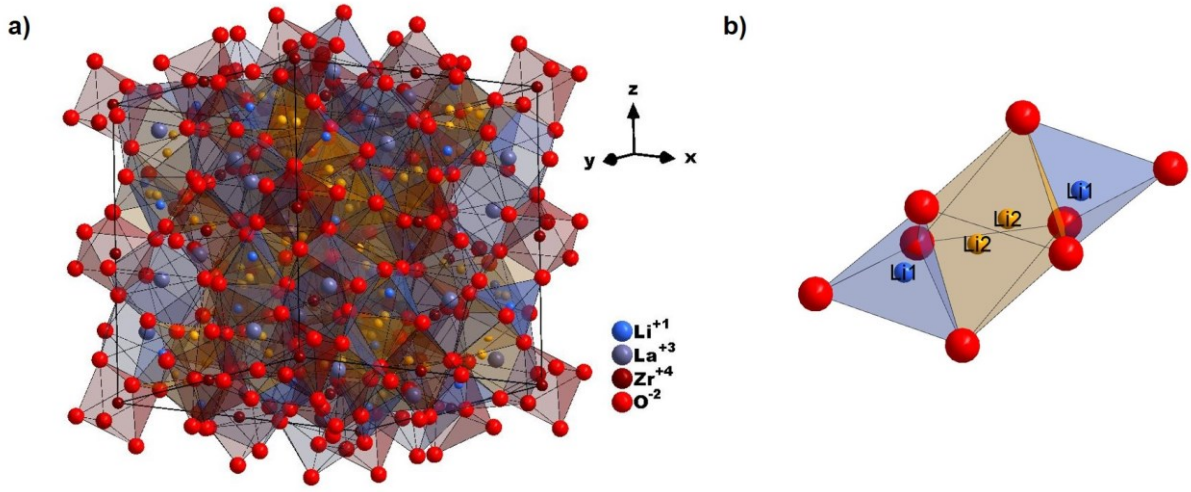

Figure 2.3: a) Structural representation of cubic LLZO. b) Li ion connecting polyhedral within the LLZO framework.

2.2.1.2 Lithium ion conduction in inorganic solid electrolytes

For the development of new solid electrolytes for ASSLIBs, it is critical to understand the Li ion dynamics within these systems. Within the solid inorganic electrolytes, the ionic transport can be understood on the basis of the classical diffusion model in which ion diffusion within the lattice is achieved via hopping of an ion from one site to another adjacent vacant site. This is termed as direct hopping. The vacancy within the lattice is as a result of defects which widely exist in crystalline lattices and therefore play an important role towards ionic conduction. Point defects for example are the 0 dimensional atomic defects and their influence is limited to adjacent neighboring sites. Vacancies, interstitial atoms or ions fall under this category. In a solid crystalline inorganic ionic conductor, the ion conduction can be induced via the motion of mobile cations or anions [19]. Therefore, ionic conduction in such systems results from the motion

of vacancies or interstitial ions. The point defects can be intrinsic as well as stoichiometric defects. For example; Frenkel defects where in the defects are vacancies accompanied by an interstitial ion or Schottky defects in which the defects are anion vacancies accompanied by a cation vacancy [19]. On the other hand, in the transition metal containing compounds, intrinsic defects are not limited to the stoichiometric compositions since a transition metal ion can have mixed valence states which allows for maintaining electroneutrality via oxidation or reduction of the transition metal ion cation. The intrinsic defect formation depends on the thermal energy and the number of defects follows an Arrhenius-type equation:

$$N_D = N\ exp\left(-\frac{E_F}{2kT}\right)$$

where N_D is the total number if defects, N is the number of ion pairs, E_F, K and T are the energy of formation, Boltzmann constant and temperature, respectively. Extrinsic point defects can also exist which are due to the impurity or the dopants substituted in the lattice.

The ionic conductivity (σ) of a solid inorganic material is dependent on its crystal structure and depends on the ion concentration (n), charge of the ion (q) and the mobility (μ) of the ionic specie under consideration:

$$\sigma = nq\mu \text{ and } \mu = \frac{qD}{kT}$$

Where D is the diffusion coefficient.

For the mixed ion and electron conducting materials the total conductivity is the sum of ionic (σ_i) and electronic conductivities (σ_e) and can be given as:

$$\sigma = \sigma_i + \sigma_e$$

The individual contributions from the ionic and the electronic part towards the total conductivity can be represented by the so called transference number:

$$t_i = \frac{\sigma_i}{\sigma}, t_e = \frac{\sigma_e}{\sigma}$$

where t_i and t_e are the ionic and electronic transference numbers respectively.

Usually the ionic conduction follows the classical Arrhenius type temperature dependence:

$$\sigma_T = A \exp\left(-\frac{E_a}{kT}\right)$$

A low activation energy E_a along with high concentration of mobile ionic charge carriers is therefore important prerequisite for high ionic conductivity.

2.2.1.3 Polyethylene oxide

Poly(ethylene oxide) (PEO) is a type of polyether compound whose chemical structure is given as H-(O-CH_2-CH_2)$_n$-OH. PEO has been extensively researched over the last 45 years after the discovery of ionic conductivity in PEO based alkali metal based complexes by Wright et al. [58]. It is also commonly known as polyethylene glycol (PEG). The discrepancy in the name originates from the molecular weight. Usually PEO is the name given to the polyether with the molecular weight greater than 20000 g mol^{-1} whereas PEG refers to the polymer of molecular weight below that [24]. PEO is widely commercially available with applications ranging from medical to industrial manufacturing. Additionally, PEO is nontoxic and therefore well suited to be used as a solid polymer electrolyte in ASSLIBs.

On its own PEO is an insulating polymer, however it can complex with various different lithium salts (Li^+) making it an interesting material for its application as electrolyte in ASSLIB due to its ability to conduct Li-ions [24]. PEO is buildup ethylene oxide (EO) units which have high donor number for Li^+ and high chain flexibility, which play a significant role in promoting ionic transport [24, 25]. Additionally, PEO also possesses high dielectric constant which is beneficial for Li salt solvating ability.

2.2.1.4 Lithium ion conduction mechanism in PEO

In order to develop PEO-based electrolytes with high lithium ion conductivity, PEO should not only be able to dissolve lithium salts but also allow for Li^+ transfer within the PEO chain. In PEO, this is achieved via the electron-donating oxygen group (-O-) which acts as the effective building block for dissolving and coordinating with lithium salts. The lone pair on oxygen in PEO coordinates with the Li-ions of the lithium salt via the Columbic interaction resulting in the dissociation of lithium salt into anion and cation. Thus, PEO acts as the solvent dissolving lithium salt and also implies that lithium salts with low lattice energies would be the salts of choice. When an electric field gradient in applied, the process of formation and breaking of Li-O bonds occurs and the transport takes place along the PEO chain segment or from one PEO chain segment to another. The resulting transport mechanism is shown in Figure 2.4, demonstrating Li-ions are coordinated with the ether oxygen atoms on the PEO segmental chain. Within the PEO-Li salt complex, the total ionic conductivity is not attributed to the Li-ions only, but also to the counter-anions which are produced by the decomposition of the lithium salts and migrate under the influence of an electric field. Therefore, the concept of ion transference plays a significant role in polymer-rich electrolytes. Usually the Li-ion transference number for PEO-based electrolytes is lower (0.22), however this is dependent on both the salt concentration and type of Li salt [59]. Further, transference have been reported to be improved via the introduction of ceramic fillers in the polymer matrix [24, 25], resulting in improved ionic conductivity within polymer-rich composite electrolytes [60].

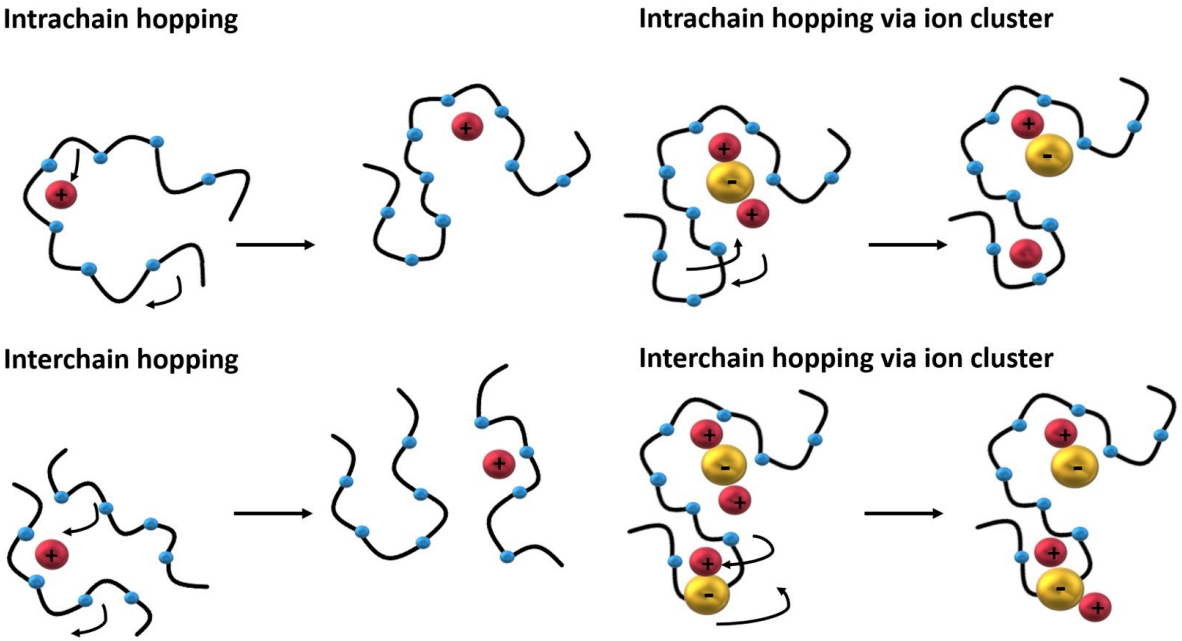

Figure 2.4: Schematics showing intrachain and interchain transport of Li^+ within PEO.

In the PEO-Li salt complex, large size of the polymer chain and the boundary effects prevent the free movement of ions. Thus, two factors play a significant role towards total ionic

conductivity in polymer electrolytes, i) total number of Li^+ ions available for transport and ii) crystallinity of PEO.

The ability of any polymer to dissociate Li-salt into the Li^+ cation and the anion depends on the dielectric constant of the polymer and the lattice energy of the lithium salt [24]. PEO is known to have comparably high dielectric constant (ε~5) [61] which allows it to dissolve majority of Li-salts [24, 62]. The choice of lithium salt is also highly important and depends on its anion, with bulkier anions resulting in higher ionic conductivity [24]. Hence, a salt whose anion has a well delocalized negative charge and low basicity usually shows higher ionic conductivity. Lithium-bis(trifluoromethanesulfonimidate) (LiTSFI) not only has a large anion but also high solubility, ionic conductivity and electrochemical stability. The larger anion ($TSFI^-$) can dissociate easily in the PEO matrix resulting in the formation of free and mobile Li^+ cations, therefore resulting in a positive impact on ionic conductivity.

As already mentioned PEO-Li salt complex offers usually low Li-ion conductivity of about 10^{-7} – 10^{-6} S cm^{-1} at room temperature. This low Li-ion conductivity has primarily been attributed to the coexistence of the amorphous and crystalline phase in PEO-Li salt complexes. It is widely believed that Li-ion conductivity is mainly due to the presence of amorphous PEO, whereas the crystalline PEO hinders the Li-ion transport [24, 63]. As such, reducing PEO crystallinity is of interest. Variety of methods have been employed to reduce PEO crystallinity ranging from adding plasticizers, formation of copolymers with other polymers or by addition of inorganic fillers [22, 64]. Amongst them addition of inorganic of fillers has been widely favored due to handling, cost and scalability consideration. This will be discussed in detail in section 2.2.2.

The ionic conductivity in the PEO/polymer electrolytes under the steady state conditions can be expressed as:

$$\sigma = \sum nq\mu$$

Similar to inorganic electrolytes, the increment to the conductivity is due to the increase in the concentration of the charge carriers (n) and mobility (μ) of these carriers within the polymer host. The concentration depending on the free ions available for conduction is related to the dissociation of the Li-salt by the polymer matrix and mobility which depends on the polymer chain mobility.

In comparison to inorganic crystalline solid electrolytes, three different theories have been given to explain the ionic transport in polymers i.e. Vogel-Tammann-Fulcher (VTF) theory, William- Landel-Ferry (WLF) theory and their combinations [19]. The classical Arrhenius equation is used to explain the temperature dependence of Li-ion migration as a result of segmental motion of polymer chains and expressed as:

$$\sigma_i = A \exp\left(-\frac{E_a}{KT}\right)$$

The contributions from Li-ion jump motion, polymer chain relaxations and/or segmental motion of polymer chain can also contribute towards ionic conductivity. This results in a nonlinear response of conductivity vs.1/T. This type of response in dependent on the glass transition temperature of the polymer under investigation and results in a well-known VTF equation:

$$\sigma_{VTF} = A\, T^{-\frac{1}{2}} \exp\left(-\frac{B}{T - T_o}\right)$$

Here, A is the pre-exponential factor, B is the action factor, T_o is the reference temperature, which can be expressed in T_g (glass transition temperature of the polymer). T_g is an important factor in polymer and polymer-rich electrolytes. Below T_g the ionic conductivity is found to be low. Therefore, for improving the ionic conductivity of the polymer-rich electrolytes, reduction of polymer crystallinity is beneficial. Adding inorganic ceramic fillers has widely been employed for reducing polymer crystallinity and in the process lead to the development of hybrid composite electrolytes. Within this thesis the classical Arrhenius equation was used for evaluation of impedance data since the linear response of conductivity vs 1/T was observed, which can be due measurement of the impedance data below the melting temperature of PEO, above which the chain motion would be enhanced and contribute further to towards the ionic conductivity and result in nonlinear response.

2.2.2 Composite electrolytes for all-solid-state lithium-ion batteries

To limit the drawbacks of the ceramic and polymer electrolytes, a reasonable strategy is to combine them to form CEs. Ceramic-based electrolytes mainly suffer from unavoidable disadvantage of poor contact with metallic Li anode [52], which leads to high interfacial resistance at Li/ceramic electrolyte interface. This could be improved by the addition of soft polymer to the ceramic, leading to "polymer in ceramic" composite, which would in principle benefit from the high lithium ion conductivity of ceramic garnet electrolyte and soft contact of PEO. On the other hand, addition of garnet to the PEO-rich or "ceramic in polymer" electrolyte might result in improved ionic conductivity and mechanical strength. The improved performance of CEs is known to be influenced by the type, composition, weight percentages and structure of the filler [10, 22, 64]. Therefore, an overview of CEs with variety of ceramic fillers ranging from composition of the ceramic filler, dimensionality of the fillers and transport pathways for Li-ions within the CEs.

2.2.2.1 Compositional dependence of inorganic ceramic fillers for composite electrolytes

As already mentioned, the polymer-based electrolytes suffer from low ionic conductivities (~10^{-8} S cm^{-1}) and low Li-ion transference numbers (0.22), which is as a result of poor ion pair dissociation of polymer chains and low mobile ion concentrations [24]. In comparison garnet electrolytes offer 5 orders of magnitude higher ionic conductivity along with transference number of 1 [10]. Both these issues can be addressed via the incorporation of inorganic ceramic fillers into the polymer matrix, i.e. fabrication of CEs. Within the CEs, two different types of ceramic fillers can be introduced into the polymer, i) Inert, which are non Li-ion conducting and ii) active, which are Li-ion conductors and can participate towards Li-ion conductivity via bulk Li-ion conduction.

2.2.2.2 Inert inorganic fillers

Inert fillers are non Li-ion conducting inorganic ceramic particles that do not intrinsically contribute towards Li-ion transport in the CEs and also do not significantly change the conduction mechanism within the CEs. They indirectly influence the Li-ion transport mechanism. The addition of small weight percentages of inert nano-fillers has similar effect as the molecular plasticizers resulting in the increase of the free volume within the polymer matrix and enhancing the segmental polymer chain dynamics. This results in the reduced glass transition temperatures and reduced polymer crystallization of the polymer matrix [22]. For low weight percentages of the inert ceramic fillers (less than 10 wt%), increase in the polymer amorphous phase fractions has been known to cause enhanced Li-ion conduction [22, 64]. Additionally, the Lewis acid-base interaction between the inert filler and ion pairs promotes their

dissociation which increases the number of free Li^+ within the polymer matrix and contributes positively towards Li-ion conduction. Further, inert fillers can provide additional Lewis acid or base surface sites which can attract the anions or cations, respectively. A Lewis acid surface site can be beneficial as it can interact with the anion of the Li salt (for example, $TSFI^-$ anion) and immobilize it, which can improve the Li transference number within the CEs. Despite these advantages, a poor dispersion of ceramic filler can adversely affect the Li-ion conductivity within the CEs. These fillers can act as cross-linking sites for the polymer chains containing polar groups and anion, which has detrimental effect on the polymer segmental motion and reduces both the ion mobility and conductivity.

For a CE containing Al_2O_3 as the ceramic filler, the polar O atoms (Lewis base site) on the filler surface interacts with the positive Li^+ of the $LiClO_4$ salt, increasing its concentration at the filler/polymer interface [22]. However, the interaction between the Li^+ and the polar O on the inert filler, immobilizes the Li-ion and results in increased anion concentration, leading to the reduced Li^+ transference number [22, 64]. This suggests the use of Lewis acid-based inert ceramic fillers in polymer rich CEs can be beneficial. Indeed, this was recently demonstrated by Liu et al. wherein Y_2O_3 doped ZrO_2 nanowires were used as inert ceramic fillers. The presence of positively charged oxygen vacancies on the nanowire surface interacts with the Li-salt anions (ClO_4^-) and provides the continuous ion conductive pathway along the filler/polymer interface. It was found that the filler containing CE demonstrated both higher ionic conductivity (1.07 x 10^{-5} S cm^{-1} at 303 K) and Li^+ transference number (0.56), which were higher than the filler free polymer electrolyte [65].

2.2.2.2.1 Active inorganic filler

The active ceramic fillers are the Li-ion conducting electrolytes which are added to the polymer matrix. Variety of different fillers i.e. garnets, perovskites etc. have been incorporated within the CE framework. The use of active fillers, can lead to additional Li-ion transport pathways where in the filler itself can intrinsically contribute towards the ion condition process. Additionally, the use of active fillers can lead to enhanced electrochemical stability [66].

As already mentioned in chapter 1 of this cumulative thesis, the use of ceramic-rich CEs can benefit from the high Li-ion conductivity of ceramic. This is due to the intrinsically Li-ion conducting 3 dimensional percolation pathway that can form above a certain ceramic to polymer weight ratio threshold referred to as percolation limit. Dietrich et al. developed the percolation model and suggested a significant enhancement in ionic conductivity above the percolation limit [67]. With the addition of active ceramic filler, not only can the interface contribute positively to ionic conductivity but also the filler due to its intrinsic ionic conductivity as opposed to the inert filler.

2.2.2.3 Dimensionality of ceramic fillers in composite electrolytes

Composite electrolytes containing 0-dimensional ceramic fillers are usually easiest to fabricate using simple solvent-based approach, wherein the ceramic fillers are dispersed into a solvent followed by addition of Li-salt and polymer. Herein, 0-dimensional refers to the inorganic nanoparticles. Most of the research on 0-dimensional containing CEs is focused on polymer-rich composites, wherein both active and inert fillers have been used to modify the polymer matrix [22, 64].

As already mentioned in section 2.2.1.4, the ionic conduction in polymers mainly depends on movement of polymer chains in the amorphous regions. The role of ceramic filler in polymer-rich composite is mainly to reduce the polymer crystallinity, irrespective of the type of ceramic

filler used [64]. Recently, Goodenough et al. showed that addition of garnet ceramic filler to the PEO+LiTSFI electrolytes lead to gradual reduction of melting temperatures in PEO (T_m) and reduced area of the endothermic peak in DSC, which corresponds to lowering of the PEO crystallinity. The reduced PEO crystallinity was found to result in increased Li-ion conductivity in PEO-rich CE (10 wt% of LLZO particles in PEO), with the highest ionic conductivity of 1.17 x 10^{-4} S cm^{-1} at 303 K and 1.58 x 10^{-3} S cm^{-1} at 353 K being reported [68]. The addition of ceramic garnet nanoparticles increases the free volume for segmental motion of PEO chain, resulting in increased Li-ion conductivity [68]. Similarly, Zhao et al. showed that addition of $Li_{10}GeP_2S_{12}$ (LGPS) powder to PEO-based electrolytes resulted in reduced glass transition temperatures (T_g) from 233.4 K to ~231.4 K [69]. The melting temperature was also found to decrease from 339.5 K to 330.8 K - 332.9 K. The reduced glass transition and melting temperature generally indicate increased amorphous phase and reduced crystallinity. This resulted in Li-ion conductivity of 1.18 x 10^{-5} S cm^{-1} and 1.21 x 10^{-3} S cm^{-1} at 298 K and 353 K for the LGPS containing PEO-rich CE compared to that of 6.16 x 10^{-6} S cm^{-1} (298 K) and 1.18 x 10^{-5} S cm^{-1} (353 K) for PEO+LiTSFI electrolyte [69]. However, the addition of ceramic fillers was found to have two opposite effects. Firstly, the addition of ceramic filler resulted in reduced crystallinity of PEO and formation of PEO/LGPS interface, which is beneficial towards Li-ion conductivity and suggests the use nanoparticles, since they offer higher surface area. Secondly, the micro sized fillers offer small filler /PEO interface regions and acts as cross-linking sites between EO-segments, which enhances the PEO crystallinity. Hence, upon increasing the filler weigh ratios the cross linking sites increase which suppresses the plasticizing effect of the ceramic filler on the polymer and lead to reduced ionic conductivity [70]. Zagorski et al. showed that addition of LLZO to the PEO lead to the gradual monotonic decrease in ionic conductivity from 6.97 × 10^{-4} S cm^{-1} for filler-free PEO(LiTFSI) to 4.47 × 10^{-4}, 3.26 × 10^{-4}, 2.10 × 10^{-4}, and 1.42 × 10^{-4} S cm^{-1} for 10, 20, 30, and 40 vol % LLZO measured at 313 K, respectively [71]. The conductivity values were found to be comparable to that of PEO suggesting that LLZO fillers do not contribute towards the ionic conductivity. However, for the loading fractions above 40 vol%, a significant decrease (2-3 orders of magnitude) in the conductivity was observed. The addition of LLZO beyond the percolation limit, physically constrains the polymer chains between the LLZO fillers, which lowers the chain mobility and limits the Li-ion transport. Similarly, Wu et al. used $Gd_{0.1}Ce_{0.9}O_{1.95}$ and perovskite type $La_{0.8}Sr_{0.2}Ga_{0.8}Mg_{0.2}O_{2.55}$ as the ceramic filler in PEO-rich CE, both being Li-ion inert and containing high amount of oxygen vacancies [72]. The CEs were found to demonstrate the ionic conductivity of an order of 10^{-4} S cm^{-1} at 303 K. The positively charged oxygen vacancies on the surface of oxide nanoparticles tend to bond with the $TSFI^-$, which leads to the accumulation of electrons between the surface of the oxide nanoparticle and $TSFI^-$-ion. The immobilization of the $TSFI^-$ due to its absorption on the oxide nanoparticle surface can benefit the Li-ion transport and additionally improve the Li-ion transference number in such polymer-rich CEs. Also, the interaction of the $TSFI^-$ with the oxygen vacancies on the surface of the oxide nanoparticles can weaken the interaction between the Li^+ and the $TSFI^-$, which can contribute towards salt dissolution which manifest as improved Li-ion conductivity.

Although the ceramic fillers irrespective of their composition are known to result in enhanced ionic conductivities in polymer-rich CEs on account of reduced polymer crystallinity, for the inverted case where ceramic phase acts as the matrix and polymer plays the role of filler, the use of active Li-ion conducting ceramic phase would be required to achieve high ionic conductivities. So far, attention has mainly been given to the polymer-rich CEs whereas there are only limited reports on ceramic-rich CE [73]. The lack of interest could be due to the poor Li-ion conductivity in ceramic-rich CEs due to: i) insufficient contact between the filler/polymer, ii)

high ceramic/ceramic interface impedances, iii) segregation of ceramic fillers from the polymer due to their high density, iv) tortuosity effects v) interfacial instability between the ceramic and polymer and vi) difficulty in preparing such CEs via solvent free approach. Nevertheless, from the fundamental point of view, taking advantage of highly conductive ceramic matrix and use of polymer as the grain boundary Li-ion transport promoter within ceramic matrix has not been explored in detail.

1-dimensional fillers refer to the nanorods, nanotubes or nanofibers that are usually employed as ceramic fillers in CEs. One of most important advantages of the 1-dimensional fillers is that they enhance the ceramic/polymer interface which is widely believed to result in enhanced ionic conductivities in polymer-rich CEs [74-76]. Liu et al. demonstrated that CE containing 15 wt% of $Li_{0.33}La_{0.557}TiO_3$ incorporated into the polymer matrix showed Li-ion conductivity of 2.4 x 10^{-4} S cm^{-1} at room temperature [74]. Similarly, Chan et al. showed for the CE containing 5 wt% of LLZO nanowires prepared by electrospinning, the room temperature ionic conductivity of 1.3 x 10^{-4} S cm^{-1} which is three orders magnitude higher than the pure polymer electrolyte [76]. Additionally, they showed the ionic conductivity is influenced by the morphology of the ceramic filler, with the CE containing 5 wt% of LLZO nanoparticles showing Li-ion conductivity of 1.13 x 10^{-5} S cm^{-1} which is an order of magnitude lower than the nanowire containing CE. Therefore, establishing the advantage of continuous ceramic/polymer interface towards Li-ion conductivity [76]. Despite these improvements in ionic conductivity, they have an inherent drawback. Within the LIBs, Li-ions migrate perpendicular to the electrode surfaces under the influence of external electric field. This warrants the need for alignment of 1-dimensional fillers in the perpendicular direction to the electrode surfaces whereas the nanofibers alignment parallel to the surface does not have a much impact to the Lithium ion transport [22, 77]. Similar to 1-dimensional fillers, in 2-dimensional filler containing CEs, Li-ion transport would be directional.

3-dimensional ceramic filler or matrix (depending upon the weight or volume fraction), can not only offer continuous path for Li-ion transport similar to 1-dimensional filler containing CEs but also limit the ceramic/ceramic particle interface impedances as in 0-dimensional containing CEs. Bae et al. recently demonstrated a 3-dimensional nanostructured ceramic matrix of $Li_{0.35}La_{0.55}TiO_3$ using a hydrogel-based approach [73]. The CEs comprised of 44 wt% ceramic matrix and exhibited Li-ion conductivity of 8.8 x 10^{-5} S cm^{-1} at room temperature. Within such a system, a pre-percolated network of $Li_{0.35}La_{0.55}TiO_3$ prevents the agglomeration of particles and benefit from the pre-sintered ceramic network which would offer higher intrinsic Li-ion conductivity compared to that simple contacted ceramic fillers. $Li_{0.35}La_{0.55}TiO_3$ network offers continuous 3-dimensional interface phase, which creates additional Li-ion transport pathway. Nonetheless, ionic conduction is low, which can be due to higher grain boundary resistance, which is known to result in lower Li-ion conductivities in perovskite type $Li_{0.35}La_{0.55}TiO_3$ electrolyte [78]. So far to the best of the knowledge of the author of this thesis, such porous garnet networks have not been prepared, which mainly can be due to the difficulty in achieving such porous garnet networks via the conventional solid state and sol gel approach since they require high sintering temperatures and times to achieve the garnet phase. Here, NSP offers an advantage since porous garnet networks can be prepared via this route mainly due to low sintering temperatures and times.

2.3 Perovskite materials

The typical perovskite type structure has a general formula given as ABX_3. Perovskite type compounds are known to demonstrate variety of interesting electrical, magnetic and catalytic properties which is closely related to their structure. Therefore, the crystal and electronic structure of the perovskite type oxide compounds are briefly examined and their influence on bifunctional catalytic oxygen evolution and oxygen reduction reaction are discussed.

2.3.1 Crystal structure

Basically, perovskite is a mineral with the composition $CaTiO_3$ [29]. The generalized chemical formula of the perovskite structure is ABX_3, where A (alkaline earth or lanthanide) and B (transition metal ion) are the cations and X is the anion (oxide, fluoride, hydroxide). The ideal structure of the cubic aristotype (space group *Pm*-3*m*) can be understood as being built up of a cubic close packed (*ccp*) arrangement of AX_3 layers with the B cations occupying 1/4th of the octahedral voids. The large sized A cation occupies the 12-fold coordinated site. Different combinations of charged cations in the A and B sites within the perovskite framework are known, such as +1 +5, +2 +4, and +3 +3. Furthermore, variety of different ABX_3 compounds crystallize in polymorphic forms with just a minor deviation from the ideal perovskite structure.

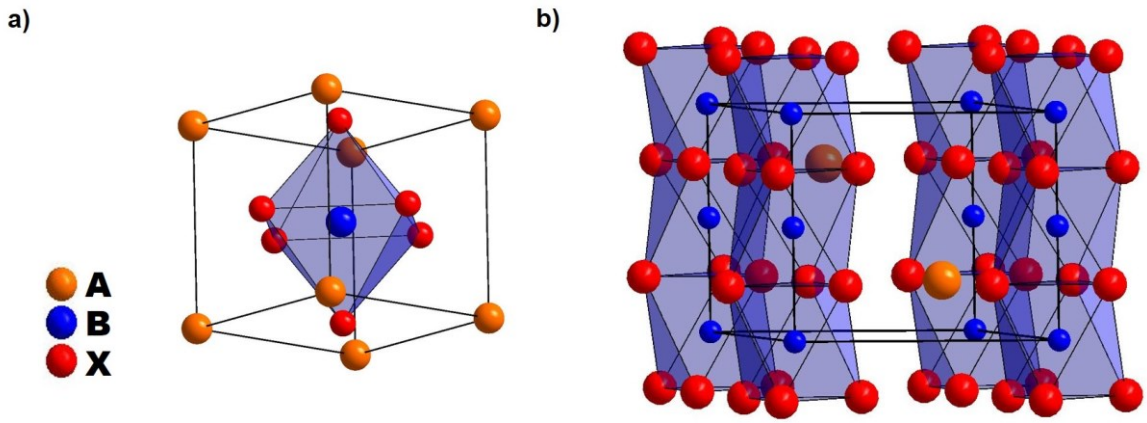

Figure 2.5: a) Unit cell of ideal cubic perovskite with space group *Pm*-3*m* showing octahedral coordination of B site cation. b) Unit cell of hexagonal perovskite with face sharing polyhedron.

In an ideal perovskite (space group *Pm*-3*m,* Figure 2.5a) three different crystallographic sites of the ions within the unit cell can be identified, wherein the A and B sites can either occupy the 1*a* or 1*b* site, depending on the structural setting and X occupies the 3*c* site. $SrTiO_3$ shows such a cubic structure where Sr is located at the 1*a* site (0 0 0), Ti at 1*b* site (½ ½ ½) and O at 3*c* site (½ 0 ½) [79]. Although, this is an ideal structural setting, only few compounds are known to crystallize within this high symmetry space group. Many different oxides are known to crystallize in the slightly distorted variants with lower symmetry. Such, symmetry lowering from the ideal perovskite structure originates from; i) large difference in the ionic sizes of the cations, ii) cation deficiency and/or iii) vacancies on the anion sub-lattice.

In order to have an idea about the possible deviation from the ideal cubic symmetry for perovskites, perovskite must be regarded as an ionic crystal. The lattice parameter *a* is then geometrically related to the ionic radii of the A and B cation (r_A, r_B) and the anion (r_x). The relation can be expressed as:

$$a = 2(r_B + r_x) = \sqrt{2}r_A + r_x$$

The ratio between these two expression for lattice parameter gives the so called Goldschmidt tolerance factor, *t:*

$$t = \frac{(r_B + r_x)}{\sqrt{2}r_A + r_x}$$

Despite its simplicity, the tolerance factor has a decent predictive capability, particularly for oxides. Although the value close to 1 is desired for an ideal cubic perovskite, it has been shown that cubic perovskites are also possible if t lies within 0.9-1 range. For the values between 0.71-0.90, structural distortions due to tilting of the BO_6 octahedron are observed, which results in symmetry lowering below the cubic. For t values lower than 0.7, ilmenite-type structures are known occur in which A and B cations are of similar sizes, an example of this is $ZnTiO_3$, wherein both Zn and Ti are octahedrally coordinated with O. The values above 1 are quite often encountered when there is a large difference in the ionic radii between the A and B cation. This is the case for Ba-rich stoichiometric oxide perovskites where instead of *ccp* stacking with corner sharing octahedron, hexagonal closed packing with face sharing octahedron is observed (Figure 2.5b).

Many essential physical properties of perovskites, such as magnetic, electronic and catalytic are based on the BO_3 octahedron, since they rely on the electronic configuration of the B site, which can be modified by the surrounding anions. Although the A site is of relevance, these cations tend to be closed shell with fixed oxidation states and therefore have lesser influence on the chemical and physical properties. The perovskite structure is highly flexible with respect to both anion or cation deficiency. Anion deficiency is of more interest in the transition metal containing perovskite oxides since it plays a major role in crystal chemistry, determining the catalytic and electronic properties [80-83]. This also is dependent on the ability of B site cation to adopt various oxidation states, spin states and lower coordination, i.e. pyramidal, tetrahedral or square planar, and therefore plays a major role in influencing the properties of perovskites.

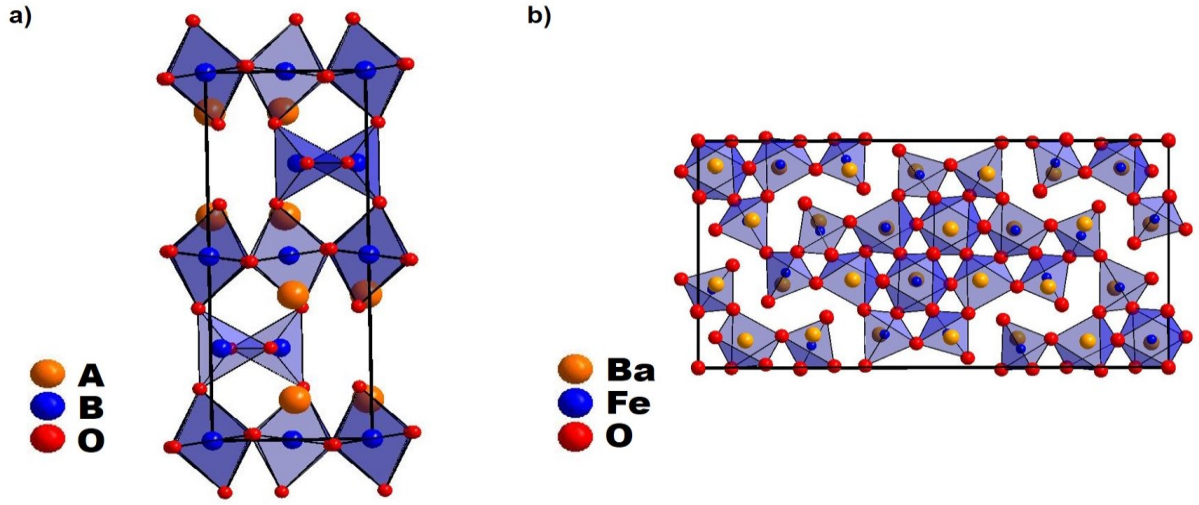

Figure 2.6: a) Typical brownmillerite structure with overall composition $ABO_{2.5}$ with alternate layers of BO_6 and BO_4 polyhedron. b) Alternative vacancy ordered structure found for $ABO_{2.5}$-type $BaFeO_{2.5}$.

For $ABO_{3-\delta}$ perovskites, where δ is the amount of anion vacancy, the value of up to δ~1 has been realized. The tuning of anion vacancies is highly dependent on the synthesis conditions being used and determines the value of δ and its influence on the resulting structure. Amongst the oxygen deficient perovskites, brownmillerite is well known. Brownmillerite is the mineral with the approximate composition Ca_2FeAlO_5. The typical formula for the brownmillerite-type

structure can be given as $ABO_{2.5}$ i.e. δ =0.5 and the schematic representation is shown in Figure 2.6a. With respect to ideal perovskite, the Brownmillerite structure is realized by ordered introduction of the oxygen vacancies along the [110] direction. Within this arrangement, two equatorial oxygen atoms are removed from each BO_6 octahedron and the B cation is displaced from its initial positions to form a tetrahedron. This results in alternate sheets of BO_4 tetrahedral chains running along [110] in an ordered arrangement in ideal cubic perovskite structure. However, not all $ABO_{2.5}$ perovskite compositions crystallize in this type of structural setting and instead adopt a different vacancy ordered modification of cubic perovskite. An example of this is $BaFeO_{2.5}$ which is known to have a complex vacancy ordered structure with Fe present in 4-fold, 5-fold and 6-fold coordination [84]. The structure of $BaFeO_{2.5}$ is shown in Figure 2.6b.

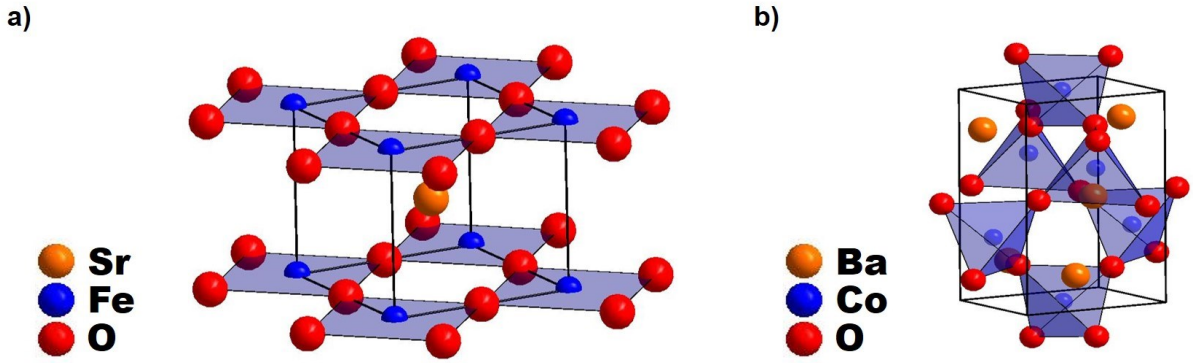

Figure 2.7:a) Schematics of 4-fold infinite layer coordination of Fe (B site) observed in $SrFeO_2$. b) Structure of $BaCoO_2$ with tetrahedral coordination of Co (B site).

Highly oxygen deficient perovskites with δ~1 have also been realized, i.e. ABO_2. Rosseinsky et al. showed that by using metal hydrides (CaH_2, NaH, LiH) as the reducing agents, vacancy rich perovskite systems can be synthesized at very mild temperatures [85]. For example, $LaNiO_3$ can be reduced to $LaNiO_2$ at 473 K by using NaH as the reducing agent [85]. Similarly, for $SrFeO_3$, it was shown that δ=1 can be obtained which leads to structurally remarkable feature, i.e. local square planar coordination around Fe in $SrFeO_2$ [86] (Figure 2.7a). Such a square planar coordination is interesting since cuprates show similar coordination for their high temperature superconductivity. However, other types of structures have also been observed within such highly oxygen deficient perovskite systems where in the B cation is found in tetrahedral coordination. Trigonal $BaCoO_2$ [87] and $CaFeO_2$ [88] being examples. It must be kept in mind, in order to obtain an infinite layer coordination, multistep synthesis procedure is usually required, wherein the oxygen rich perovskite is prepared first followed by its low temperature hydride reduction at low temperatures.

The presence of oxygen vacancies can lead to oxygen ion conduction within the oxygen deficient perovskite systems along with the possibility of filling such vacancies with variety of different anions which can influence their properties. For example, filling the anion with fluoride or hydroxyl ions. The incorporation of water is of interest due to the application of such perovskites in proton conducting fuel cells and as bifunctional catalyst for ORR and OER. When the perovskite oxides are exposed to water vapor, the oxygen vacancies present within the structure can be replaced by the hydroxyl groups. The proton is intimately bonded to the oxygen ion rather than being free and forms an OH^- ion. This can have significant impact on the crystal structure i.e. transition from water free to water rich phase (Figure 2.8) which is related to structural relaxations around the protons. The water incorporation (or dissolution) reaction can be described as follows:

$$H_2O\ (g) + V_o^{\cdot\cdot} + O_o^x \rightarrow 2OH_o^{\cdot}$$

Such water containing phases have previously been synthesized via two-step process involving first the preparation of oxygen deficient perovskite followed by its hydration by passing a stream of wet gas over the as-synthesized powders [89]. Recently, Knöchel et al showed that water-rich perovskite compositions can be prepared directly via NSP [37]. Additionally, as will be discussed in chapter 4, the as-synthesized hydrated powders were found to contain higher amounts of water compared to the ones prepared via the solid-state route showing the uniqueness of the NSP process.

In this thesis variety of oxygen deficient phases and OH^- rich phases have been synthesized and investigated for their structural, electronic and catalytic ORR and OER properties.

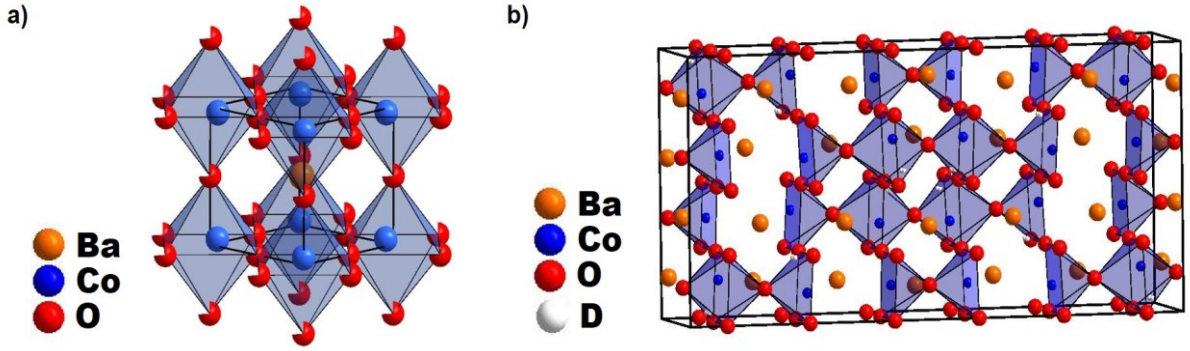

Figure 2.8: a) Schematics of structure of water free cubic $BaCoO_{2.23}$ and b) Water-rich counterpart of $BaCoO_{2.23}$ with orthorhombic structure and composition $BaCoO_{1.80}(OH)_{0.86}$.

2.3.2 Electronic structure

Transition metal (TM) containing compounds demonstrate variety of different physical properties which are directly related to the electronic structure of the TM cation [90]. This is mainly due to the ability of the TM cations to exhibit variety of different oxidation states and several types of coordination environments. Especially for cobalt containing oxides, wherein cobalt not only exists in three distinct oxidation states: Co^{+2}, Co^{+3}, and Co^{+4} but also in different coordination environments: square planar, tetrahedral, pyramidal, and octahedral. As a result, cobalt oxides provide a broad spectrum for the development of a variety of frameworks, which includes both the stoichiometric and nonstoichiometric oxides with a mixed valence of cobalt and/or the inclusion of oxygen vacancies. Further, the ability of cobalt to be present in the various spin states i.e. low spin (LS), intermediate spin (IS) and high spin (HS) provides additional factor to be taken in to account and makes Co more attractive than other TM cations.

In an ideal stoichiometric perovskite oxide, the transitional metal cation is present within an octahedral environment. Within such a coordination, electrostatic interaction between the ligand electrons and TM 3*d* orbital electrons takes place, which lifts the degeneracy of the five degenerate 3*d* orbitals. Due to the direction and shape of the orbitals, two of the 3*d* orbitals i.e. $3d_{x^2-y^2}$ and $3d_{z^2}$ or e_g, which point directly towards the ligand, increase in energy when the ligands are brought closer towards the TM cation. Similarly, the remaining 3*d* orbitals i.e. $3d_{xy}$, $3d_{xz}$ and $3d_{yz}$ or t_{2g} point in the direction between the ligands, causing lower repulsion between the ligand electrons and negatively charged t_{2g} electrons, consequently resulting in lower energy of this set of orbitals. Figure 2.9 shows the *d* orbitals and their splitting in an octahedral environment.

The spin state of the TM cation is highly dependent on the crystal field splitting $\triangle_O$. It is the difference between the energies of t_{2g} and e_g orbitals in an octahedral complex. According to Hund's rule every orbital in the sublevel is first singly occupied by an electron in a parallel spin configuration before a double occupation. i.e. maximization of the total spin number. Therefore, for a TM cation to be in a high spin state, the energy $\triangle_O$ has to be overcome. However, if the $\triangle_O$ is too high, then the pairing of electrons takes place resulting in a low-spin state. The crystal field splitting $\triangle_O$ depends both on the oxidation state and as well as the ligand. Ligands producing large splitting are referred to as strong field ligands (e.g. CN^-) whereas those resulting in small splitting are called as weak ligands (e.g. I^-). The tailoring of the spin state of the transition metal ion has been found of relevance in oxygen reduction and oxygen evolution reaction, which will be elaborated in chapter 4.

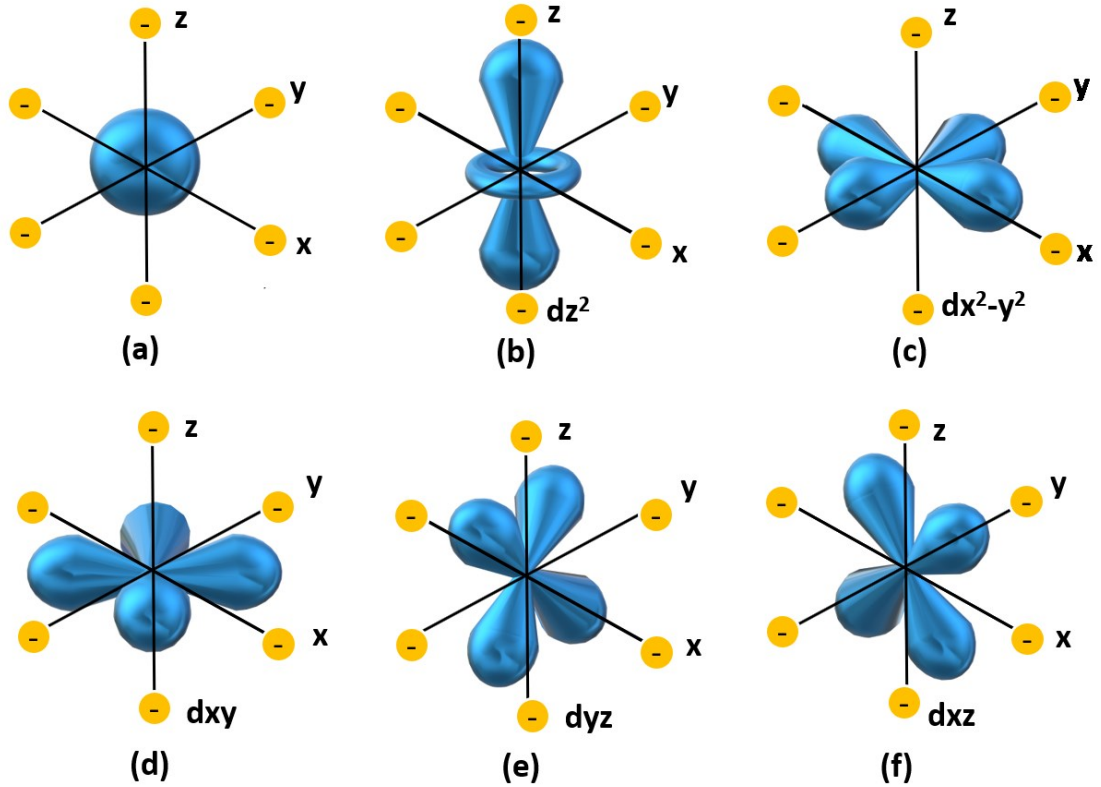

Figure 2.9: Schematics showing the shapes and directionality of d orbitals.

2.3.3 Catalytic activity

The oxygen reduction and oxygen evolution reactions are the two fundamental electrochemical reactions catalyzed by bi-functionally active catalysts. Due to the naturally sluggish kinetics of the ORR and OER reaction, bi-functional catalysts play a significant role in the practical operation of metal–air batteries, fuel cells and electrolysis cells. Briefly, in the ORR process oxygen molecules are first diffused towards the catalyst surface followed by their adsorption onto it. Electrons from the anode are then transferred to the adsorbed oxygen molecule resulting in the weakening and breaking of oxygen double bond. The resulting hydroxide ions are then transferred to the alkaline electrolyte after their removal from catalyst surface. OER on the other hand is more complex due to complex electrochemical reactions with multi-step electron-transfer processes. The mechanics of ORR and OER are discussed in the subsections that follow.

2.3.3.1 Oxygen reduction reaction

Metals and metal oxides are the two types of traditional oxygen catalysts, and the mechanism of ORR using these catalysts has been extensively studied. Depending on the kind of oxygen adsorption, ORR can proceed via a four-electron pathway or a two-electron pathway for metal-based catalysts. Two types of oxygen adsorption that can occur are: bidentate O_2 adsorption, in which two oxygen atoms interact with the metal and another is end-on adsorption of O_2 molecule. The overall four electron process can be given as:

$$O_2 + 2H_2O + 4e^- \rightarrow 4OH^-$$

This reaction can be broken further in to single electron process steps. However, multiple reaction pathways can become accessible depending on the electrolyte pH and the catalyst. The dissociative and associative pathways are the two ORR reaction mechanisms. The O-O bond is broken in the dissociative pathway when O_2 adsorbs onto two active metal sites. As a result, there is no peroxide intermediate formation. The dissociative pathway is highly unlikely, since it requires high amounts of energy to break the O-O bond. On the other hand, the associative pathway involves the adsorption of O_2 molecule onto a single active metal site and forms a peroxide intermediate:

$$O_2 + 2H_2O + 2e^- \rightarrow HO_2^- + OH^-$$

The breaking of O-O bond via this pathway is easier. The formed peroxide can then either react electrochemically at the catalyst surface:

$$HO_2^- + H_2O + 2e^- \rightarrow 3OH^-$$

or desorb from the surface of the catalyst under redox disproportion:

$$2HO_2^- \rightarrow 2OH^- + O_2$$

The oxygen produced here undergoes further reduction via electron transfer. An important point to bear in mind is that the ORR takes place at a triple point (oxygen-electrocatalyst-electrolyte), and hence signifying the importance of the number of active sites at the triple interface.

2.3.3.2 Oxygen evolution reaction

The OER mechanism and pathways are quite complex. Since oxygen is usually produced from an oxide phase rather than a bare metal, the mechanisms may differ based on the different site geometries of metal cations. Here, the variable oxidation state of the metal cation is of high importance. The OER process is initiated by the metal cation and oxygen intermediate interaction, leading to the formation of a bond via changes in the metal ion oxidation state. The local site geometry of the active metal cation also plays a critical role since it determines the kinetics of the OER process via changes in the adsorption energy of the oxygen species. The OER mechanism for transition metal oxide catalyst in the alkaline media can be given as:

$$M^{m+} - O_2^- + OH^- \rightarrow M^{(m-1)+} - O - OH^- + e^-$$

$$M^{(m-1)+} - O - OH^- + OH^- \rightarrow M^{m+} - O - O^{2-} + H_2O + e^-$$

$$2M^{m+} - O - O^{2-} \rightarrow 2M^{m+} - O^{2-} + O_2$$

Typical electrocatalyst for the OER are the precious metal oxides like IrO_2 and RuO_2.
However, these are very costly and also show limited ORR activity and therefore, not ideal as bi-functional catalyst for metal air-batteries.

2.4 Diffraction

This section gives an overview of the basic fundamentals of diffraction and Rietveld method. A comparison between X-ray and neutron diffraction is made, two diffraction techniques used within this thesis. These diffraction sets can be treated via Rietveld analysis and the information that can be obtained is highlighted. Further, the factors determining the positions and shapes of the diffraction peaks are briefly introduced. Towards the end of this section a brief introduction to Rietveld method is given. The discussion presented in the following sub-sections has been obtained from the text books of crystallography [91, 92] and Rietveld method [93].

2.4.1 Fundamentals of diffraction

Powder diffraction is a widely used method for the characterization of crystalline materials in order to determine their crystal structures, phase identification and its quantification. For the investigation of crystalline materials build of up periodically repeating motifs via diffraction, the wavelength of the incident wave must be similar to the interatomic distances, ~2-3 Å. Radiations based on particles (i.e. neutrons and electrons) or X-rays fullfil this criterion and offer suitable wavelengths. Although in principle, all the three can be used for determination of the crystal structure, they are fundamentally different based on their interaction with the atomic nuclei or electronic shell and can be used as complementary techniques to each other. Within the scope of this thesis, only powder X-ray and neutron diffraction techniques were used, therefore only these will be discussed further.

Two approaches have been widely used for the treatment of diffraction i.e. Laue equations and the Bragg's law. Amongst these Bragg's treatment is more widely used due to its simplified treatment in deriving Bragg's law. For powder diffraction, considering the Bragg's law is sufficient in understanding the observed phenomenon. According to Bragg's approach, the crystals are built up of planes which act as semi-transparent mirrors. All the planes whose miller indices hkl are identical triplets, will be equally spaced and parallel to each other. Therefore, implying periodic nature in the direction perpendicular to the plane with the interplanar distance d_{hkl}. For a specular reflection, the angle of incidence θ i.e. the angle formed between the incident waves and the reflecting planes (hkl), should be equal to the angle of reflection (Figure 2.10). For the constructive interference, the path difference $2\triangle$ introduced in the pair of waves after their reflection from the adjacent neighboring planes should be an integral multiple of the wavelength λ:

$$2\triangle = n\lambda$$

This simple geometrical analysis gives the Bragg's law:

$$n\lambda = 2d_{hkl} \text{ Sin } \theta_{hkl}$$

where n is the order of reflection. Thus implying that constructive interference i.e. intensity maxima, can only take place at the Bragg's angle. For all other angles destructive interference or cancellation is observed.

For a better visualization of the diffraction phenomenon, Ewald introduced the geometrical formulation of the Bragg's law involving the reciprocal space. Consider an incident wave with propagating vector $\overrightarrow{k_i}$ and a wavelength *λ*, with the length of the incident wave vector selected as inverse of wavelength. For the elastic scattering, the wavelength of the scattered wave $\overrightarrow{k_s}$ remains constant i.e. $\overrightarrow{k_i}$ = $\overrightarrow{k_s}$ = *1/λ*. The angle between $\overrightarrow{k_i}$ and $\overrightarrow{k_s}$ is 2θ and since they are considered to have same lengths regardless of the direction of $\overrightarrow{k_s}$ (with the fixed direction of $\overrightarrow{k_i}$

by the origin of the reciprocal lattice), a sphere of radius 1/λ is delineated in three dimensions for all possible orientations of $\overrightarrow{k_s}$ and referred as the Ewald's sphere shown in Figure 2.11 The diffraction in the direction of $\overrightarrow{k_s}$ only occurs when its end coincides with the reciprocal lattice point intersecting the sphere. Conversely, the diffraction does not take place if the reciprocal lattice point does not intersect the sphere. i.e. the Bragg's law is not satisfied.

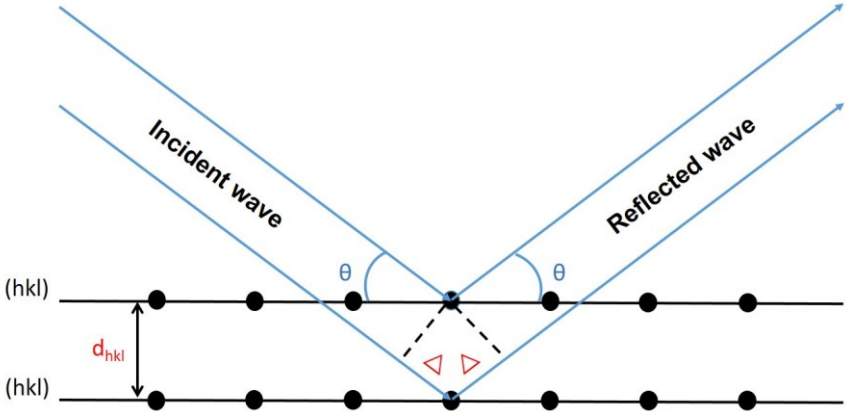

Figure 2.10: Simplified geometrical illustration of the Bragg's law.

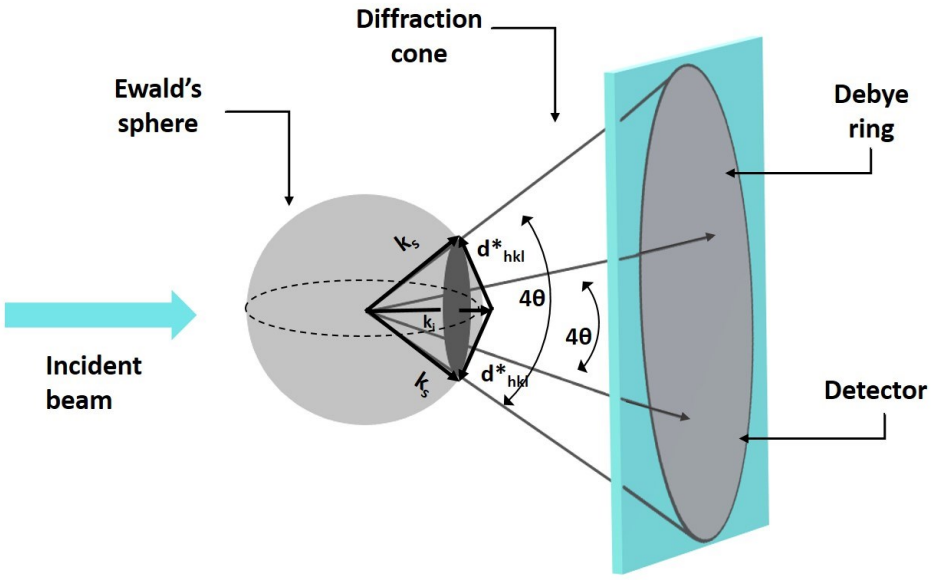

Figure 2.11: Illustration of the Ewald's sphere. Diffraction occurs at reciprocal lattice sites on the sphere, forming diffraction cones that can be seen on a screen as a spot pattern for single crystals or as a ring pattern for polycrystalline samples.

For the powder samples, the specimens contain multiple single crystallites which are randomly oriented. In this case, the reciprocal lattice vector d^*_{hkl} is arranged in a circle on the surface of Ewald's sphere, perpendicular to the incident wave vector $\overrightarrow{k_i}$, while the scattering vector is aligned along the surface of the cone (Figure 2.11). The center of the Ewald's sphere coincides with the apex of the cone, while the cone subtends a solid angle of 4θ, with the cone axis being parallel to the incident wave vector $\overrightarrow{k_i}$. Thus resulting in the formation of a diffraction cone which corresponds to a Debye ring on the film or area detector placed perpendicular to the direction of both the incident wave vector and the cone axis. Similar Debye rings, however with the different intensities and diameters will result from other reciprocal lattice vectors.

In the powder diffraction, the diffracted intensity is usually plotted as a function of a single variable like Bragg angle 2θ, interplanar distance d or the Q value ($Q=1/d^2$) i.e. a 1-dimensional diffractogram. The diffraction pattern is a Fourier transform of an ordered reciprocal lattice rather than being a direct image of the crystal. The 3 dimensional arrangement of the lattice can only be restored after transforming the diffraction pattern back into the direct space. As already mentioned, coherent scattering is of relevance for diffraction. In general, the interaction between the incident radiation with the crystal lattice is complex and can be treated with *kinematical* or *dynamical* approximations. In the *kinematical* diffraction approach, an incident beam is scattered once and the interaction of the diffracted beam with the crystal lattice is significantly small. On the other hand, *dynamical* diffraction is complex and deals with the multiple scattering of the diffracted wave inside the crystal. The kinematical approach is widely used as it is simple and adequate to describe the diffraction from polycrystalline specimens.

In order to obtain structural information from the diffraction pattern obtained from the powder X-ray or neutron diffraction techniques, it is important to understand diffraction pattern as the set of discrete reflections, which can result from several overlapping reflections from a single or multiple phases present within the sample, superimposed over a continuous background. The powder diffraction pattern is mainly determined by two factors (i) the size and shape unit cell and (ii) position and number of atoms within the unit cell. A typical diffraction patterns contains multiple Bragg reflections, whose positions, shapes and intensities reveal information about the crystal structure of the material under investigation, properties of the specimen as well as the instrumental parameters. In order to determine their contribution towards defining a diffractogram and the information that can be extracted from them, a deeper understanding of these features must be developed and will be discussed briefly here. This is important if the structural solution is attempted to determine the crystal structures via Rietveld method, which will be discussed in section 2.4.2.

2.4.1.1 Peak Positions

As already mentioned, the Bragg reflections only occur at angles θ where the Bragg's equation is satisfied. Clearly, the θ is discontinuous function of interplanar spacing d (which depends on the unit cell lattice parameters) and the wavelength of radiation used, implying both the unit cell dimensions and the wavelength play a major role for determining the Bragg or scattering angles. The interplanar spacing is dependent on the Miller indices, *h, k, l* which are used for the description of the lattice planes. The interplanar distance or the d-spacing for the simple crystal systems with the orthogonal axis can be easily calculated. As an example, the corresponding formula for the orthorhombic system can be given as

$$\frac{1}{d^2} = \frac{h^2}{a^2} + \frac{k^2}{b^2} + \frac{l^2}{c^2}$$

where a, b and c are the lattice parameters. Other factors affecting the peak positions in the diffraction patters are the systematic aberrations arising from various instrumental and specimen features, for example sample displacement and the zero shift error. Therefore, care must be taken that the instrument is properly aligned and the specimens are well prepared before recording a diffraction pattern. This is important if the lattice parameters are to be determined precisely. Other than lattice parameters, it is also possible to determine the crystal system and possibly also the space group of an unknown phase via indexing i.e. assigning *h*, *k*, *l* indices to the Bragg's reflection. Systematic absences of the reflections in the diffraction pattern can further help in narrowing down the possible space groups. These are as a consequence of the architecture of the unit cell i.e. centered instead of the primitive unit cells

and the presence of translation symmetry elements like glide plane and/or screw axis. For example, the face centered cubic lattice will contain reflections in which all *h*, *k*, *l* are either all odd or all even integers.

2.4.1.2 Peak Intensity

In the strict terms the true peak intensity is the area under the diffraction peak and is referred to as integrated peak intensity I_{hkl} (excluding the background), scattered from a set of lattice planes (hkl) in real space or lattice points in the reciprocal space. I_{hkl} is affected by atomic structure and other factors resulting from the instrumental parameters and the specimen. In the powder diffraction, I_{hkl} can be described by

$$\mathrm{I}_{hkl} = S \cdot p_{hkl} \cdot L_\theta \cdot P_\theta \cdot A_\theta \cdot T_{hkl} \cdot E_{hkl} \cdot |F_{hkl}|^2$$

Where S is the scaling factor, p_{hkl} is multiplicity factor, L_θ is Lorentz multiplier, P_θ is polarization factor, A_θ is absorption multiplier, T_{hkl}, E_{hkl} and $|F_{hkl}|^2$ denote the preferred orientation factor, extinction multiplier and structure factor respectively. Both T_{hkl} and E_{hkl} were not used within the scope of this thesis, therefore will not be discussed further.

The scaling factor is used for the direct comparison of the experimental measured intensities and the calculated intensities. This is achieved via the normalization of the observed intensities in respect to the calculated intensities via the scaling factor. It is used to obtain the weight fraction W_α of a crystalline phase present in a multi-phase mixture via the following relationship

$$W_\alpha = \frac{S_\alpha (ZMV)_\alpha}{\sum_{j=1}^{n} S_j (ZMV)_j}$$

where S_α is the scaling factor for phase α obtained from the Rietveld fit, ZM is the mass of the unit cell, V is the volume of the unit cell and n is the number of phases.

Due to the one dimensional nature of the powder diffraction pattern, the scattering from a three dimensional reciprocal lattice vectors results into peaks at identical Bragg angles. This is as a result of symmetry considerations i.e. equivalent reciprocal lattice points will have similar intensity in addition to the same Braggs angle. For example, in an orthorhombic system $h00$ and $\bar{h}00$ will result in same reciprocal lattice vector and hence a reflection at the same Bragg angle. Therefore, if the intensity corresponding to one Bragg peak is known, it can simply be multiplied by the equivalents in the group. Therefore, implying the dependence of p_{hkl} on the symmetry and the Miller indices.

The absorption multiplier A_θ, is dependent on both the geometry and the specimen property. This correction factor takes into account the reduction of the scattered intensity due to absorption. For a material with high linear absorption coefficient, there is a negligible transmission of the incident beam through the sample at any Bragg angle, resulting in an absorption factor which is constant and usually neglected since it becomes part of the scaling factor. However, if the sample has low absorption coefficient or the sample is thin, incident beam can be transmitted through the sample as a function of Bragg angle, resulting in the underestimated calculated intensity at high Bragg angles. Therefore, this correction should also be taken into account in the refinements.

All the pre-factors discussed so far are independent of the underlying atomic structure of the specimen. The remaining factor, $|F_{hkl}|^2$ which is the square of the absolute value of structure amplitude, F_{hkl}, includes contribution from atomic type and their arrangement within the unit cell. For a unit cell, containing multiple atoms with different scattering capability, the amplitude of scattered intensity can be described by structure amplitude as:

$$F_{hkl} = \sum_j f_j \cdot \exp(-B_j \frac{\sin^2 \theta}{\lambda^2}) \cdot N_j \cdot \exp(2\pi i(hx_j + ky_j + lz_j))$$

where summation takes place over all the atoms j in the unit cell, f_j, B_j and N_j are the scattering factor, displacement and the occupancy factor of the atom j respectively. The second exponent denotes the phase angle φ_j between the atom with Miller indices *hkl* and positional coordinates $x_j, y_j and\ z_j$.

The occupancy factor or the population factor relates to the occupancy of an atom at a particular site within the unit cell, whose value can range from 0 to 1. It is possible that some of the atomic sites can be partially occupied, in such cases the lattice is said to contain defects. The partial site occupancies were also observed within the scope of this thesis. The atomic displacement parameter is introduced into the general structure amplitude equation and takes into account the oscillation of an atom about its equilibrium position at temperatures above absolute zero. In its simpler form, it can be represented for the j^{th} atom as:

$$t^j = \exp\left(-B_j \frac{Sin^2\ \theta}{\lambda^2}\right)$$

where B_j is the displacement parameter for the j^{th}atom, θ is the Bragg angle and λ is the wavelength of the radiation used. Such an approximation is referred to as an isotropic parametization, where in the atoms have equal probability to deviate in any direction and $B_j = 8\pi^2(\bar{u}^2)^j$, where $(\bar{u}^2)^j$ denotes the root mean square deviation of the j^{th} atom from its equilibrium position in Å. In reality, atoms describe an ellipsoidal motion depending upon the site symmetry, which represents the anisotropic displacement.

The atomic scattering factor in the structure amplitude equation describes the scattering ability of an atom. It not only depends on the type of atom but also on the type of radiation used i.e. X-ray or neutron (two radiations of interest within the scope of this thesis). The X-rays are almost exclusively scattered by the radial distribution of the electronic cloud surrounding the atom whereas for the neutron the coherent scattering is due to the atomic nuclei.

For the X-rays, due to the scattering nature of the electron density surrounding the atomic nuclei, the scattering factor is found to increase with the increase in atomic number. At zero angle, all the scattered waves interfere constructively and therefore the scattered amplitude can be given as the sum of contributions of all the electrons, i.e. $f = Z$. With the increase in scattering angle, the destructive interference effects increase which results in f falling below Z. The atomic scattering for X-rays are expressed as function of $\sin\theta/\lambda$ (Figure 2.12).

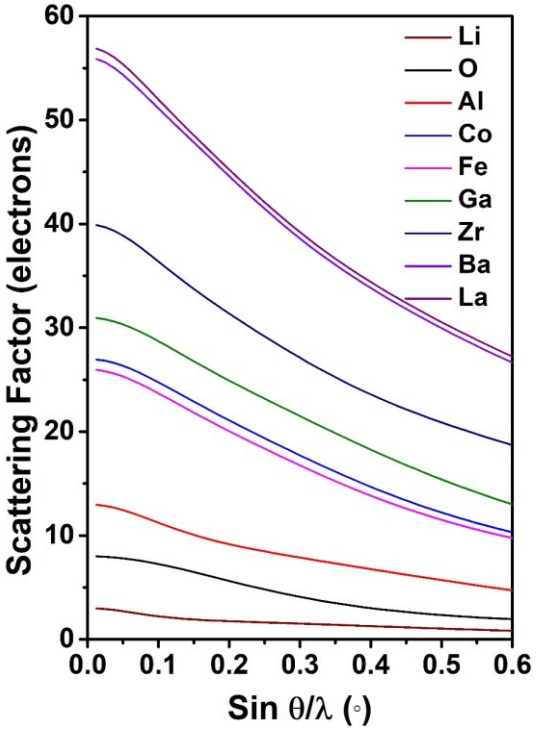

Figure 2.12: X-ray atomic scattering factors for the various elements measured in this thesis as a function of $\sin\theta/\lambda$.

For the neutron, the scattering is dependent solely on the nuclei, which are much smaller than the electron cloud and independent of the Bragg angle. The scattering factor for the neutron are referred to as scattering length and is strongly dependent on the atomic number and the type of isotope (Figure 2.13). Different isotopes of the same element have different scattering length, which helps in their detection (e.g. hydrogen and deuterium).

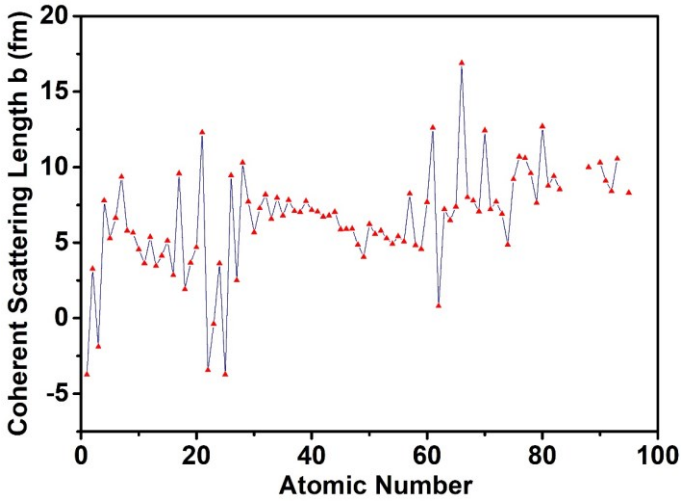

Figure 2.13: a) X-ray scattering factors as a function of ($\sin\theta/\lambda$).b) Nuclear scattering lengths of elements as a function of their atomic weight (taken from reference [94])

Due to the difference in the fundamental process of diffraction between X-ray diffraction and neutron diffraction, the two techniques are complementary to each other and have been used within thesis (Table 2.1). From the above discussion, it becomes clear that low atomic number elements like hydrogen or oxygen cannot be detected in the X-ray diffraction experiments. This further stems from the fact that light elements or weak scatterers like oxygen in presence of strong scatterers like lanthanum, barium, cobalt and iron cannot be observed due to the dominance of scattering intensity of the heavy elements. Additionally, determining the vacancy

or disorder on the oxygen anion sub lattice is significantly difficult via the use of X-ray diffraction. On the other hand, scattering contrast between the adjacent elements or the light elements in the periodic table is possible via the neutron diffraction. Therefore, for the structural analysis of the oxygen deficient phases or to determine the atomic positons/occupation of light elements, the use of coupled analysis of neutron and X-ray diffraction data set was necessary.

Table 2.1: Comparison between X-ray and neutron radiations widely used in powder diffraction experiments.

	X-rays	Neutron
Nature	Wave	Particle
Scattering by	Electron density	Nuclei and magnetic spins
Scattering Function	*f(s)* $\propto$ Z	*f* is constant
Lattice image	Reciprocal	Reciprocal
Applicable theory	Kinematical	Kinematical
Wavelength	~0.5 to 2.5 Å	~ 1 Å

2.4.1.3 Peak width and shape

Due to one dimensional nature of the powder diffraction, the reflections can be composed of several Bragg peaks. The observed reflection shapes can be described as the peak profile function which results from convolution of three different functions (i) wavelength dispersion, Ω, (ii) instrumental broadening, Ψ, and (iii) specimen function, Λ. This can be described as

$$PPF\ (\theta) = \ \Omega\ (\theta)\ \Psi(\theta)\Lambda(\theta) + \mathrm{b}(\theta)$$

where b represents the background function. Amongst these the isotropic broadening due to the specimen is of interest since it results from the physical state of the sample i.e. crystallite size (τ) and microstrain (ε). The peak broadening resulting from these two effects can be given as:

$$\beta = \frac{\lambda}{\tau \cdot \mathrm{Cos}\ \theta}$$

and

$$\beta = \ k \cdot \varepsilon \cdot \tan\theta$$

k being the constant. Because of the θ dependence, these two effects can be distinguished. An important point to note is that β is not the total peak broadness but the additional width on top of the all instrumental contributions. Therefore, profile fitting using suitable peak shape functions are required to obtain the position and intensities of each Bragg reflection.

For the description of the peak shapes, fundamental parameter approach is used, since it models all the three components of the peak profile function. The Bragg peaks especially in the X-ray diffraction can be described by the pseudo-Voigt function, which is the linear combination of Lorentz and Gauss functions. The pseudo-Voight function can be given as

$$PV(x) = \eta * L(x) + (1 - \eta) * G(x)$$

where η is the mixing parameter whose value varies between 0 (pure Gauss) to 1 (Lorentz) and the argument x shows the position of the peak, which is located at $x = 0$.

2.4.1.4 Peak asymmetry

The peak shapes in the diffractogram are usually asymmetric i.e. they are not centrosymmetric with respect to the argument x, which mainly manifests from the different instrumental factors

like axial divergence of the beam and also specimen geometry. As a result, the Bragg reflections are considerably broader at the low θ angles compared to that of high angles and hence is highly prominent at 2θ values below ~ 30° for Cu radiation and not visible at higher angles. Although the peak asymmetry cannot be completely eliminated, it can be significantly reduced by proper instrument alignment and configuration.

2.4.1.5 Fundamental parameter approach

Fundamental parameter approach can be used to determine the influence of the wavelength dispersion and instrumental contribution on the peak shape parameters. The approach is based on the comprehensive description of both the instrumental configurations and experimental conditions which allows for the computation of peak shape parameters. This is achieved by measuring a crystalline standard sample like LaB_6 for which the crystallite and strain effects are known, thereby enabling adjusting all non-sample related parameters (for example, slit opening, axial divergence, source sample geometry and dimensions). The obtained parameters are fixed during the subsequent refinements of specimens. The fundamental parameter approach is already implemented in the Topas V5.0 software [95], which was used to perform Rietveld fits during the course of this thesis.

2.4.2 The Rietveld method

Rietveld method is a powerful refinement tool for crystal structure analysis which relies on the minimization of the least squares fit. Also known as full profile refinement, it is similar to Pawley or Le Bail method, however different in the sense that integrated intensities are not determined iteratively (Le Bail) or treated as free least square variables (Pawley). For the successful implementation of the method, a reasonable initial information about the unit cell dimensions, atomic positions peak shape parameters of the crystal structure are required. The mathematical quantity that is minimized in the Rietveld fit is the residual S_y:

$$S_y = \sum_i w_i (y_i - y_c)^2$$

where w_i = $1/y_i$, y_i is the observed intensity in the diffraction experiment and y_c is the calculated intensity. The total intensity y_i at point i, is the sum of the contributions from the individual Bragg reflections. The calculated intensities y_c resulting from the structural model used in the Rietveld refinements are determined from $|F_{hkl}|^2$ by summing up contributions from all the neighbouring Bragg reflections in addition to the background:

$$y_c = S \sum_k L_k \cdot |F_k|^2 \cdot \varphi \cdot (2\theta_i - 2\theta_k) \cdot P_k \cdot A + y_{bi}$$

Herein, S is the scaling factor, k represents the miller indices, L_k denotes contributions from Lorentz, polarization and multiplicity factors, φ is the reflection profile function which depends on various instrumental and sample related contributions, P_k denotes the preferred orientation function, F_k is the structure factor of k^{th} Bragg reflection and y_{bi} is the background intensity factor at step i. As already mentioned, the Rietveld method involves with the minimization of the least squares, leading to a set of normal equations involving the derivatives of the calculated intensities y_c, with respect to each refineable parameter. The obtained set of equations are solvable via the inversion of the normal matrix M_{jk} described as:

$$M_{jk} = -\sum_i 2\, w_i \left\{ (y_i - y_c) \frac{\partial^2 y_c}{\partial x_j \partial x_k} - \left(\frac{\partial y_c}{\partial x_j} \right) \left(\frac{\partial y_c}{\partial x_k} \right) \right\}$$

where $x_j$and x_k are the set of adjusted or refined parameters resulting in the m by m matrix which is inverted and m denotes the adjusted parameters. Due to the non-linear nature of the residual function S_y, the solution is obtained by an iterative procedure where in the shifts $\triangle x_k$ can be given as

$$\triangle x_k = \sum M_{jk}^{-1} \left(\frac{\partial S_y}{\partial x_k} \right)$$

The shifts calculated are applied back to the starting parameters in order to improve the model. Care must be taken to avoid some false minima which is due to the divergence of the refinement and is intrinsic to the least squares fittings. This can be achieved via the use of constraints or with the use multiple data sets of different kind, for example coupled Rietveld analysis of X-ray and neutron diffraction data. Additionally, care must be taken when refining high number of refinement parameters simultaneously within the refinements which can lead to strong correlations leading to the similar effects on the calculated intensity. The parameters usually refined within the Rietveld refinements are listed in Table 2.2.

Table 2.2: Parameters refineable during the Rietveld fitting.

Global	For each phase present
2θ-Zero	Atomic positions $(x_i, y_{i,} z_i)$
Instrumental profile	Scaling factor (S)
Profile asymmetry	Lattice parameters $(a, b, c, \alpha, \beta \text{ and } \gamma)$
Background	Sample-profile width parameters
Wavelength	Occupation factor
Sample displacement	Isotropic thermal parameters (B_i)
Sample transparency	Individual anisotropic thermal parameters
Absorption	Crystallite size and microstrain
	Extinction
	Preferred orientation

To determine the quality of the refinements, a set of variables referred to as figures of merit (FOM), i.e. R_p, R_{wp}, R_{Bragg} and Goodness of fit (GOF) should be taken into consideration. During the Rietveld fitting, these parameters should show minimal fluctuations and gradually decrease to certain minimum values. Of course, lowering of these values is not the only indication of the valid structural model, the model obtained should also make chemical and physical sense, e.g. cation-cation and cation-anion bond distances should be in agreement with the respective ionic radii. Among the FOM values, R_{wp} and R_{Bragg} are most meaningful and can be given as:

$$\mathrm{R_{wp}} = \sqrt{\frac{\sum_i w_i \cdot (y_i - y_c)^2}{\sum_i w_i \cdot (y_i)^2}}$$

And

$$\mathrm{R_{Bragg}} = \frac{\sum_k \left| \sqrt{I_{ki}} - \sqrt{I_{kc}} \right|}{\sum_k \sqrt{I_{ki}}}$$

where $I_k$denotes the intensity of the Braggs reflection k.

The goodness of fit (GOF) is another term often used to judge the quality of the fitting and is given by:

$$\mathrm{GOF} = \frac{\mathrm{R_{wp}}}{\mathrm{R_{exp}}} = \sqrt{\frac{N-P}{\sum_i w_i \cdot (y_i)^2}}$$

where N and P are the number of measurement points and refined parameters respectively.

2.4.3 X-ray diffraction

Within the scope of this thesis, other than its use for complex structural analysis, X-Ray diffraction was regularly used for phase analysis. Although the underlying fundamentals of diffraction have already been discussed in section 2.4.1, a brief introduction to the fundamental of the technique and the setup would be presented within the context of this thesis.

In almost all the laboratory based X-ray diffractometers and the one used during the course of this thesis, X-rays are produced when a beam of electrons (produced by heated tungsten filament) is accelerated through a high potential, e.g. 30 kV, and allowed to strike a target metal anode like Cu. Such high incident electron energies are capable of ionizing the Cu 1*s* (K-shell) electron which leads to the electron present in the outer shell (2*p* or 3*p*) to transit into the vacant 1*s* shell and in the process release X-ray radiation. For the Cu anode, both K_α i.e. 2*p* to 1*s* and the K_β i.e. 3*p* to 1*s* transition are possible, which result in X-rays corresponding to the wavelength of 1.5418 Å and 1.3922 Å respectively. K_α radiation is most widely used in the diffraction experiments and is in fact a doublet with $K_{\alpha1} = 1.54051$ Å and $K_{\alpha2} = 1.54433$ Å. For filtering the K_β radiation and to obtain a reasonably clean X-ray beam of K_α radiation, nickel foil is used.

For the diffraction measurements, the powder polycrystalline samples were measured in a Bragg-Brentano geometry. This geometry, also referred to as the flat plate geometry offers good peak intensity and as well as the resolution. Within this reflection geometry, the divergent and diffracted beams are focused at a fixed radius from a flat plate sample which is at the center of the goniometer circle. Both, the source and the detector move –θ and θ with respect to the fixed sample. As-produced X-ray beam requires collimation which is achieved by placing slits between the X-ray source and the sample. The slit used is called as the divergence slit and both fixed or variable slits can be employed. The axial divergence of the beam can be controlled by the use of soller slits, which are the set of parallel equally spaced metal plates.

The detection of the scattered X-rays can be achieved via a position sensitive detector which consists of multiple microstrip anode fixed on a glass substrate produced via photolithography[96]. Each anode strip is at a fixed 2θ position with respect to other strips and acts as an individual detector. The working principle of PSD is based on absorption of scattered X-rays resulting in the formation of ion pairs i.e. Xe ion-electron pairs. The electrons are accelerated towards the anode due to the applied electric field which can result in further ionization of Xe atoms. The electrons are discharged resulting in an electric current pulse in the anode circuit. In a point detector this pulse is measured on one end of the wire whereas for the line detector the propagates on both the ends of the anode. By measuring the time difference between the arrival times of the same pulse at both the ends of the anode, the position of the discharge event can be determined.

2.4.4 Neutron diffraction

The powder neutron diffraction experiments were carried out at the ISIS high resolution powder diffractometer (HRPD), Rutherford Appleton Laboratory, Didcot, United Kingdom. The neutrons for the diffraction experiments are produced via spallation, where accelerated protons are produced in a synchrotron and targeted towards tungsten metal maintained in a target station,

where they collide and result in spallation of neutron from the tungsten metal. The emitted white neutrons are then channeled via beamlines towards the ISIS instruments.

The neutron powder diffraction experiment at the ISIS is based on the time of flight analysis of the pulsed neutron with different wavelengths. The wavelength and the corresponding d-spacing can be calculated by recording the time each neutron pulse takes to reach the detector. The relation between the neutron wavelength (λ), mass of the neutron $m_{neutron}$, flight path length (L) can be given as:

$$\lambda = \frac{h}{m_{neutron} \cdot v} = \frac{h \cdot t}{m_{neutron} \cdot L} = 2dSin\theta$$

The angle θ is constant due to the stationary position of detector banks.

2.5 Electrochemical impedance spectroscopy

Electrochemical impedance spectroscopy (EIS) is a widely used non-destructive technique employed for the investigation of electrochemical systems. The technique allows for probing the resistance of an electrochemical system to an applied alternating current (AC) as a function of frequency which spans ~10^9 orders of magnitude (mHz to MHz). In a typical EIS experiment small perturbation voltage is applied to a system which is in equilibrium state, triggering a response determined by the initial state of the system. The response generated contains information related to equilibrium state and perturbation. In strict terms, the concept of impedance is valid only for the systems which fullfil the conditions of linearity, causality and stationarity. Linearity implies that response of the system is proportional to the excitation. Causality refers to the response resulting only from the applied perturbation and stationarity means that the system is in equilibrium and does not undergo any change with time.

In a typical EIS experiment, frequency response analyzer is used to measure the response of the specimen under investigation to a voltage stimulus as a function of frequency. The applied sinusoidal voltage of the form $V(t) = V_o\, sin(\omega t)$ leads to a current response given by $I(t) = I_o\, sin(\omega t + \Phi)$, where ω is the angular frequency, which is related to the AC frequency as $\omega = 2\pi f$ and Φ is the phase shift between the voltage and current. The phase shift Φ of 0°, -90° and 90° denotes an ideal resistor, capacitor and inductor respectively. Therefore, the impedance of an electric circuit is given as the ratio of the two quantities:

$$Z(\omega) = \frac{V(\omega)}{I(\omega)} = \frac{V_o\, sin(\omega t)}{I_o\, sin(\omega t + \Phi)} = Z_0 \frac{sin(\omega t)}{sin(\omega t + \Phi)}$$

implying that impedance can be represented in terms of magnitude Z_0 and phase shift Φ. Since, the impedance contains both the magnitude and phase, it can be represented as complex number with real and imaginary components i.e. Re(Z) or Z' and Im(Z) or Z" using the Eulers relationship:

$$e^{i\Phi} = \cos(\Phi) + isin(\Phi)$$

The potential $V(t) = V_o \exp(i\omega t)$ and current $I(t) = I_o \exp(i\omega t - \Phi)$ leads to the complex impedance given as:

$$Z(t) = \frac{V(t)}{I(t)} = \frac{V_o \exp(i\omega t)}{I_o \exp(i\omega t - \Phi)} = Z_0 e^{i\Phi} = Z_0\big(\cos(\Phi) + isin(\Phi)\big) = Z' + i \cdot Z"$$

This enables impedance to be visualized as a vector in a complex plane plot wherein the real part is plotted on the X-axis and imaginary part on the Y-axis as shown in Figure 2.14a. For the practical purpose, the impedance data is represented as Nyquist and Bode plots. The

Nyquist plot shows the negative imaginary part as a function of real part of the impedance. A main drawback of the Nyquist plot is that it is 2-dimensional and does not contain any information about frequency dependence unless these data points are labelled individually corresponding to their respective frequencies. Therefore, nearly always Bode plots are used as the complementary to the Nyquist plot, since they show the frequency dependence of phase angle and the magnitude of impedance. An example of the Nyquist and Bode plots are given in Figure 2.14b&c respectively, measured for an RC circuit connected in parallel at room temperature, where R is the resistance and C is the capacitance.

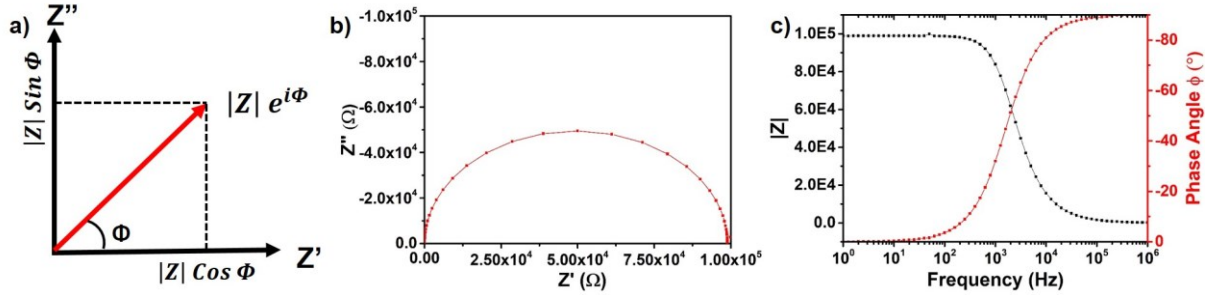

Figure 2.14: a) Complex plane representation of impedance. b) Nyquist plot for one RC element connected in parallel. c) The corresponding Bode plot for the same RC element. Here the impedance measurement was carried out on a standard RC sample with a resistor R with the resistance of 100000 Ω and a capacitor C in parallel with a capacitance of 10^{-9} F.

Both the Nyquist and Bode plot together help in establishing an equivalent circuit model which is based on the impedance of the individual circuit elements and also their combinations. The equivalent circuit models usually contain series and parallel arrangement of resistances R, capacitances C and inductances L and their contribution to the impedance is given as:

$$Z_R = R,\ Z_C = \frac{1}{i\omega C},\ Z_L = i\omega L, \qquad Z_{RC} = \frac{R}{1 + i\omega RC}$$

where Z_R, Z_C, Z_L and Z_{RC} are the impedances due to a resistor, capacitor, inductor and a parallel arrangement of RC element. Due to their relationships, the impedance of an ideal resistor coincides with the real axis in the Nyquist plot whereas an impedance of an ideal capacitor can be observed at a vertical parallel line along the negative imaginary axis. An ideal resistor forms a plateau in the absolute impedance plot due to the frequency independence of its impedance. Further, both resistor and a capacitor can be distinguished by their phase shift of 0° and -90°, respectively. The parallel arrangement of a resistor and a capacitor manifest as a semicircle of diameter R in the complex plane plot. The maximum of the semicircle is found at ω_{max}, which is the relaxation or resonance frequency of the RC element:

$$\omega_{max} RC = 1,\ \ 2\pi f_c RC = 1,\ \ 2\pi RC = \frac{1}{f_c},\ \ 2\pi RC = \tau$$

where $\omega_{max} = 2\pi f_c$ and f_c in the critical relaxation frequency. Semicircles resulting from the RC elements connected in series can be differentiated if their respective time constant are more than two orders of magnitude apart.

In the real systems however, the frequency dependence of impedance is much more complex and it is rare to see perfect semicircles in the Nyquist plot due to overlapping of the processes with similar time constants, which necessitates detailed modelling and fitting of spectra. This is accomplished via the equivalent circuit modelling which attempts to approximate the experimental data with an electric circuit using complex non-linear least squares fitting. The deviation from ideal semicircle behavior in the real materials results from inhomogeneities and

imperfections in the bulk and at the interfaces such as defect, roughness, porosity and compositional variation. This manifest as asymmetric and depressed semicircle. RC elements are inadequate for modelling such behavior and therefore an ideal capacitor is replaced by the so called constant phase element (CPE) whose impedance can be given as:

$$Z_{CPE} = \frac{1}{T\,(i\omega)^{\eta}}$$

Where T is related to impedance and η is the constant phase element exponent. For the value of η = 1, 0 and -1, CPE behaves like an ideal capacitor, resistor and inductor respectively. The value between 0 and 1 leads to a depressed semicircle in the Nyquist plot. For fitting the impedance data, it is important to choose the right equivalent circuit model. This is important since, two or more RC elements with similar time constant can result in the depressed semicircle. Additionally, multiple models can result in the same impedance spectrum and fitting. Therefore, a prior knowledge of the physical and chemical processes taking place in the cell is required. For the assignment of the various processes or RC elements to the different parts of the region, capacitance values can be calculated from the fitting of the equivalent circuit parameters:

$$C = (T \cdot R^{1-\eta})^{\frac{1}{\eta}}$$

For a parallel plate capacitor with the area of plates A and the distance between the plates d, the capacitance can be given as:

$$C = \varepsilon_r \varepsilon_o \frac{A}{d}$$

where ε_r and ε_o are the relative permittivity and vacuum permittivity respectively. Since the value of relative permittivity of a dielectric lies in the range of 10-100, this corresponds to the capacitance of 10^{-12} F for a specimen with the A/d ratio of ~ 1 cm^{-1}. The obtained capacitance values can be related to different phenomenon as seen from Table 2.3.

Table 2.3: Capacitance values typically observed and their origin. The listed capacitances are normalized by the A/d.

Capacitance (Fcm^{-1})	Phenomenon
10^{-12}	Bulk dielectric relaxation
10^{-11}	Impurity or minor phase contributions
10^{-11}-10^{-8}	Grain boundary contribution
10^{-9}-10^{-7}	Surface layer
10^{-7}-10^{-5}	Sample-electrode interface
10^{-4}	Electrochemical reactions

2.6 Simultaneous thermal analysis

Simultaneous thermal analysis (STA) refers to simultaneous measurement of thermogravimetry (TGA) and differential scanning calorimetry (DSC) of the specimen. STA measures certain physical and chemical properties like heat capacity, enthalpy, mass and thermal explosion coefficient of the specimen as a function of temperature.

In TGA, mass of the specimen is recorded as a function of temperature, time and atmosphere. These measurements are mostly used to determine the composition of the specimen and/or predict its thermal stability. Further, the technique can be used to characterize materials exhibiting weight gain or loss due to absorption/desorption of volatile species (for example

water) or due to oxidation and reduction. TGA consists of a sample pan supported by a highly sensitive balance placed inside of a furnace which is heated and cooled during an experiment. The whole set-up is thermostated to minimize the environmental influences. Different gases can be purged inside the set-up depending upon the requirements. Changes in mass of the specimen is recorded during the heating and the cooling cycle.

DSC is used both as a stand-alone as well as complementary method to TGA and measured on the same instrument to allow for the perfectly identical experimental conditions. DSC allows for analyzing the molecular structure of the polymer because the peaks in DSC profile correspond to endo or exothermic processes which are associated with the structural changes occurring as a function of temperature. DSC measures the changes in the heat capacity as changes in heat flow during the heating and the cooling cycle. This allows the user to determine the transition points like, melting, glass transition, phases changes etc. For example, if a specimen undergoes melting then the heat will be absorbed resulting in an endothermic peak whereas exothermic processes like crystallization will result in the exothermic peak. During a DSC measurement, heat flow difference between the specimen and standard is measured as a function of time or temperature over a constant heating and/or cooling rate (e.g. 10 $Kmin^{-1}$) which allows for identifying the thermal transitions due to enthalpy changes ($\triangle H$) resulting in the endo or exothermic response.

Within this thesis, STA has been mainly used for two purposes. i) To determine the degree of crystallinity of the composite electrolytes. This can be achieved via using the following equation:

$$\chi_c = \frac{\triangle H_m}{\triangle H_{PEO} f_{PEO}} \times 100\%$$

Here, χ_c is the relative percentage of PEO crystallinity, $\triangle H_m$ is the measured melting enthalpy of the composite electrolyte, $\triangle H_{PEO}$ is the melting enthalpy of completely crystallized PEO and f_{PEO} is the PEO mass percentage in the composite electrolyte. ii) To determine the weight change upon oxidation and water loss.

2.7 ^{57}Fe Mössbauer spectroscopy

Mössbauer spectroscopy is a technique which allows energy levels of a nucleus situated in an atom and a solid, which are modified by the environment to be investigated by measuring the energy dependence of resonant absorption of gamma rays by the nuclei. The method is based on Mössbauer effect in which a nucleus in a solid matrix can emit and absorb gamma radiation without recoil i.e. recoilless resonant emission and absorption of gamma radiation, therefore allows to measure very small hyperfine interactions between the nucleus and its surrounding electrons allowing for the determination of oxidation state, coordination environment and magnetic state of the Mössbauer active nuclei.

In a typical experiment, a radioactive source containing the Mössbauer isotope (^{57}Co) undergoes a spontaneous electron capture resulting in the metastable ^{57}Fe which further decays to the ground state via the emission of Mössbauer gamma rays with the energy of 14.4 KeV. The produced gamma rays are passed through an absorber containing the material that is to be investigated, which results in their partial absorption followed by their detection by a suitable detector. To modify the energy of the incident gamma rays so that their energy is apt for the resonant absorption i.e. the energy of the gamma rays should match the nuclear transition energy of the Mössbauer nucleus under investigation. This is achieved by moving the source relative to the stationary absorber which gives an energy shift to the gamma rays

due to first order relativistic Doppler effect. The oscillatory motion of the source provides an energy scan. As a result, Mössbauer spectrum is obtained consisting of gamma ray counts as a function of source velocity (measured in mms^{-1}). A Mössbauer spectrum depends on various types of hyperfine interactions which can be characterized by number, position, share and relative intensity of the absorption lines.

2.8 X-ray photoelectron spectroscopy

X-ray photoelectron spectroscopy (XPS) is a surface characterization method widely employed for obtaining information on the surface compositions, oxidation states as well as the electronic structure. The technique uses the photoelectron effect wherein the specimen under investigation emits a photoelectron upon irradiation by photons of sufficient energy. Usually for an XPS measurement, a monochromatic incident X-ray radiation with characteristic energy interacts with the valence or the core electrons within the specimen leading to the ejection of photoelectrons. In the XPS measurements photons in the X-ray regime with the energy in the range of 100 eV to >1000eV are employed, which enables the analysis of core electrons. The resulting photoelectrons are differentiated on the basis of their kinetic energy which provides information about the chemical nature and the electronic structure of the surface species. For the photoelectric effect to occur, an important criterion to be met is the energy of the incident photon $h\upsilon$ should be higher than the electron's binding energy E_B plus the work function Φ_s of the specimen under investigation. The binding energy is a function of specific element and the atomic energy level. The resultant photoelectron will have the kinetic energy given as:

$$E_{kin} = h\upsilon - E_B - \Phi_s$$

The emitted photoelectrons are collected and then focused on to the entrance slit of a concentric hemisphere analyzer using a magnetic collection lens followed by focusing by two electrostatic lenses.

The photoelectrons reaching the entrance slit are retarded by an application of retardation voltage V_R to the pass energy E_{pass}. By varying the applied potential, only the electrons with certain energy can pass through the analyzer based on the deflections which depend of the kinetic energy of the incoming photoelectron. This pass energy is defined by the potential of the concentric hemisphere analyzer. In order for the electrons to pass through the analyzer, their energy should be in the range of $E_{pass} + \triangle E$. The small energy difference between electrons can be compensated by the shorter or the longer path an electron has to take to reach the detector.

2.9 Fourier transform infrared spsectroscopy

Fourier transform infrared spectroscopy (FTIR) is a widely used non-destructive analytical chemical analysis technique for characterizing the molecular structure of compounds by monitoring the molecular vibrations of the functional groups.

FTIR is based on studying the frequency of vibrations in the molecules by passing the infrared radiation through the sample and recording the absorption spectra as a function of frequency. When the frequency of the incident radiation matches the characteristic vibrational frequency of the molecule, changes in the amplitude of the vibrations are caused. These vibrations are a result of bending and stretching movements of the molecules. IR spectrum is divided into different regions based upon the wavenumber

Near IR:- between 12500-4000 cm^{-1}

Mid IR:- Region between 4000-600 cm^{-1}. The region most used in IR spectroscopy. Region below 1400 cm^{-1} is called as the finger print region, where specific absorptions of the sample can be analyzed.

Far IR:- Region between 650-200 cm^{-1}

Within this thesis, FTIR was used to confirm the compatibility of the cryo-milling process for the composite electrolyte membrane preparation and presence of protons within the hydrated barium-rich perovskites.

2.10 Raman spectroscopy

Raman spectroscopy is a spectroscopic technique typically employed for determining the vibrational modes of molecules which are excited as a result of inelastic scattering of photons, generally known as Raman Scattering.

To measure the spectra, a monochromatic light from the laser within visible or infrared range is incident on the sample. The interaction of the light with the molecular vibrations i.e. phonons within the specimen results is energy shift of the laser photons. This shift can be either up or down. Among these the most frequent interaction is the Rayleigh scattering due to the elastic scattering. During this process, the system relaxes back to the initial state by emitting a photon of the same energy as the absorbed photon. The inelastic scattering or the Raman scattering results in the emitted photon whose energy is higher or lower compared to that of the incident photon. This is due to the relaxation of the system from an excited state to an energy level higher or lower than the initial state. If the energy of the emitted photon is higher, it is referred to as the anti-stokes shift, whereas the photon emission with the lower energy is referred to as the lower probability of this scattering event resulting in orders of magnitude weaker intensity than the emitted light.

Within the scope of this thesis, Raman spectroscopy was primarily used to determine the compatibility of the cryomilling process for the fabrication of composite electrolyte membranes by confirming the stability of the molecular polymer entities and to determine the presence of carbonate species in $BaCoO_{3-\delta}$ systems.

2.11 Magnetometric measurements

stands for superconducting quantum interference device and are generally sensitive towards small magnetic fluxes within the samples. IN SQUID, a sample is periodically moved through a super conducting input coil, resulting in the variation of the magnetic flux due to the changes in the external magnetic field. The super conducting input coil is inductively coupled to the SQUID sensor, which measures the changes in the magnetic flux and translates them into voltage signals. The working principle of the SQUID is based on the phenomenon of Josephson tunneling and flux quantization.

Within this thesis SQUID was mainly used to determine the magnetic state of the $BaCoO_{3-\delta}$ and $BaFe_{1-x}Co_xO_{3-y-\delta}(OH)_y$.

2.12 Scanning electron microscopy

To investigate the morphology and dispersion of ceramic particles within the CEs, scanning electron microscopy can be used. In SEM, a focused electron beam (1-30 keV), produced in an electron gun maintained under ultra-high vacuum conditions is incident on the sample. The electron beam is focused and deflected via variety of different electromagnetic lenses. The incident electron beam interacts with the sample in the sample chamber, which is maintained under high vacuum to limit electron scattering with air. This interaction results in the emission

of low-energy secondary electrons. These secondary electrons are formed due to the inelastic interaction between the primary focused electron beam and the electrons within the sample under investigation. The low energy and small mean free path of the secondary electrons results in the emission and detection of only surface electrons with very high resolution. The detection of secondary electrons is achieved via an Everhard-Thornley detector.

3 Composite electrolytes for all-solid-state lithium-ion batteries

This chapter deals with the major scientific findings related to synthesis and characterization of the solid composite electrolytes for the all solid state lithium ion batteries reported in the below listed publications. Before these articles are given, a summary in context of literature is of the results presented in these articles is provided in order to bridge the two publications and make it convenient for the reader to follow the course of the project and its evolution.

3.1 Compositional Dependence of Li-Ion Conductivity in Garnet-Rich Composite Electrolytes for All-Solid-State Lithium-Ion Batteries – Towards Understanding the Drawbacks of Ceramic-Rich Composites

3.2 PEO Infiltration of Porous Garnet-Type Lithium-Conducting Solid Electrolyte Thin Films

The work presented here is a part of a broader project, which is a joint collaboration between three groups at TU Darmstadt, i.e. surface science division, macromolecular chemistry division and materialdesign durch synthese division, with each having specific objectives to contribute to towards the project.

Within the materialdesign durch division, the individual goal was to address the following questions:

- The role of ceramic filler morphology on the Li-ion conductivity within the composite electrolytes.
- The role of filler type (inert and active) on the Li-ion conductivity within the composite electrolytes.
- Influence of garnet elemental composition on the Li-ion conductivity in composite electrolytes.
- To study the interfacial stability between the garnet and the polymer in composite electrolytes.

Initially, a model composite electrolyte system was to be chosen which could be studied and used as a standard system within the project, furthermore then extend the studies further to other relevant systems. The organic polymer was commercially purchased for the preparation of CEs. For the preparation of CEs, PEO was chosen as the polymer of choice due to its commercial availability, non-toxicity and cost considerations. Pure PEO is an insulating polymer and therefore requires a lithium salt that can act the source of lithium ions for ionic conduction. Bis(trifluoromethane)sulfonimide (LiTSFI) is an appropriate choice since it has a heavy anion which favors the salt dissociation into Li^+ and $TSFI^-$ and in the process provides free Li^+ ions for conduction.

For the preparation of CEs, the traditional preparation method is via the solvent-based approach, where in ceramic fillers are dispersed into a solvent like acetonitrile and ultra-sonicated for several hours to have a homogenous particle dispersion. This is followed by addition of Li-salt and polymer of choice. One of the major drawbacks of this method is that it is not suitable for garnet based ceramic electrolytes, since they are susceptible to moisture and form Li_2CO_3 on the surface, which is a Li-ion insulating phase and can lead to high interfacial resistance at the garnet/PEO interface [21]. Also, inorganic ceramic fillers like garnets have higher density compared to that of PEO, which may cause filler segregation and result in inhomogeneous distribution of garnet filler inside the PEO matrix, irrespective of the weight

ratios between these components. Therefore, an alternative preparation strategy was required. In this respect, cryo-milling approach is a suitable technique for CE preparation as it does not require any solvent and also due to the fact that milling vials can easily be filled with the respective powders inside an inert gas filled glove box, which limits the exposure of a ceramic fillers like garnets towards ambient atmosphere.

In the beginning, optimization studies were carried out to find a suitable PEO to LiTSFI weight ratio which offers the maximum possible Li-ion conductivity. These measurements were carried out using PEO of molecular weight of 100000 g mol^{-1} and by varying the PEO to LiTSFI molar ratio, i.e. 1:1, 1:10,1:20,1:30 and 1:100. It is observed that as the LiTSFI molar fraction increases within the polyelectrolyte (PEO+LiTSFI), the conductivity increases. The increase in conductivity with the higher weight ratios of LiTSFI is in agreement with the higher Li-salt concentration, which under steady state conditions can be expressed as

$$\sigma = nq\mu$$

Here, n is the number of free ions, q is the number of charges and μ is the mobility. Therefore, increasing the concentration of Li^+ ions increases the conductivity of the polyelectrolyte. For the PEO:LiTSFI molar ratio of 1:30, the maximum Li-ion conductivity was observed as seen from the Arrhenius plot shown in Figure 3.1a. However, as the molar ratio increases further (1:100), not much significant change in conductivity is observed. Further, it was observed that the polyelectrolyte with higher PEO to LiTSFI weight ratio, the polyelectrolyte membrane loses its structural integrity, which is of importance here as during the impedance measurements polyelectrolyte membranes can change their aspect ratio (thickness to area) that would eventually result in an error calculating the Li-ion conductivity of such a membrane. Therefore, PEO to LiTSFI molar ratio of 1:30 was chosen for the subsequent studies. Further, optimizations were attempted by varying the molecular weight of the PEO while maintaining the PEO to LiTSFI weight ratio of 1:30. As can be seen from the Figure 3.1b, the maximum Li-ion conductivity was observed for the PEO of 100000 g mol^{-1}. Therefore, for the preparation of composite electrolytes this was chosen as the polyelectrolyte of choice.

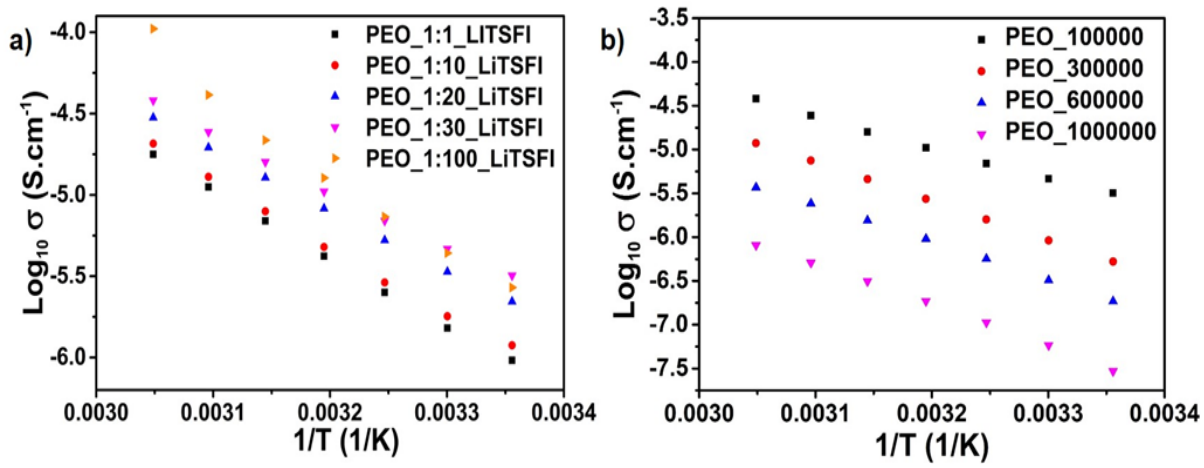

Figure 3.1: (a) Temperature dependent Arrhenius plot measured for PEO of molecular weight 100000 g mol^{-1} with different molar ratios of LiTSFI salt. (b) Arrhenius plot for PEO with different molecular weight and 1:30 molar ratios of LiTSFI salt.

Traditionally, composite electrolytes have been prepared by dispersing nano-sized ceramic fillers within the polymer matrix [23, 66]. Although, this has known to result in enhanced Li-ion conductivity within polymer-rich composite electrolyte on account of favourable filler/polymer interfacial interactions [22, 97], for the ceramic-rich CEs nanoparticles will result in high

concentration of loosely contacted particle/particle interface, which may not necessarily have a positive impact on ion conductivity but instead lead to high impedances at this interface. Similarly, On the other hand, large sized particles would limit polymer/filler interfacial interactions which have been known to be beneficial towards Li-ion conductivity [22]. Therefore, particle sizes lying in between the nanometer to micrometer regime would be a decent compromise to benefit from both the morphology and as well as the particle size. Since, NSP offers a synthesis route which offer particle sizes within such a range, hence was used for synthesizing garnet powders.

As already discussed in section 2.1, NSP has previously been used for the synthesis of garnet powders [34]. For the garnet synthesis, the tiny droplets of the solution containing nitrates of various salts are produced via an ultrasonic nebulizer. These droplets were then injected into a reaction chamber, i.e. a hot zone furnace, maintained at 1173 K via a constant flow of O_2, where the particle synthesis takes place. The particles produced were then deposited on to a filter paper in the deposition chamber, which was maintained at temperatures above 373 K to prevent the condensation of the solvent, usually water. The garnet particles are not directly obtained after the synthesis, instead as-synthesized powders are composed of $La_2Zr_2O_7$ and Li_2CO_3, which are then sintered at 1273 K for 180 min to obtain the desired garnet phase. As can be seen from Figure 3.2a and b, as-synthesized particles show a spherical morphology and after the heating step necking between the particles occurs, which might prove to be beneficial in composite electrolytes by providing a continuous garnet/PEO interface.

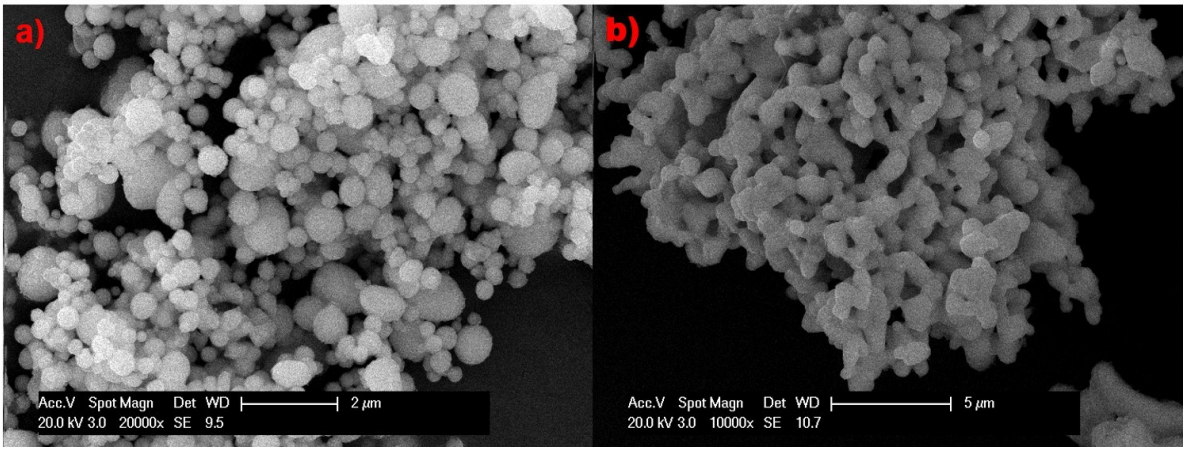

Figure 3.2: (a) SEM micrograph of the as-synthesized garnet powders obtained from NSP. (b) Morphology of the heated treated garnet powders showing inter connected particles.

Using NSP as the garnet synthesis method for CE preparation can have an additional advantage. The garnet particles obtained via this method can be directly used as fillers within the PEO matrix as reported previously in several works [71, 98]. Additionally, blends of composite electrolyte membranes comprising of different garnet to PEO weight ratio can be easily prepared via the cryo-milling method. Although, such a particle dispersion will be loosely held within the PEO matrix, the favourable necking between the particles and the smaller size of the particles can prove to be beneficial in the sense of providing higher garnet/PEO interface that is known to be favourable towards Li-ion conductivity [76, 97]. Additionally, the necking between the garnet particles lowers concentration of the particle/particle interfaces that might also prove to be beneficial for Li-ion transport within the ceramic filler and also the CE. Additionally, the inherent porous morphology of the NSP synthesized powders can provide continuous 3-dimensional garnet backbone that can be infiltrated by a Li-ion conducting polymer, resulting in a thin film based composite electrolyte. The pores within such a network can be accessed

at micrometers scale as compared to larger length scales, therefore a thin film approach can prove to be beneficial. Both, garnet dispersion within polymer matrix and thin film approach for the preparation of CE and their impact on Li-ion conductivity were investigated in this work.

Within the works of this cumulative thesis, three different garnet compositions were used as ceramic fillers in CEs with PEO acting as the polymer matrix. These consisted of tetragonal garnet (Tet-LLZO) and two cubic garnet compositions i.e. Al-doped LLZO (Al-LLZO) and Ga-doped LLZO (Ga-LLZO). Cubic garnets are of interest due to their two orders of magnitude higher Li-ion conductivity compared to that of tetragonal garnets [10]. Using these compositions within the composite electrolytes could therefore help in determining the role of intrinsic conductivity of the ceramic filler towards total ionic conductivity observed within the composite electrolytes.

Initially, CE membranes were prepared by mixing Al-LLZO and PEO in different weight ratios, from “polymer-rich composite electrolytes” to “ceramic-rich composites electrolytes” to study the influence of Al-LLZO:PEO weight ratio on Li-ion conductivity. These membranes were characterized via XRD, which indicated the phase purity of the pure components as well as the CE membranes. As will be discussed in detail in section 3.1, X-ray diffractogram of the polymer-rich composites indicated a broad feature between 15° and 25° 2θ range, which is due to the presence amorphous PEO in polymer-rich CEs [99]. In comparison, X-ray diffraction pattern of PEO+LiTSFI polyelectrolyte shows clear reflections belonging crystalline to PEO within the same angular range. To confirm that addition of Al-LLZO to the PEO reduces PEO crystallinity and leads to PEO amorphization, DSC measurements were carried out in collaboration with Dr. Klaus Dirnberger and Prof. Sabine Ludwigs. These measurements confirmed lowering of PEO crystallinity upon AL-LLZO addition and also accompanied by the lowering of PEO melting point in comparison to pristine PEO, which is in agreement with the literature [99]. The successful preparation of CE is indicated by the uniform distribution of ceramic filler within PEO. This was verified by the SEM micrographs which show even dispersion of Al-LLZO ceramic filler within the polymer-rich composite electrolytes (see Figure 3.10). For the ceramic-rich composites lower porosity of the membranes was observed upon addition of PEO compared to the of PEO free isostatically pressed Al-LLZO pellet.

Different blends of Al-LLZO containing CEs were characterized for their ionic conductivity via impedance spectroscopy. In general, a trend was observed where the conductivity is found to decrease with an increase in Al-LLZO filler weight ratio. The results indicated maximum conductivity for the Al-LLZO free polyelectrolyte, which is in contrast to earlier reports that suggest enhanced Li-ion conductivity upon addition of ceramic filler [22, 64]. However, the absence of such an occurrence here can be explained by the lower surface area of the filler particles used (usually nanoparticle or nanowires with sizes below 100 nm are used which enhance Lewis acid-base type interactions) and the possibly that higher weight ratios were used (enhanced Li-ion conductivity has been reported for CEs with 5 wt% of the ceramic filler [76]). The lewis acid-base interactions occur between the polymer chain segments and the filler surface groups. In these interactions the Lewis acidity of the ceramic filler competes with the Lewis acid character of the lithium salt which is important to form complex with the ether oxygen centers within PEO that acts as the Lewis base.

For filler free PEO+LiTSFI membrane, ionic conductivity of 3.2 x 10^{-6} S cm^{-1} at 298 K was observed, which is higher than the conductivity value observed for the CE containing 10 wt% of Al-LLZO filler for which the ionic conductivity of ~2 x 10^{-6} S cm^{-1} at 298 K was observed. As the Al-LLZO filler wt% increases, the conductivity was found to decrease further. The lowest

ionic conductivity was observed for PEO free isostatically pressed Al-LLZO pellet. For Al-doped LLZO pellets synthesized via FAST, ionic conductivity of 3.4 x 10^{-4} S cm^{-1} at 298 K has been reported previously [35]. This reported value is two orders of magnitude higher than the NSP synthesized AL-LLZO pellet, which demonstrated conductivity of 4.4 x 10^{-6} S cm^{-1} at 298 K [34]. The higher conductivity of FAST synthesized Al-doped LLZO is due to higher relative density of the synthesized Al-LLZO pellets. For FAST synthesized pellets, relative density of 93% has been reported whereas for the NSP synthesized pellets relative density of 47% to 55%, which is mainly due to low sintering times and temperatures used for NSP resulting in highly porous pellets. Nevertheless, a simple isostatic pressing of garnet powders would lower the pellet density further along with high concentration of loosely held particle/particle interfaces that may be highly impeding towards the Li-ion transport and thus resulting in significantly low ionic conductivity of an order of 10^{-10} S cm^{-1}. Interestingly, it was observed that the ionic conductivity of CE containing 10 wt% of PEO was found to be increase significantly by ~3 orders of magnitude. Nonetheless, the observed conductivity is still far lower than a well sintered LLZO pellet like the one obtained from FAST procedure.

Although, the lower conductivity within the polymer-rich can be explained on the bases of particle size and agglomeration, the question of lower conductivity in garnet-rich CE is of interest since the intrinsic conductivity of the garnet Al-LLZO is known to be significantly higher than the PEO-based polyelectrolytes [10]. The answer to this question is also importance since within CEs different Li-ion transport pathways are known to be available depending on the filler to polymer weight ratio [100]. In polymer-rich composite electrolytes, it is known that Li-ion transport mainly takes place via the polymer and along the filler/polymer interface, which is known to be favourable towards enhancing Li-ion conductivity within such polymer-rich CEs [75, 76, 100]. For higher weight percentages of filler, i.e. above the percolation limit, Li-ion transport pathways through the Al-LLZO filler become accessible [100], which should in principle result in increased conductivity since the intrinsic conductivity of garnets is high. However, such a behavior is not observed, which raises an important question, why does one see a down trend in conductivity upon increasing the Al-LLZO weight ratio?

To address this question, different blends of CEs were prepared with variety of different Li-ion conducting (Al-LLZO, Ga-LLZO and Tet-LLZO) and non Li-ion conducting (SiO_2 and Y doped $BaZrO_{3-\delta}$) ceramic fillers with different filler to PEO weight ratios. This study was undertaken to specifically address the role of intrinsic Li-ion conductivity and particle size of the ceramic filler on the overall conductivity of the CE. For PEO-rich electrolytes containing 10 wt% of ceramic fillers, it was observed that resulting conductivity does not rely on nature of the filler but the particle size. The composite electrolyte membrane containing SiO_2 nanoparticles that is an inert filler demonstrated maximum conductivity of ~1.2 x 10^{-5} S cm^{-1} at 298 K which is higher than the filler free PEO polyelectrolyte showing the conductivity of ~3 x 10^{-6} S cm^{-1} at 298 K. The observed conductivity is comparable to that of tantalum doped LLZO containing LLZO [23]. As reported by Zhang et al., the resulting ionic conductivity of the CE is highly dependent not only on the weight percentages but also particle size. For example, the ionic conductivity of the CE containing tantalum doped LLZO with the particle size of 10 µm, 400 nm and 40 nm was found to be 3.8 x 10^{-6} S cm^{-1}, 1.3 x 10^{-5} S cm^{-1} and 2.1 x 10^{-4} S cm^{-1}, respectively. Thus indicating the role of particle size on ionic conductivity within CEs. The fact the ionic conductivity of the CE containing SiO_2 is similar to tantalum doped LLZO containing CE with particle size of 400 nm confirms that for polymer-rich CEs the surface area of the filler is of importance rather than its composition. In contrast, Y doped $BaZrO_{3-\delta}$ inert filler containing composite electrolyte demonstrated conductivity of ~1 x 10^{-6} S cm^{-1} at 298 K, which is an order

of magnitude lower than the SiO_2 containing composite electrolyte. Here, the size of Y doped $BaZrO_{3-\delta}$ particles is in the range of 20 µm, which further confirms the significant of particle size of the filler in polymer-rich CEs, Similarly, all the garnet containing CEs demonstrated similar conductivities of ~2 x 10^{-6} S cm^{-1} at 298 K, which is higher than the Y doped $BaZrO_{3-\delta}$ containing CE but significantly lower than SiO_2 containing CE. The particle size of the garnets used is approximately around 1 µm. From a deeper understanding of the impedance data, it was clear that Li-ion transport takes place via the bulk polymer and along the filler/PEO interface, which was evident from the Nyquist and the Bode plots (see Figure 3.16 in section 3.1.3.4). As already mentioned, filler/PEO interface is known to enhance Li-ion transport within polymer-rich composite electrolytes [76]. Since, SiO_2 particles have lowest particle size, this implies a higher particle surface area and hence the highest filler/PEO interface among the blends studied here, which resulted in the maximum conductivity in this composite electrolyte.

For ceramic-rich composite electrolytes i.e. 70 wt% ceramic filler loading fraction, the resulting conductivity again seems to be independent of the type of filler being used. This is an important observation because additional Li-ion transport pathway through the filler is known to form above the percolation limit, i.e. ceramic loading fraction of 40 wt% [100]. This would mean that CEs containing Li-ion active or conducting fillers can in principle offer higher Li-ion conductivity compared to that of inert filler containing CEs. However, this trend was not observed here. Instead Tet-LLZO filler containing CE demonstrated the maximum Li-ion conductivity of ~5 x 10^{-7} S cm^{-1} at 298 K among the series of blends studied and lowest being the composite electrolyte containing Y doped $BaZrO_{3-\delta}$ ceramic filler with the conductivity value of ~2 x 10^{-7} S cm^{-1} at 298 K. Both cubic garnet containing CEs showed similar conductivities to that of Y doped $BaZrO_{3-\delta}$ containing CE. Therefore, implying for this particular weight ratio of filler to PEO, the intrinsic conductivity of the filler does not seem play an important role.

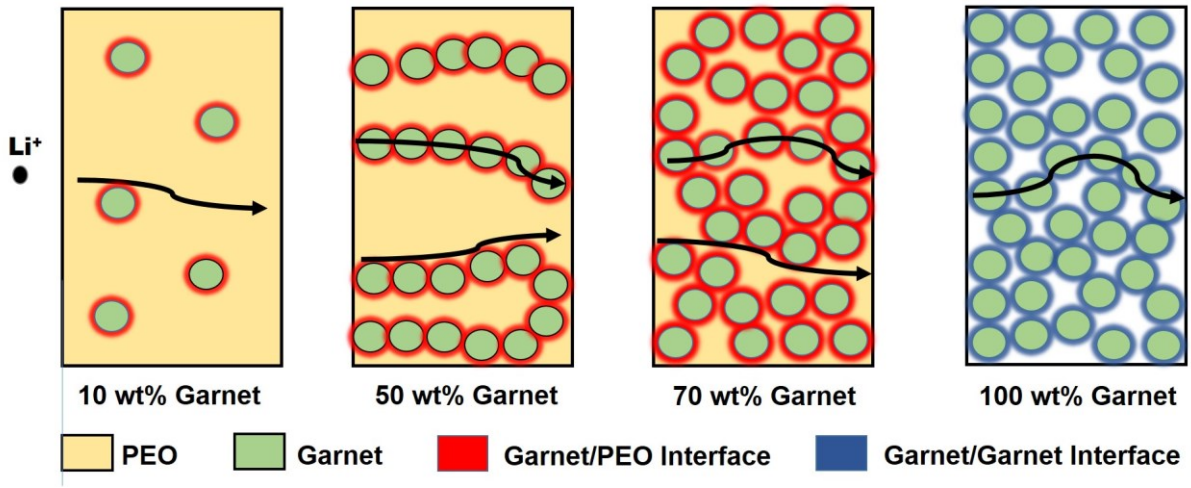

Figure 3.3: Schematics indicating the lithium ion transport via the CEs.

In comparison to PEO free isostatically pressed AL-LLZO pellets, the conductivity of all the composite electrolytes containing 10wt% of PEO is considerably higher. Within such ceramic-rich composite electrolytes, its becomes clear that intrinsic conductivity of the filler plays a significant role. The conductivities of all the garnet containing CEs were considerably higher than both SiO_2 and Y doped $BaZrO_{3-\delta}$ containing CEs with Ga-LLZO containing CE demonstrating conductivity of ~1.6 x 10^{-7} S cm^{-1} at 298 K, which is nearly three orders of magnitude higher than the isostatically pressed Al-LLZO pellet, which demonstrates the conductivity of the order of 10^{-10} S cm^{-1}. For the pressed Al-LLZO pellets, the particles are in mere mechanical contact with each other with only small inter particle contact area which

causes high resistance. A small amount of PEO addition, i.e. 10 wt%, acts as the particle binder and lowers the porosity of the pellet, i.e. fills in the voids between the particles leading to better particle/particle interfacial contact which lowers the resistances in comparison to PEO free Al-LLZO pellet and therefore results is higher conductivity. Since, within these CEs the transport mainly takes place via the filler, composite electrolytes containing Li-ion active fillers perform better than the inert filler containing composite electrolytes. Figure 3.3 shows the schematics of Li-ion transport pathways within composite electrolytes as a function of garnet to PEO weight ratio.

Therefore, it becomes clear that within composite electrolytes both the particle size and intrinsic Li-ion conductivity of the fillers play a role depending upon the filler to PEO weight ratio. In PEO-rich composite electrolytes, filler type is of less importance however, the particle size of the filler is of significance. Above the percolation limit, additional Li-ion transport pathways along the filler/PEO interface become accessible, however this does not necessarily result in improved Li-ion conductivity. Intrinsic Li-ion conductivity of the filler, i.e. via the bulk, was found to contribute only in ceramic-rich systems i.e. CE with 90 wt% cubic Ga-LLZO. A question of relevance here is, why the transport of ionic charge carriers through the garnet/PEO interface is not favourable, which can activate the Li-ion transport via the garnet bulk and result is improved Li-ion conductivity.

This question is of significant importance within the CEs and has not been addressed yet. This was also one of the objectives of this project. Therefore, an attempt was made to study the garnet/PEO interface via the combination of XPS and impedance spectroscopy. Here, it is important to mention that garnet thin film synthesis and XPS studies were carried out by Manuel Donzelli (materialdesign durch synthese division) and Thimo Ferber (surface science division), respectively and is not part of research carried out by the author of this thesis but objective of the project. To understand the role of garnet/PEO interface, a study was designed wherein model surface-coated garnets films were studied via the XPS and to complement these studies a multi-layer hetereostructure of PEO/LLZTO/PEO was studied via impedance spectroscopy. Via XPS, it was observed that within 1 min deposition of PEG and LiTSFI on LLZTO thin film, along with the emission lines belonging to PEG and LiTSFI, additional emission lines belonging to LiF were observed. Further, peaks belonging to $LiSO_2CF_3$, Li_2SO_3 and $Li_xNSO_2CF_3$ were also observed which are the reaction side products due to the deposited LiTSFI at the garnet interface. For extended PEG and LiTSFI deposition times, mainly the emission lines belonging to these components are observed and none from the LLZTO film. This suggests a full surface coverage. Other signals from LiF, $LiSO_2CF_3$ and polysulfide Li_xS_y. were also observed, which suggests an interfacial instability at garnet/PEO+LiTSFI interface.

The resulting side products at the garnet/PEO interface can also impact the Li-ion transport through this interface. This is in particular a case within CEs where the Li-ions can not only travel along the garnet/PEO interface i.e. in parallel direction but also though this interface i.e. in perpendicular direction from one system to another. Although, the parallel transport is known to be beneficial towards Li-ion transport, there isn't much information about how the Li-ion transport behaves perpendicular to this interface. As suggested from the XPS analysis, there are side reactions occurring at the garnet/PEO interface. To study the Li-ion dynamics through this interface, a novel method was used where in the multilayer PEO/garnet/PEO hetereostructure was studied. Initially, impedance measurements were carried out on the well sintered garnet pellet. LLZTO pellets were used to have easy comparison to the XPS study. The sintered pellet was used to obtain the maximum possible conductivity from the garnet pellet and limit grain boundary contributions. The conductivity of this pellet was found to be 3.6

x 10^{-4} S cm^{-1} at 298 K. The activation energy of 0.32(1) was calculated. This was followed by applying a layer of PEO on one side of this pellet and measuring the impedance spectra in the temperature range of 298 K to 328 K. As already mentioned, the conductivity of the cryo-milled PEO was found to in the order of 10^{-6} S cm^{-1}, which implies that garnet in comparison would have much lower contribution to overall resistance and it could be possible to observe the interfacial resistances. Upon inspection of the Nyquist and Bode plots for this system, two clear semicircles and a tail were observed. This implies two different Li-ion transport processes. The fitting of this spectra was carried out and it became evident that the conductivity of this systems is significantly lower than both the individual components, which highlights the resistive nature of the interface. The conductivity was found to be 3 orders of magnitude lower than the pure garnet and an order of magnitude lower than PEO polyelectrolyte. From the fitting, capacitance values of 10^{-11} F and 10^{-9} F were calculated for the high frequency and intermediate frequency semicircles, respectively. The capacitance value of 10^{-11} F fits well to the grain contributions originating from the bulk of the PEO and garnet. However, the capacitance value of 10^{-9} F is usually attributed to the grain boundary [101]. However, this capacitance can have origin from the garnet/PEO interface. The garnet/PEO interface can be thought of as a pseudocapacitor where the Li-ions can diffuse though the interface, which does not build a stern layer and therefore resulting in lower capacitance. Further, validation of the resistive nature of garnet/PEO interface was obtained by applying another layer of PEO on the opposite face to make a sandwiched structure of PEO/garnet/PEO and impedance measurements were carried out. The conductivity of this structure was found to decrease further compared to that of single-layered structure. The results discussed so far were the basis of the article published in *ACS Materials and Interfaces* and given in section 3.1.

An important prerequisite of the composite solid electrolyte is high Li-ion conductivity at room temperature. This clearly was not observed within this study so far and prompted a change in fabrication strategy for preparing CEs. The conventional solvent or the cryo-miiling approach used for the preparation of the CE membranes involves dispersion of garnet particles of different sizes in a polymer matrix. However, irrespective of the preparation route, this would mean that within the CEs garnet particles are loosely held together, which in principle can lead to resistances at the particle/particle interface and as discussed above through the garnet/PEO interface. An alternative membrane preparation strategy was therefore needed.

Recently, Bae et al. reported on porous 3-dimensional nanostructured LLTO network derived from hydrogel. It was observed that the CE containing pre-percolated porous 3-dimensional LLTO structure resulted in the ionic conductivity of 8.8 x 10^{-5} S cm^{-1} at room temperature. In their study, 3-dimensional LLTO framework was obtained by adding LLTO precursor with polyvinyl alcohol (PVA), which was gelated by a cross-linker glutaraldehyde (GA) and HCL was used as the reaction initiator. The obtained hydrogel was heated at 1073 K for 2 hours to form a 3-dimensional LLTO network followed by PEO infiltration. Although the conductivity of this ceramic-rich CE prepared via hydrogel method is higher than the PEO-rich CE containing dispersed SiO_2 nanoparticles reported in this study, the conductivity is still low for the application of such CE in ASSLIBs. It is well known that the grain boundary conductivity of LLTO is several orders of magnitude lower than the grain conductivity (of the order of 10^{-3} S cm^{-1}) resulting in lowering of overall conductivity [78]. In this respect, garnet are interesting since their overall conductivity is higher than LLTO [10]. Additionally, the inherent porous morphology of the garnet powders obtained via NSP can be beneficial here, since it forms a porous 3-dimentional framework without a need for additional polymer or acid like in the case of hydrogel based synthesis of LLTO. From Figure 3.2, it is clear that the heat treatment of the as-

synthesized NSP powders results in necking between the particles, which creates interconnection between the particles and forms a porous continuous 3-dimensional garnet network. Previously, NSP synthesized Al-LLZO pellet heated treated at 1273 K for 60 min was shown to demonstrate conductivity in the order of 10^{-6} S cm^{-1} [34]. The low conductivity of these pellets compared to that of solid state synthesized pellets was due to low pellet density (47-56%). Although, such low densities resulting from high porosity ((Figure 3.2b)) of the pellets is undesired within the solid ceramic electrolytes but this can be beneficial in CEs. The porous garnet network would in principle provide a backbone and a continuous porous 3-dimensional Li-ion pathway, which can be infiltrated with a Li-ion conducting polymer such as PEO. This could result in filling of the pores within the garnet pellet along with a continuous garnet/PEO interface, both of which can have a positive impact on Li-ion conductivity.

Initially, attempts were made to infiltrate a heat treated NSP synthesized garnet pellet with thickness of >1mm. However, only fraction of the pores were accessible due to large thickness of the pellet. An alternative to garnet pellets can be a porous garnet thin film that can make the whole thickness of the film accessible to infiltration. Therefore, porous garnet thin films were prepared using the as-synthesized garnet powders and spin coating. As-synthesized NSP powders were used instead of heated treated powders not only to preserve the particle morphology but also to limit the Li loss due to successive high temperature heating steps, which can promote Li loss and formation of $La_2Zr_2O_7$. For the film preparation Cu substrates were used. Cu was the substrate of choice since it can form one side of electronic contact during a through plane impedance measurement. Garnets films were heat treated at 1073 K for different durations to optimize the phase purity, porosity and conductivity of the films. Once the synthesis conditions were optimized, impedance measurements were carried out. Interestingly, the conductivity of the optimized garnet film was found to be significantly lower (10^{-13} S cm^{-1}). This lower conductivity compared to that of garnets pellets synthesized via the same route can have variety of different reasons: i) low sintering temperatures, ii) reduced sintering times and iii) high porosity and density. Nevertheless, this system provides 3-dimensional continuous pathway and backbone for PEO infiltration (see Figure 3.4).

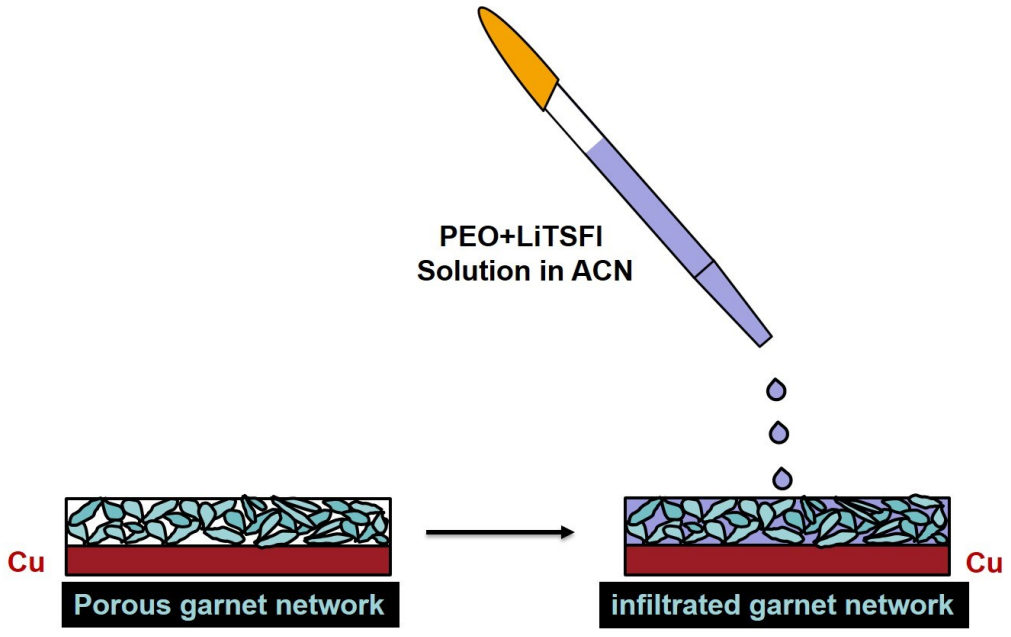

Figure 3.4: Schematics showing the porous continuous 3-dimenionsal garnet network deposited on a Cu substrate, which can be infiltrated with a Li-ion conducting polymer to fill in the empty pores and in the process result in a thin film composite electrolyte.

After optimizing the sintering times to obtain maximum possible conductivity, the garnet films were infiltrated with the PEO+LiTSFI containing acetonitrile solution by drop wise pouring of the solution onto the garnet films via a micropipette. Here, it is important to mention that the solvent to PEO ratio needs to be tuned so that the solution is not too viscous, which would result in the PEO deposition on the top on the film instead of infiltrating it. The infiltration step was carried out in an Ar-filled glove box and repeated several times (20-30 times). The films were then heat treated at 323 K under vacuum to remove any residual solvent within PEO. This was followed by the impedance measurements.

The impedance spectra of the infiltrated films indicated two semicircles in Nyquist and Bode plots followed by a low frequency tail, which indicated blocking electrode response at low frequencies. Using an equivalent circuit of two R-CPE elements (for the two semicircles) and a CPE element (to model low frequency capacitive response) in series, the total conductivity of the infiltrated films was calculated to be 5.3 x 10^{-7} S cm^{-1} at 298 K. From the fitting, the capacitance value of 10^{-11} F and 10^{-7} F were determined, which correspond well to the grain and interfacial transport. From the Arrhenius plot the activation energies of be 0.40(1), 0.09(1) and 0.14(1) eV for grain (bulk grain conduction via garnet), interface (garnet/PEO interface) and overall activation energy were determined. The low activation energy for the interface might have its origin from the synergistic effect of 3D interconnected garnet backbone providing a continuous interface between PEO/garnet network.

The infiltrated film here represents a ceramic-rich composite with garnet to PEO ratio of 85:15, assuming a ceramic density of 47% for the NSP synthesized garnet pellet with similar heat treatment conditions. The conductivity of this film, although low was still found to be an order of magnitude higher as compared to the composite electrolyte prepared via the cryo-milling approach (5.3 x 10^{-7} S cm^{-1} vs. 8 x 10^{-8} S cm^{-1}).

Although the continuous 3-dimensional porous garnet network would be beneficial towards Li-ion conductivity compared to that of dispersed garnet particles within the polymer matrix, the low Li-ion conductivity of the backbone used here is the main concern. This mainly originates from the narrow necks between the garnet particles which limits the inter particle Li-ion transport (Figure 3.5). Nevertheless, as observed from the impedance results, the transport of Li-ions parallel to garnet/PEO interface in favourable towards overall Li-ion transport whereas the transport through this interface is unfavorable due to the formation of decomposition products at the garnet/PEO interface as previously mentioned and discussed in detail in section 3.1.3.5 of this cumulative thesis. These results were recently published in MDPI Ceramics and are given in section 3.2.

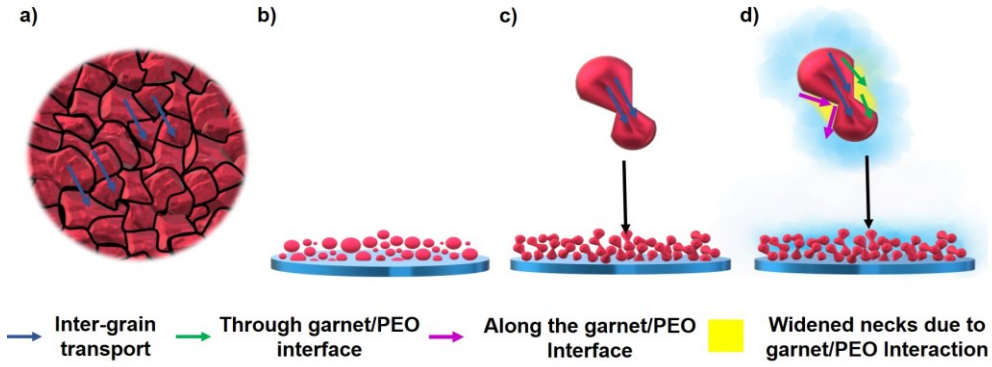

Figure 3.5: Schematic illustrating a) Li-ion transport in dense sintered ceramic with large grain size, b) spin coated NSP powder on the Cu substrate, c) necking between the particles in the annealed NSP synthesized garnet powders and d) Li-ion transport pathways with in the infiltrated films.

3.1 Compositional Dependence of Li-Ion Conductivity in Garnet-Rich Composite Electrolytes for All-Solid-State Lithium-Ion Batteries – Towards Understanding the Drawbacks of Ceramic Rich Composites

Aamir Iqbal Waidha, [a,b] Thimo Ferber, [c] Manuel Donzelli, [a,b] Niloofar Hosseinpourkahvaz, [b] Vanita Vanita, [a,b] Klaus Dirnberger,[d] Sabine Ludwigs,[d] Rene Hausbrand, [c] Wolfram Jaegermann, [c] Oliver Clemens, [a,b*]

[a] Materials Synthesis Group, Institute of Material Science, University of Stuttgart, Heisenbergstraße 3, 70569 Stuttgart, Germany

[b] Technische Universität Darmstadt, Institut für Materialwissenschaft, Fachgebiet Materialdesign durch Synthese, Alarich-Weiss-Straße 2, 64287 Darmstadt, Germany.

[c] Surface Science Division, Department of Materials Science, TU Darmstadt, Otto-Berndt-Straße 3, 64287, Darmstadt, Germany

[d] IPOC-Functional Polymers, Institute of Polymer Chemistry, University of Stuttgart, Pfaffenwaldring 55, 70569 Stuttgart, Germany

* Corresponding Author: oliver.clemens@imw.uni-stuttgart.de

Abstract

Composite electrolytes comprising a polymer plus Li salt matrix and embedded fillers have the potential of realizing high lithium-ion conductivity, good mechanical properties, wide electrochemical operational window, and stability against metallic lithium, all of which are essential for the development of high-energy-density all solid-state lithium-ion batteries. In this study, a solvent-free approach has been used to prepare composite electrolytes with tetragonal and cubic phase garnets synthesized via nebulized spray pyrolysis with polyethylene oxide (PEO) being the polymer component. Electrochemical impedance spectroscopy (EIS) is used to examine a series of composites with different garnets and weight fractions. The results show that with the increase in the ceramic weight fraction in the composites, ionic conductivity is reduced and alternative Li-ion transport pathways become accessible for composites as compared to the filler-free electrolytes. An attempt is made to understand the ion transport mechanism within the composites. The role of the chemical and morphological properties of the ceramic filler in polymer-rich and ceramic-rich composite electrolytes is explained by studying the blends of non-conducting ceramics with the Li-conducting polymer, indicating that the intrinsic conductivity of the ceramic filler significantly contributes to the overall conductive process in the ceramic-rich systems. Further, the stability of the garnet/PEO interface is studied via X-ray photoelectron spectroscopy, and its impact on the lithium-ion transport is studied using EIS.

Keywords: all-solid-state Li-ion batteries, composite electrolytes, impedance spectroscopy, interface, X-ray photoelectron spectroscopy

3.1.1 Introduction

All solid state batteries (ASSBs) are promising alternatives to conventional lithium-ion batteries with liquid electrolytes, which can overcome significant safety issues due to flammability, leakage and dendrite growth on overcharging [8]. In addition to limiting such safety concerns, ASSBs could potentially increase the energy density of the battery by enabling the use of metallic Li as the negative electrode, which has an order of magnitude higher theoretical specific capacity than the traditional carbon based anodes (3860 mA h g^{-1} vs 372 mA h g^{-1}) [8] . For conventional batteries, the use of metallic lithium as an anode has so far been neglected due to the inherent instabilities of the liquid electrolytes with the lithium metal and dendritic growth during cell cycling [102]. Solid electrolytes in ASSBs could enable the use of metallic lithium as the anode due to their high mechanical strength and safety. However, the high reactivity of the Li metal with the solid electrolyte at the interface along with the large volume changes during cycling are still the key concerns to be addressed [41]. Further, the interfacial resistance between the solid electrolyte and Li metal is responsible for the low charge transfer kinetics and cell short circuit as a result of non-uniform Li^+ ion current distribution leading to the lithium dendrite formation [103].

Solid electrolytes based on ceramics or polymers have gathered wide spread interest for their application in ASSBs [8, 41]. Among ceramic solid electrolytes, oxide-based garnets have been studied widely due to their intrinsically high room temperature Li-ion conductivity and stability against metallic Li [41]. Further, garnets have been reported to have a large electrochemical window of operation, potentially enabling the use of high voltage cathodes like $LiNiPO_4$ [41, 42], which can further increase the energy density of the whole battery.

Nevertheless, also garnet based electrolytes show certain disadvantages. They are sensitive to moisture and suffer from poor interfacial contact with Li metal due to high brittleness [41]. This poor contact has been shown to increase the interfacial resistance at the Li/LLZO interface leading to non-uniform Li current distribution, which can be considered as the origin of the lithium dendrite formation at high current densities [104].

On the other hand, polymer based solid electrolytes offer flexibility and soft interfacial contact with Li metal [25]. Among polymers, polyethylene oxide (PEO) has been extensively studied due to its high flexibility and commercial availability. However, the Li-ion conductivity of PEO and the ionic transference number of Li^+ therein is low [24]. Also, polymer electrolytes in general have low mechanical strength, making them susceptible to lithium dendrite growth, and a small width of the electrochemical stability window, which is a limiting factor for the use of high voltage cathodes [24].

An alternative approach to ceramic and polymer electrolytes that has attracted much interest is their combination within composite electrolytes (CEs). Such CEs containing polymer matrix and ceramic filler particles have been widely studied. It has been shown that CEs have a high Li-ion conductivity, a wider electrochemical stability window compared to the pure polymers [23, 97] and a superior flexibility than the ceramic electrolytes [25]. Further, it has been shown that the conductivity is highly dependent on the weight fractions and surface area of the fillers being used [23] . Recently, Goodenough et al. showed that a conductivity of 1.17×10^{-4} S cm^{-1} at 303 K can be reached when 10 wt-% of LLZO particles are dispersed in a PEO matrix [68]. The group of Hong Li reported that an increase in conductivity depends on the particle size of the ceramic filler [23]. Chen et al. reported that higher conductivities can be achieved with lower weight fractions of the ceramic filler if nanowires are used [76]. Further, they also demonstrated that both the intrinsic ionic conductivity and the morphology of the fillers have an effect on the overall

conductivity, and that rod-shaped morphologies of ion-conducting fillers can be preferable. However, all these studies are based on the model of “ceramic in polymer”, i.e. polymer-rich composite where the Li ion transport takes place mainly via the polymer [75]. From a fundamental viewpoint, the opposite would also be of strong interest. In order to maintain an electrolyte system with properties close to a ceramic electrolyte, the use of a polymer acting as a grain boundary transfer promoter within a ceramic matrix could be considered. Recently, the group of Randall has fabricated highly conductive ceramic rich composite electrolytes using dimethylformamide as transient liquid and grain boundary transport promoter via cold sintering [105]. However, so far there are only limited reports [68, 73, 100, 106] which target the understanding of the transport properties within such ceramic rich systems, which could help in designing of ceramic rich composite electrolytes with improved ionic conductivity.

The study reported in this article is comprised of two parts, the first one focusing on the composite solid electrolyte membranes and the second one on elucidation of the garnet/PEO interfaces in thin films. In the first part reported in section 3.1.3.1, we present an alternative solvent free approach for fabricating composite solid electrolytes containing different garnet and reference materials such as nanocrystalline SiO_2 and coarse grained Yttrium-doped $BaZrO_3$ (Y-$BaZrO_3$) particles as the ceramic fillers, PEO as the polymer and lithium bis(trifluoromethanesulfonyl)imide (LiTFSI) as the Li salt. The solvent free membrane preparation has been chosen since garnets are known to undergo Li^+/H^+ exchange, which can effect its intrinsic Li-ion conductivity [107]. The ceramic garnet particles are synthesized via nebulized spray pyrolysis (NSP), which has been reported to provide particles with high surface area compared to solid state synthesis routes due to significant lowering of annealing temperatures and times [34, 80, 82], with particle sizes in the range of ~ 1 µm and below. Although, nanoparticles have been the choice of the filler and are known to increase the conductivity in of the polymer rich composites, the garnet particles chosen in this study aim to be a compromise for providing sufficient surface area for ceramic-polymer interactions, while maintaining longer conductive pathways within the ceramic particles (which have a higher grain conductivity than the polymer) due to their larger sizes. Rietveld analysis of X-ray powder diffraction (XRD) data is carried out for phase analysis. Fourier transform infrared spectroscopy (FT-IR) and Raman spectroscopy are used to determine the non-invasive nature of the cryomilling process on the PEO and composite electrolytes. Differential scanning calorimetry (DSC) is used to study the effect of filler to PEO weight fractions on the PEO crystallinity and melting temperature. Scanning electron microscopy (SEM) further helps to develop a microstructural understanding of the particle dispersion in the polymer. The conductivity of the composite electrolytes is measured using electrochemical impedance spectroscopy (EIS), which shows that both type of filler material and weight ratios influence the lithium ion conductivity of composite electrolytes, especially in ceramic rich systems. The results in the first part are complemented by the second part reported in section 3.1.3.5, where we study the garnet/PEO interface on model films using X-ray photoelectron spectroscopy (XPS) and establish a correlation with impedance studies of well sintered-garnets which are coated with layers of PEO. We highlight that the garnet additive only contributes well to the overall conduction pathway in ceramic-rich systems due to the high transfer resistance encountered for conduction through the garnet-polymer interface. In contrast, the type of filler plays a minor role for the preparation of polymer-rich composites within such solvent-free preparation approaches, where the filler changes the conductivity of the ion-conducting polymer mainly by reducing its degree of crystallinity.

3.1.2 Experimental section

3.1.2.1 Studies on composite membranes

3.1.2.1.1 Material synthesis

Nano- to microcrystalline powders with compositions (nominal compositions from the La to Al/Ga ratio neglecting the small amounts of impurity phase) of $Li_{6.49}Al_{0.17}La_3Zr_2O_{12}$ (Al-LLZO), $Li_{6.34}Ga_{0.22}La_3Zr_2O_{12}$ (Ga-LLZO) and $Li_7La_3Zr_2O_{12}$ (Tet-LLZO) were synthesized using nebulized spray pyrolysis (NSP). The water-based precursor solution (total cation concentration 0.1 mol l^{-1}) was prepared in three steps: (i) the Zr precursor ($Zr(C_5H_7O_2)_4$, ABCR, 98%) was dissolved in a small volume of methanol; (ii) the nitrate based precursors of Li, La, Ga and Al ($LiNO_3$, Sigma Aldrich, 99.99%, $La(NO_3)_3{\cdot}6H_2O$, Alfa Aesar, 99.9%, $Ga(NO_3)_3{\cdot}xH_2O$, Alfa Aesar, 99.9% and $Al(NO_3)_3{\cdot}9H_2O$, Merck, 98.5%) were added to the methanolic solution and (iii) deionized water was added to the precursor solution to maintain the desired concentration of 0.1 mol l^{-1}. A water to methanol volume ratio of 20:1 was used. The as prepared mixture was then stirred for 1 h to produce a homogeneous transparent solution. The Li-precursor was used in molar excess (30 %) in order to compensate for Li losses occurring during the subsequent sintering process of the powders. The as-prepared precursor solution was nebulized inside a glass chamber using an ultrasonic generator (Dr. Hielscher UM20-1.6 MHz). The mist of the precursor solution was transported into the hot-wall reactor by flowing oxygen (3 slm O_2 flow rate controlled by a MKS mass flow controller, MFC). A syringe pump (TSI) was used for continuous precursor delivery at a rate of 100 ml h^{-1} to maintain a constant level of precursor solution inside the nebulizer. The process pressure was held constant at 900 mbar using a Baratron absolute pressure gauge and a butterfly valve connected to a backing pump. Powders were synthesized at a temperature of 1173 K and collected by using a filter-based collector. In order to prevent water vapor condensation on the filter, the collector was heated to 393 K. As-synthesized powders were subsequently annealed at 1173 K for 3 hours in ambient air. A constant heating rate of 6 K min^{-1} and a cooling rate of 6 K min^{-1} were used. The garnet powders were removed from the furnace at 873 K and swiftly transferred to an Ar filled glove box with the oxygen and water level maintained below 0.1 ppm to prevent reaction with H_2O/CO_2. Due to the large amount of powder used and the material shrinking on heating, the powder surface which is exposed to the environment directly during transfer is low, which can be considered helpful to avoid degradation.

3.1.2.1.2 Polymer electrolyte preparation

The composite membranes were prepared by first mixing PEO (Alfa Aesar, MW 100.000 g mol^{-1}) and LiTFSI in a cryomill (Retsch CryoMill) with the PEO and LiTFSI salt in the weight ratio of 11:1. The cryomilling consisted of two cycles of precooling to 78 K for 5 minutes at a vibration frequency of 5 Hz followed by milling for 10 minutes at a frequency of 25 Hz. Filling, sealing, and reopening of the milling vials were carried out in an Ar filled glove box.

3.1.2.1.3 Composite electrolyte membrane preparation

For the preparation of CEs, the PEO+LiTFSI mixture was mixed in different weight percentages with the ceramic filler. The mixtures were filled in a vial within the glovebox and subjected to another cycle of cryomilling step at 25 Hz for 10 minutes. Filling, sealing, and reopening of the milling vials were carried out in an Ar filled glove box. The composite membranes were prepared by first uniaxially pressing the composite powders followed by subsequent isostatic pressing at 700 kN and then sputtered with a thin layer of gold on both sides for electronic contacting. Each membrane was then heated to 328 K for 12 hours in a vacuum furnace inside the glovebox.

3.1.2.1.4 Diffraction experiments

Room temperature XRD patterns of the various samples were recorded on a Bruker D8 diffractometer using Bragg-Brentano geometry with a fine focusing X-ray tube with Cu $K_{\alpha 1,2}$ radiation. A VANTEC detector (3° opening) and a fixed divergence slit (0.3°) were used. The total scan time was set to 1 hour for the angular range between 10° and 80° 2θ at a step size of 0.0066°. Structural refinements and phase analysis were performed on the XRD patterns by the Rietveld method with the program TOPAS 5 (Bruker AXS, Germany) [95]. The instrumental intensity distribution was determined empirically within a fundamental parameter approach [108] using a reference scan of LaB_6 (NIST 660a), and the microstructural parameters were refined to adjust the peak shapes for the XRD data. An overall isotropic parameter was refined, which was constrained to be identical to all atoms of all phases to account for absorption corrections and minimize quantification errors for multiphase mixtures.

3.1.2.1.5 Electrochemical impedance spectroscopy

Alternating current (AC) electrochemical impedance spectroscopy was carried out to characterize the conductivity of the pure components and the composite electrolytes. A membrane of each sample was placed inside a JANIS STVP-200-XG cryostat, which was operated under a static helium atmosphere of 1 bar pressure. All samples were investigated in the temperature range of 298 K to 328 K. Impedance measurements were recorded using a Solartron 1260 frequency response analyzer, applying an AC signal of 100 mV amplitude with the frequency ranging from 1 MHz to 100 mHz. Fitting of the data was performed using the Z-view program [109].

3.1.2.1.6 Scanning electron microscopy

The scanning electron microscopy (SEM) images were taken using the secondary electron detector of a Philips XL30 FEG scanning electron microscope operating at 30 keV.

3.1.2.1.7 Fourier transform infrared spectroscopy

Fourier-transform infrared spectroscopy measurements were conducted on composites obtained after cryomilling and heat treatment (328 K for 12 hours) using a Varian spectrometer. Samples were characterized via attenuated total reflection (ATR) by mounting an ATR unit into the sample compartment of the spectrometer. The spectra were recorded in the range of 550 cm^{-1} to 4000 cm^{-1} with a spectral resolution of 0.5 cm^{-1}.

3.1.2.1.8 Raman spectroscopy

A micro-Raman HR8000 spectrometer (Horiba Jobin Yvon) was used to record Raman spectra from 400 cm^{-1} to 4000 cm^{-1} with a laser wavelength of 514.5 nm. The measurements were carried out on the cryomilled mixtures, which were heat treated at 328 K prior to measurements similar to the composite electrolyte pellets.

3.1.2.1.9 Differential scanning calorimetry

Differential scanning calorimetry was performed on a DSC 4000 from Perkin Elmer on the cryomilled powders after the heat treatment. The melting point as well as the melting enthalpy were taken from the first heating curve. The temperature range of the heating curve was between 213 K to 373 K with a heating rate of 10 K min^{-1}.

3.1.2.2 Studies of the garnet/PEO interface

3.1.2.2.1 Garnet Thin Film synthesis

For the interface studies, $Li_{6.4}La_3Zr_{1.4}Ta_{0.6}O_{12}$ (LLZTO) thin-films were deposited by LASER assisted chemical vapor deposition (LA-CVD) on a Si wafer in (100) orientation (CrysTec GmbH). This composition was chosen due to our previous experiences with its synthesis using LA-CVD as the synthesis method [110] and better phase purity of the garnet films compared to that of Al or Ga doped LLZO which would be beneficial for interface studies using XPS. Detailed descriptions of the deposition setup can be found in previous publications [110]. As precursors 2,2,6,6-tetramethyl-3,5- heptanedionato lithium ($LiC_{11}H_{19}O_2$, STREM Chemicals GmbH, 98%), lanthanum(III) acetylacetonate hydrate ($La(C_5H_7O_2)_3 \cdot 4H_2O$, abcr GmbH, 99.9%), tantalum(V) tetraethoxyacetylacetonate ($TaC_{13}H_{27}O_6$, STREM Chemicals GmbH, 99.99%) and zirconium(IV) acetylacetonate ($Zr(C_5H_7O_2)_4$, STREM Chemicals GmbH, 98%) were mixed in stoichiometric ratio, with a 50 wt-% excess of Li. A mixture of argon (1.45 slm, Air Liquide, 99.999%) and oxygen (1.0 slm, Air Liquide Deutschland GmbH, 99.999%) were used as process gases during the 15 min deposition step, together with a substrate temperature of 923 K. After deposition, a 15 min annealing step under the same gas atmosphere and temperature was added.

After synthesis, the garnet thin film was directly transferred to the XPS chamber for XPS analysis. in contrast to the synthesis of powders, surface contaminations of Li_2CO_3 exist after synthesis and originate from the use of carbon rich precursor materials here. Thus, the synthesized films were subjected to thermal treatment for 1 hour at 923 K hour under ultra-high vacuum conditions (~ 10^{-7} Pa) to remove such contaminations like Li_2CO_3. Subsequently, XPS analysis was performed before the deposition of the polymer and Li-ion salt.

For the deposition of thin films of poly(ethylene glycol) (PEG) and LiTFSI via physical vapor deposition (PVD) thermal co-evaporation from two independent sources is used. Each source consists of a self-made Knudsen cell with an electrically heated Al_2O_3 crucible. The PEG source is located directly under the garnet substrate and the LiTFSI source is positioned at 45 ° to the PEG source at a distance of around 14 cm from the garnet film. PEG (2000 g mol^{-1}, Alfa Aesar) and LiTFSI (Sigma Aldrich) are used. Both PEG and LiTFSI are vacuum dried at 10^{-6} Pa for at least 24 hours prior to use. Evaporation is performed at temperature at the outside of the crucible at $T_{crucible}$= 483 K for the PEG and $T_{crucible}$= 518 K for the LiTFSI at a pressure between 10^{-5}-10^{-6} Pa. The total deposition time is doubled for each deposition step from 1 min up to 8 min for a total deposition time of 16 min.

3.1.2.2.2 X-ray photoelectron spectroscopy

XPS analysis of the garnet thin films and interface are performed at the integrated cluster tool Daisy-Bat with a Phi VersaProbe 5000 using monochromatized Al Kα radiation (1486.6 eV), a spot size of 200 µm and 50 W power. The pass energy was set to E_{pass} = 23.5 eV for all detail XP spectra with an analyzer angle of 45 °. During the measurement the analyzer chamber exhibits a pressure between 10^{-8}-10^{-7} Pa.

A symmetric pseudo-Voigt function with 70 % Gaussian and 30 % Lorentzian contribution with the Shirley algorithm for background subtraction are used for deconvolution of most XP spectra using the software CasaXPS version 2.3.22PR1.0. For the deconvolution of PEG and LiTFSI an asymmetric line profile of A(a ,b ,n)GL(p) on the basis of *Wertheim* is used with a=0.25, b=0.125, n=0, p=30 for the PEG and a=0.25, b=0.115, n=3, p=30 for the LiTFSI [111]. For the quantification of the XP spectra, the CasaXPS software was used, taking into account the

transmission function of the VersaProbe, active angle distribution and the sensitivity factors (RSF) supplied by the Phi software Multipack version 9.1.0.9. No further escape depth correction has been applied. All spectra are referenced to the C1s emission of the PEG with a binding energy of E_B = 286.5 eV and the Zr3d of the as is and “heated” spectra are referenced to the Zr3d after 1 min of deposition.

3.1.3 Results and discussion

3.1.3.1 Study of composite membranes

3.1.3.1.1 Characterization of Composite electrolyte membranes

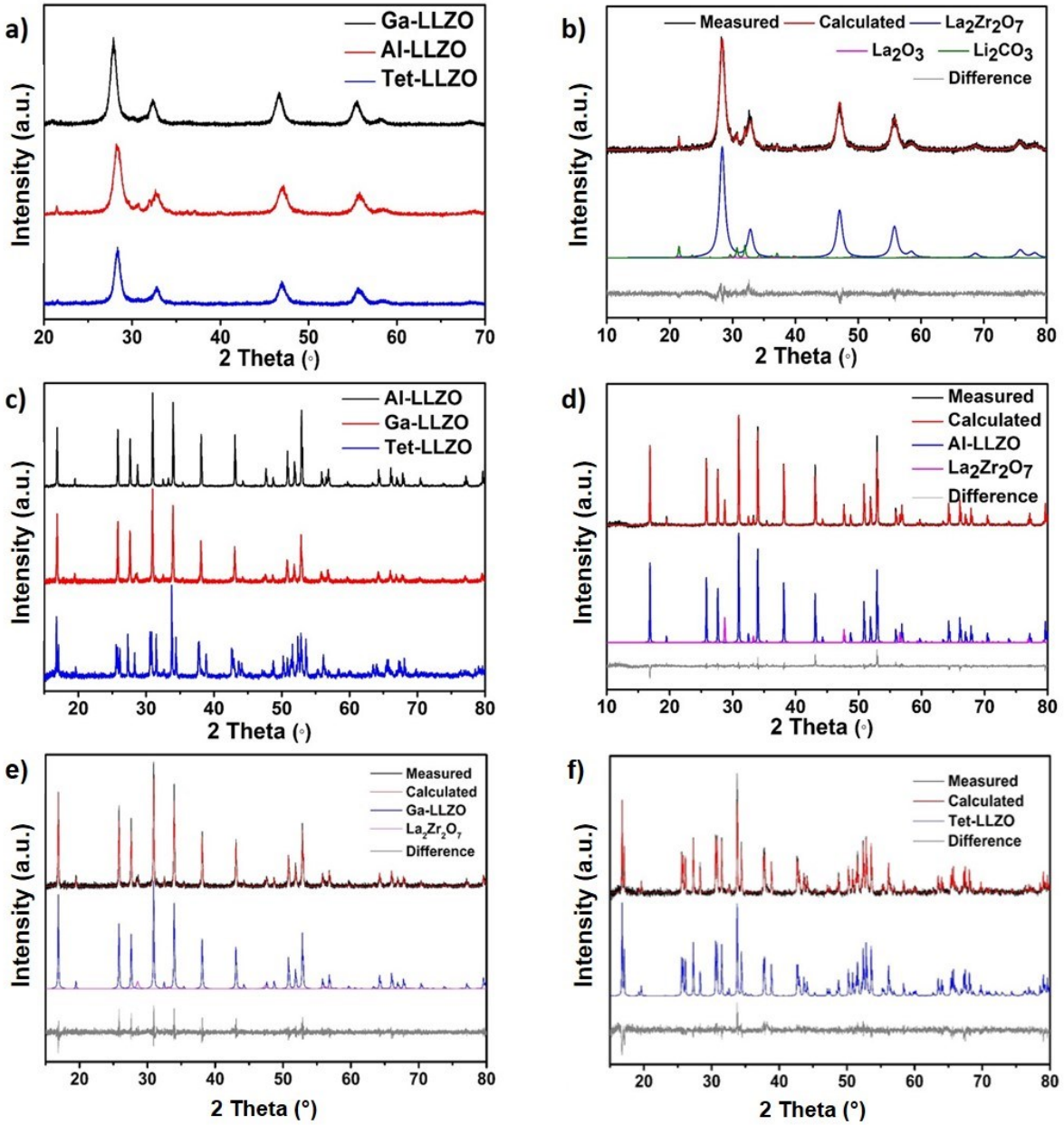

Figure 3.6: a) X-ray diffractograms for the as synthesized powers of Ga-LLZO, Al-LLZO and Tet-LLZO. b) Representative Rietveld fit for the X-ray diffraction pattern for an as-synthesized Al-LLZO powder containing a mixture of several phases. c) X-ray diffraction pattern of the heat treated NSP powders. d-f) Rietveld fit of heat treated Al-LLZO, Ga-LLZO and Tet-LLZO powders, respectively.

Tetragonal LLZO with well-ordered Li-ion distribution crystallizes in the space group $I4_1/acd$ whereas cubic LLZO with disordered distribution of Li-ions by aliovalent doping makes the material a fast Li-ion conductor [41]. The stabilization of LLZO in a cubic structure can be achieved via aliovalent doping [41] with elements such as Al or Ga according to $Li_{7-3x}(Al,Ga)_xLa_3Zr_2O_{12}$, which creates disorder and vacancies in the lithium sublattice, with Al/Ga being located on the 24*d* site [112]. In order to study the compositional dependence of composite electrolytes on conductivity, three different garnet compositions were used: two

aliovalently doped cubic garnet phases (i.e., Al-LLZO and Ga-LLZO), and the undoped tetragonal garnet phase (Tet-LLZO). The cubic and tetragonal garnets were chosen since it is well known that cubic garnets have two orders of magnitude higher conductivity than the tetragonal garnets [41], in order to derive potential intrinsic impacts of the garnet material itself while maintaining comparable morphology.

Figure 3.6a shows the X-ray diffraction patterns of the as-synthesized powders recorded at room temperature. In agreement with previous reports of Djenadic et al.[34] and Botros et al. [35], it is observed that all compositions contain a mixture of CaF_2 type $La_{0.5+\delta}Zr_{0.5-\delta}O_{1.75-\delta/2}$ as well as Li_2CO_3 and La_2O_3. An exemplary Rietveld fit of the XRD pattern of the as-synthesized powders of Al-LLZO is presented in Figure 3.6b.

The as-synthesized powders were post annealed at 1173 K for 3 hours in order to obtain the desired garnet phases. Figure 3.6c shows the XRD patterns of the annealed powders, which confirms the formation of mainly garnet type phases for all the compositions. From the Rietveld analysis (See Figure 3.6d and e) a small fraction (5 - 7 wt-%) of $La_2Zr_2O_7$ can be observed for Al and Ga doped LLZO, which is a common impurity phase observed in Li-containing garnets occurring due to lithium loss at higher temperatures [41], and is not a strong inhibitor for obtaining high conductivities due to the large crystallite sizes and particulate nature [35]. For these phases, Al/Ga are known to be incorporated on the tetrahedrally coordinated Li site, following the formula $Li_{7-3x}(Al,Ga)_xLa_3Zr_2O_{12}$ [112]. For the tetragonal LLZO phase pure powders were obtained. The lattice parameters obtained from the Rietveld fit for all the compositions are presented in Table 3.1 and are in good agreement with the values reported in literature [34, 113].

Table 3.1: Lattice parameters determined from the Rietveld analysis of the X-ray diffractograms of Al-LLZO, Ga-LLZO and Tetragonal LLZO respectively.

Composition	Space group	Lattice Parameter	
		a	c
$Li_{6.49}Al_{0.17}La_3Zr_2O_{12}$	*Ia-3d*	12.97076(5)	
$Li_{6.34}Ga_{0.22}La_3Zr_2O_{12}$	*Ia-3d*	12.9838(6)	
$Li_7La_3Zr_2O_{12}$	*$I4_1/acd$*	13.11924(4)	12.66747(5)

In order to prepare composite electrolytes, PEO and LiTFSI were first cryomilled followed by adding different weight fractions (see Figure 3.7) of the ceramic powders and a subsequent cryomilling process. The use of a non-invasive solvent free approach for obtaining homogenous ceramic dispersions in PEO is important to enable membrane fabrication with varying amounts of ceramic content, i.e., from PEO rich to ceramic-rich membranes and also to avoid PEO degradation. To confirm that the cryomilling approach used here does not cause degradation of the PEO, FT-IR measurements and Raman measurements were carried out on the cryomilled mixture of PEO+LiTFSI and compared to that of the pure PEO and LiTFSI, which confirm the compatibility of the cryomilling process (see the discussion section 3.1.3.2). Figure 3.8a shows the X-ray diffraction pattern of the pure PEO, LiTFSI, PEO+LiTFSI and CEs with different weight fractions of Al-LLZO. After the cryomilling, none of the characteristic peaks belonging to the LiTFSI can be observed which points to the solvation of LiTFSI into the PEO matrix [114]. Further, an overall broadening of the PEO reflections after cryomilling can be observed, indicating lower degree of crystallinity. As the Al-LLZO is introduced in PEO+LiTFSI, the characteristic peaks of cubic Al-LLZO can be observed which increase in intensity with increased loading fraction. Also, an increased background in the diffractograms of CEs can be observed which could be explained by presence of amorphous PEO. It is well known that

introduction of ceramic fillers in the polymer matrix inhibits polymer crystallization leading to amorphous regions in the PEO matrix [25, 74, 98]. The results were found to be in agreement with the DSC measurements shown in Figure 3.8b,c and summarized in Table 3.2. For a meaningful comparison of the CE samples the DSC curve of the used semicrystalline PEO is shown in Figure 3.8b, which showed a melting temperature of 341.5 K and a melting enthalpy of 175.4 J/g. Assuming that the standard melting enthalpy of a 100 % crystalline PEO is $\triangle H$ = 196.6 J/mol [115], the degree of crystallinity of the pristine PEO can be calculated as 89 % (see Table 3.2). For all the CEs, the melting point was found to be lower than for pure PEO, with the CE containing 10 wt-% of Al-LLZO filler having the lowest melting point which is also in agreement with the lower degree of crystallinity and broadening of the PEO reflections in the XRD pattern. The degree of crystallization is found to strongly decrease on the addition of Al-LLZO, but stays nearly constant around 70 % above a threshold of ~ 30 wt-% of Al-LLZO (Figure 3.8c).

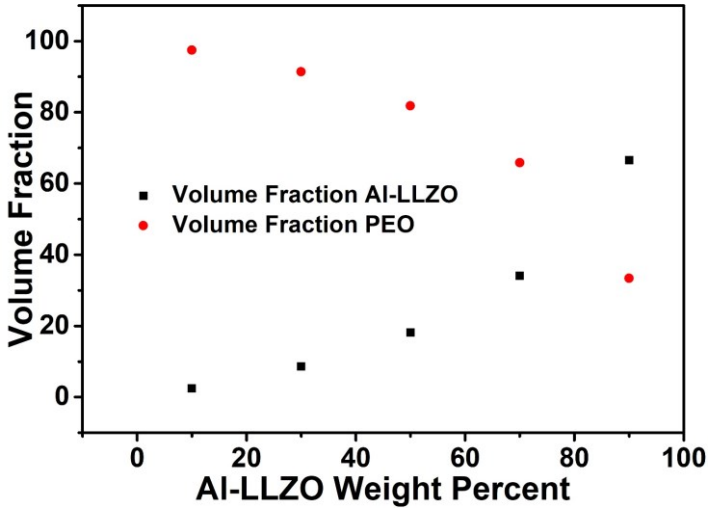

Figure 3.7: Volume fractions of Al-LLZO/PEO as a function of Al-LLZO weight percentages in PEO.

Figure 3.9 shows photographs of a characteristic composite electrolyte membrane which was obtained by uniaxially pressing a mixture containing PEO, LiTFSI and 50 wt-% Al-LLZO into a thin membrane. The high flexibility of the membrane is highlighted. Figure 3.10 shows the SEM micrographs of the composite electrolyte pellets. For the PEO-rich samples, the micrographs (Figure 3.10a) show a rather continuous and smooth film of PEO. Once the Al-LLZO particles are introduced in the PEO, i.e. for 10, 30 and 50 wt-% of added Al-LLZO, the surface roughness increases. The PEO acts as the dominant phase and the particles are found to be well dispersed within the PEO matrix. For higher weight percentages of Al-LLZO, i.e. 70 and 90 wt-%, there are regions of uneven distribution of polymer and garnet particles. For the PEO free garnet, it is clear that the porosity is high due to mere mechanical contacting of the particles in the isostatically pressed pellets.

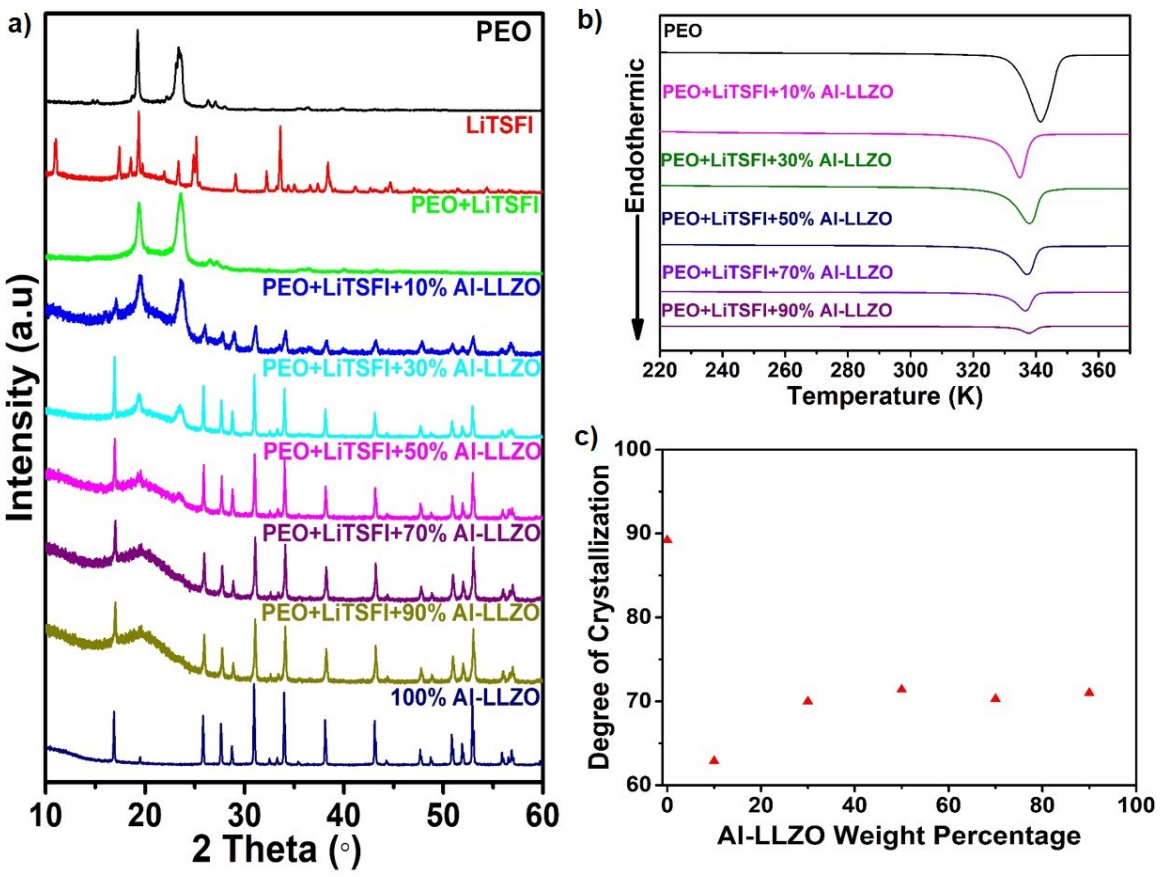

Figure 3.8: a) X-ray diffraction patterns for the pure components and the composite electrolytes with different weight percentages of Al-LLZO as the ceramic filler. b) Comparison of DSC measurements for the PEO and different CE compositions. c) Degree of crystallization for PEO in different CEs.

Table 3.2: Comparison between melting temperatures, enthalpy of melting and degree of crystallinity for different CEs. The degree of crystallinity for the different samples are calculated by using 196.6 J/g as $\triangle H_m^0$ for a fully crystalline PEO and the equation $X_c = \triangle H_m / (wt_{PEO} * \triangle H_m^0)$.

Sample	Melting Point (K)	Enthalpy of Melting $\triangle H_m$ (J/g)	Degree of Crystallinity X_c
PEO	341.5	175.4	89.2
10 wt-% Al-LLZO	334.9	99.3	62.9
30 wt-% Al-LLZO	337.9	96.3	70.0
50 wt-% Al-LLZO	337.3	70.1	71.4
70 wt-% Al-LLZO	336.7	41.4	70.3
90 wt-% Al-LLZO	337.7	14.0	71.0

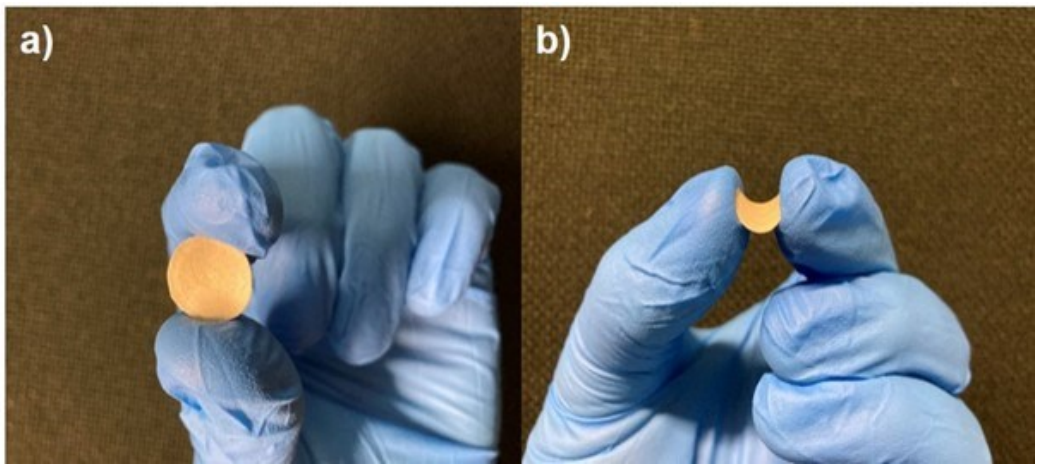

Figure 3.9: a) & b) Photographs showing a composite electrolyte membrane containing 50 wt-% of Al doped LLZO and flexibility of the membrane respectively.

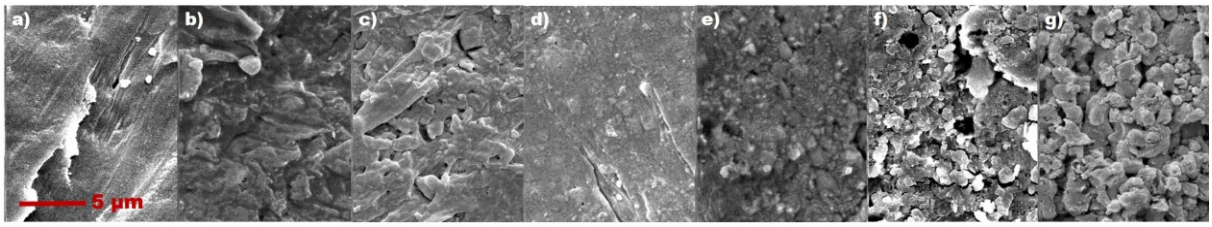

Figure 3.10: SEM micrographs for the composite membrane pellets a) pure PEO, b to g) CE with 10, 30, 50, 70, 90 and 100 wt-% of Al-LLZO respectively.

3.1.3.2 Interpretation of Fourier Transform infrared spectroscopy and Raman spectroscopy

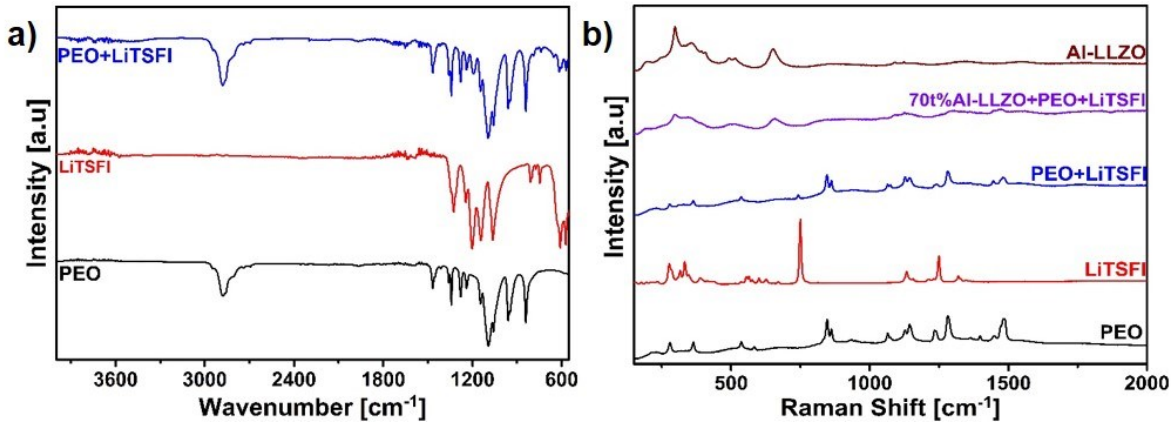

Figure 3.11: a) FT-IR measurement for the pure PEO, LiTFSI and cryomilled PEO+LiTFSI mixture. b) Raman spectra measured for the pure components and CE with 70 weight percent of Al-LLZO.

The use of a noninvasive solvent free approach for obtaining homogenous ceramic dispersions in PEO is important to enable membrane fabrication with varying amounts of ceramic content i.e from PEO rich to garnet rich membranes and also to avoid PEO degradation. To confirm that the cryomilling approach used here does not cause degradation of the PEO, FT-IR measurements were carried out on the cryomilled mixture of PEO+LiTFSI and compared to that of the pure PEO and LiTFSI and the results are shown in Figure 3.11. Pure PEO contains bands at 1464 cm^{-1}, 1096 cm^{-1} and 839 cm^{-1} which correspond to the CH_2 scissoring mode, C-O-C stretching mode and CH_2 wagging mode, respectively, which are in agreement with the reported values [116]. PEO is known to be sensitive towards moisture which can lead to the water uptake. Since pure PEO samples were handled in air prior to the FT-IR measurement for a

short time, an additional peak at 3000 cm^{-1} was observed which indicates the uptake of a small degree of moisture [80, 82]. Similarly, the FT-IR spectra of the pure LiTFSI salt shows vibrational bands at 1242 cm^{-1} attributed to asymmetric stretching of SO_2, 1144 cm^{-1} due to asymmetric stretching of CF_3 and 1060 cm^{-1} which is reported to be due to symmetric stretching of SO_2. Further the symmetric stretching band at 745 cm^{-1} attributed to CF_3 can also be observed [117, 118]. The cryomilled mixture of PEO+LiTFSI shows the peaks belonging to that of the pure PEO and additional peaks at 739 cm^{-1} ,1060 cm^{-1} and 1142 cm^{-1} which resemble the characteristic peaks of LiTFSI. However, the intensity of these peaks is low due to the small concentration of LiTFSI in the PEO. No additional peaks other than the pure components can be seen, which confirms the noninvasive nature of the cryomilling process.

Additionally, Raman spectra were also measured and are shown in Figure 3.11b. The addition of LiTFSI to the PEO can cause conformational changes to the PEO chains which can result in changes to the vibrational frequencies. Therefore, it is important to first understand the Raman spectra of the pure components. For the pure PEO polymer, peaks at 235 cm^{-1}, 279 cm^{-1} and 364 cm^{-1} have been attributed to the D-LAM (disorder-longitudinal acoustic mode), -C-C/C-O-C bending + C-C rocking and coupled C-O-C/O-C-O bending vibrations respectively [119]. Additional vibration modes due to C-O stretching and CH_2 rocking can be seen at 845 cm^{-1} and 860 cm^{-1} [119, 120]. Between 1000 cm^{-1} and 1200 cm^{-1} three distinct peaks can be seen. These peaks at 1063 cm^{-1}, 1126 cm^{-1} and 1142 cm^{-1} have been reported to correspond to coupled C-O-C stretching/CH_2 rocking, coupled C-C stretching/CH_2 wagging and coupled C-C/C-O-C stretching vibrations respectively. For the solid pure LiTFSI salt, the vibrational modes at 140 cm^{-1}, 278 cm^{-1}, 315 cm^{-1} and 332 cm^{-1} correspond to internal, CF_3 rocking and SO_2 rocking respectively [119]. The prominent band at 750 cm^{-1} has been reported to be due to $TFSI^-$ anion [120]. Further, the bands at 1135 cm^{-1} and 1250 cm^{-1}correspond to SO_2 stretching and CF_3 stretching [121]. For the cryomilled PEO+LiTFSI mixture, in general reduced intensities of the reflections belonging to the pure PEO can be observed along with the superimposed peak of LiTFSI at 750 cm^{-1}, however this peak is shifted to lower wavenumber, which has been reported due to the different environment for the $TFSI^-$ anion [122]. Due to the weak interaction of the of the anion with the PEO, the perturbation of the S-N stretching mode can be due to anion-cation association [122]. Also, the addition of the Li salt has been reported to influence the positon of the D-LAM mode, indicating different conformation of the polymer backbone [119]. Raman Spectra were also measured on the CE containing 70 wt-% of Al-LLZO. As can be clearly seen, for this composite membrane, bands belonging to Al-LLZO garnet can only be observed and no further information could be obtained from this spectrum. Further, attempts were made to carry out the Raman spectra on other composite electrolytes as well, however they were unsuccessful due to the broadening of the peaks and the reason of this broadening could not be understood at the moment.

3.1.3.3 Impedance spectroscopy

Commonly, the conductivities of garnet type materials reported in literature [10] are measured on well-sintered ceramics with high densities. For the comparison to garnet-polymer composites, this must be considered as a non-ideal reference state, though not without value. For composites, high sintering temperatures are inapplicable to polymer-containing systems, and any ceramic-rich CE will have to contain a significant higher amount of grain boundaries in comparison to a well sintered ceramic pellet. Clearly, any ceramic-rich composite will not only contain polymer-ceramic interfaces, but it will also contain a significant amount of unsintered ceramic-ceramic interfaces. To take this important aspect into account, we are using compacted garnet powder using the same compaction and preparation strategy as for the CEs

within this article. Therefore, although the intrinsic conductivity of cubic garnets is higher than the one of PEO+LiTFSI, the picture reported in the following is reversed, i.e., pure polymers have higher conductivities than the pure garnets and the reader must be aware of this to avoid confusion.

The compacted unsintered garnet powders show low conductivities of the order of 10^{-10} S cm^{-1} at 298 K which is significantly lower than these of the conventionally sintered garnet pellets (see Figure 3.30 in supplementary information given in section 3.3). The strong impact of powder morphology and the resulting sintering behavior also becomes clear from the following. For NSP synthesized Al-LLZO pellets, maximum conductivity values of 4.4 x 10^{-6} S cm^{-1} have been reported [34], which is two orders of magnitude lower than the solid state synthesized Al doped LLZO [123, 124]. The reduced conductivity is a result of porous microstructure (see Figure 3.31 in supplementary information given in section 3.3) and low relative density (47-56 % of the crystallographic density) compared to sintered pellets of powder prepared from solid state synthesis (> 96% of the crystallographic density [125]). We further acknowledge that once the material is further compacted via spark plasma sintering, ceramics with very high conductivities in the order of 10^{-3} to 10^{-4} S cm^{-1} can be prepared [35]. Thus, the comparison of the garnet-garnet interfaces within compacted powders, porous ceramics as well as dense ceramics already highlights the complexity of this interface itself.

The CEs were evaluated for their ionic conductivities using AC electrochemical impedance spectroscopy. Figure 3.12 shows the Nyquist and Bode plots for the composite electrolytes containing different weight percentages of Al-LLZO as the ceramic filler. It can be seen that the shape of the semicircles as well as the frequency dependence of the absolute of the impedance and the phase angle show a strong dependence on the composition of the CE. The evaluation of the impedance data was carried out using equivalent circuit models consisting of R-CPE elements as illustrated in Figure 3.32 (supplementary information given in section 3.3). Here R is a resistor and CPE is a so-called constant phase element. The total conductivity of the composite electrolytes was determined according to the equation,

$$\sigma = t/RA$$

where *t* is the thickness of the electrolyte, *R* is the resistance obtained from the low frequency intercept on the x-axis and *A* is the cross-sectional area. The total ionic conductivity (σ) for different CEs as a function of Al-LLZO weight fraction and temperatures in PEO at 298 K is shown in Figure 3.12d&f. It is observed that filler-free PEO+LiTFSI electrolyte shows higher conductivity as compared to the CEs and that the conductivity decreases with the increase of the Al-LLZO loading fraction in the CEs. The addition of the ceramic filler to the pure polymer electrolyte has been known to increase the lithium ion conductivity, however, this increase is highly dependent on the particle size and weight percentages used. The Al-LLZO ceramic fillers used in this study have particle sizes of an order of 1 µm, which is

higher than the particle sizes previously used, with sizes ranging from 40-400 nm [23, 97]. Larger particle sizes would mean lower surface area of the filler, which will lower the Lewis acid base type interactions between the ceramic filler and the lithium salt [97], therefore not contributing towards the enhanced lithium ion conductivity. Furthermore, particle agglomeration can also occur which is known to reduce the ionic conductivity of composite electrolytes [126]. Therefore, although the degree of crystallization of PEO is reduced, it is not the only factor responsible for increasing the lithium ion conductivity of the composite electrolytes.

In general, the temperature dependent ionic conductivity of the pure components and CEs follows the classical Arrhenius type relationship

$$\sigma(T) = A\, exp\left(-\frac{E_A}{kT}\right)$$

there A is a pre-exponential factor and can be temperature dependent by itself, T is the absolute temperature, k is the Boltzmann constant and E_A is the activation energy. Figure 3.12d shows the temperature dependent ionic conductivity of the PEO+LiTFSI, isostatically pressed Al-LLZO and CEs with different Al-LLZO weight fractions. In the filler free membranes, the Li ions are known to diffuse in

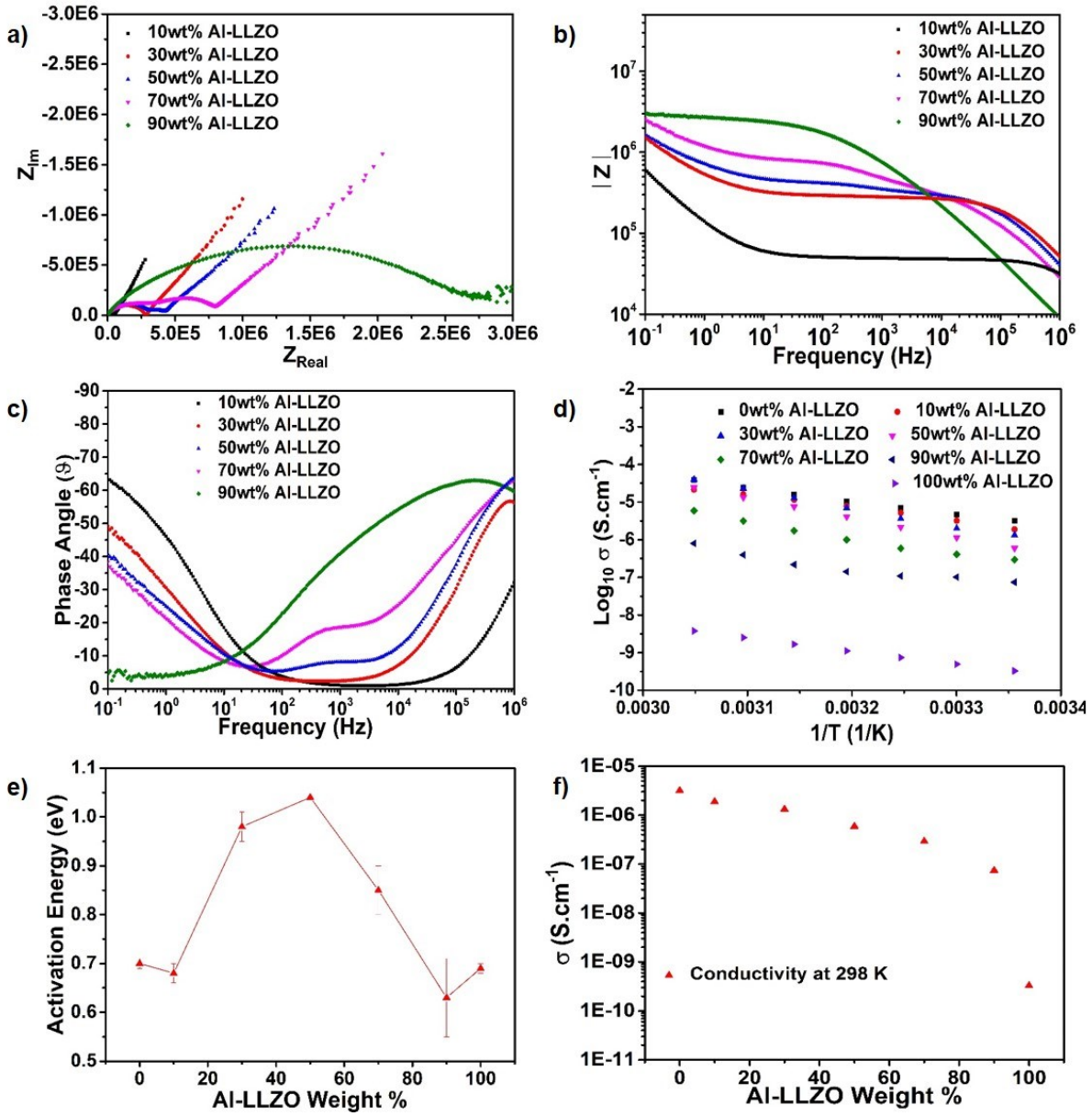

Figure 3.12: a) Nyquist plots for the CEs with different weight percentages of Al-LLZO as the ceramic filler, b) and c) show the corresponding Bode plots for the impedance measurements of CEs. d) Temperature dependent Arrhenius plots of the overall conductivity for pure components (i.e. PEO+LiTFSI or isostatically pressed powder of Al-LLZO) and CEs with different weight fractions of Al-LLZO in PEO matrix. e) Activation energies as a function of Al-LLZO weight fraction in CEs. f) Conductivities at 298 K obtained for the CEs as a function of Al-LLZO weight fractions in PEO+LiTFSI matrix (y axis in log scale for better visualization).

the amorphous phase assisted by the segmental motion of PEO chains [25]. As previously reported by different groups, the addition of ceramic filler results in increased conductivity of the CEs due to increased carrier mobility on account of enhanced segmental motion of

polymers, likely related to a reduced degree of crystallinity, which is in principle in agreement with what we observe from DSC measurements [23, 68, 74, 76], a conductivity enhancement of PEO [60, 127] and the introduction of additional percolation pathways for Li^+ ion conduction [75, 100, 128]. As already mentioned, increased conductivity upon Al-LLZO addition was not observed for the samples reported here, related to the higher particle size of the Al-LLZO particles, which will limit the Lewis-type acid-base interactions between the filler and the LiTFSI salt [76, 97]. Further, for the garnet rich composites, high weight percentages of ceramic filler cause particle agglomeration [23] and dominance of grain boundary resistances hence leading to lower ionic conductivity. The conductivity enhancement in the CEs is highly dependent on the surface area of the ceramic fillers and their weight percentages [23, 76, 97]. For LLZO nanowires, the conductivity was found to increase by an order of magnitude as compared to the LLZO nanoparticles, which is due to the local

continuous conduction pathways provided by the nanowire morphology, indicating that the Li^+ conduction mechanism is dominated by the polymer/filler interface in the polymer rich CEs [76]. Since the particle size of the LLZO powders obtained after sintering of the starting powders prepared by NSP is in the order of micrometers [34], this leads to a lower surface area, hence leading to lower conductivities for the CEs [23]. This indicates that although the addition of ceramic filler results in amorphization of the polymer (section 3.1.3.1.1), which is beneficial for the enhanced ionic conductivity [74, 76], this is counteracted by the reduced surface interaction between the lithium salt and garnet, which limits the Lewis acid-base interactions. In general, it is clear that the ionic conductivity decreases with the increasing loading fraction of the Al-LLZO, with the CE of equal weight ratio of Al-LLZO and PEO+LiTFSI showing a conductivity of 4.2×10^{-7} S cm^{-1} at 298 K. The activation energies were calculated from the slope of the Arrhenius plot *(ln(σ) vs. 1/T*, Figure 3.12d) and show a volcano type behavior (Figure 3.12d) with the CEs with 10 and 90 weight fraction of Al-LLZO filler possessing the lowest activation energies of 0.68(2) and 0.63(3) eV, respectively. We also observed lower activation energies for PEO+LiTFSI compared to the previously reported value of 1.01 eV [73], which can be due to the cryomilling procedure used here, which results in a reduced PEO crystallinity as confirmed by the X-ray diffraction and DSC analysis, as discussed in section 3.1.3.1.1 of this article. The high activation energy observed for the isostatically pressed pellets compared to the sintered pellets is due to the dominance of the grain boundary resistances and low pellet density. For the CEs, an increase in the activation energies (E_a) up to 50 wt-% of Al-LLZO is observed, which is likely due to particle agglomeration and contributions from the additional interfaces generated between PEO/Al-LLZO. There onwards lowering of E_a is observed due to a decreased volume fraction of PEO which also reduces the PEO/Al-LLZO interfacial area. Therefore, the decrease of conductivity with the increase of the Al-LLZO weight fraction can be related to one or an interplay of the following effects: (1) the LLZO aggregation in the PEO matrix [74], (2) high ceramic-polymer interfacial resistances [129] (see section 3.1.3.5) and (3) particle-particle interfacial resistance.

In order to understand the composition dependent behavior of the different transport effects to develop an improved understanding of the Li-ion pathways in the CEs, a detailed analysis of the individual components of the equivalent circuits illustrated in Figure S6 used to fit the impedance spectra was carried out. From the NYQUIST plots recorded at 298 K and shown in Figure 3.12a, the PEO rich CEs (i.e., 10 wt-% to 30 wt-% of Al-LLZO) show a single depressed semicircle at high frequencies followed by the capacitive tail at the lower frequencies. However, an additional semicircle in the mid frequency range becomes evident on close inspection of the BODE plots (see Figure 3.12c) in the CEs as compared to pure PEO+LiTFSI. Therefore, the

spectra for CEs were fitted with an equivalent circuit consisting of (R-CPE)(R-CPE)(CPE) elements in series compared to (R-CPE)(CPE) elements used for PEO+LiTFSI. For PEO+LiTFSI, R1 and CPE1 correspond to the bulk resistance and bulk capacitances due to the polymer chains and ions migration [25]. The presence of a low frequency tail confirms the ionic domination towards total conductivity [35]. The capacitance values corresponding to a depressed semicircle described with the aid of a CPE can be obtained from the fitted values using the equation

$$C = (R)^{\left(\frac{1}{n}-n\right)}\ (Q)^{\frac{1}{n}}$$

Here C is the capacitance, R is the resistance value obtained from the low frequency intercept of the NYQUIST plot with the real-axis, Q is the pre-factor of the CPE and n is its exponent [130]. From the individual capacitances of the respective semicircles, an overall capacitance C_{Total} can be calculated further by use of the following equation

$$\frac{1}{C_{Total}} = \frac{1}{C_1} + \frac{1}{C_2} + \frac{1}{C_3} \ldots\ldots$$

The temperature dependence of the capacitance values for the pure components and the CEs are shown in Figure 3.13. For the pure PEO+LiTFSI electrolyte the lowest capacitance value of the order of 10^{-12} F is observed, which shows a small dependence on temperature. The capacitance value observed here is in agreement with the value expected for a bulk capacitance [101], which is in agreement with the bulk Li ion transport in PEO due to absence of any grain boundary contribution and interfacial contributions. For CEs, however, individual capacitance values in the order of 10^{-6} F were found which correspond well to the capacitance values of the interface [101].This implies that for PEO and PEO rich samples i.e. 0 wt-%, 10 wt-%,30 wt-% weight ratio of AL-LLZO fillers, the Li ion transport predominantly takes place via the bulk PEO and in part also along the interfaces for CEs. This is in principle agreement with reports using NMR as the instrumental tool to determine the Li ion migration pathways in polymer-rich CEs [75, 100].

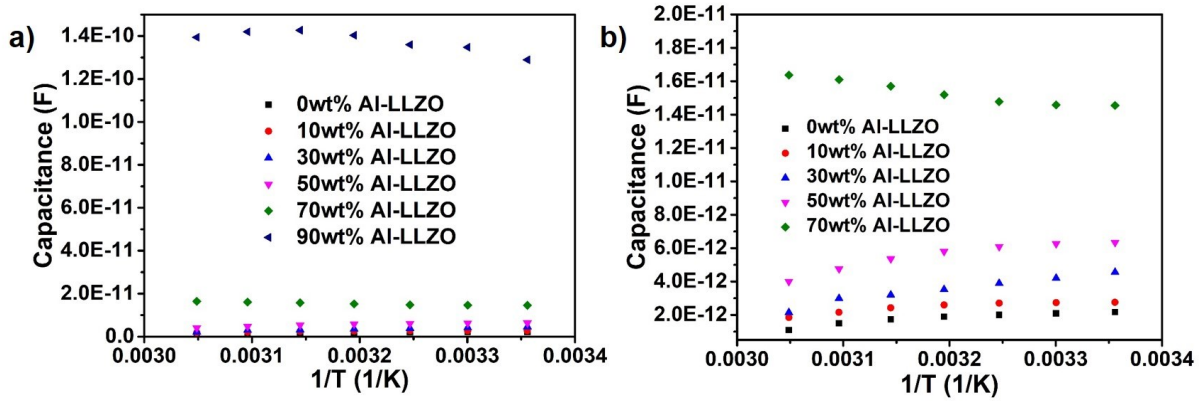

Figure 3.13: a) Temperature dependent total capacitance plot for PEO+LiTFSI and CEs containing Al-LLZO as the ceramic filler from 0 to 90 wt-%. b) Temperature dependent total capacitance for the CEs (without the CE with 90 wt-% fraction of Al-LLZO for better visualization).

For the CE with an equal weight fraction of Al-LLZO and PEO+LiTFSI (i.e., 50 wt-% Al-LLZO and 50 wt-% PEO+LiTFSI), three semicircles could be discerned in the NYQUIST plot as shown in Figure 3.14a, indicating the presence of a further transport mechanism within this system. The equivalent circuit consisting of (R_1-CPE_1)(R_2-CPE_2)(R_3-CPE_3)(CPE_4) elements was used for impedance data fitting. For high weight ratios of ceramic to polymer, alternative pathways for lithium ion transport can become available above a certain threshold

corresponding to the Al-LLZO content in the PEO-LiTFSI matrix. This percolation threshold for composite electrolytes has been reported to be above 40 wt-% of ceramic filler in a polymer matrix [100]. Below this percolation threshold, the conductivity of the composite electrolytes is mainly determined by the segmental motion of polymer [25] and Li ion transport along the interfaces of ceramic fillers [76, 97]. Above the percolation threshold, Li ion conductivity is possible through the PEO matrix, the interface between the PEO/LLZO and the ion conducting LLZO itself [75, 100]. From the fitting of the EIS data, the total conductivity of 5.92 x 10^{-7} S cm^{-1} and capacitances values of an order of 10^{-12} F, 10^{-9} F and 10^{-7} F were determined for the first, second and third semicircle respectively. These capacitances can be assigned to the lithium ion conductivity in the bulk polymer, grain boundaries between LLZO/LLZO and PEO/LLZO interfaces, respectively [101]. Further, the activation energies obtained from the temperature dependent conductivity of the individual R-CPE elements (Figure 3.14c) are 0.96(1), 1.62(2) and 0.58(1) eV respectively) indicating that Li-ion transport along the Al-LLZO/PEO interface can have a reduced activation barrier, can most likely be explained by the presence of increased amounts of defects on the surface of the garnet Al-LLZO.

Figure 3.15 shows the plot of the capacitance as a function of inverse temperature. For the bulk (Figure 3.15a), the capacitance follows the behavior similar to that of pure PEO+LiTFSI, confirming Li ion transport takes place via the polymer part of the CE matrix. A similar trend is observed for the Al-LLZO/PEO interfacial capacitances shown in Figure 3.15c, which decrease with the increase in temperature. However, it is interesting to see that for the grain boundaries, the capacitance value increases with the temperature in Figure 3.15b. This increase in grain boundary capacitance is likely related to a change of the thickness of the barrier layer at the particle/particle interface. The width of the barrier layer *d* is proportional to L_{Gb}/L_G, where L_{Gb} is the density of the trapped Li ions at the grain boundaries and L_G is the density of the free Li ions in the bulk PEO+LiTFSI. As the temperature increases, the conductivity of the grain boundaries increases and the thermal depopulation of the trapped Li ions in the barrier layer takes place. On the other hand, increased conductivity in PEO matrix would imply that Li ions are more mobile in bulk PEO compared to grain boundaries hence decreasing d. Since the capacitance can be written as $C = \varepsilon_{gb} A/d$, hence, decrease of d with temperature would result in an increase in $C_{gb.}$ The grain boundary capacitances and interfacial capacitance between Al-LLZO/PEO are found to lie in the range of 10^{-9} – 10^{-8} F and 10^{-7} F, respectively, indicating that grains have a pronounced effect which can be seen from Figure 3.15d, which shows the total capacitance from the CPE as a function of inverse temperature.

For the CEs containing 70 wt-% and 90 wt-% of Al-LLZO, two semicircles at the high and mid frequencies followed by the capacitive tail at the low frequencies can be seen in the NYQUIST plot. The data can be fitted using the equivalent circuit consisting of (R_1-CPE_1)(R_2-CPE_2)(CPE_3) elements. For those CEs with higher weight percentages of Al-LLZO a significant reduction in the conductivity by an order of magnitude is observed, which can be attributed to the reduced polymer weight fraction. This indicates a strong reduction of transport paths via the percolated polymer network for the lithium ion transport. Although the Li ion conducting garnet does contribute towards the total Li ion conductivity in CEs (see section 3.1.3.4), a poor particle/particle contact plays a significant role towards reducing the overall conductivity in such garnet-rich CEs.

From the Arrhenius fit, a conductivity value of 3.27 x 10^{-10} S cm^{-1} at 298 K was determined for isostatically pressed pure Al-LLZO pellets. It is interesting to note that the addition of polymer can strongly enhance the transport properties, e. g., an increase of conductivity by two orders of magnitude is observed for the CE with 90 wt-% of Al-LLZO and further by an order of

magnitude for the CE with 70 wt-% of Al-LLZO. The increased conductivity is likely due to a lower porosity of pellets since PEO acts as the particle binder, therefore enhancing particle/particle contact, which leads to an increase of the overall interacting surface between the particles in the composite electrolyte.

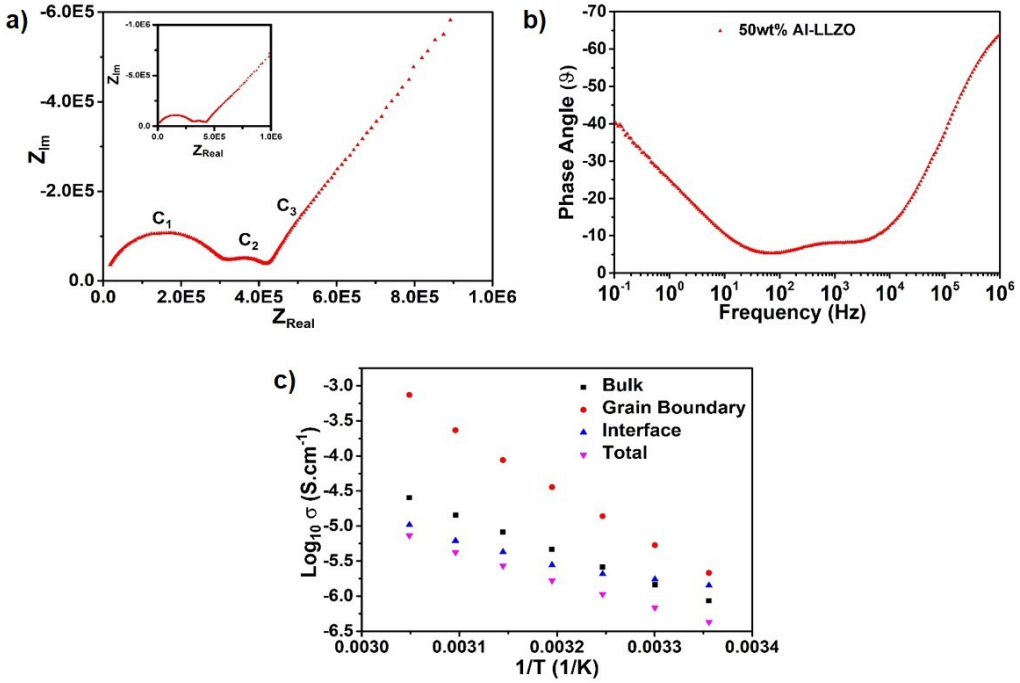

Figure 3.14: a) NYQUIST and b) BODE plot for CEs containing 50% weight percentages of Al-LLZO and PEO+LiTFSI c) Temperature dependent conductivity for individual circuits used in the fitting of the impedance data.

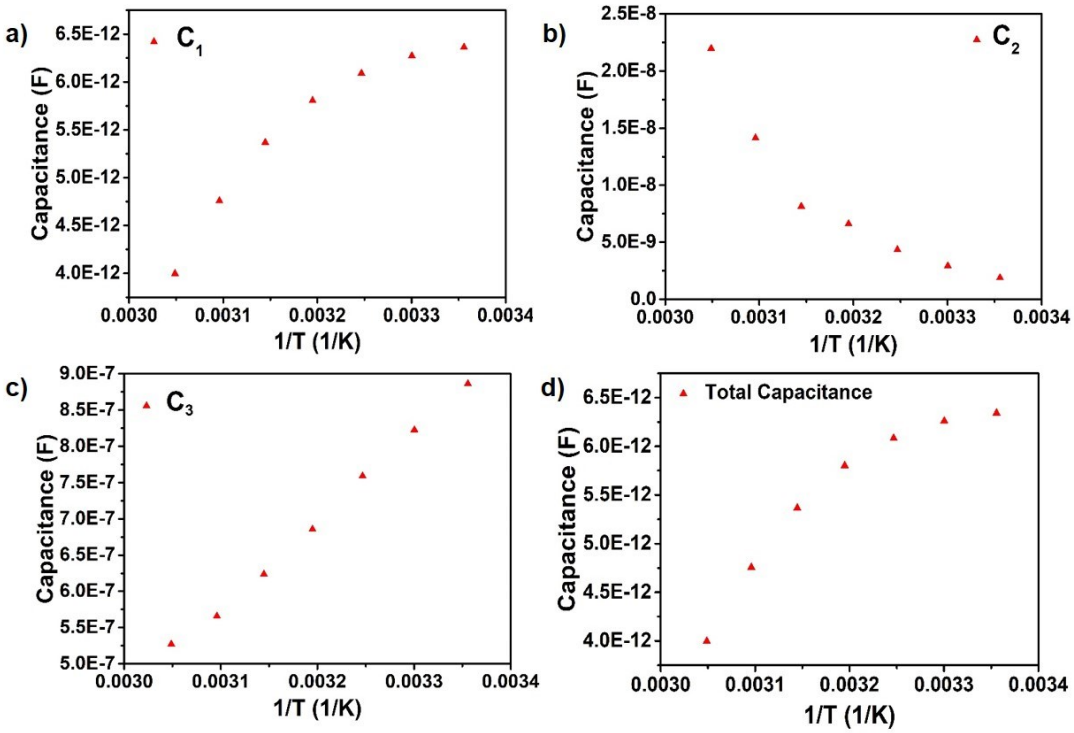

Figure 3.15: a,b,c) Capacitance vs 1/T plots for the individual R-CPE elements used in the fitting of impedance data for CE with 50% weight fraction of Li ion conducting Al-LLZO. d) Total capacitance calculated from the individual capacitances showing the dominance of the grain capacitance.

3.1.3.4 Filler-type dependence of the conductivity

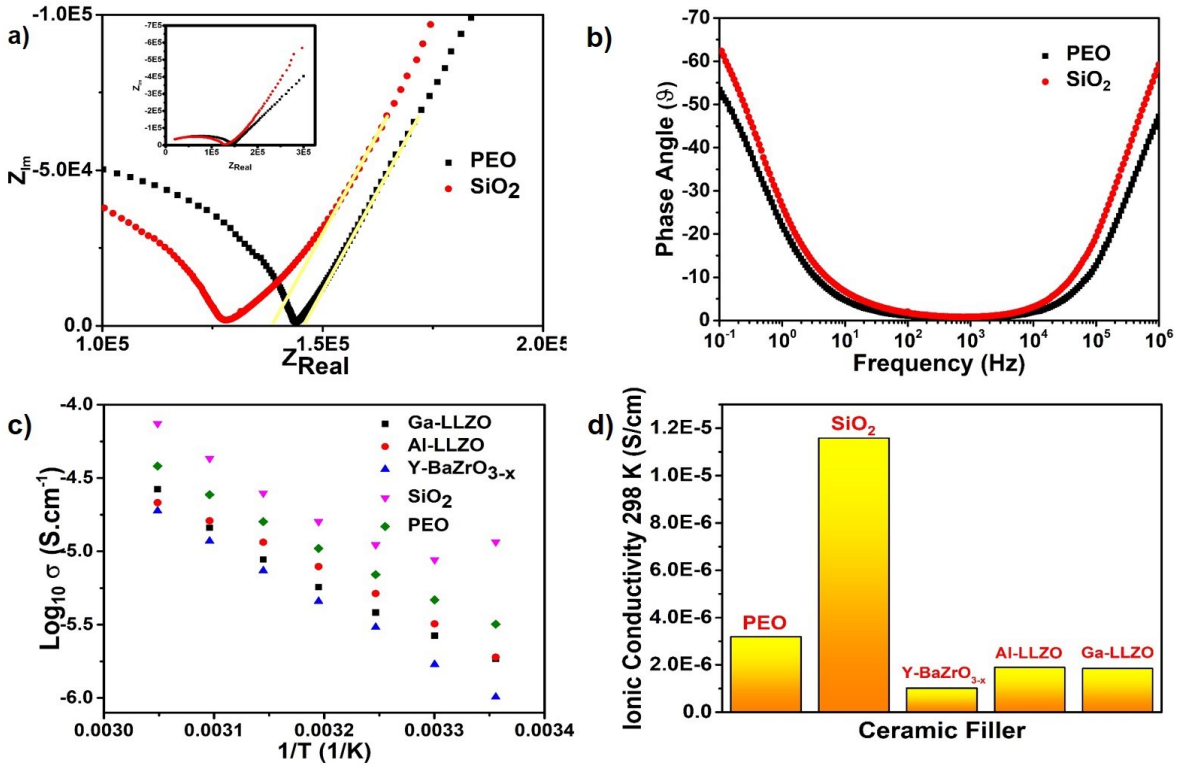

Figure 3.16: a) and b) comparison of NYQUIST and BODE plot for PEO+LiTFSI and CE containing 10 wt-% of SiO_2 particles. c)Temperature dependent conductivity of CPE's containing Li active and inert ceramic filler d) Conductivity values for PEO and CEs at 298 K.

Investigating the role of the ceramic filler by considering exclusively ion-conducting fillers can be misguiding. In order to elucidate the role of the chemical and morphological nature of the ceramic fillers and to obtain a first indication whether they contribute to the overall conductivity of CEs significantly, different ceramic compositions comprising of Li ion conducting and inert ceramic oxide particles were used as the fillers. An exemplary Nyquist and Bode plot for PEO+LiTFSI and CE containing 10 wt-% of SiO_2 particles are shown in Figure 3.16a & b. From the NYQUIST plot (inset of Figure 3.16a), a single semicircle in the high frequency region can be seen followed by a linear tail in the low frequency region assigned to the capacitive response due to ion blocking gold electrodes. Similar to Al-LLZO containing CE, for all the CEs containing 10 wt-% of the filler (Figure 3.16a) another semicircle in the mid frequency range (10-10^3 Hz) can be observed. From the fitting, the capacitance values of 4.29 x 10^{-12} F and 2.18 x 10^{-6} F were obtained for the two RCPE elements respectively, which can be assigned to the Li ion transport in the bulk PEO and along the PEO/SiO_2 interface [101]. From the Arrhenius plot (Figure 3.16c), the composite with 10 wt-% of SiO_2 shows the highest conductivity, which is well explained by the smaller size of the SiO_2 particles used in this study (See Figure 3.33 in supplementary information given in section 3.3). For the inert fillers dispersed in the polymer matrix, the increased conductivity can be explained on the basis of Lewis-type acid-base interactions between the polymer chain segments and the ceramic surface groups. The Lewis acidity of the ceramic fillers competes with the Lewis acidic character of the Lithium cations in the Li salts in order to form complexes with the ether oxygen centers of the PEO which act as the Lewis base [131, 132].

We further used Y-doped $BaZrO_3$ as the ceramic filler since it is highly crystalline with high crystallite sizes, similar density than LLZO and does not conduct Li ions [133]. The presence of

positively charged oxygen ion vacancies on the particle surface can serve as the Lewis acid sites (e. g., $BaZrO_3$ is reactive towards CO_2, similar than LLZO) which can interact strongly with the anion of LiTFSI, in a process setting free the positively charged Li^+ ions and improving the ionic conductivity of the polymer electrolyte [97]. However, the ionic conductivity of the CE containing 10 wt-% of Y-$BaZrO_3$ showed lower conductivity than that of the PEO and SiO_2 containing CE which is most likely due to larger particle size and particle agglomeration which has been shown to decrease the conductivity in PEO based CEs [23]. For CEs containing Li-ion conducting garnets with similar particle sizes as the ceramic fillers, the conductivity was found to be systematically above the CE with the Y-doped $BaZrO_3$ filler, though lower than the nano-crystalline SiO_2 filler. The results here indicate the role of the particle size on the conductivity, therefore concluding that irrespective of the filler composition used the conductivity depends on the surface area of the particles. Therefore, the use of 1D nanowires [76] as the filler providing continuous local sites for Lewis acid-base type interaction is an effective strategy for conductivity improvement in polymer rich CEs.

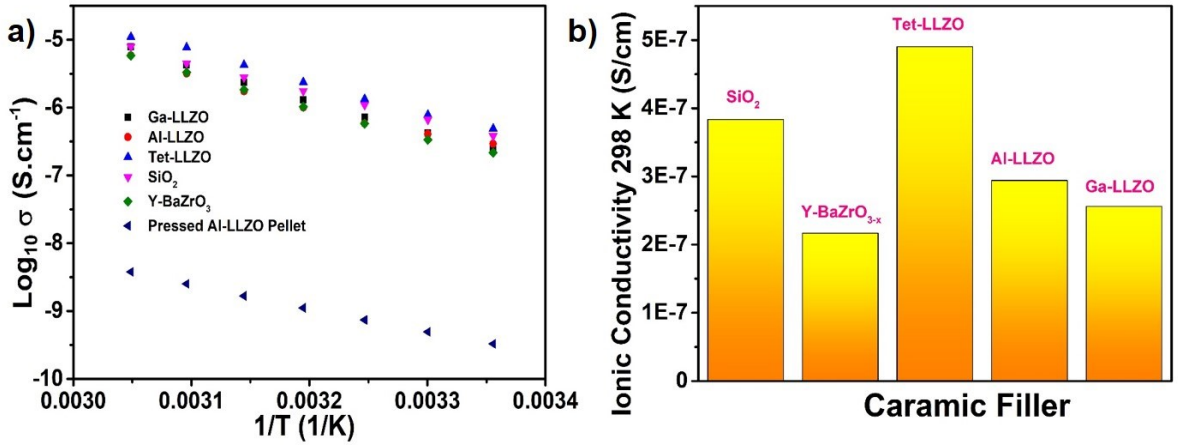

Figure 3.17: a) Arrhenius plot for CEs containing 70 wt-% of the ceramic filler and 30 wt-% of PEO+LiTFSI. b) Li Ion conductivity of the different CEs observed at 298 K.

Figure 3.17a shows the temperature dependent conductivity of CEs containing 70 wt-% of ceramic loading fraction. As expected, the conductivity of the CEs decreases with increasing ceramic loading ratio. The ionic conductivity trend seems to be independent of the type of filler used with Tet-LLZO showing maximum conductivity among the series of compositions used in this study. The total ionic conductivity observed for the CEs at 298 K is shown in Figure 3.17b. Although an alternative Li ion migration pathway via the bulk Li ion conducting ceramic has been proposed for CEs beyond a certain ceramic weight percentage threshold, the results here indicate that for such ceramic-richer systems Li ion transport still predominantly takes place via the PEO matrix. It is interesting to see that tetragonal and cubic LLZO containing CEs show similar conductivity though the cubic garnet structure shows two orders of magnitude higher conductivities than the tetragonal counterparts [41]. Since we do not observe a similar behavior in CEs it likely indicates the dominance of Li ion transport mainly via the bulk polymer and along the ceramic/PEO interface instead of the bulk garnet.

Compared to isostatically pressed Al-LLZO pellets, the CEs show a significant improvement in their total ionic conductivities when 10 wt-% of PEO+LiTFSI is added (Figure 3.18a,b). For CE containing 90 wt-% of Al-LLZO, the conductivity is still orders of magnitude higher than the isostatically pressed Al-LLZO particles. For isostatically pressed pellets, the particles are only in loose mechanical contact. This low internal contact area between particles within the system increases the resistance between the particles, and hence lowers the conductivity. As

discussed in the previous section, the addition of PEO+LiTFSI would act as the particle binder and fill the voids between the particles, hence resulting in better contact between the particles and denser pellets. This results in improved conductivity due to PEO addition which forms the preferred pathway for Li ion transport. To validate the argument, we made CEs with non-Li-conducting SiO_2 and Y-doped $BaZrO_3$ with similar loading fractions. For CE with SiO_2 filler, we found its conductivity to be an order of magnitude lower than the CE comprising of Ga-LLZO. For CE comprising of Y-doped $BaZrO_3$ fillers, the conductivity is found be significantly lower than the other CEs, however it is still higher than the isostatically pressed Al-LLZO. The lower conductivity of Y-doped $BaZrO_3$ compared to SiO_2 can be well assigned to the higher particle sizes of Y-doped $BaZrO_3$, which seem to hinder the existence of a percolated PEO network. For SiO_2, the conductivity found is therefore best explained by Li ion conductivity taking place via PEO. Hence, it is clear that for ceramic rich composite electrolyte systems, Li ion conducting filler does contribute towards total Li ion conductivity. However, since the filler particles are in loose mechanical contact with each other, this contributes towards higher Li ion resistance at the particle/particle interface, which significantly lowers the total ion conductivity.

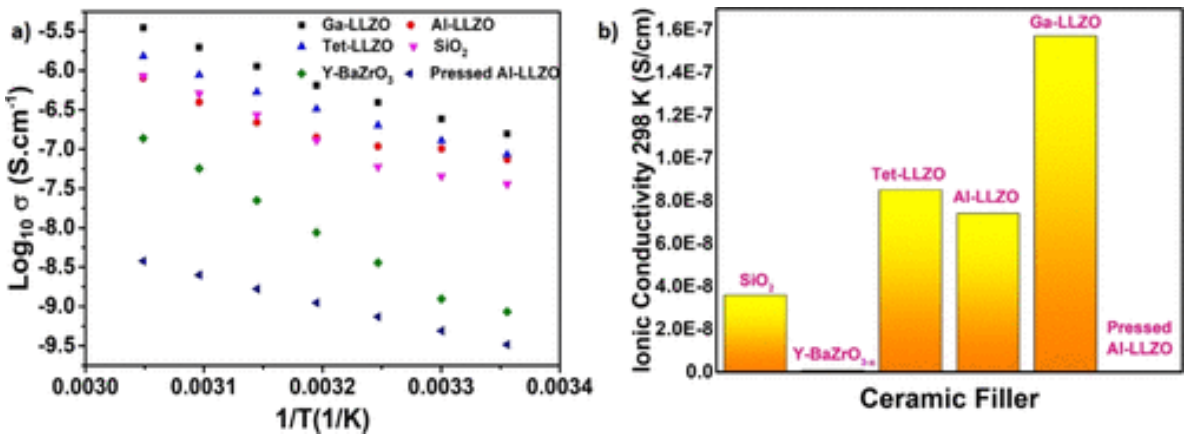

Figure 3.18: a) Arrhenius plot for CEs containing 90 wt-% of the ceramic fillers and 10 wt-% of PEO+LiTFSI. b) Li Ion conductivity of the different CEs observed at 298 K.

In summary, for the CEs, the lithium ion transport pathways are dependent on the PEO to ceramic weight ratio. The fact that the type of filler plays a minor role on the conductivity for polymer-rich CEs indicates that the ceramic weight percentages do not allow for the formation of a well-conducting percolation network; there Li ion transport takes place predominantly via the bulk PEO and along the interface (Figure 3.19). With increasing the ceramic weight ratio, higher than the percolation limit, additional pathways for the lithium ions become available, e.g., along the interface via the grain boundaries along the garnet network. Only for garnet-rich systems, one can conclude that there is significant contribution via the bulk of the garnet particles from the comparison to non-conducting materials.

The findings shown so far present a conceptual understanding of the role of the filler on the overall conductivity. In the following section 3.1.3.5 we will provide a more detailed understanding why the transport of ionic charge carriers through the garnet/PEO interface is not favorable to activate the bulk transport within the ion conducting ceramic fully. For this, we use the combination of an XPS study of surface-coated model garnet films in combination with impedance studies, which clearly show a high resistivity perpendicular to the garnet-polymer interface.

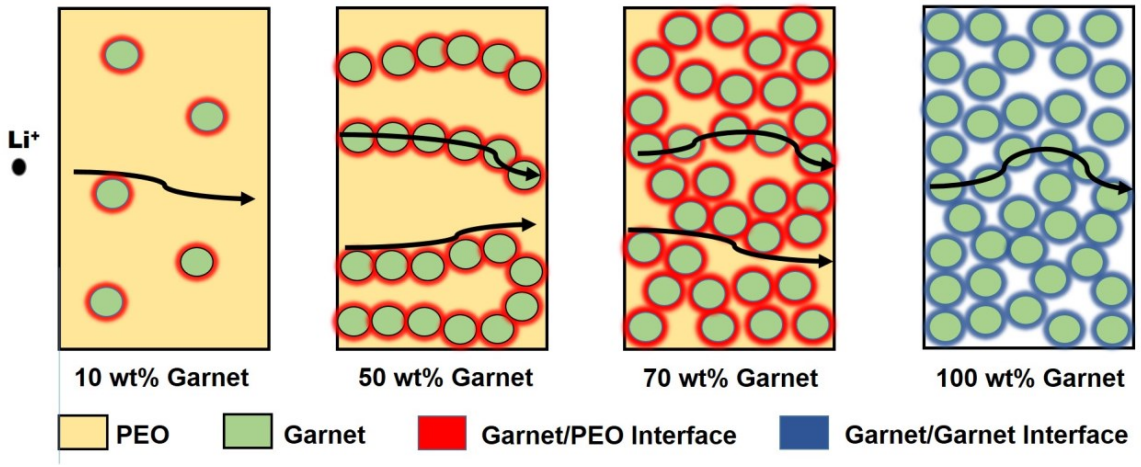

Figure 3.19: Schematics indicating the lithium ion transport via the CEs.

3.1.3.5 Interfacial studies at garnet/PEO interface

To understand the interfacial stability at the garnet/PEO+LiTFSI interface and to develop an understanding on why different lithium ion transport pathways are taken depending upon the garnet to PEO weight fraction, XP spectra were recorded. Initially, attempts were made to study the garnet/PEO interface using garnet rich composites directly via XPS. However, only the signals belonging to the PEO+LiTFSI were observed due to strong coverage of garnet particles far above the emission depth for photoelectrons (>> 10 nm). Hence, a model system consisting of a garnet thin film coated with PEO+LiSFI was developed to study the interface precisely. As a choice of garnet, a thin film of $Li_{6.4}La_3Zr_{1.4}Ta_{0.6}O_{12}$ was used due to our previous experiences with its synthesis using LA-CVD as the synthesis method [110] and better phase purity of the garnet films compared to that of Al or Ga doped LLZO (see Figure 3.34 in supplementary information given in section 3.3). For the as-synthesized LLZTO thin film, XP spectra show typical emission of the $La3d_{5/2}$ and $La3d_{3/2}$ with their corresponding satellite and plasmon structure. Both $La3d_{5/2}$ and $La3d_{3/2}$ are split into three final states i.e. $\underline{cf}^0$, $\underline{cf}^1\underline{L}$ bonding and anti-bonding that are a result of the co-excitation process from the valence band into the 4f band. Deconvolution was done on the basis of Sunding et al. [134]. The $La3d_{5/2}$ $\underline{cf}^0$ and $La3d_{5/2}$ $\underline{cf}^1\underline{L}$ are located at a binding energy of E_B = 833.6 eV and 838.1 eV, respectively, as is expected for LLZO [135]. The $La3d_{3/2}$ $\underline{cf}^0$ is found to be located at E_B = 850.5 eV corresponding to the energy difference of 16.9 eV to $La3d_{5/2}$ $\underline{cf}^0$ which corresponds well to the previous reports [136]. For the Zr, two emissions at E_B = 181.2 eV and E_B = 183.5 eV corresponding to $Zr3d_{5/2}$ and $Zr3d_{3/2}$ respectively can be observed. Further, an emission peak at 290.2 eV can be observed which is attributed to the formation of Li_2CO_3 during the synthesis process [137, 138]. Additionally, four signals starting at 284.7 eV, 285.4 eV, 286.5 eV up to 287.8 eV can be observed and are assigned to the formation of C-C, R-O-Li, C-O-C and C=O species [135, 139-143]. These formations are also reflected in the O1s spectrum, displaying the R-O-Li and C=O components of the Li_2CO_3 roughly in a 2:1 ratio at E_B = 531.5 eV and E_B = 532.2 eV [139 144]. A shoulder towards smaller binding energies is also seen, which originates from the lattice oxygen found on LLZTO at E_B = 529.5 eV and minor contributions of Li_2O at E_B = 528.3 eV [135, 137].

In order to get rid of the impurity components, an additional heating step at 923 K was carried out for one hour under UHV conditions. As can be seen in Figure 3.20, the XP spectra of the heat treated LLZTO thin film does not show any emission corresponding to that of the C1s spectrum, therefore implying the removal of the carbonate from the garnet surface. Further, an increase in the O1s emission for the LLZTO can be seen whereas the emissions corresponding to R-O-Li and R=O can no longer be observed. However, the LLZTO emission exhibits a

shoulder towards higher binding energies at E_B = 530.7 eV, which has been attributed to LiOH by Sharafi et al.[145] and Cheng et al. [146] but might as well be due to the presence of Li_2O_2 as shown by Fingerle et al. [135]. A composition of $Li_6La_{2.8}Zr_{2.9}O_{12}$ (normalized to 12 O) is calculated from the $La3d_{5/2}$, O1s, $Zr3d_{5/2}$ and Li1s spectra from the "heated" step. This corresponds, despite the surplus of zirconium, to a stuffed LLZTO Garnet [147].

Upon 1 min of PEG and LiTFSI deposition, new emissions can be observed in the F1s, O1s, C1s and S2p spectrum originating from the PEG and LiTFSI but as well be as a result of reaction products. In the F1s spectrum two new emissions at E_B = 688.4 eV and E_B = 684.3 eV can be seen which can be attributed to LiTFSI and LiF respectively [139, 148, 149]. The formation of LiF from LiTFSI under X-ray exposure is well studied and has been found to be independent of the substrate used [150, 151], nevertheless, the amount might vary depending upon the reaction with the substrate. For the C1s spectrum five new components can be fitted, mainly -C-O-C- from the PEG at E_B = 286.5 eV and alkyls (C-C and C-H) at E_B = 284.7 eV. Additionally, minor amounts of semi-carbonates (O-C=O) at E_B = 289.0 eV, R=O at E_B = 287.7 and eV R-O-Li at E_B = 285.4 eV are detected. Three newly formed compounds are fitted into the S2p spectrum, LiTFSI at E_B = 170.1 eV, $LiSO_2CF_3$ at E_B = 169.6 eV and Li_2SO_3 at E_B = 168.5 eV [148, 149, 151]. The deposited LiTFSI is found to strongly react at the interface, forming Li_2SO_3, $LiSO_2CF_3$ and $Li_xNSO_2CF_3$ due to the cleavage of the S-N bond that shows a similar binding energy as LiTFSI [152-154] . These reactions are reflected in the O1s spectrum as well, forming a less well-defined shoulder at higher binding energies with PEG and LiTFSI found at E_B = 532.9 eV, R=O at E_B = 531.9 eV, Li_2SO_3 at E_B = 531.75 eV and R-O-Li at E_B = 531.3 eV [143, 148, 155].The La3d, Zr3d and Li1s (Zr4s) components do not display any binding energy shift or change in shape, but only a damping of the signal due to the surface coverage. With the increase in deposition time to 4 minutes, PEG and LiTFSI emissions increase in intensity while the LLZTO intensity decreases due to the formation of PEG+LiTFSI layer on top of the LLZTO film and the surface sensitivity of the XPS method (See Figure 3.22 in supplementary information given in section 3.1.3.6). The C1s spectrum shows the $-CF_3$ group of the LiTFSI at E_B = 292.5 eV as well. The composition of the PEG is exactly as expected, while the LiTFSI is carbon deficient, nevertheless both show a composition of the stochiometric compound within the margin of error observed for XPS quantification **[156]**. Moreover, the carbon containing reaction products exhibit a carbon to oxygen ratio of 1:1 for both C=O and R-O-Li as expected, furthermore the Li_2SO_3 continuously has a sulphur to oxygen ratio around 1:3.

After 16 minutes of deposition evidently a fully surface coverage is achieved due the lack of any LLZTO signal. The La3d spectrum shows no LLZTO emission but only the F KLL from the LiTFSI and LiF [136] while the Zr3d spectrum does not have any emission at all. As before, the F1s shows the same LiTFSI and LiF emissions while at the O1s only the PEG and LiTFSI emission with a shoulder towards smaller binding energies for the Li_2SO_3 are detected. No change in the N1s spectrum in observed. In the C1s spectrum mainly the PEG and LiTFSI increase in intensity, with a slight growth for the C=O as well. C-C and R-O-Li do not increase further and the O-C=O emission has vanished. The same trend is observed for the S2p spectrum, where the LiTFSI and $LiSO_2CF_3$ emissions increase in intensity and the Li_2SO_3 does not. However, a fourth emission towards lower binding energies of E_B = 163.6 eV is observed and attributed to poly sulfides Li_xS_y [139]. Thus, it becomes clear that the chemical nature of the polymer electrolyte is mainly affected at the interface directly.

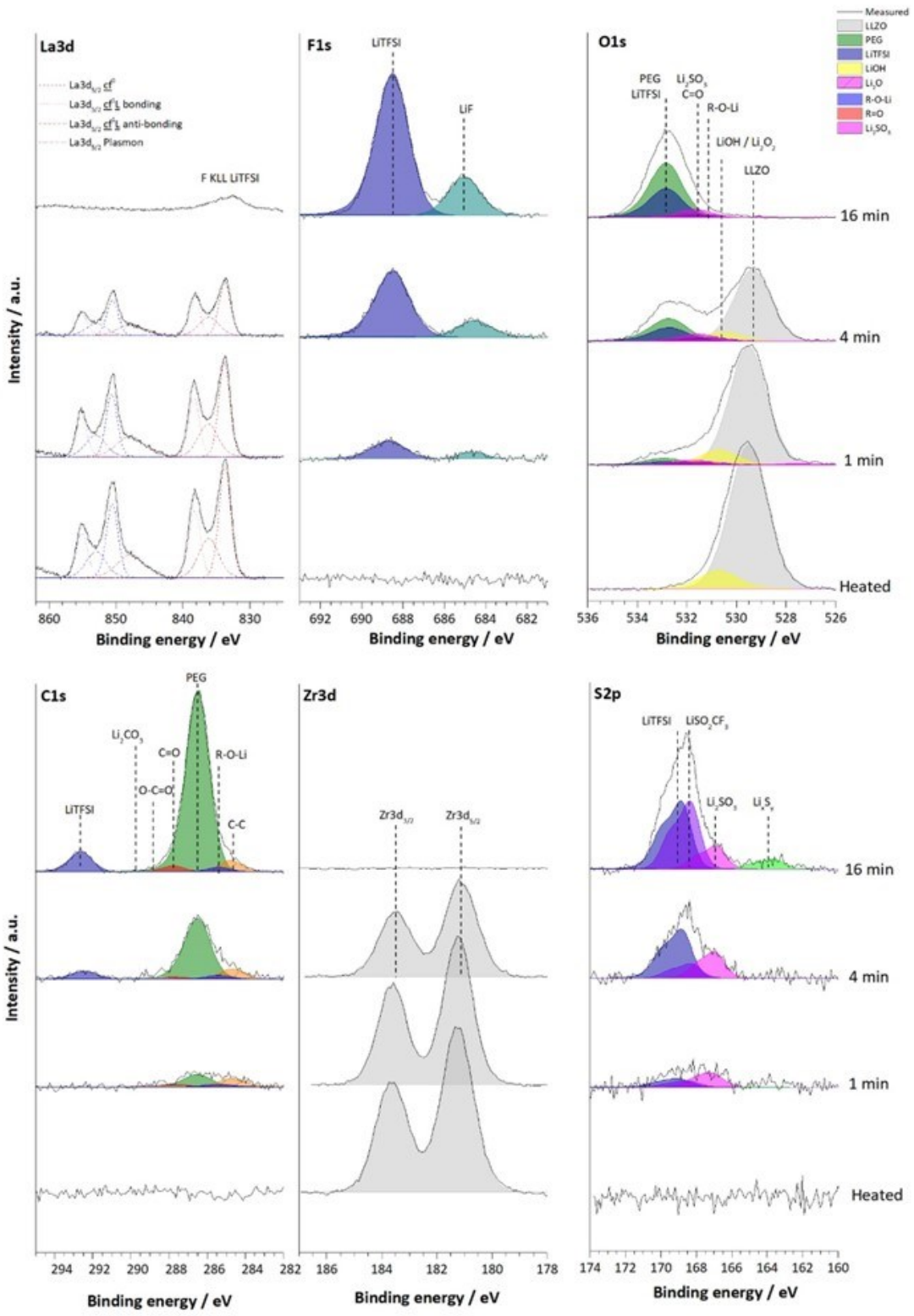

Figure 3.20: XP spectra of La3d, F1s, O1s, N1s, C1s, Zr3d, S2p and Li1s of the interface between LLZTO and PEG LiTFSI. All spectra a referenced to the C1s of the PEG with a binding energy of E_B = 286.5 eV and the Zr3d of the "as-is" and "heated" spectra are referenced to the Zr3d after 1 min of deposition.

To further elucidate the role of this chemical changes at the garnet/PEO interface on interfacial resistance between the ceramic filler and PEO interface, impedance measurements were carried out on the heterostructures comprising of garnet pellet and PEO layers. It has been shown in several reports so far that the interfacial transport is responsible for the increased

conductivity. However, this mainly has been linked to the enhanced Li ion dynamics parallel/along the garnet/PEO interface [76, 97]. Although conductivity enhancements have been observed for composite electrolytes, they have been seen in composites with smaller weight fractions of the ceramic fillers i.e. 5-10 wt-% [76, 97]. The question has not been addressed in the ceramic rich systems. This question is important since for ceramic-rich systems, the lithium ion transport can take place i) via the polymer [100] ii) the garnet network [75, 100], iii) along the garnet/PEO interface [76, 97] and iv) through the garnet/PEO interface, i.e., perpendicular to the interface. Since the conductivity of the ceramic-rich systems is significantly lower than the polymer rich systems as discussed in the section 3.1.3.3, the idea here is to understand the transport of lithium ions perpendicular to the garnet/PEO interface, i.e. from ceramic system to PEO or vice versa. The XPS studies show that the garnet/PEO+LiTFSI interface is not stable, resulting in the formation of side products, which can therefore result in increased resistances. Therefore, in order to understand Li ion transport perpendicular to the garnet/PEO interface, a strategy was developed wherein a heterostructure comprising of PEO/garnet/PEO was studied. For a meaningful comparison with the thin film studies, pellets with the same composition were used.

Initially, impedance measurements were carried out on the sintered garnet pellet (see Figure 3.35 in supplementary information given in section 3.3). This was done in order to obtain maximum possible conductivity and rule out the grain boundary contribution. For sintered garnets, the room temperature conductivity was calculated to be 3.59 x 10^{-4} S cm^{-1} at 298 K. Since the conductivity of the garnet pellet was high at room temperature, low temperature measurements were carried out to determine the contributions towards the ionic conductivity. As shown in Figure S10, only a single semicircle could be seen whose capacitance was found to be in the order of 10^{-12} F, implying the domination of lithium ion transport via the grains [34, 101]. This can be explained by the high temperatures used for sintering, which would increase the grain sizes and lower the concentration of grain boundaries. Further, from the slope of the Arrhenius plot the activation energy of 0.32(1) eV was calculated which agrees well with the literature reports [10].

The investigation of the dense ceramic was followed by adding a layer of cryomilled PEO+LiTFSI on one side of the sintered garnet pellet (Figure 3.21a), followed by measuring impedance spectra in the temperature range of 298 K and 328 K. This temperature range was chosen since PEO+LiTFSI mixtures offer room temperature conductivity in the order of 10^{-6} S cm^{-1} and sintered garnets would in comparison have lower contribution towards the resistance. Therefore, it could be possible to observe the interfacial resistance between the garnet/PEO reliably within the device measurement limits. As can be seen from the Figure 3.21b, the Nyquist and Bode plots clearly signify more than one Li ion transport process. In the high frequency range, a small semi-circle can be seen followed by a larger semicircle in the intermediate frequency range and the low frequency blocking effect tail. Therefore, in agreement with the observed semicircles, two R-CPE elements connected in series were used to fit the two semicircles and a CPE element was used to mimic the low frequency tail. Firstly, it is clear that in comparison to the sintered garnet pellet, the conductivity of this layered structure is significantly reduced. The overall conductivity was found to be 8.54 x10^{-7} S cm^{-1} at 298 K, which is three orders of magnitude lower than the pure garnet pellet and an order of magnitude lower than the pure PEO+LiTFSI electrolyte. Therefore, this lowering of the conductivity in such a layered arrangement has most likely originated from the interface as well as the lower conductivity of the PEO. Since the measurement was carried out in the through plane geometry, wherein the Li ion would have to cross the garnet/PEO interface, this would

imply that transport of Li ions through this interface is not favorable compared to the transport along the interface. This can also be seen from the capacitance values obtained from the fitting of the two semi-circles. For the first semicircle, the capacitance value of 10^{-11} F was determined which is an order of magnitude higher than the capacitance values observed for the Li ion transport within the bulk polymer [101]: This increased capacitance suggests the contribution from both the bulk polymer and interface layer, which is formed at the garnet/PEO interface as suggested from the XPS studies. For the second semi-circle a capacitance value of 10^{-9} F was calculated, which has been attributed to the surface layers or grain boundaries in the literature [101]. However, in case of this layered structure this can be thought of as a diffuse layer, wherein the Li ions build up a pseudocapacitor at the garnet/PEO interface and can diffuse through the interface, therefore not building up a stern charge layer, and thus leading to a lower value for interfacial capacitance [101] than the one expected for a proper interface with no charge transfer. From the Arrhenius plot shown in Figure 3.21f, an activation energy of 0.83(1) eV was found.

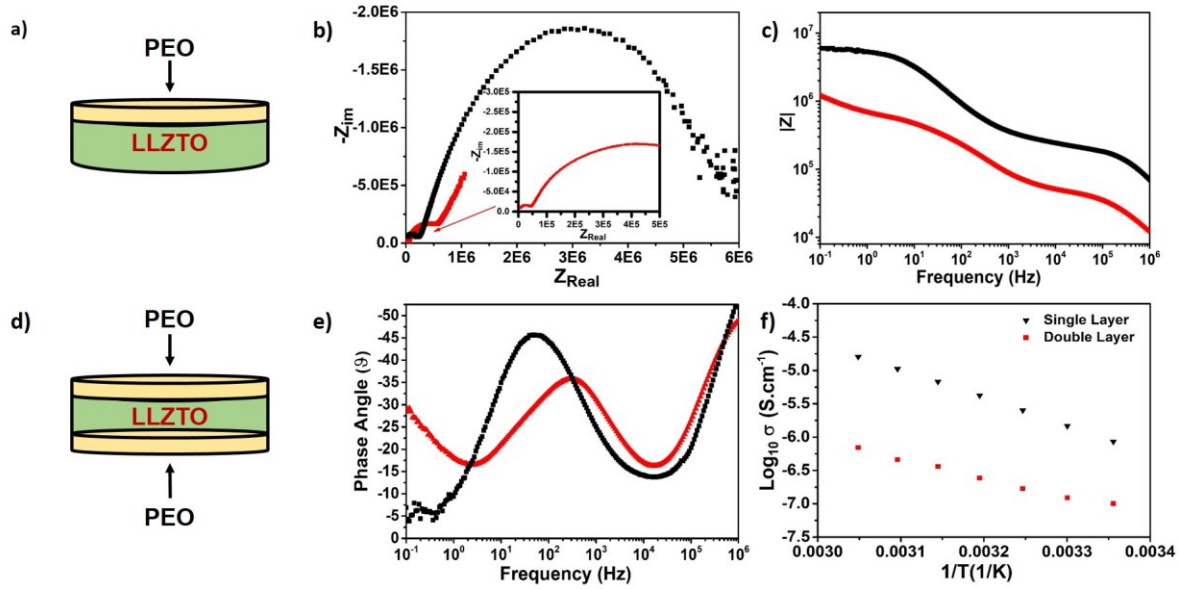

Figure 3.21: Comparison of Impedance spectra for the coated sintered LLZTO garnet pellet measured at 298 K. a) & d) showing the schematics of the Garnet/PEO heterostructure with corresponding b) Nyquist plot and c & e) showing the respective Bode plots. f) Temperature dependent Arrhenius plot measured in the temperatures range of 298 K and 328 K.

Impedance measurements were also carried out on a sandwiched structure, i.e. PEO/garnet/PEO (Figure 3.21d), wherein another layer of PEO+LiTFSI was coated on the other side of the sintered garnet. As discussed previously the contribution to the overall resistance from the sintered garnet is not significant within the temperature range of the measurement and the major contributions are from the PEO itself and from the interface between the garnet and PEO. Similar to the single layered structure, two semicircles are visible in the NYQUIST plots, therefore, representing two different transport mechanisms. However, the resistance of the system is found to increase. As already shown from the XPS studies, the garnet/PEO interface is chemically not stable, leading to the formation of side products, which can contribute towards the resistance in the sandwiched structure. This can be seen from the NYQUIST plot for this sandwiched structure shown in Figure 3.21a, wherein both the high frequency semicircle, the semicircle in the intermediate and in the low frequency range are found to increase with respect to their intercepts on the x-axis, indicating increased resistances. In case of the sandwiched structure, there would be the presence of two interfaces between garnet and PEO, which should therefore be the main cause of this increased resistance. The

conductivity of this system was found to be 1.01 x 10^{-7} S cm^{-1} at 298 K, which is significantly reduced compared to the single layered structure.

The results discussed here are not only important to understand the lithium ion transport pathways within the CEs, but also throw light on the interface between the garnet and PEO. Drawing all the experiments together, we conclude that ion conducting polymers can serve as Li ion transport promoter between garnet particles, which are not in direct contact with each other, in garnet-rich composites. This is in contrast to polymer-rich systems, for which the contribution of the ceramic admixtures is low, and where the ceramic admixtures mainly serve as defect-creating agents to distort the structure of the polymer itself. Our experiments highlight that though a conductivity enhancement can be found along the garnet-PEO interface, chemical interactions at the interface directly due to acid-base related reactions are the likely origin to limit ion transport between the interfaces.

3.1.3.6 Quantitative analysis and reaction layer formation at the garnet-polymer interface

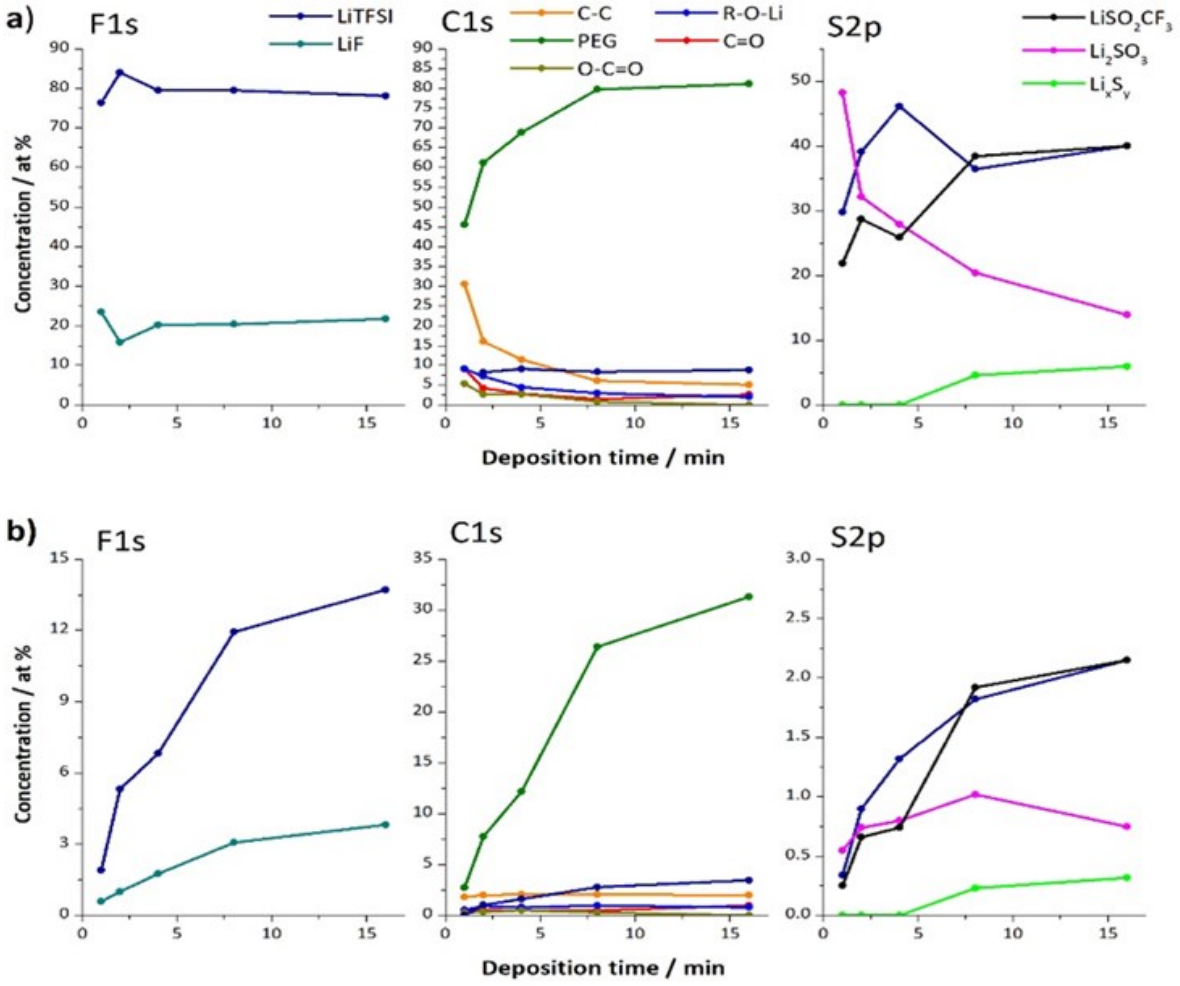

Figure 3.22: a) Relative concentration of the F1s, C1s and S2p core emissions. b) total concentration of the deconvoluted F1s, C1s and S2p core level emissions. The formation of LiF is continuously increasing over time, while Carbon and Sulphur (Li_2SO_3) containing reaction products takes place at the very interface.

The evolution for the concentration of the F1s, C1s and S2p are shown in Figure 3.22 with a) the relative contribution of each compound to the total core emission and in b) the total at % of the compounds measured. At the F1s the ratio between LiTFSI and LiF is around 80:20 for all deposition steps during the interface. With an increasing amount of LiTFSI, the amount of LiF is also increased and it is independent of the layer thickness. Since the measuring spot is only

200 µm in diameter it cannot be assured, that each deposition step is measured at the exact same spot and therefore the formation of LiF seems only be dependent on the X-ray exposure time that is kept constant. The carbon containing reaction products on the other hand only form in the very first deposition steps (1-4 min) and do not increase further. On the other hand, the PEG and LiTFSI Carbon are increasing with deposition time as expected. The Sulphur shows the most reactivity at the interface as well with a relative contribution of the Li_2SO_3 to the S2p of around 50 %. With ongoing deposition, the amount of Li_2SO_3 increases only slightly and decreases after 16 min while the amount of LiTFSI and $LiSO_2CF_3$ increase continuously. Hence, the formation of the Li_2SO_3 seems not to be linked to the X-ray exposure as the LiF. Additionally, after 16 min about 5 % of the S2p show the formation of poly sulfides Li_xS_y.

3.1.4 Conclusion

In summary, CEs with different garnet compositions as filler are fabricated via a solvent free approach. Garnet particles are synthesized via nebulized spray pyrolysis process and are then cryomilled together with a PEO+LiTFSI mixture to fabricate composite electrolyte membranes. For CEs with 10 wt-% of ceramic filler, it is observed that the size and morphology of the particles plays a crucial role in enhancing the conductivity of the CEs compared to that of filler free membranes. Electrochemical impedance spectroscopy showed that additional Li+ ion diffusion pathways along the filler/PEO interface become accessible, which explains the higher ionic conductivity in CEs with lithium ion inactive SiO2 filler due to smaller particle sizes compared to Li ion active garnet containing CEs. Above the percolation limit, additional lithium ion transport pathways via the filler become accessible, and only then the high intrinsic lithium ion conductivity of the filler plays a crucial role for the overall conductivity, e.g., for CE containing 90 wt-% of Li ion active cubic LLZO, the conductivity is 3 orders of magnitude higher than the composite containing non Li-ion conducting Y-doped $BaZrO_3$. From the comparison of the electrochemical performance of the ceramic-rich composite electrolyte to a non-sintered (only compacted) pellet made of garnet particles and in relation to the interface studies performed, it is possible to conclude that

1) non-sintered garnet to garnet interfaces have a strong impact for the conductivity in ceramic-rich composites and limit the intergranular transport at least partially.

2) in ceramic rich systems, the polymer helps to facilitate transfer between garnet particles.

3) the transport via the polymer-garnet interface has a high interface resistance. This increased resistance originates from the formation of decomposition products, which originate from an acid-base type reaction of basic garnet particles with the PEO + LiTFSI, confirmed by additional chemical species which are observed in the XP spectra directly at the interface to the garnet material, but do not appear within the polymer electrolyte itself.

Garnet-rich composites cannot be sintered in order to increase the amount of well-contacted garnet interfaces between particles. Thus, we have shown that the garnet-PEO interface has a high resistivity by using XPS and EIS on model films and coated well-sintered garnet pellets. These studies highlight the peculiar role of the formation of side products at the interface, which contribute towards the interfacial resistances.

Though garnet-rich composites might combine advantages of high conductivity of the ceramic with mechanical advantages of the polymer, the achievement of high conductivities is inhibited for particulate garnet systems. Thus, this article emphasizes that there is a need of alternative

strategies to prepare composite electrolytes in order to improve their ionic conductivities for their application is all solid state lithium ion batteries.

Acknowledgements

A. I. Waidha, T. Ferber, M. Donzelli, R. Hausbrand, W. Jaegermann and O. Clemens acknowledge funding within CL551/3-1 and HA6128/3-1 by the German Research Foundation (DFG).

3.2 PEO Infiltration of Porous Garnet-Type Lithium-Conducting Solid Electrolyte Thin Films

Aamir Iqbal Waidha, [a,b] Vanita Vanita, [a,b] Oliver Clemens, [a,b*]

[a] Materials Synthesis Group, Institute of Material Science, University of Stuttgart, Heisenbergstraße 3, 70569 Stuttgart, Germany

[b] Technische Universität Darmstadt, Institut für Materialwissenschaft, Fachgebiet Materialdesign durch Synthese, Alarich-Weiss-Straße 2, 64287 Darmstadt, Germany.

[*] Corresponding Author: oliver.clemens@imw.uni-stuttgart.de

Abstract

Composite electrolytes containing lithium ion conducting polymer matrix and ceramic filler are promising solid state electrolytes for all solid state lithium ion batteries due to their wide electrochemical stability window, high lithium ion conductivity and low electrode/electrolyte interfacial resistance. In this study, we report on the polymer infiltration of porous thin films of aluminum-doped cubic garnet fabricated via a combination of nebulized spray pyrolysis and spin coating with subsequent post annealing at 1173 K. This method offers a simple and easy route for the fabrication of 3-dimensional porous garnet network with the thickness in the range of 50 to 100 μm, which could be used as the ceramic backbone providing a continuous pathway for lithium ion transport in composite electrolytes. Porous microstructure of the fabricated thin films is confirmed via scanning electron microscopy. Ionic conductivity of the pristine films is determined via electrochemical impedance spectroscopy. We show that annealing times have a significant impact on the ionic conductivity of the films. The subsequent polymer infiltration of the porous garnet films shows the maximum ionic conductivity of 5.3×10^{-7} S cm^{-1} at 298 K, which is 6 orders of magnitude higher than the pristine porous garnet film.

Keywords: Lithium ion batteries, Garnet, Thin films, Composite electrolyte.

3.2.1 Introduction

All solid-state Li-ion batteries (ASSLBs) with metallic lithium (Li) as the negative electrode are potential alternatives to conventional Li-ion batteries, which contain carbon-based anodes and liquid electrolytes [20, 157, 158]. The use of metallic Li as an anode gives rise to high energy density of the Li-ion battery since it offers an order of magnitude higher capacity as compared to the conventional carbon based anodes currently being employed (3860 mAh g^{-1} vs 372 mAh g^{-1}) [8, 9] at a lower anode potential. On the other hand, the use of solid electrolytes can subside the long-standing safety issues of hydrocarbon-containing liquid electrolytes employed in batteries with liquid electrolytes, i.e. flammability, leakage, dendrite growth, etc. [10, 20], and provide an alternative to room-temperature ionic liquids (RTIL) [159], which can be expensive for their fabrication.

Both inorganic and polymer-based solid electrolytes (PSEs) have gathered widespread interest over the years for their application in ASSLBs [8, 10, 25, 160]. PSEs comprise of a polymer matrix, which dissolves Li salts. A variety of PSEs, like polyvinylidene fluoride (PVDF), polyacrylonitrile (PAN), poly(ethyl carbonate) (PEC), poly(methyl methacrylate) (PMMA) and polyethylene oxide (PEO) have been of interest [22]. Amongst them, PEO is considered a promising host due to its commercial availability, low cost and non-toxicity. PEO is a polyether with the chain composed of $(CH_2\text{-}CH_2\text{-}O)_n$ structural units. PEO is particularly interesting due to its excellent lithium-salt solubility, superior flexibility and adhesivity, which can be beneficial for reducing interfacial resistance [24, 25] by forming an even contact with the metallic Li anode and can also adapt to the volume changes of the active electrode materials during battery cycling. However, it lacks mechanical strength, which makes it susceptible to dendrite growth in combination with metallic Li anodes [24, 25, 161, 162]. Further, PEO-based electrolytes show low Li-ion conductivity (10^{-7} – 10^{-6} S cm^{-1}) [22], low Li-ion transference number (i.e., 0.22 for PEO:LiTFSI), instability against metallic lithium anodes and a comparably small electrochemical stability window (4.25 V vs. Li^+/Li) [23, 24]. The low Li-ion conductivity in PEO has been known to be as a result of coexistence of crystalline and amorphous phases. It is widely believed that amorphous PEO offers higher Li-ion conductivity compared to that of crystalline PEO [163]. Although, alternative approaches to improve polymer conductivity by using different conductive salts have been explored, e.g. via the use of room-temperature ionic liquids (RTILs), these are expensive compared to conventionally used Li-containing salts [159]. Therefore, other methods for reducing PEO crystallinity for conductivity enhancement are of interest.

On the other hand, inorganic solid electrolytes based on oxides have been within the focus of latest research [8, 10, 19, 164-167]. Oxide-based garnets ($Li_7La_3Zr_3O_{12}$ (LLZO)) have been considered due to their high intrinsic lithium-ion conductivity (1.3 x 10^{-3} S cm^{-1})[10], their wide electrochemical stability window (>6 V vs Li/Li^+)[52] and their compatibility with the Li metal anode [10, 168-170]. However, due to their high brittleness, achieving good contact with metallic Li is often a challenge, which results in increased interfacial resistances at the Li/LLZO interface and uneven stripping/plating of lithium, which can result in the dendrite formation at high current densities [10, 19, 20]. Further, they are also known to be highly sensitive towards moisture and CO_2, which can result in the formation Li_2CO_3 via an intermediate LiOH phase on the particle surface [107, 171].

In order to overcome the drawbacks of both organic and inorganic electrolytes, an alternative strategy of mixing the two into composite electrolytes (CEs) might result in harnessing the advantages of both the systems, while limiting the disadvantages. Such CEs have already been investigated over the last years [73, 75, 172-176]. CEs comprise of polymer matrix and dispersed ceramic filler [71, 74] and offer higher Li-ion conductivity (6.24 x 10^{-5} S cm^{-1} at 298 K)[68], higher

mechanical strength, enhanced electrochemical window (5 V vs Li/Li^+)[74] and higher Li-ion transference number (0.46)[23] than the pure polymers [63, 177]. Compared to the pure ceramic-based electrolytes, CEs offer higher flexibility and softness, thus forming a smooth and even contact with the Li metal at the Li/CE interface [68], which can result in even Li stripping/plating, thus preventing lithium dendrite formation [23]. So far the research has been focused on the polymer rich composites, wherein the dispersion of the low weight percentages of ceramic filler has been known to increase the conductivity and Li-ion transference number [23]. However, the room temperature conductivities of such CEs are still ~2 orders of magnitude lower for their application in a room temperature [10] ASSLB. Since the sintered ceramic LLZO is known to offer high conductivities (~10^{-3} S cm^{-1}) [10], an alternative strategy therefore could be the use of ceramic-rich CEs. However, such high conductivities are not observed in the CEs containing high weight percentages of ceramic filler dispersion, due to high grain boundary impedances towards Li-ion transport. To mitigate the high grain boundary impedances due to ceramic filler dispersion, an alternative strategy of forming a continuous and sintered porous 3-dimensional garnet network followed by its infiltration with the Li-ion conducting polymer can prove to be advantageous in terms of conductivity enhancements in these CEs for their application in ASSBLs. A porous sintered network would in principle lower the ceramic/ceramic boundary resistances and promote Li-ion conductivity within the garnet framework as opposed to the ceramic dispersion in the ceramic-rich CEs, thus enhancing the overall ionic conductivity. Recently, the group of Wachsman has shown that porous electrolyte architectures can be realized in principle and are scalable for their application in solid state batteries[178]. The fabrication method used by them results in thin films with large particle sizes and low porosity, which would result in small garnet/PEO interfacial contact area. The ceramic/polymer interface is considered to be crucial for conductivity enhancement in CEs [74, 76]. Overall, the fabrication of such networks has not been investigated in strong details, and different fabrication techniques and microstructures can provide different functional properties.

In this article, we report for the first time the synthesis and polymer infiltration of porous garnet thin films prepared by the combination of nebulized spry pyrolysis (NSP) and spin coating. Initially garnet powders were synthesized via NSP route, followed by spin coating. NSP offers the advantage of reduced sintering times and temperatures in order to obtain the desired garnet phase with a highly porous microstructure, which significantly lowers the ceramic density (47-55%) compared to that of theoretical density [56], a precondition to synthesize porous ceramic materials. Phase analysis is carried out by Rietveld analysis of the X-ray powder diffraction (XRD) data. The porous garnet thin films are then infiltrated by PEO+LiTFSI solution via drop technique. Scanning electron microscopy (SEM) is used to get an understanding about the microstructure and success of infiltration. The conductivity measurements of the mere garnet film and the infiltrated garnet films are carried out using electrochemical impedance spectroscopy (EIS). The results show that polymer infiltration leads to increased ionic conductivity in the infiltrated garnet thin films along with the additional lithium ion transport pathways in the infiltrated films.

3.2.2 Materials and methods

3.2.2.1 Material synthesis

For the synthesis of nano to microcrystalline powders of $Li_{6.49}Al_{0.17}La_3Zr_2O_{12}$, NSP method was used. Three step process was used for the preparation of water based solution: i) first, the Zr precursor ($Zr(C_5H_7O_2)_4$, ABCR, 98%) was dissolved in a small volume of methanol; ii) the Li, La, Al nitrate based salts were then added to this methanolic solution ($LiNO_3$, Sigma Aldrich, 99.99%, $La(NO_3)_3$ $6H_2O$, Alfa Aesar, 99.9%, $Al(NO_3)_3{\cdot}9H_2O$, Merck, 98.5%); iii) finally,

deionized water was added to this solution in order to maintain overall desired concentration of 0.1 mol l^{-1}. A water to methanol volume ratio of 20:1 was used. The obtained solution was then subjected to magnetic stirring for 1 hour in order to produce a homogenous transparent solution. In order to compensate the Li loss in the subsequent high temperature sintering processes, 50 % excess of Li precursor was used. This precursor solution was then injected at a constant flow rate of 100 ml h^{-1} into a glass chamber using a syringe pump (TSI), where the nebulization took place using an ultrasonic generator (Dr. Hielscher UM20-1.6 MHz). The mist of the precursor solution was then transferred into a hot-wall reactor using a constant flow of oxygen (3 SLM (standard litre per minute), flow rate controlled by a MKS mass flow controller, MFC). The whole process was carried at a constant pressure of 900 mbar maintained using a Baraton absolute pressure gauge and a butterfly valve connected to a backing pump. The powders were synthesized at a temperature of 1173 K and collected by using a filter-based collector, which was maintained at 393 K to prevent water vapor condensation (referred to as "as-synthesized" in the following). As-synthesized powders were subsequently sintered at 1173 K for 3 hours in ambient air. A constant heating rate of 6 K min^{-1} and a cooling rate of 6 K min^{-1} were used (referred to as "sintered" in the following). This experimental procedure followed has already been reported by us in several other reports [34, 35, 175], and could be well reproduced here.

3.2.2.2 Garnet thin film fabrication

To obtain the garnet thin films, as-synthesized NSP powders were utilized in order to obtain the porous garnet films. As-synthesized NSP powders were weighed (0.100 mg) and stirred in 400 µl of TBE (1,1,2,2-tetrabromoethane) for 30 min; this high density solvent is necessary in order to obtain a dispersion, which is stable for subsequent treatment. The solution was then spin coated on to the copper substrate using a three step spinning program based on the following rotating steps: 425 rpm for 1 min, 325 rpm for 0.6 min and 225 rpm for 2 min. The as-obtained films were then sintered at 1073 K for 60 min at the heating and cooling rate of 3 K/min in the tube furnace under the flow of argon. The films were then transferred to an Ar-filled glove box for the subsequent steps and to limit the exposure to the ambient atmosphere. This is important since garnets are known to be susceptible towards moisture, which can result in the formation of Li_2CO_3 on the garnet surface [21] and contribute towards the interfacial impedances at the garnet/PEO interface.

3.2.2.3 PEO infiltration

For the infiltration of the porous garnet thin films, PEO+LiTFSI (bis(trifluoromethane)sulfonimide) containing solutions was used. The solution was prepared by first dissolving 0.1 g of LiTFSI in 5 ml of acetonitrile. After stirring for 15 min, 0.2 g of PEO were added to the solution and stirred until PEO was completely dissolved into the solution. The solution was then poured drop-wise onto the garnet thin film using a micropipette. The dropwise pouring was repeated several times (20-30 times) and the films were dried in the vacuum furnace for 12 h at 323 K before carrying out impedance measurements. We emphasize here that the amount of PEO+LiTFSI used within the solution is of high importance. Increasing the PEO amount in the solution was found to result in a solution with higher viscosity, which resulted in PEO depositing on the surface of the garnet film. The infiltration procedure was found to reproducible for the thin films reported here.

3.2.2.4 Diffraction experiments

Room temperature XRD patterns of the various samples were recorded on a Bruker D8 diffractometer using Bragg-Brentano geometry with a fine focusing X-ray tube with Cu $K_{\alpha 1,2}$

radiations. A VANTEC detector (3° opening) and a fixed divergence slit (0.3°) were used. The total scan time was set to 1 h for the angular range between 10° and 80° 2θ at a step size of 0.0066°. The Rietveld method was used to carry out the structural refinement and phase analysis of the XRD patterns using the TOPAS 5 program (Bruker AXS, Germany) [95]. Using a reference scan of LaB6 (NIST 660a), the instrumental intensity distribution was calculated empirically within a fundamental parameter approach [108], and the micro-structural parameters were adjusted to adjust the peak morphologies for the XRD data. To account for absorption adjustments, an overall isotropic value was refined, which was constrained to be identical for all atoms in all phases.

3.2.2.5 Impedance spectroscopical analysis

Alternating current (AC) electrochemical impedance spectroscopy was carried out to characterize the conductivity of the pure and the infiltrated garnet films. The films were sputtered with a thin layer of gold on the top for electronic contacting, whereas the Cu substrates serve as the bottom contact. The measurements were carried out within a through-plane geometry. Films were then placed inside a JANIS STVP-200-XG cryostat, which was operated under a static helium atmosphere of 1 bar pressure. LLZO films were investigated in the temperature range of 298 K to 473 K, whereas the infiltrated films were investigated in the temperature range of 298 K to 328 K due to the higher conductivity. Impedance measurements were recorded using a Solartron 1260 frequency response analyzer, applying an AC signal of 100 mV amplitude with the frequency ranging from 1 MHz to 100 mHz. Fitting of the data was performed using the Z-view program [109].

The authors would like to emphasize that attempts to prepare and characterize pure and infiltrated films have been performed on at least three films independently. Film compositions are highly reproducible with insignificant (below 1-2 %) changes of phase compositions. Though some fluctuations of film thickness in the order of ~ 10 – 30 % and also smaller fluctuations in conductivity can occur (i. e., comparing different infiltrated films, e. g. in the range of $10^{-6.0}$ – $10^{-6.2}$ S cm^{-1}, see Figure 3.36 in supplementary information given in section 3.3), the principle phenomenon of increased conductivity of the film after infiltration by several orders of magnitudes with the corresponding phenomenological behavior of the semicircles observed in the impedance spectra can be well reproduced between different samples.

3.2.3 Results and discussion

3.2.3.1 X-ray diffraction

Lithium stuffed garnets can crystallize in tetragonal ($I4_1/acd$) or cubic ($Ia\text{-}3d$) space groups depending on the Li-ion distribution within the lattice and the doping chosen [10]. The tetragonal polymorph is thermodynamically stable in the low temperature regime, whereas the cubic polymorph is stable at higher temperatures (above 673 K, depending on the impurity level) [10]. Cubic garnets are of greater interest than their tetragonal counterparts since they are known to offer two orders of magnitude higher Li-ion conductivity. They can be stabilized via aliovalent doping (i.e., with Al^{3+}) leading to the disordered distribution of Li-ions, thus making the material a fast Li-ion conductor [10]. Therefore, within this study cubic garnets were used to prepare a 3D garnet framework backbone for the composite electrolyte thin films.

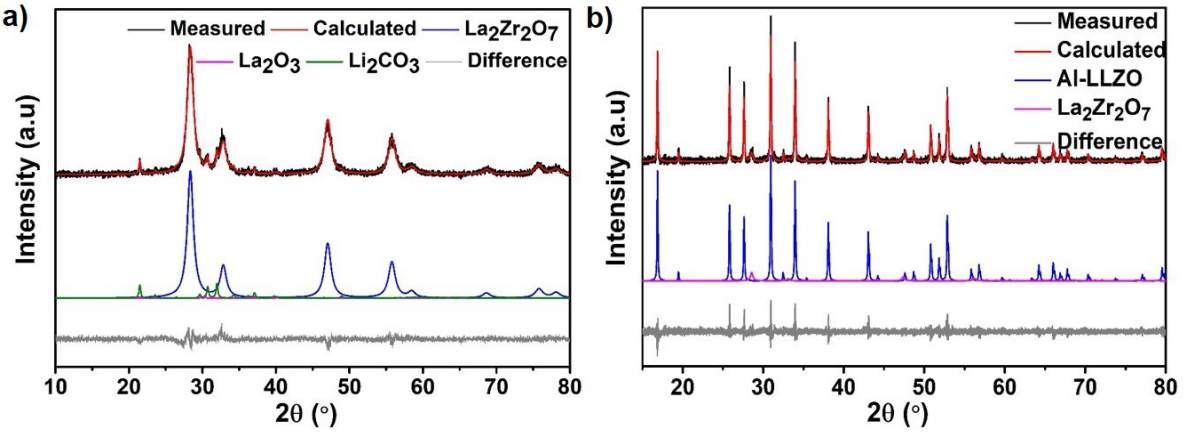

Figure 3.23: a) Rietveld fit of the as-synthesized powders obtained from the NSP. b) Rietveld fit of the X-ray diffraction pattern of Al-doped cubic garnet powders after heat treatment.

Figure 3.23a shows the room temperature X-ray diffraction patterns of the as-synthesized NSP powders of cubic Al-doped garnet powders. Rietveld fit (Figure 3.23a) of the powder X-ray diffractogram of as-synthesized NSP powders showed that the powders are mainly composed of fluorite type $La_2Zr_2O_7$ and Li_2CO_3, which is typical to NSP synthesized powders with this composition [34, 35]. The lattice parameters of $La_2Zr_2O_7$ and Li_2CO_3 are found to be in good agreement with the previously reported values [34, 35]. In order to obtain the desired garnet phase, an additional heating step is typically required. Figure 3.23b shows the Rietveld fit of X-ray diffraction patterns of the Al-doped cubic garnet powders. The formation of cubic garnet was observed, which is consistent with the successful incorporation of Al into garnet powders [34]. The lattice parameter of 12.9712(6) Å was calculated; from a comparison to a previous composition dependent studies [34, 35] of the lattice parameter using the same synthesis method, the targeted composition of $Li_{6.49}Al_{0.17}La_3Zr_2O_{12}$ could be well deduced. Additionally, approximately 8 wt-% of pyrochlore type $La_2Zr_2O_7$ was also observed, which is a common impurity phase present in garnet powders due to Li loss [35].

For the fabrication of porous garnet thin films via spin coating, as-synthesized NSP powders were utilized instead of the sintered powders in order to maintain the porous garnet microstructure and limit the additional sintering step which can result in Li loss and promote the formation of non-conducting pyrochlore phase ($La_2Zr_2O_7$) [34]. Spin coating has previously only been used for the fabrication of the dense garnet thin films [179, 180]. Figure 3.24a shows the room temperature X-ray diffractograms of the Al-doped garnet films obtained after heat treatment at 1173 K for different times. Figure 3.24b shows the Rietveld fit of the Al-doped cubic garnet film sintered at 1173 K for 180 min. Other than the presence of cubic garnet phase,

an additional impurity phase of $Li_{0.5}Al_{0.5}La_2O_4$ (up to ~ 7.7 wt-%) can also be observed. Increasing the heating time to 240 min leads to the formation of additional impurity phases (see Figure 3.37 in supplementary information given in section 3.3), therefore for further studies 180 min of annealing time was considered to be the optimum.

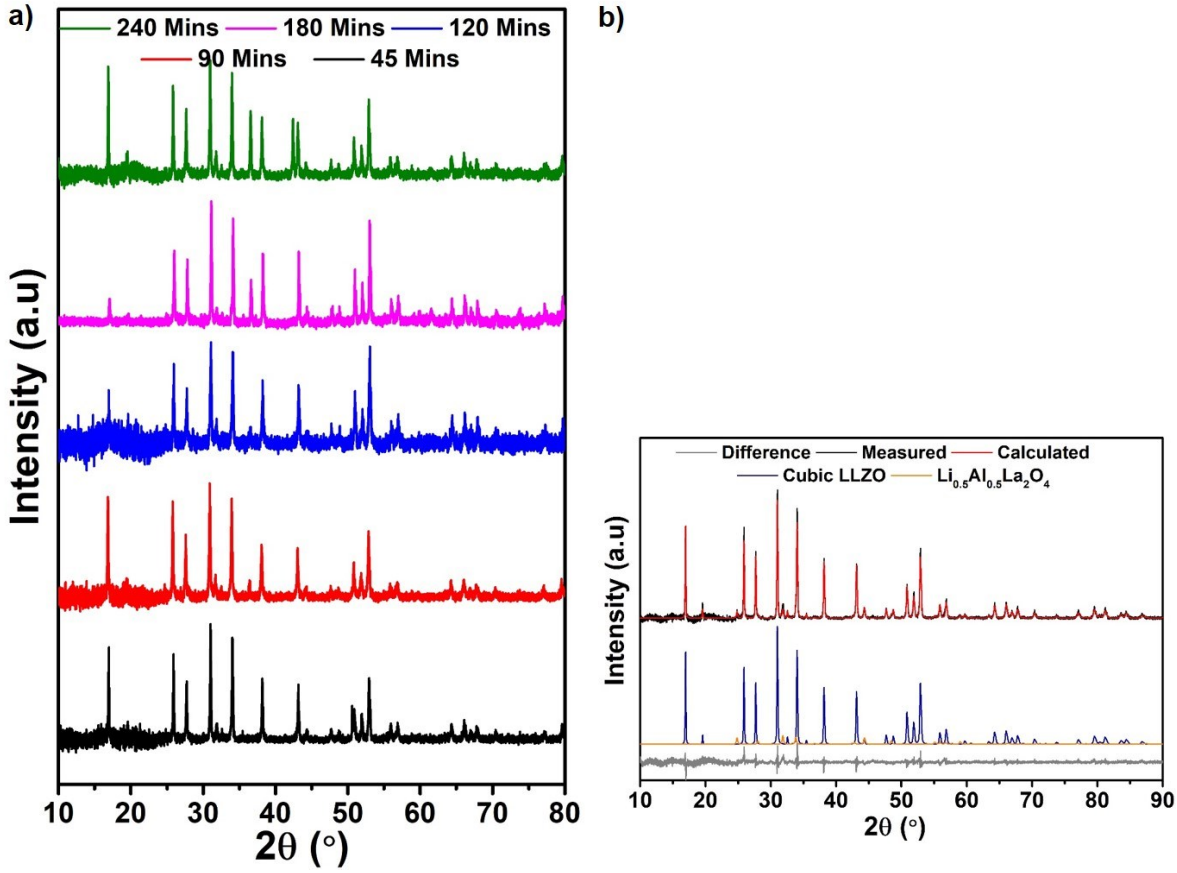

Figure 3.24: a) X-ray diffraction patterns recorded for Al-doped garnet sintered at 1173 K for different durations. b) Rietveld fit for the Al-doped LLZO annealed for 180 min at 1173 K. The increased noise at low angles originates from subtraction of the background from the air tight sample holder.

3.2.3.2 Microstructure

For the microstructural analysis, SEM micrographs were recorded and are shown in Figure 3.25. Figure 3.25a and b show the SEM micrograph of the as synthesized and heat-treated garnet powders, respectively. The as-synthesized powders mainly show hollow spherical morphology with broad particle size distribution, which is typical for the powders synthesized via the NSP route [34]. As discussed previously, the as-synthesized powders mainly contain $La_2Zr_2O_7$ and Li_2CO_3 as the main phases, therefore requiring an additional heating step to obtain the garnet phase. In a previous report using the same setup, heating at 1273 K for 1 h was found to be required in order to obtain the desired garnet phase [34]. Within this study, it was found that the synthesis procedure can be further optimized and the sintering is carried out at 1173 K for 3 h, which results in the formation of Al-doped cubic garnet phase. The additional heating step significantly influences the morphology of the powders, which tend to agglomerate via the formation of necks between the particles. However, since the heating temperature and time for the garnet synthesis via the NSP route is significantly reduced compared to that of a solid-state route, the pellets are usually porous with densities between 47 % to 55 % with respect to the crystallographic density [34]. Clearly, this morphology provides also a higher surface area compared to that of powders obtained from a solid state route. This could be

beneficial in CEs as high surface of the filler material has been shown to improve the conductivity of the CEs [65, 97]. Figure 3.25c-f show the top view of the Al-doped LLZO thin films annealed at different temperatures. It is found that the porous microstructure is retained irrespective of annealing times chosen, though they will show to strongly influence the total ionic conductivity of the garnet thin films (see section 3.3). The porous morphology of the garnet backbone is inherent to the NSP synthesized powders sintered at low temperatures and times irrespective of the ceramic composition [34, 181]. This is most likely influenced by the hollow-sphere structure obtained for the as-synthesized material, which facilitates fairly high porosities and thus prohibits strong densification by sintering significantly below the material's melting temperature.

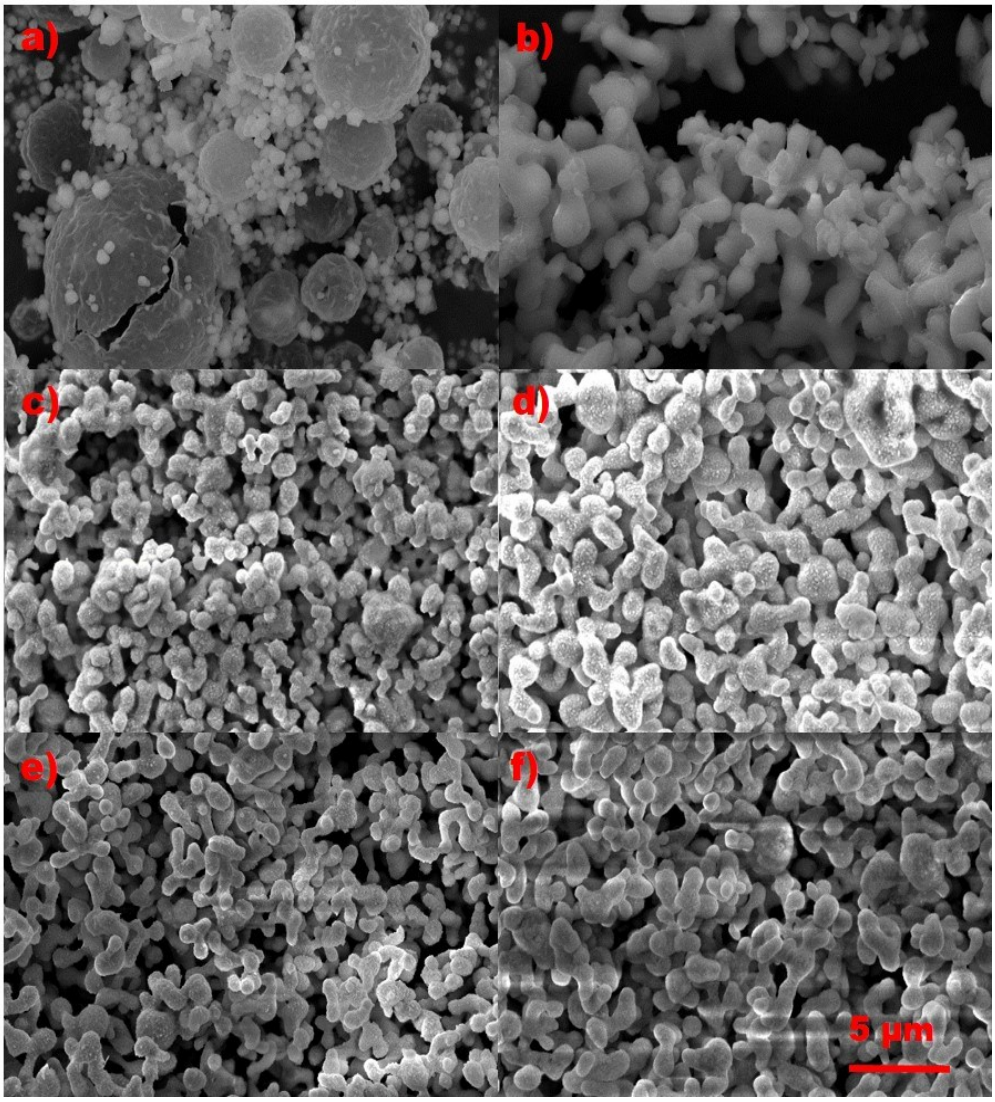

Figure 3.25: a, b) Scanning electron micrograph of as-synthesized and heat treated NSP powders, respectively. c-f) Top view of the Al-doped garnet thin films sintered at 1173 K for 60, 90, 120 and 180 min, respectively.

Initially, attempts were made to infiltrate porous pellets with a thickness of > 1 mm. On this scale, it was found that only a fraction of the pore volume is accessible via an infiltration approach. Therefore, garnet thin films with the thickness ranging from 50 to100 µm were fabricated via spin coating method. Figure 3.25 shows the top view of the heat treated garnet thin film showing the porous garnet network (see Figure 3.38 in supplementary information given in section 3.3 for cross sectional view). This network was then infiltrated with PEO+LiTFSI containing acetonitrile solution. Figure 3.26a, b shows the top and the cross-sectional view of

the infiltrated garnet films, respectively. This results in a significantly improved homogeneity and degree of infiltration as compared to a porous pellet, though a small degree of inhomogeneity can still be observed.

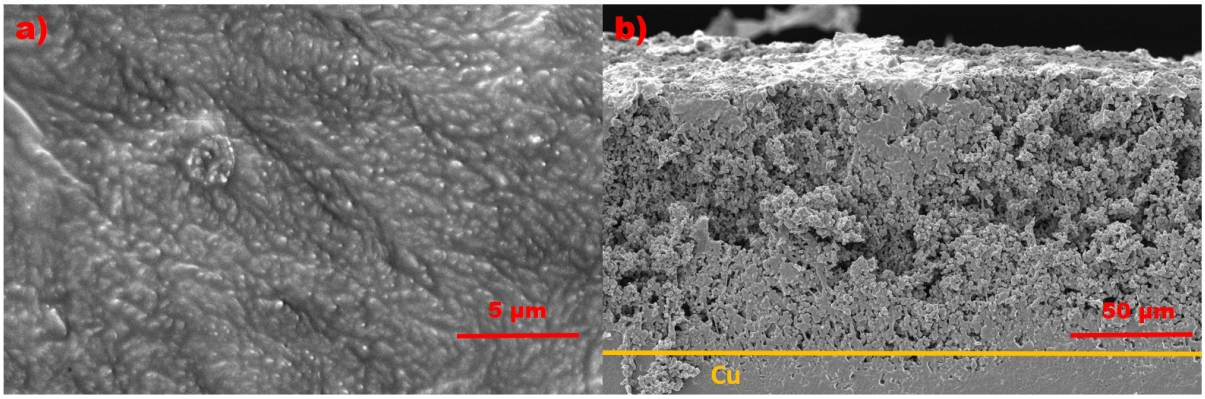

Figure 3.26: a, b) Scanning electron micrograph of top and cross sectional view of the infiltrated garnet thin film. The Cu substrate seen as the dense material in the lower part of Figure 3.26b.

3.2.3.3 Impedance spectroscopy

For garnets, it is well known that the crystal structure, sintering temperatures and times play a crucial role on the obtained total Li-ion conductivity [10, 56, 182]. Cubic garnets are known to offer 2 orders of magnitude higher conductivity than their tetragonal counterparts. Although there is only a small difference between the structural arrangement within the cubic and tetragonal garnet framework of the heavy cations, it has been shown that small amounts of Al doping influences the Li vacancy density in the Li octahedral sites near the dopants, which has been shown to be key to increased conductivity [10]. The fully ordered tetragonal garnet consists of three Li sites (one tetrahedrally coordinated site Li1 (8*a*), two octahedrally coordinated sites Li2 and Li3 (16*f* and 32*g*) with site occupancy factor of 1. For the cubic garnet, three Li sites (one tetrahedral Li1 site (24*d*), one octahedral Li2 site (48*g*/96*h*)) are present. The Al dopant is known to occupy the tetrahedral site and leads to significant disorder in the Li sub-lattice due to the electrostatic effects, which splits the octahedral Li2 site into two 96*h* sites being separated by the 48*g* site. The active vacancy density in this group is known to contribute towards the increased Li-ion conductivity. Further, it has been shown that the density and the microstructure of the garnets synthesized via different synthesis and compaction methods have a pronounced effect on total Li-ion conductivity and activation energy [34, 35, 183-185]. For pellets made of NSP synthesized Al-doped pure cubic garnet, total Li-ion conductivity of 4.4 x 10^{-6} S cm^{-1} with an activation energy of 0.49 eV has been reported [34].

AC impedance spectroscopy was used to determine the conductivity of the non-infiltrated garnet thin films. The Nyquist and the corresponding Bode plots for the Al-doped garnet thin film recorded at 473 K are shown in Figure 3.27. From the Nyquist plot (Figure 3.27a), a strongly depressed semicircle in the high and intermediate frequency range can be seen along with a low frequency tail due to the Li-ion blocking at the gold electrodes, demonstrating that the material under investigation is a Li-ion conductor [34]. The presence of a single semicircle suggests the use of one R-CPE element to fit the impedance data, which can further be confirmed from the Bode plots (Figure 3.27b,c). Here, R is the resistor and CPE is the constant phase element used to mimic the behaviour of an imperfect capacitor. Another CPE connected in series is used to model the capacitive behaviour at low frequencies. The total conductivity of the prepared garnet thin film was determined according to the equation:

$$\sigma = t/RA$$

where *t* is the thickness of the electrolyte, *R* is the resistance obtained from the intercept on X-axis and *A* is the area of the sputtered gold electrode. From the fitting, the total conductivity of 4.08 x 10^{-9} S cm^{-1} is determined at 473 K. Although the room temperature conductivity of the garnet thin films could not be determined from the impedance measurements due to the high impedances at low temperatures, extrapolation of the Arrhenius plot (Figure 3.27d) shows that the room temperature conductivity of the Al-doped cubic garnet thin films is of the order of 10^{-13} S cm^{-1}, which is significantly lower than the other garnet thin films previously reported [186-189]. In comparison to the bulk ceramics made of the NSP powder, the low conductivity of such porous films can be well explained due to the following points: i) reduced sintering temperature (1173 K), ii) reduced sintering duration (180 min), iii) the high porosity and low density of fabricated thin films required to achieve sufficient infiltration. Although high conductivities are desirable, we would like to emphasize that the main focus of this study lies in the formation of a porous network of Li-ion conducting matrix phase, which can be used as the 3-dimensional backbone for composite electrolytes and offer continuous Li-ion migration pathways in composite electrolytes; thus a reduction of the overall conductivity is intrinsic for such porous systems

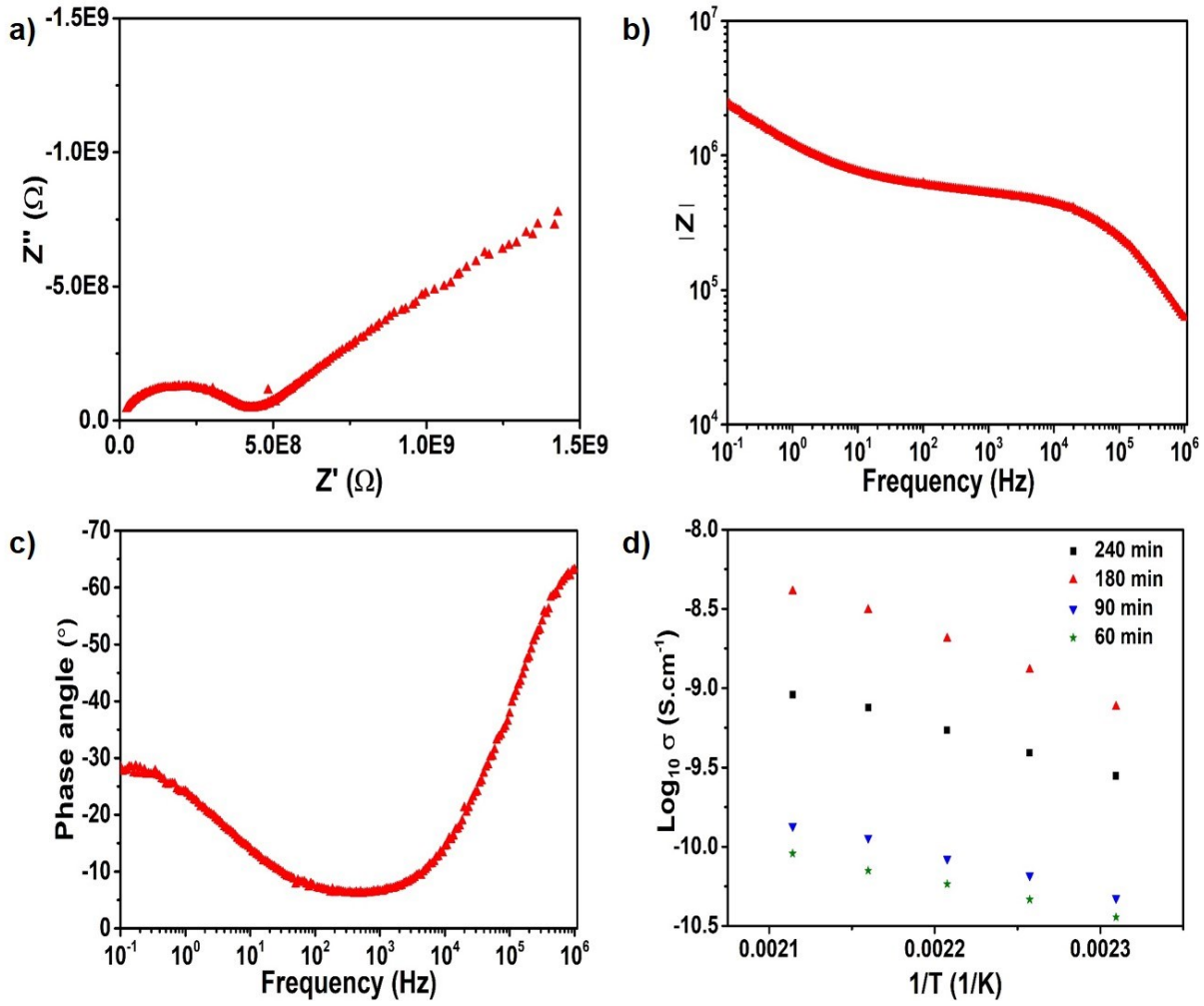

Figure 3.27: a) Complex plane plot for Al-doped LLZO garnet thin film recorded at 473 K. b, c) Respective Bode plots. d) Arrhenius plot for the Al-doped LLZO garnet thin films sintered at 1173 K at different temperatures.

To assign the R-CPE element to grain or grain boundary contribution, capacitance values were calculated from the following equation:

$$C = CPE^{\frac{1}{n}} R^{1-\frac{1}{n}}$$

where C is the capacitance and n is the exponential factor. From the fitting, the single RCP element used to fit the impedance data showed a capacitance of an order of 10^{-12} F, which is an indication of grain dominated Li-ion transport [101].

Figure 3.27d shows the temperature dependent total ionic conductivity of the garnet thin film, which can be expressed in form of an Arrhenius equation given by $\sigma_{tot}(T) = \sigma_o \exp(-E_a/RT)$, where σ_o is the pre-exponential constant, E_a is the activation energy, R is the molar gas constant and T is the absolute temperature. As seen, the conductivity of the Al-doped cubic garnets is highly dependent on the sintering times. As the annealing temperature increases from 60 min to 180 min, the conductivity is found to increase, which can be explained by an increase of grain growth. However, for the sample annealed for 240 min, the conductivity is found to decrease again which can be due to the presence of additional impurity phases in the films, confirmed from diffraction data analysis (see Figure S2). For the film annealed for 180 min, an activation energy of 0.75(1) eV was determined from the slope of the Arrhenius plot, which is higher than the NSP synthesized pellets previously reported (0.49 eV for Al-doped LLZO) [34]. The higher activation energies again originate from lower sintering temperatures compared to that of NSP synthesized pellets.

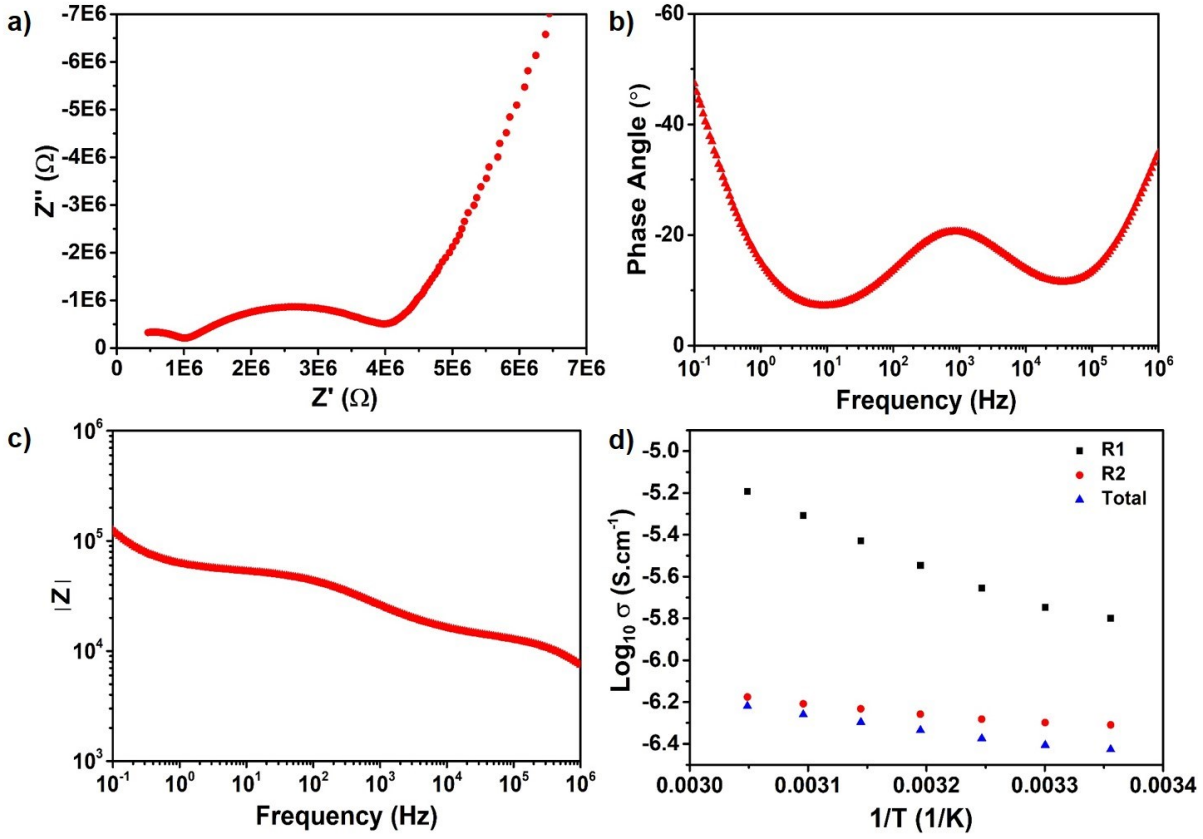

Figure 3.28: Nyquist plot for the infiltrated Al-doped LLZO garnet thin films measured at 298 K. b, c) Bode plots corresponding to the complex plane plot measured at 298 K. d) Arrhenius plot for the infiltrated garnet film measured in the temperature range between 298 K and 328 K (See Figure 3.36).

For a reasonable understanding of the contributions to the overall conductivity, impedance measurements were also carried out on a thin film of PEO-LiTFSI as a reference system (Figure S4 in Supplementary Information), for which the total ionic conductivity of 3.65 x 10^{-5} S

cm^{-1} was determined and the activation energy calculated from the slope of the Arrhenius plot was found to be 0.93(2) eV.

As-prepared porous Al-doped LLZO garnet thin films were infiltrated with the PEO+LiTFSI containing solution, in order to achieve filling of the empty voids with the Li-ion conducting polymer, aiming to introduce additional pathways “garnet – polymer – garnet” and to increase the intrinsic accessible surface area for the transport of Li^+ ions. Figure 3.28 shows the Nyquist and Bode plots of the infiltrated Al-doped LLZO garnet film. Overall conductivities are found to increase by ~6 orders of magnitude as compared to the non-infiltrated films, and impedance measurements could therefore be carried out in a lower temperature range of 298 K and 328 K. As seen from Figure 3.28a, the complex plane plot clearly shows two semicircles, one at high frequencies followed by another one at intermediate frequencies. At low frequencies, the capacitive behaviour due to the Li-ion blocking can be observed. The presence of two semicircles in the Nyquist plot is also complemented by Bode plots, which confirm two different transport processes in the infiltrated films. Therefore, two R-CPE elements connected in series were used to fit the impedance data in the high and mid frequency range, followed by a CPE element to model the low frequency blocking behaviour. The total Li-ion conductivity was calculated from the resistance values obtained from the equivalent circuit used and found to be equal to 5.3×10^{-7} S cm^{-1} at 298 K. The calculated capacitances for the individual R-CPE elements were found to be of the order of 10^{-11} and 10^{-7} F for the first and second R-CPE element, respectively, which are in agreement with the grain and interfacial capacitances [101]. This indicates a strong contribution of Li-ion transport via the garnet network and along the garnet/PEO interface within the incorporated polymer in the infiltrated films.

Figure 3.28d shows the Arrhenius plot for the infiltrated films. The activation energies were determined from the slope of the Arrhenius plot and were found to be 0.40(1), 0.09(1) and 0.14(1) eV for grain, interface and overall activation energy of the sample, respectively. The first activation energy obtained for the semicircle with bulk capacity corresponds well to what would be expected for bulk grain conduction of garnet-based materials [35], and strongly differs from the activation energy observed for a pure PEO film. The observed activation energy for the second semicircle (which dominates the overall conductivity) is significantly lower from what has been reported in the literature for composite electrolytes [63, 74]. We assume that this lower activation energy observed for the semicircle with a capacity of 10^{-7} F, thus might originate mostly from a synergistic effect of 3D interconnected garnet backbone providing a continuous interface between PEO/garnet network. We will detail this explanation in the following.

For PEO-rich composite electrolytes i.e. ceramic weight percentages lower than 10%, it is well known that the Li-ion transport takes place via the bulk PEO and along with ceramic/PEO interface, irrespective of the composition of the ceramic filler [74, 76]. The interfacial contribution in such polymer rich composite electrolytes has been known to result in enhanced Li-ion conductivities compared to that of pure polymer electrolytes [75, 76]. For an increase of the ceramic weight fraction, agglomeration of the ceramic particles takes place, and conduction also takes place via the ceramic particles [68]; however, transport resistances perpendicular to the garnet-polymer interface are high, which is a limiting factor for accessing the high bulk conductivity.

Thus, it is important to estimate if the film prepared here represents a polymer-rich or a ceramic-rich scenario. Though a precise determination of the thin film density is difficult, it is possible to approximate the ratios of PEO to garnet compared to the composite electrolytes reported previously [174]. Assuming similar overall ceramic density of 47% [34] as obtained for the sintered

NSP powders, this would correspond to the weight ratio between garnet and polymer of 85:15 at the maximum under the assumption that the cavities are fully filled by the polymer.

A continuous and porous ceramic network would be beneficial to take advantage of ceramic/PEO interfacial contribution; the ideal sintered ceramics have strong grain conduction and high surface interactions between the crystallites (Figure 3.29a). In comparison, the low sintering times and temperatures used here are disadvantageous for creating wide sintering necks between the particles (but necessary to achieve a network which can be infiltrated, Figure 3.29b, c). Thus, the fact that the porous films show a low conductivity regardless of the high phase purity must be assigned to the existence of narrow sintering necks, which act as bottlenecks for the ionic transport in the porous garnet matrix (see Figure 3.29c). The increase of conductivity observed in the infiltrated films reported in this article thus might originate from additional contributions from electrically active garnet/PEO interfaces around the bottlenecks, in agreement with the capacities observed for the second semicircle in the impedance measurement. Thus, the bottlenecks of ionic transport are widened due to the interaction of the polymer with the garnet matrix, increasing the contribution of the garnet matrix on the overall conductivity (Figure 3.29d).

The intrinsic conductivity of the filler indeed plays a crucial role in ceramic rich composite electrolyte systems [175] by investigating composites of NSP-synthesized garnet particles and PEO+LiTFSI prepared via a solvent-free approach. Within such conventional composite electrolyte membrane preparation, the ceramic fillers would be in mere mechanical contact with each other. In contrast, the approach used here shows the development of connected porous and continuous network. The infiltration of Li-ion conducting PEO not only increases the overallconductivity, but also results in the additional Li-ion transport pathway via the garnet/PEO interface. Further, the conductivity is significantly higher to what would be expected for a composite with the similar garnet to PEO+LiTFSI ratio of particle agglomerates within a polymer matrix (5.3 x 10^{-7} S cm^{-1} vs. 8 x 10^{-8} S cm^{-1}) [175].

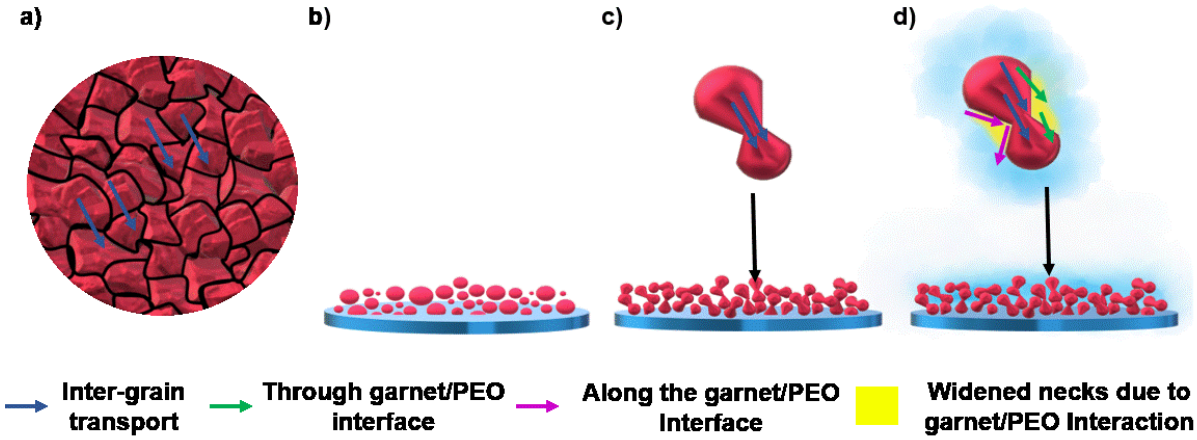

Figure 3.29: Schematic illustrating a) Li-ion transport in dense sintered ceramic with large grain size, b) spin coated NSP powder on the Cu substrate, c) necking between the particles in the annealed NSP synthesized garnet powders and d) Li-ion transport pathways with in the infiltrated films.

Thus, the main advantage of the porous annealed 3D garnet network would in principle offer higher ionic conductivity than the mechanically contacted garnet filler particles which are traditionally used in composite electrolytes [23, 68]. However, the infiltration may still not be ideal and smaller degrees of unfilled voids might still exist, which could contribute towards higher impedance. Regardless of these considerations, the conductivity reported here is comparable

to those reported in the literature for 50:50 wt% ratio of PEO to garnet [68]. Thus, though the overall conductivity of the film is not sufficient for achieving a functional solid state battery, we conclude that infiltrable networks of ion conductors can play an important role for achieving contribution of the inorganic matrix within composite electrolytes on the overall conduction process.

It is also interesting to put this finding in the context to previous findings. For composite electrolytes, the morphology of the ceramic filler and weight percentages was already discussed to have some impact on the overall conductivity [68]. For low weight fractions of ceramic fillers, nanowire-containing composite electrolytes are shown to improve the ionic conductivities compared to ceramic-free or nanoparticle-containing composites. This was assigned to a higher surface area and suitable directionality of the nanowire morphology, thus affecting the recrystallization kinetics and enhancing Lewis acid-base type interactions [74, 76, 97]. However, the higher the polymer content, the more difficult it might become to hinder the dendritic growth of lithium. It is well known that garnets offer higher ionic conductivities than the polymer-based electrolytes or composite electrolytes [10]. However, in conventionally mixed ceramic-rich composites, the garnet framework is just a dispersion of more or less loose particles within a polymer-matrix, which leads to high impedances for Li-ion transport at the particle/particle interfaces and has significant grain boundary contribution towards total Li-ion transport. Thus, the morphologies reported here might be suitable for combining the advantageous mechanical properties of the polymers with the beneficial properties of ceramic ion conductors.

We would like to acknowledge that, although the conductivities of the composite thin films reported here are too low for their application in ASSBs, an alternative method might be applicable to improve them. For example, using sintering aids during the heat treatment of garnet thin films might provide broader necks between the particles, and thus widen the bottlenecks currently encountered in the garnet-based framework; this has been shown to increase the conductivity of the garnets even in conventional dense ceramics [190]. Apart from this, the conductivity can be sufficient for thin film batteries, for which an aspect ratio d/A is of the order of 100 – 1000 times smaller than for pellet morphologies, and thus the electrolyte can be of reduced conductivity in order to be functional; here the preparation of even thinner porous films in the order of 1-10 µm would be preferable.

3.2.4 Conclusion

In this work, we show that porous 3-dimensional garnet thin films can be prepared by combining nebulized spray pyrolysis and spin coating. Although the post fabrication heat treatment does not show much influence on the microstructure, it is observed that the ionic conductivity is affected by the annealing duration. Polymer infiltration of the porous garnet films results in increased ionic conductivity by approximately 6 orders of magnitude, activating the ionic transport pathway through the garnet network. Electrochemical impedance spectroscopy measurements show the contribution of the PEO/garnet interface towards ionic conductivity, which is assigned to providing additional pathways around the sintering necks of the garnet matrix, thus widening the bottlenecks of the ionic conduction pathways. Though the conductivity of the film is low, it might still be sufficient for the use within thin film batteries. The additional reduction of thickness will be targeted in a further study.

Further, we emphasize that the porosity of the film might be modified further by the addition of sintering aids or combustible organic compounds, leading to denser or less dense films, respectively.

Supplementary Materials: Available online at www.mdpi.com.

Author Contributions: Conceptualization, O.C. and A.I.W; methodology, A.I.W.; sample preparation, V.V.; X-ray diffraction, impedance measurements and SEM, A.I.W.; data analysis, A.I.W; writing—original draft preparation, A.I.W.; writing—review and editing, A.I.W. and O.C.; funding acquisition, O.C. All authors have read and agreed to the published version of the manuscript.

Funding: A. I. Waidha and O. Clemens acknowledge funding within CL551/3-1 by the German Research Foundation (DFG).

Data Availability Statement: Data shown within this manuscript can be obtained from the authors on request.

Conflicts of Interest: The authors declare no conflict of interest.

3.3 Supplementary information for chapter 3

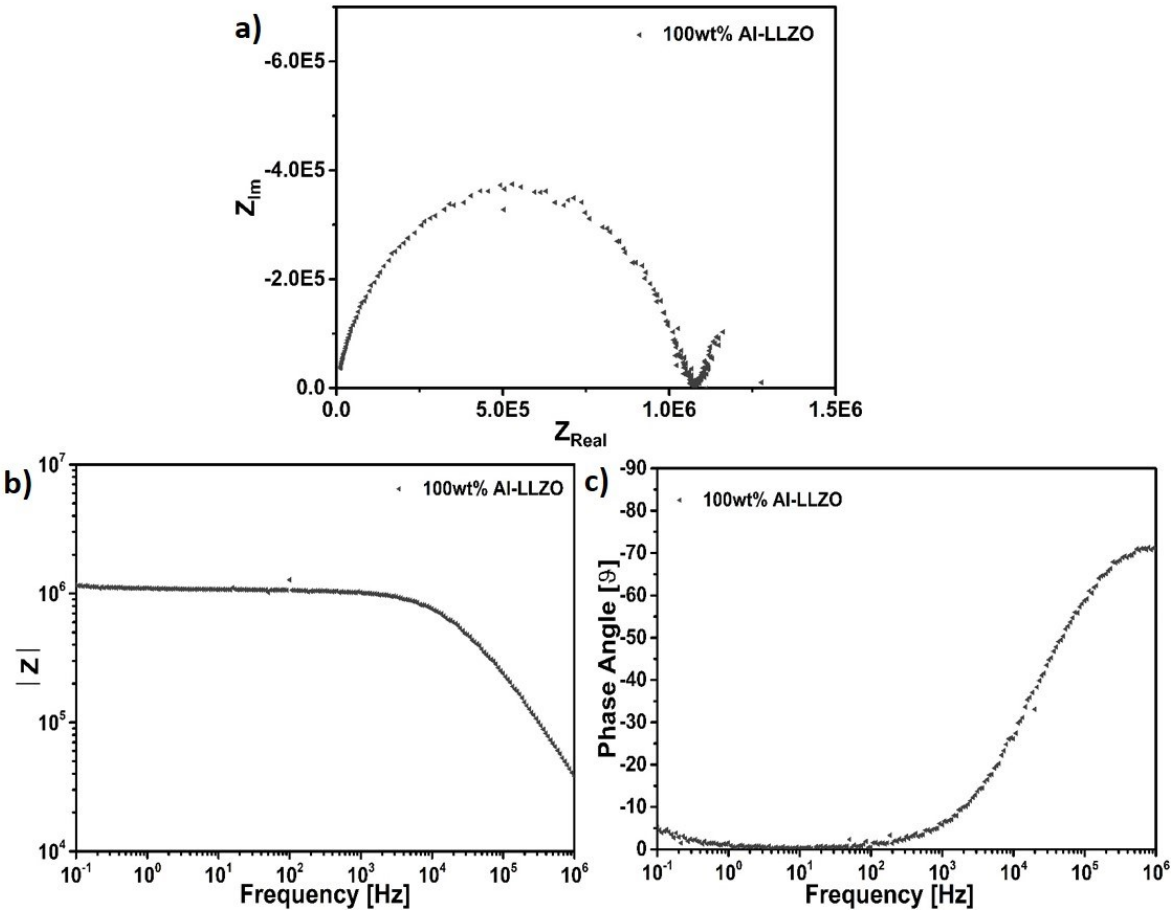

Figure 3.30: a) Nyquist, b&c) corresponding Bode plots for the isostatically pressed Al-LLZO garnet pellet measured at 403 K.

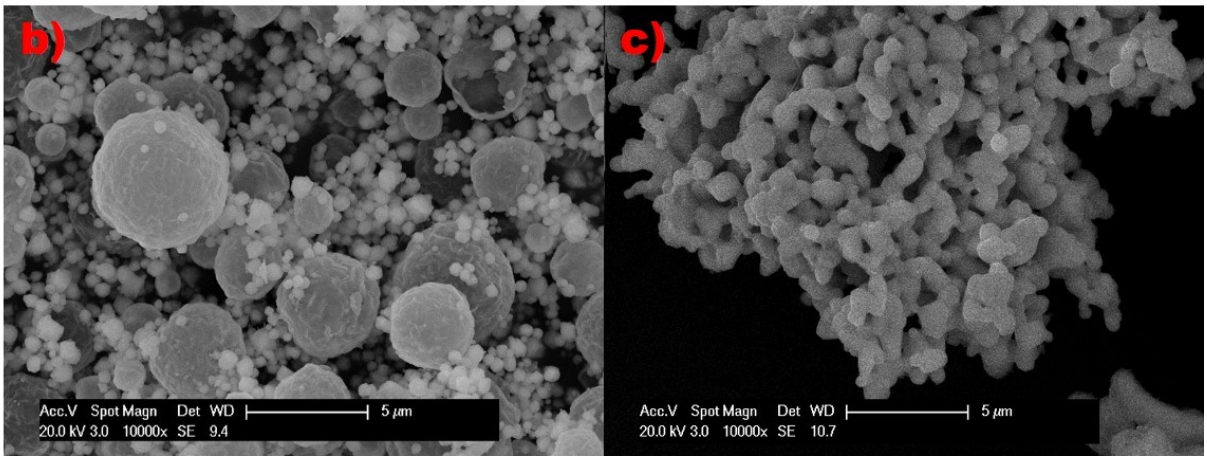

Figure 3.31: SEM micrographs of the as synthesized and sintered Al-doped LLZO particles.

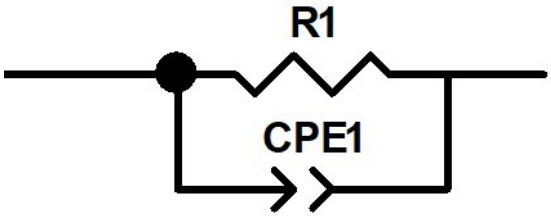

Figure 3.32: Equivalent circuit comprising of a resistor in series with a constant phase element.

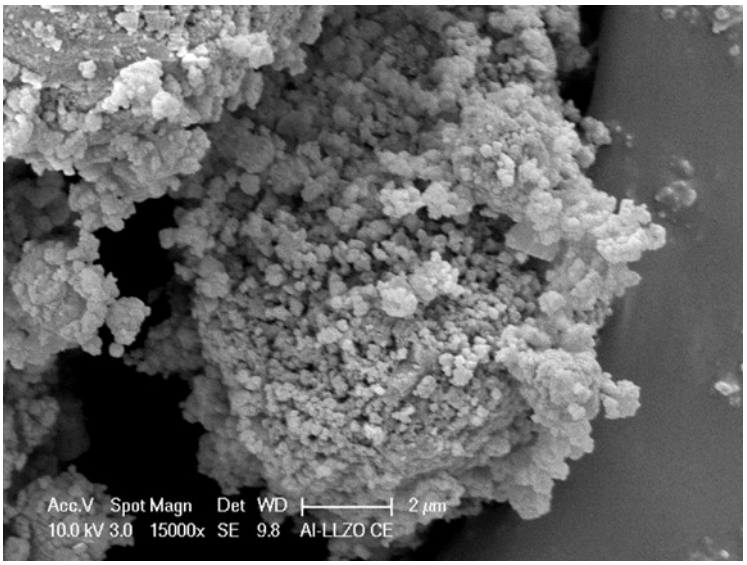

Figure 3.33: SEM micrograph of SiO_2 particles.

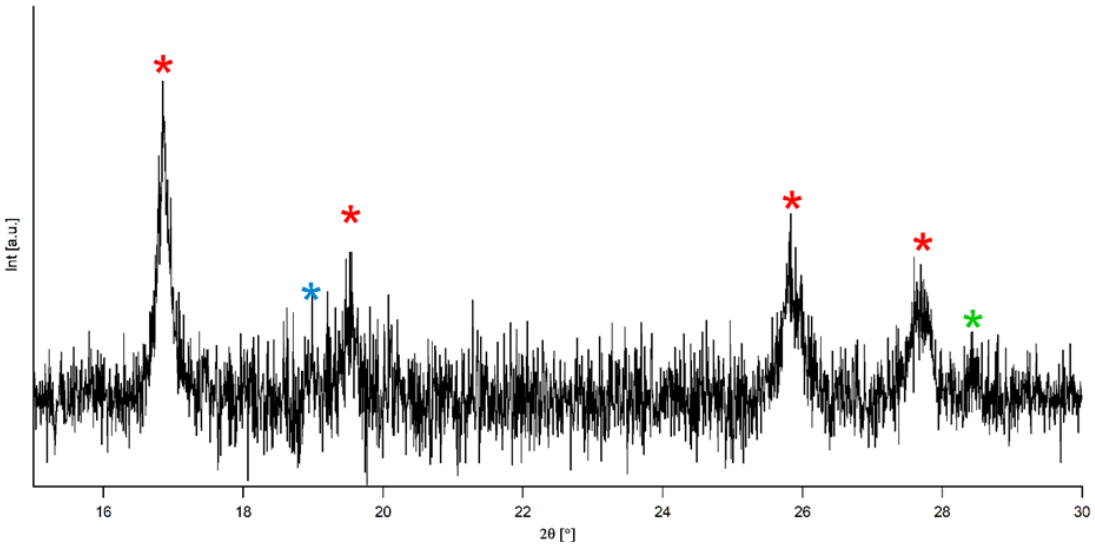

Figure 3.34: XRD of the synthesized garnet with the characteristic reflexes of LLZTO (red), Li_2SiO_3 (blue) and $La_2Zr_2O_7$ (green).

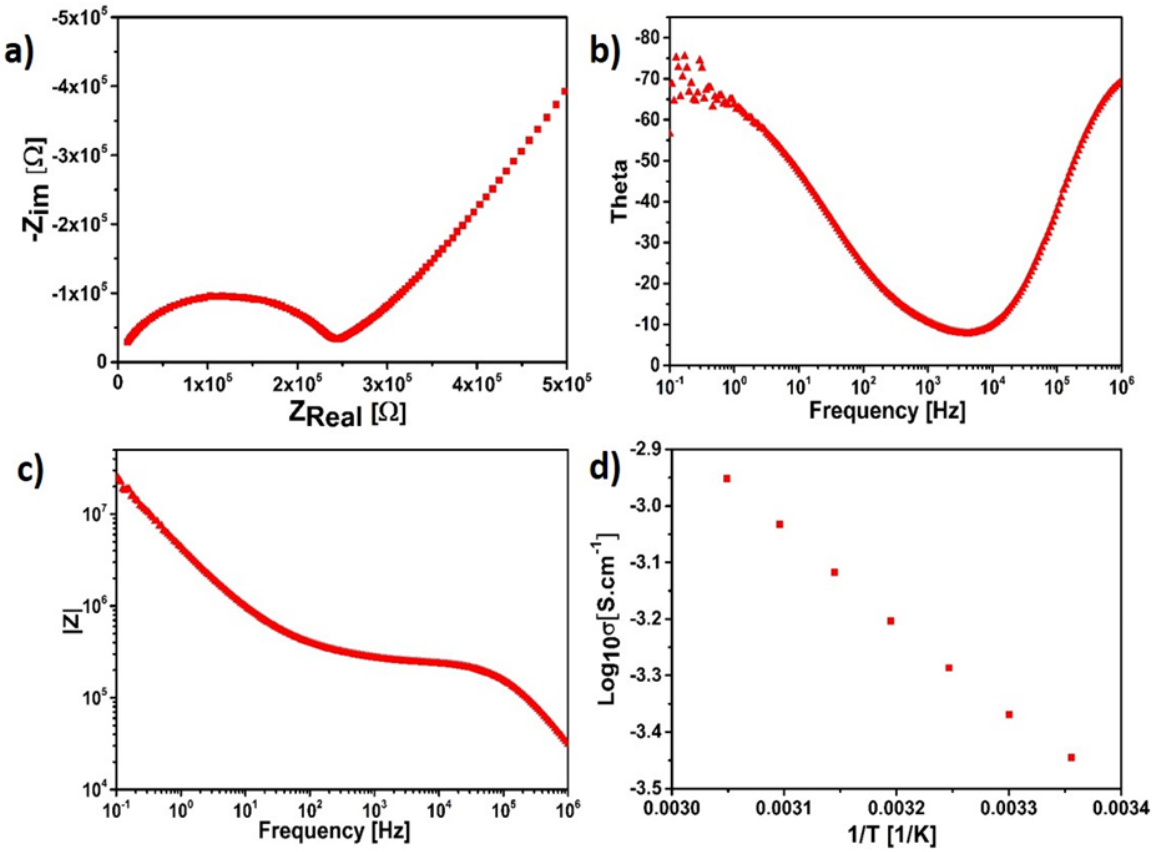

Figure 3.35: a-c) Nyquist and Bode plots for LLZTO garnet pellet sintered at 1413 K for 12 Hours recorded at 228 K. d) Temperature dependent Arrhenius plot for the same garnet pellet recorded in the range of 298 K and 328 K.

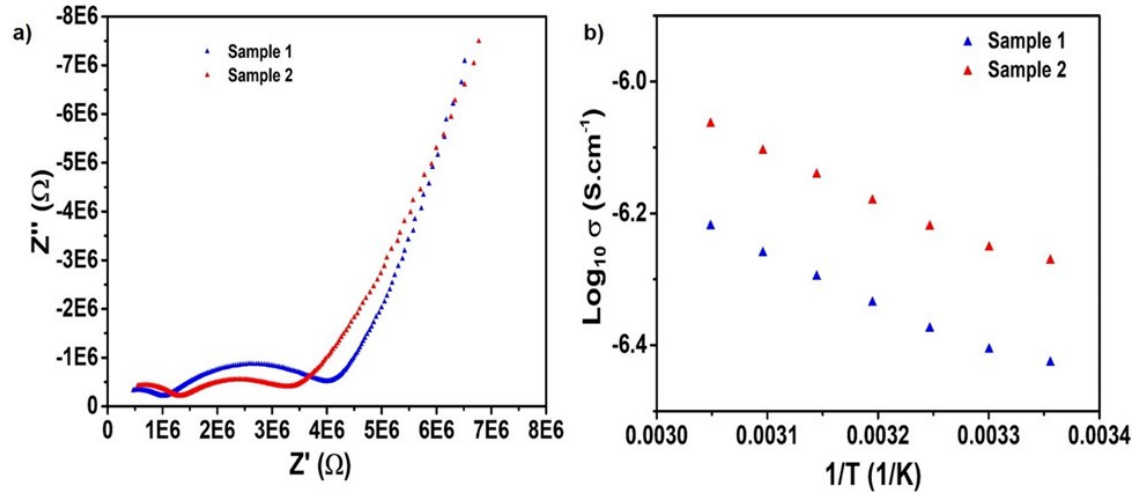

Figure 3.36: (a) Nyquist plot for two different infiltrated cubic Al-doped garnet films measured at 298 K. (b) Temperature dependent Arrhenius plot measured for the two different Al-doped garnet films measured in the temperature range of 298 K to 328 K.

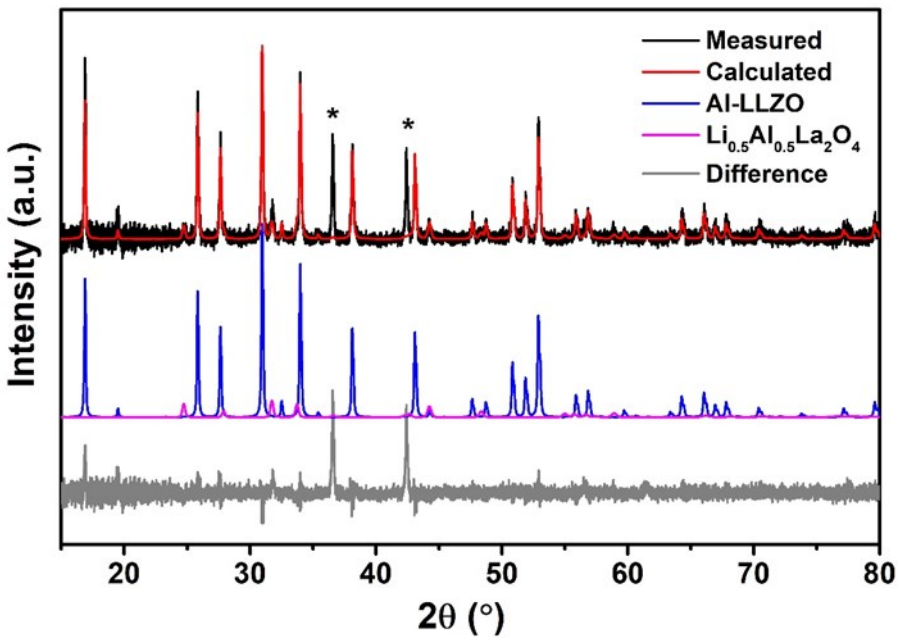

Figure 3.37: Rietveld fit of the X-ray diffractogram of the Al-doped LLZO garnet thin film annealed for 240 minutes

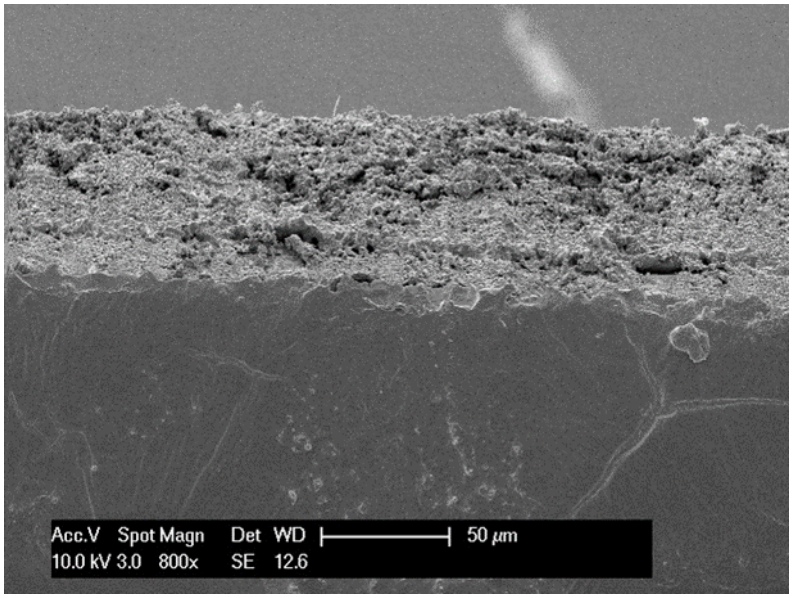

Figure 3.38: Cross sectional view of the garnet thin film.

4 Oxygen deficient perovskite $BaCoO_{3-\delta}$ systems

Within this chapter, the major scientific findings reported in the following publications will be summarized in context of NSP synthesis, topochemical modification and catalytic activity of perovskite-based barium cobaltates. This will be followed by the listing of these publications with relevance to make it easier for the reader to follow.

4.1 Synthesis, structure and electrical conductivity of a new perovskite type barium cobaltate $BaCoO_{1.80}(OH)_{0.86}$

4.2 Synthesis of bifunctional $BaFe_{1-x}Co_xO_{3-y-\delta}(OH)_y$ catalysts for the oxygen reduction reaction and oxygen evolution reaction

4.3 Structural, Magnetic and Catalytic Properties of a New Vacancy Ordered Perovskite Type Barium Cobaltate $BaCoO_{2.67}$

4.4 $BaCoO_{2+\delta}$: A new highly oxygen deficient perovskite-related phase with unusual Co coordination obtained by high temperature reaction with short reaction times

The aim of this work was to synthesize catalytically active barium cobaltates and to study the influence of topochemical modification via hydration and oxidation on their electronic and catalytic properties. Before summarizing the results obtained during this work, it is important to present a short prelude on the $BaCo_{3-\delta}$ systems, to make the reader aware of the different barium cobaltate phases that were known before the start of this thesis.

Cobalt based systems have received significant attention over the years for their electronic, magnetic and catalytic properties [90]. This is due to the fact that cobalt has the capacity to adopt variety of different oxidation states within variable coordination [90]. Zanne and co-workers [191] were the first to carry out the systematic study of the $BaCoO_{3-\delta}$ system on the powder samples, revealing a number of unidentified hexagonal polytypes. They've been attributed to 2H-$BaCoO_3$ ($2.85 < 3-\delta > 3.0$), 7H ($2.52 < 3-\delta > 2.575$), 12H ($2.43 < 3-\delta > 2.49$), 15H ($2.10 < 3-\delta > 2.23$), orthorhombic $BaCoO_{2.63}$ [192], $BaCoO_{2.07}$ and highly oxygen deficient $BaCoO_2$ [87] (Figure 4.1). Two other phases, cubic $BaCoO_{2.72}$ and a non-indexed $BaCoO_{2.31}$ have also been reported [87]. Recently, Mentré et al. reported on the most oxygen deficient *ccp*-related perovskite with the composition $BaCoO_{2.22}$ (Figure 4.1) [193].

For the stoichiometric $BaCoO_3$ [194], an ideal hexagonal 2H structure (Figure 4.1) is observed with face-sharing CoO_6 octahedra running along the *c* axis. h-[BaO_3] layers are replaced by defective ordered cubic c-[BaO_2] layers during reduction, resulting in 12H-$BaCoO_{2.83}$ (chain of four face-sharing octahedra with terminal disconnected CoO_4 tetrahedra), which are corner-shared with linear face-sharing octahedron. Early works [192] assigned to this structure meant an oxygen stoichiometry of $O_{2.6}$ from redox-titration, however given the multiphase sample used in this early work and the uncontested aggregation of vacancies in c-[BaO_2] layers (five [BaO_3] for one c-[BaO_2]), this phase was later considered to have the composition of $BaCoO_{2.83}$ [193]. Further, oxygen deficiency is shown to result in compound with the composition 5H-$BaCoO_{2.8}$ [195], with the oxygen content determined from the neutron diffraction and a structure containing three face sharing octahedron followed by terminal CoO_4 tetrahedron. The polytype 5H-$BaCoO_{2.74}$ [196] (structure detected by high resolution electron microscopy (HREM)) should also be mentioned here. Thermogravimetric reduction was used to determine the oxygen content of the sample. $BaCoO_{2.23}$, has been known to be synthesized under Ar atmosphere and was

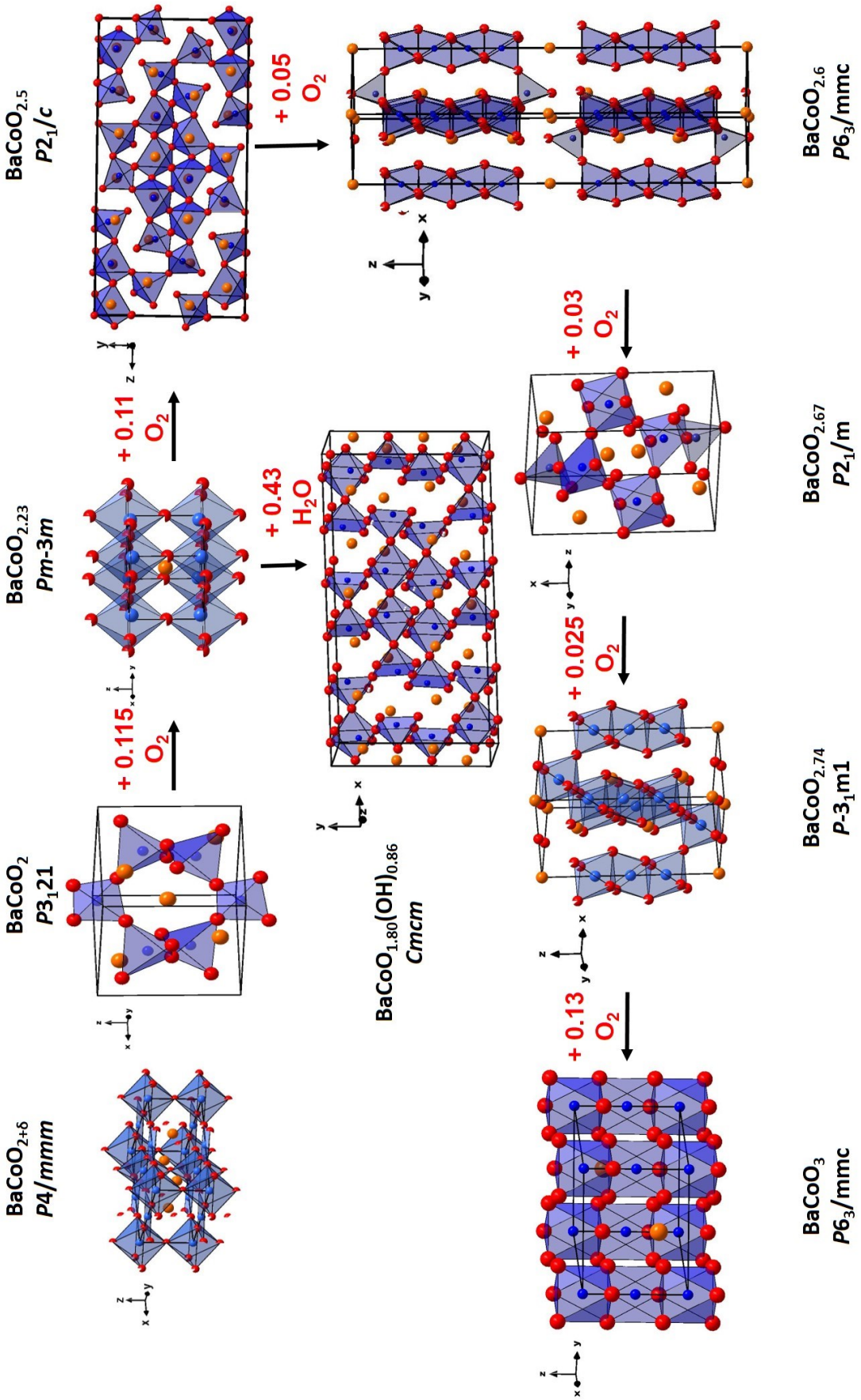

Figure 4.1: Structural schematics variety of different compositions within the $BaCoO_{3-\delta}$ system. * The arrows do not imply that the following composition or structure can be marely obtained via the oxidation of the former composition.

recently reported to be most anion deficient *ccp*-related perovskite phase within the $BaCoO_{3-\delta}$ systems.

Within the perovskite framework, the highest oxygen vacancy concentration has been known to occur for δ=1 phases. For the $BaCoO_{3-\delta}$ system with δ = 1, an early work suggests a trigonal type $BaCoO_2$ phase, containing only corner sharing CoO_4 tetrahedra (Figure 4.1). The compound was reported to be highly air sensitive. The structural schematics of different compositions within the $BaCoO_{3-\delta}$ family are given in Figure 4.1. Figure 4.2 shows the X-ray diffraction patterns of different $BaCoO_{3-\delta}$ compositions, which shows that it is in principle possible to resolve and identify each composition with a laboratory scale X-ray diffractometer due to different splitting of the main reflections. This further shows that $BaCoO_{3-\delta}$ system demonstrates both compositional and structural diversity. Therefore, a system of interest, most importantly due to the flexibility of tuning oxygen stoichiometry, cobalt oxidation states, coordination environment and spin states, which are all important for tuning the electronic and catalytic properties.

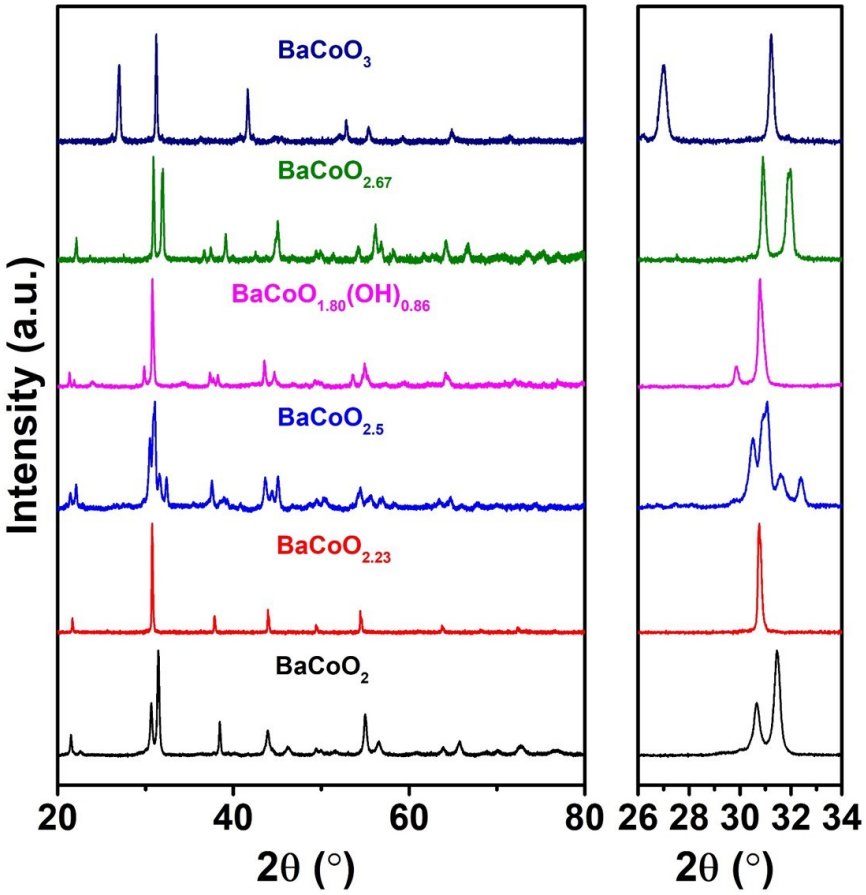

Figure 4.2: X-ray diffraction patterns of different $BaCoO_{3-\delta}$ systems synthesized during this thesis.

During the master thesis of the author of this thesis, NSP was used for the first time as the synthesis route for synthesizing barium cobalt based perovskites and indicated formation of a new oxide hydroxide $BaCoO_{1.80}(OH)_{0.86}$. The cue to this study resulted from a recent study on $BaFeO_{2.5}$ in which two different hydrated phases were reported, i.e. $BaFeO_{2.33}(OH)_{0.33}$ and $BaFeO_{2.25}(OH)_{0.5}$ [37]. In their findings, Knöchel et al. used solid-state synthesized $BaFeO_{2.5}$ as the starting material followed by its hydration by passing a wet stream of gas over the powders placed inside the NSP hot chamber or tube furnace that acts as the reaction chamber. It was observed that degree of hydration was dependent on the hydration temperatures. The high water phase $BaFeO_{2.25}(OH)_{0.5}$ was formed at 393 K and the low water phase $BaFeO_{2.33}(OH)_{0.33}$

was formed at 423 K [37]. However, NSP can also be used as a method for direct synthesis of oxides powders as well [197]. Additionally, as mentioned in section 2.1 and section 3, particles synthesized via NSP are nanocrystalline with hollow spherical morphology, which can be beneficial in terms of application of such cobalt containing perovskites as electrocatalyst due to high surface area containing active sites that are beneficial towards catalytic activity [28]. During this doctoral thesis, studies were carried out further to determine the crystal structure (via the combined Rietveld analysis of X-ray and neutron powder diffraction data) and the role of iron doping on various properties including that of electrocatalytic performance towards ORR/OER of the series $BaFe_{1-x}Co_xO_{3-y-\delta}(OH)_y$.

NSP was first used to synthesize $BaCoO_{1.80}(OH)_{0.86}$. The cation composition of the powders was determined from the EDAX, which indicated a 1:1 ratio of Ba to Co, in agreement with the experimentally used ratio. From the iodometric titrations, the average oxidation state of +2.46 was determined for Co. This is similar to the oxidation state of Co in $BaCoO_{2.22}$ [193]. However, the X-ray diffraction profile of this compound was significantly different from that of cubic $BaCoO_{2.22}$ (see Figure 4.2). Interestingly, the X-ray diffraction pattern of this phase showed striking similarity to that of $BaFeO_{2.33}(OH)_{0.33}$, which is the water-rich phase of $BaFeO_{2.5}$ [37]. Using the structural model of $BaFeO_{2.33}(OH)_{0.33}$, a good description of the X-ray diffraction reflection profile of $BaCoO_{1.80}(OH)_{0.86}$ was observed with the pseudocubic lattice parameter ($a_{ps.cub} = (V_{f.u.}{}^{1/3})$) of 4.12 Å, which is higher than that of $BaCoO_{2.23}$ (4.08 Å) [193]. The higher volume has been known to correspond to the presence of water within the perovskite structure [37]. Similar observation has been previously made for $BaFeO_{2.33}(OH)_{0.33}$ ($a_{ps.cub}$ = 4.14 Å) and $BaFeO_{2.5}$ ($a_{ps.cub}$ = 4.07 Å) [37]. The presence of protons within the structure was further confirmed by the FT-IR measurements, which showed a broad band within the spectral range of 3300-3500cm^{-1}, indicating the presence of OH stretching band [37]. STA measurements were therefore carried out in collaboration with Dr. Maren Lepple to determine the water content. From these measurements, a weight loss starting from 398 K was observed, with total weight loss of ~2.8-3.2 wt%. This corresponds to ~0.38-0.43 H_2O molecules per formula unit of $BaCoO_{3-\delta}$, resulting in an approximate composition of $BaCoO_{1.80}(OH)_{0.86}$ for the sample. Upon heating to high temperatures, i.e. 1273 K, cubic $BaCoO_{2.22}$ is obtained, which can therefore be considered the water free oxide of $BaCoO_{1.80}(OH)_{0.86}$. The structural refinements where carried out using coupled Rietveld analysis of powder X-ray diffraction and neutron diffraction data, which indicated three different Co sites within the structure. Further, the position of protons within the structure were identified and strong structural relaxation were found to occur around them in order to accommodate them within the structure. The electronic conductivity of the sample was determined from the impedance spectroscopy which indicated the conductivity of an order of 10^{-4} S cm^{-1}, which is ~4 orders of magnitude higher than $BaCoO_{2+\delta}$, in agreement with the presence of Co in mixed valent state, i.e. +2 and +3, allowing of electronic charge transport via electron hopping. These results are the basis of article given in section 4.1. An important take away from this study was that hydrated phases within the $BaCoO_{3-\delta}$ can be synthesized via NSP and there is a striking similarity between the barium cobaltates and ferrates. Hydrated barium ferrate is a high temperature proton conductor, however its conductivity is still low. The results obtained were the main motivation behind the subsequent doping study not only to synthesize new materials but to test them in terms of their application as bifunctional ORR/OER catalyst.

As already mentioned, perovskite-based cobaltates and ferrates have received significant attention due to their catalytic activity towards ORR and OER [28, 198]. Therefore, a project was undertaken to investigate the series with the composition $BaFe_{1-x}Co_xO_{3-y-\delta}(OH)_y$ for their

electrical and catalytic properties. A part of this study was carried out by Jasim Ali for his advance research lab project mainly comprising of powder synthesis via NSP and impedance studies. The series was synthesized via NSP, not only because the hydrated phases could be obtained but also due to the characteristic hollow spherical morphology of the particles obtained via NSP route (see Figure 4.3). This is important, since the sizes of the particles obtained via the NSP route are in nanometer range, this results in increased surface area of the particles, which also implies higher number of active catalytic sites on the surface. The synthesized powders were initially characterized via X-ray diffraction. For the compositions $x \neq 0$, the diffraction pattern was found to be similar to $BaCoO_{1.80}(OH)_{0.86}$ [82] and $BaFeO_{2.33}(OH)_{0.33}$ [37] whereas x=0 composition the diffraction pattern resembled to that of high water composition $BaFeO_{2.25}(OH)_{0.5}$ [37], which is the high water phase of $BaFeO_{2.5}$. This is nonetheless expected since this phase is known to occur, if the hydration of $BaFeO_{2.5}$ is carried out at 393 K and since the collector temperature within the NSP was maintained at 393 K, this resulted in $BaFeO_{2.25}(OH)_{0.5}$ [37]. An important point to be kept in mind is to store the as-synthesized powders in the inert gas filled glove box to limit the exposure to the ambient atmosphere. This is due to the basic nature of the as-synthesized powders, which can react with atmospheric acidic CO_2 and form $BaCO_3$ [37].

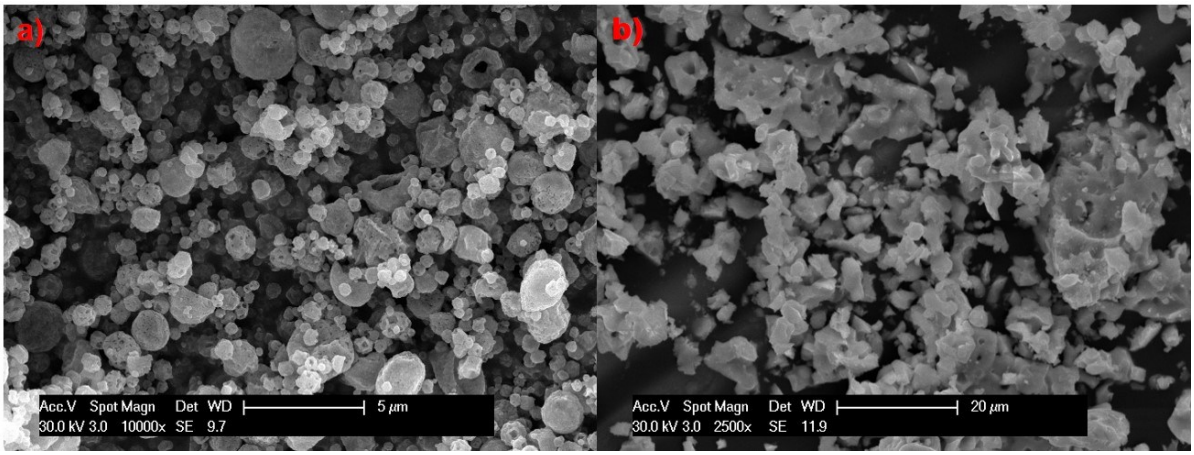

Figure 4.3: Comparison of the SEM micrographs obtained for the powders synthesized via (a) NSP and (b) solid state synthesis route.

Iodometric titrations were carried out on the whole series to determine the average oxidation states of the B site. It was observed that in general the oxidation state of the B site decreases with the increase in the value of x, corresponding to the increased Co doping. To get a deeper understanding of the distribution of oxidation states of the transition metals, Mössbauer spectroscopy was used, which is a proven technique to obtain the oxidation states and environments of Fe within the perovskite framework. Mössbauer measurement (carried in Collaboration with Lingmei Ni and Prof. Ulrike Kramm) was performed on the x = 0.5 sample which suggested the presence of Fe in +3 oxidation state. Therefore, any change in oxidation states is due to the change in Co oxidation states. This further indicates that the Co oxidation states within the perovskite framework can be tuned via doping strategies. Additionally, water loss behavior of this composition was studied via the combination of high temperature XRD and STA (performed in collaboration with Dr. Maren Lepple). Similar to $BaFeO_{2.33}(OH)_{0.33}$, the compound was found to undergo orthorhombic to monoclinic transformation upon water loss, i.e. forming a water free analog with the composition $BaFe_{0.5}Co_{0.5}O_{2.44}$. The electronic conductivity of the series was found to follow a smooth trend. As the cobalt content increases, the conductivity was found to increase, which is in agreement with the increase in the mixed valent states of Co as a function of doping. For the x = 0, the conductivity was found to be an

order of 10^{-8} S cm^{-1} at 298 K, whereas x = 0.5 demonstrated an electronic conductivity of an order of 10^{-6} S cm^{-1}, which is two orders of magnitude higher. Nevertheless, the highest conductivity was found for x = 1 compositions, i.e. for $BaCoO_{1.80}(OH)_{0.86}$. This was followed by characterizing of these compositions for their bifunctional ORR and OER catalytic activities. Catalytic measurements were carried out in collaboration with Lingmei Ni and Prof. Ulrike Kramm. It was observed that compositions x =0.8 and 1, are most ORR active with the potentials required for reaching current density of 3 mA cm^{-2} being 0.59 V and 0.34 V, respectively. Both these compositions also demonstrated highest ORR activity of 1.25 mA cm^{-2} and 1.3 ma cm^{-2} at 0.7 V with Tafel slopes of 84 and 91 mV dec^{-1}. The better performance of these two compositions compared to that of Fe rich composition can be due to the lowering of e_g orbital filling, where an average of 1 has been reported to be desired [31]. It is well known that Fe^{3+} within the perovskite framework is present in high spin state, i.e. t_{2g}^3 and e_g^2, with cobalt being incorporated and being present in 2+ (d^7) and 3+ (d^6) oxidation states, this would lower the e_g filling and therefore proving beneficial towards ORR. Similarly, OER measurement were carried out and these demonstrated a volcano type dependence with x = 0.5 composition displaying the lowest potential to reach the current density of 10, 5 or 2 mA cm^{-2}. The onset potential was found to be dependent on the x, with a decrease till x = 0.5 followed by an increase. In terms of bifunctional catalytic activity (difference between the OER potential at 10 mA cm^{-2} and ORR potential at 2.5 mA cm^{-2}), sample with x = 0.2 demonstrated the lowest different δU = 1. 10V which is comparable to that of noble metal catalyst [199] and recently reported $CaMnO_{3-\delta}$ [200].However, the performance was found to be inferior to $Ba_{0.5}Sr_{0.5}Co_{0.8}Fe_{0.2}O_{3-\delta}$ [31, 32], which is known to exhibit e_g filling of 1 that has been shown to be beneficial towards catalytic performance. The results are covered in detail in section 4.2.

In order to understand the role of NSP towards synthesis of hydrated barium cobaltate phases, attempts were made to prepare solid state powders with the aim of obtaining same product as for NSP. Similar to the two step synthesis procedure followed by Knöchel et al. [37], attempt was made first to synthesize $BaCoO_{2.5}$. To achieve this, precursor powders comprising of $BaCO_3$ and Co_2O_3 were hand milled and subjected to heat treatment at 1273 K for 60 hours with the heating and cooling rate of 5 K min^{-1} under the flow of Ar. The X-ray diffraction pattern of as-synthesized powders revealed a similarity to previously reported $BaFeO_{2.5}$ [84] with monoclinic structure, however with additional impurity phase (Figure 4.29a). It is important to note that this powder can only be obtained in a small tube furnace under a constant flow of Ar, however with the other end of the furnace not tight enough to allow for a backflow of ambient air into the furnace and not maintain a pure Ar atmosphere within. If the ends were tightened via the use of oil filled bubblers to prevent the back flow of ambient air, this resulted in powders with composition $BaCoO_{2.22}$ with cubic structure [193]. It is easy to distinguish it from $BaCoO_{2.5}$ since $BaCoO_{2.5}$ shows additional splitting of main reflections in agreement with the monoclinic distortion. This shows the influence of the gaseous environment inside the furnace on the resulting oxygen stoichiometry and the phase composition obtained. As mentioned already, the powders were found to be phase mixtures and iodometric titrations indicated the average oxygen stoichiometry of $O_{2.46}$ for this phase mixture. This demonstrates that the oxygen stoichiometry of the final composition although not same but is close to that of $BaCoO_{2.5}$. For $BaFeO_{2.5,}$ the compound is able to incorporate water, which results in increased conductivity due to the proton incorporation. The hydration of $BaCoO_{2.46}$ is of interest for its use as electrode material in solid oxide fuel cells, where mixed proton and electronic conductors are of required. Similar to hydration procedure followed by Knöchel et al. [37], as-synthesized powders of $BaCoO_{2.5}$ were subjected to wet stream of Ar gas in a NSP set up. The temperature of the furnace was maintained at 393 K. For $BaFeO_{2.5}$, this lead to successful hydration and was

easily observed from the changes in X-ray diffraction pattern along with the shifting of reflections towards lower angles in agreement with the increase of unit cell volume, furthering confirming water incorporation [37]. However, this was not observed in case of $BaCoO_{2.5}$, where the X-ray diffraction pattern was found to remain same before and after hydration attempt.

In addition to hydration, $BaFeO_{2.5}$ can also be fluorinated and oxidized which results in the compositions $BaFeO_{2.33}F_{0.33}$ [201] and $BaFeO_{2.67}$ [181], respectively. For oxidizing $BaFeO_{2.5}$ to $BaFeO_{2.67}$, this would mean mixed oxidation state of +3 and +4 for Fe. Similarly, possible oxidation of $BaCoO_{2.5}$ might also result in the formation of $BaCoO_{2.67}$ type phase with mixed valent Co which might prove to be beneficial towards catalytic performance. Although the hydration via solid-state route was not possible, the NSP synthesized powders did demonstrate possible structural similarity between barium rich cobaltates and ferrates [37, 80]. Therefore, an attempt was made to oxidize $BaCoO_{2.5}$. Using a combination of STA and high temperature XRD measurements, it was observed that the powders with composition $BaCoO_{2.67}$ can be obtained by heating the starting $BaCoO_{2.5}$ (actual oxygen stoichiometry $BaCoO_{2.46}$) powders at 473 K for 2 hours under the constant flow of O_2. From the iodometric titration the oxidation state of +3.34 was determined for Co which is in agreement with the oxygen uptake of ~0.21 at 473 K. From the coupled Rietveld analysis of powder X-ray diffraction and neutron diffraction data, a monoclinic cell within the space group $P2_1/m$ with the lattice parameters a=10.1718(3) Å, b=5.6035(2) Å, c=6.9248(2) Å and β = 91.465(4) ° was derived [202], with principle vacancy ordering similar to that of $BaFeO_{2.33}F_{0.33}$ [201] and $BaFeO_{2.67}$ [181]. The structural similarity between these compositions is plausible due to the similar anion content. The resulting structure, where in the 2*a* oxygen site was found to be vacant results in three different Co sites with different coordination environments, with Co^{3+} present in 4-fold and 6-fold coordination and Co^{4+} in a 5-fold square pyramidal polyhedra. Similar to $BaCoO_{2+\delta}$ [81] and $BaCoO_{2.22}$ [193], $BaCoO_{2.67}$ shows g-type anti ferromagnetic ordering with an average magnetic moment of 2.36(1) μ_B, in agreement with the DFT studies (carried out in collaboration with Dr. Yuji Ikeda and Prof. Blazej Grabowski at University of Stuttgart) which indicate the antiferromagnetic state being the most favourable. The presence of Co in two different oxidation states results in an electronic conductivity of an of 10^{-4} S cm^{-1}, which is 4 orders of magnitude higher than that of $BaCoO_{2+\delta}$. Due to the stability of this compound (the compound was stable for at least a week after being left outside under ambient conditions (no changes in XRD pattern were observed)), the bifunctional catalytic activity of this compound towards ORR and OER were measured (in collaboration with Humera Siddiqi and Prof. Ulrike Kramm at TU Darmstadt). Interestingly, the compound showed activities similar to that of the benchmark perovskite catalyst BSCF ($Ba_{0.5}Sr_{0.5}Co_{0.8}Fe_{0.2}O_{3-\delta}$). For BSCF, high catalytic activity has been attributed to the electronic configuration of t_{2g}^5 and $e_g^{1.25}$, if qualitatively same argument is made for $BaCoO_{2.67}$, this implies an intermediate spin state for Co^{3+} (t_{2g}^5 e_g^1) and high spin state for Co^{4+}.However, it must be noted that determining the exact spin states for Co with different crystallographic coordination and oxidation states is experimentally difficult. A detailed study on this composition is already published and given in section 4.3 of this thesis.

As mentioned previously, upon heating $BaCoO_{1.80}(OH)_{0.86}$ to high temperatures in order to get rid of water, cubic $BaCoO_{2.22}$ was formed, which is hence referred to as water free analog to $BaCoO_{1.80}(OH)_{0.86}$. To determine if this hydrated composition can also be obtained via hydration of solid state synthesized $BaCoO_{2.22}$, attempts were made to synthesize $BaCoO_{2.22}$ via solid state route. Following the experimental recipe of Mentré et al [193], instead of obtaining $BaCoO_{2.22}$ [84], $BaCoO_{2.5}$ along with an impurity phase was obtained. (see Figure 4.2). Although an unexpected outcome, this further indicated the possible structural similarity between the

barium-rich cobaltate-based perovskites and the ferrate-based perovskites. Nevertheless, the synthesis conditions were slightly modified and instead of hand milling, the initial precursor powders were ball milled to allow for the improved homogeneous precursor mixture with uniform distribution of reactants. The reactant powders were placed in a tube furnace and programed to heat for 60 hours under a constant flow of Ar. However, a mistake while setting a heating program (instead of using dwell time of 60 hours at 1273 K, the dwell time of 60 min at 1273 K was programmed), lead to a powder with a diffraction pattern showing mixture of phases, which hinted towards incomplete reaction. The obtained powders were therefore again ball milled and reheated with the same experimental conditions as before, which resulted in the formation of a single phase powder as confirmed from the X-ray diffraction pattern. It is important to mention here that even a slight change in the experimental conditions or the furnace can result in an entirely different phase, which indicates the importance of tuning the experimental conditions for the synthesis of this phase and sensitivity to $p(O_2)$. The composition of the powder was determined from the combination of EDAX and iodometric titrations which indicated the composition of $BaCoO_{2+\delta}$ (δ~0.01 – 0.02) for this compound. Interestingly, such a high temperature solid state synthesis route has not been reported before for the synthesis of highly oxygen deficient perovskite systems. Although different perovskites with δ~1 have been reported before, these have been almost exclusively synthesized via the low temperature topochemical hydride reduction method using metal hydrides as the reducing agents [88, 203, 204]. An advantage of using the high temperature synthesis route here is that pure phase powders can be obtained which is important for subsequent analysis or characterizations compared to that of hydride reduction method, in which powders are washed multiple times to obtain the phase pure powders. Combined Rietveld analysis of the powder X-ray and neutron diffraction data was undertaken to determine the crystal structure, which indicated that this compound demonstrates an unusual tetragonal distortion (c/a ratio smaller than 0.5), which has been previously found in the highly oxygen deficient perovskite systems with infinite square planar coordination of transition metal ions [204]. Interestingly, the trigonal modification of $BaCoO_2$ was found to be present as a small impurity phase but a phase pure composition of this modification could not be synthesized. From the structural solutions, the compound was confirmed to crystallize within the tetragonal space group *P*4/*mmm* with partial ordering of oxygen vacancies and presence of Co^{2+} ions in the square planar coordination. DFT calculations (performed in collaboration with Prof. Dr. Hongbin Zhang) were then carried out, which indicated that the structural setting obtained from the Rietveld analysis are least favourable which indicates the influence of small excess oxygen δ on the structural stability. From the SQUID measurements, the compound was found to be anti-ferromagnetic with the Neel's temperature of 220 K. The conductivity of the compound was found to be of the order of 10^{-8} S cm^{-1} as determined from the impedance spectroscopy, which is 4 orders of magnitude lower than both $BaCoO_{1.80}(OH)_{0.86}$ [82] and $BaCoO_{2.67}$ [202]. Although the catalytic activity of this composition could not be measured due to its metastable nature (compound was found to decompose even inside the Ar-filled glove box at room temperatures for one month, that was the minimum duration after which a X-ray diffraction pattern was collected), perovskite compounds with Co^{2+}, with Co in the low spin state would be of high interest in terms of its application as bifunctional oxygen reduction and oxygen evolution electrocatalyst. This would imply an e_g filling of 1 for low spin Co^{2+}, which has been shown to be the most favourable configuration for the bifunctional ORR/OER perovskite catalyst [31, 32]. Although, determining the spin state for Co^{2+} from the Curie-weiss fit was not possible due to the presence of impurity phases within the powders, the refined magnetic moments from neutron diffraction were found to be 3.7 μ_B, which is in agreement with the high spin state of Co^{2+}. Heating this compound under the flow of oxygen was found to result

in a hexagonal type perovskite, which is well known for the oxygen rich barium cobaltates. These results form the basis of the communication article given in section 4.4.

4.1 Synthesis, Structure and Electrical Conductivity of a New Perovskite Type Barium Cobaltate $BaCoO_{1.80}(OH)_{0.86}$

Aamir Iqbal Waidha[a], Maren Lepple[b], Kerstin Wissel[a], Alexander Benes[c], Stephan Wollstadt[a], Peter R. Slater[d], A.D. Fortes[e], Oliver Clemens[a,f*]

[a] Technische Universität Darmstadt, Institut für Materialwissenschaft, Fachgebiet Materialdesign durch Synthese, Alarich-Weiss-Straße 2, 64287 Darmstadt,Germany.

[b] Technische Universität Darmstadt, Eduard-Zintl-Institut für Anorganische und Physikalische Chemie, Alarich-Weiss-Straße 12, 64287 Darmstadt, Germany.

[c] Technische Universität Darmstadt, Institut für Materialwissenschaft, Fachgebiet Gemeinschaftslabor Nanomaterialien, Alarich-Weiss-Straße 2, 64287 Darmstadt, Germany.

[d] University of Birmingham, School of Chemistry, Edgbaston, Birmingham B15 2TT, UK.

[e] ISIS Facility, Rutherford Appleton Laboratory, Harwell Science and Innovation Campus, Didcot, Oxfordshire OX11 0QX, United Kingdom.

[f] Karlsruher Institut für Technologie, Institut für Nanotechnologie, Hermann-von-Helmholtz-Platz 1, 76344 Eggenstein Leopoldshafen, Germany.

Corresponding Author: oliver.clemens@md.tu-darmstadt.de

Abstract

Perovskite oxides exhibiting mixed protonic and electronic conductivities have interesting applications in protonic ceramic fuel cells. In this work, we report on a hydrated phase of $BaCoO_{1.80}(OH)_{0.86}$ synthesized using nebulized spray pyrolysis. Structural analysis based on X-ray and neutron powder diffraction data showed that the compound is isotypic to $BaFeO_{2.33}(OH)_{0.33}$. The water loss behaviour was studied using simultaneous thermal analysis and high temperature X-ray diffraction, indicating that protons (respectively water) can be stabilized within the compound up to temperatures significantly above 673 K, confirmed by ex-situ Fourier transform infrared spectroscopy studies. Impedance spectroscopy was used to determine the conductivity characteristics of $BaCoO_{1.80}(OH)_{0.86}$, finding a total electrical conductivity in the order of 10^{-4} S cm^{-1} at ambient temperature with an activation energy of 0.28 eV.

Keywords

Perovskites; PCFC; electrode catalysts; neutron diffraction; impedance spectroscopy

4.1.1 Introduction

Perovskite type compounds ABX_3 (A = alkaline earth or lanthanide, B = transition metal, X = anion, e. g. oxide, fluoride, hydroxide) have attracted a lot of attention over the past years due to their interesting electronic, magnetic and optical properties [205, 206]. The structure of the cubic aristotype (space group *Pm*-3*m*) can be understood as being built up by a cubic close packed arrangement of AX_3 layers with the B cations occupying 1/4th of the octahedral voids. This arrangement is highly flexible with respect to the formation of large amounts of anion vacancies, with values of y upto 1 in $ABX_{3-y}\square_y$ being possible[88,207]. Those anion vacancies can be filled with a variety of anion species by the use of topochemical reactions [208,193]. For Ba-rich compounds, it is known that the anion vacancies can be filled with large amounts of water, resulting in proton-conducting compounds [209,210]. Such compounds are of high interest for the use in proton conducting solid oxide fuel and electrolysis cells (SOFC / SOEC, also often referred to as protonic ceramic fuel cells PCFCs). A prominent example is Y-doped $BaZrO_3$, which is a promising candidate as an electrolyte material due to its high proton and negligible electronic conductivity [133, 210]. In contrast, only few compounds are known to be suitable as electrode catalysts for the oxygen side of PCFCs, which require the use of first row transition metal species (e. g. Mn, Ni, Co, Mn, Fe) to show sufficient electronic conductivity and therefore catalytic activity. With the aim to investigate water uptake and proton conductivity of such systems, our group recently reported first studies on the water uptake and proton conductivity of $BaFeO_{2.5}$ [37, 211, 212]. In these studies, we found that monoclinic $BaFeO_{2.5}$ can take up relatively large amounts of water to form compounds with composition $BaFeO_{2.33}(OH)_{0.33}$ (LW-$BaFeO_{2.5}$, LW = low water) and $BaFeO_{2.25}(OH)_{0.5}$ (HW-$BaFeO_{2.5}$, HW = high water) accompanied by an increase of conductivity due to incorporation of the protons [37].

Cobaltates with perovskite type structure (such as $La_{1-x}Sr_xFe_{1-y}Co_yO_{3-d}$ [213] and $Ba_{0.5}Sr_{0.5}Co_{0.8}Fe_{0.2}O_{3-d}$ [83]) are known for their excellent catalytic properties as oxygen electrode catalysts [213,214]. Regardless of this, no studies have been reported on the proton uptake of barium cobaltates $BaCoO_{3-y}$ with cubic close packed BaO_{3-y} lattice. The lack of such studies might relate to the difficulty of stabilizing barium cobaltates in *ccp* related perovskite type structure, with $BaCoO_{2.22}$ [193] and trigonal $BaCoO_2$ [215] being the only known two compounds which adopt this structural arrangement. Compounds with higher oxygen content were found to crystallize in various hexagonal perovskite type structures: 5H-$BaCoO_{2.8}$ [195], 12H-$BaCoO_{2.61}$, [216], 2H-$BaCoO_3$ [217, 218,219,220], Mn-doped 10H-$BaCoO_3$ [221].

In this article we report on the preparation of a new hydrated barium cobaltate phase with approximate composition $BaCoO_{1.80}(OH)_{0.86}$, which is found to be isotypic to LW-$BaFeO_{2.5}$ ($BaFeO_{2.33}(OH)_{0.33}$) [37] from a structural analysis on a deuterated sample via Rietveld refinement of X-ray and neutron powder diffraction (XRD, NPD). High temperature XRD (HT-XRD), fourier transform infrared spectroscopy (FTIR) and simultaneous thermal analysis (STA) were used to study the stability range of this phase with respect to water loss. Additionally, electrochemical impedance spectroscopy (EIS) was used to investigate the electrical conductivity of this new material.

4.1.2 Experimental

4.1.2.1 Material synthesis

$BaCoO_{1.80}(OH)_{0.86}$ was synthesized using nebulized spray pyrolysis (NSP). To prepare the starting precursor solution, $Ba(NO_2)_3$ (Sigma Aldrich,99.99%) and $Co(NO_3)_2{\cdot}6H_2O$ (Sigma Aldrich,99.99%) were dissolved in de-ionized water at a cation concentration of 0.06 mol l^{-1}, and the mixture was stirred for 30 minutes in order to obtain a homogenous pinkish transparent

solution. For the synthesis, a setup as previously described in [34] was used. The as-prepared solution was injected into the nebulizer unit using a syringe pump with the flow rate of 1.5 ml min^{-1}, while operating the ultrasonicator required to generate the nebula at a generator voltage and current of 47.0 V and 0.51 A respectively. The precursor mist formed inside the nebulizer unit was transported by a carrier gas stream of argon at the rate of 2 SLM (standard liter per minute) to the reaction tube, which was maintained at 1323 K. The as-synthesized particles were collected on glass filter paper in the collector unit. The collector unit was maintained at 373 K to prevent water vapor condensation. The whole process was carried out at the constant pressure of 900 mbar.

For electrical characterization, pellets of the title compound were prepared by uniaxially pressing the powder followed by a subsequent isostatic pressing at a pressure of 700 kN. Pellets were then sputtered with a thin layer of gold on both sides for electronic contacting.

4.1.2.2 Diffraction experiment

XRD patterns of the hydrated compound were recorded on a Bruker D8 diffractometer using Bragg-Brentano geometry with a fine focusing X-ray tube with Cu $K_{\alpha 1,2}$ radiation. A VANTEC detector (3° opening) and a variable divergence slit (4 mm) were used. The total scan time was set to 10 hours for the angular range between 5° and 130° 2θ at a step size of 0.0075°. High temperature XRD was measured using an Anton Parr HTK1200 sample stage in the temperature range between 303 K and 1023 K (heating rate of 5 K s^{-1}) in the angular range between 20° and 60° 2θ with the step size of 0.0075° (total counting time of 10 min per scan) under a flow of argon. These conditions were chosen as a compromise to obtain sufficient data quality for the determination of lattice parameters and phase composition, but to lower differences to the heating procedure used for simultaneous thermal analysis.

Time-of-flight (TOF) neutron powder diffraction (NPD) data were recorded on the high resolution diffractometer (HRPD) at the ISIS pulsed spallation source (Rutherford Appleton Laboratory, Didcot, U.K.).2 g of powdered $BaCoO_{1.80}(OD)_{0.86}$ was loaded into 8-mm-diameter thin-walled cylindrical vanadium sample cans, and data were collected at ambient temperature for a 314 μAh proton beam current to the ISIS target corresponding to the beam time of ~7.5 h.

The analysis of the nuclear structure of $BaCoO_{1.80}(OH)_{0.86}$ using both the NPD and XRD data was performed using the Rietveld method with the program TOPAS 5 (Bruker AXS, Karlsruhe, Germany) [95]. For the room temperature XRD data, the whole 2θ-range range was used, while for NPD, data collected from the high resolution backscattering detector bank (bank 1) as well as the 90° high intensity bank (bank 2) were used. The instrumental intensity distribution for the X-ray data was determined empirically from a sort of fundamental parameters set [108], using a reference scan of LaB_6 (NIST 660a), and the microstructural parameters were refined to adjust the peak shapes for the XRD data. The lattice parameters were constrained to be the same for neutron and XRD data, and the same positional parameters were used and refined for both data sets. Independent thermal displacement parameters were refined for each type of atom for neutron data. As a starting model, our structural model of LW-$BaFeO_{2.33}(OH)_{0.33}$ as described in [37] was used.

4.1.2.3 Simultaneous thermal analysis

Simultaneous thermal analysis combining thermogravimetric analysis (TGA) and differential scanning calorimetry (DSC) was conducted for $BaCoO_{1.80}(OH)_{0.86}$ on a Netzsch STA 449 F3 Jupiter thermal analyzer. The measurements were performed in the temperature range

between 300 K to 973 K using a heating rate of 10 K min^{-1}. Thermal analysis was performed in corundum crucibles under an argon flow of 50 ml min^{-1}.

4.1.2.4 Fourier transform infrared spectroscopy

Fourier-transform infrared spectroscopy measurements were conducted on a Varian spectrometer. Samples were characterized via attenuated total reflection (ATR) by mounting an ATR unit into the sample compartment of the spectrometer. The spectra were recorded in a range between 550 cm^{-1} and 4000 cm^{-1} with a spectral resolution of 0.5 cm^{-1}.

4.1.2.5 X-ray photoelectron spectroscopy

The surface composition and oxidation states were examined by ex-situ X-ray photoelectron spectroscopy (XPS) analysis using a Physical Electronic VersaProbe XPS unit (PHI 5000 spectrometer) with Al K_α radiation (1486.6 eV). All detailed spectra were recorded with 50.6 W, a step size of 0.1 eV and a pass energy of 23.5 eV. The binding energies were calibrated with respect to the carbon 1s (C1s) emission line at 284.8 eV.

4.1.2.6 Electrochemical impedance spectroscopy

Alternating current electrochemical impedance spectroscopy measurements were carried out to record the conductivity of the $BaCoO_{1.80}(OH)_{0.86}$ pellet. The pellet was placed inside the JANIS STVP-200-XG cryostat, which was operated under static helium atmosphere of 1 bar pressure. The pellet was investigated in the temperature range of 228 K to 298 K. Impedance measurements were recorded using a Solartron 1260 frequency response analyzer while applying an AC signal of 100 mV amplitude with frequency ranging from 1 MHz to 100 mHz. Fitting of the data was performed using the Z-view program [109].

4.1.2.7 Scanning electron microscopy and energy dispersive X-ray spectroscopy

The scanning electron microscopy (SEM) images were taken using the secondary electron detector of a Philips XL30 FEG scanning electron microscope operating at 30 keV. For energy dispersive spectroscopy (EDAX) analysis the EDAX Genesis system was used and an energy resolution of about 140 eV was applied. The mapped area was of the order of 100 μm^2 and the Ba to Co ratio was determined from the Ba L and Co K lines. The sample was sputtered with approximately 10 nm of Au prior to the measurements. The mean particle diameter was determined using the software “image j”.

4.1.3 Results and discussion

4.1.3.1 Microstructure, composition and crystal structure of $BaCoO_{1.80}(OH)_{0.86}$

The morphology of the as-synthesized powder was studied with scanning electron microscopy (SEM, see Figure 4.4). The formation of spherical hollow particles could be observed, with particles showing a mean diameter of 0.3 µm, which is a typical morphology obtained with this method according to our experience [34, 222].

Elemental analysis of the powder was carried out using energy dispersive X-ray spectroscopy (EDAX, see Figure 4.45 in the section 4.5), which confirmed a 1:1 ratio of Ba:Co (experimentally 1:1.02(2)). The average oxidation state of Co was determined by iodometric titration and found to be $Co^{+2.46(2)}$, corresponding to an approximate composition of $BaCoO_{2.22}$ [193]. We found that the compound contained significant amount of water, and the content of crystalline water could be approximated to 0.43 H_2O per formula unit (see high temperature behavior of the compound reported in section 4.1.3.2). From the analysis performed, we conclude that the compound has an approximate overall composition of $BaCoO_{2.22}(H_2O)_{0.43}$ = $BaCoO_{2.66}H_{0.86}$ = $BaCoO_{1.80}(OH)_{0.86}$.

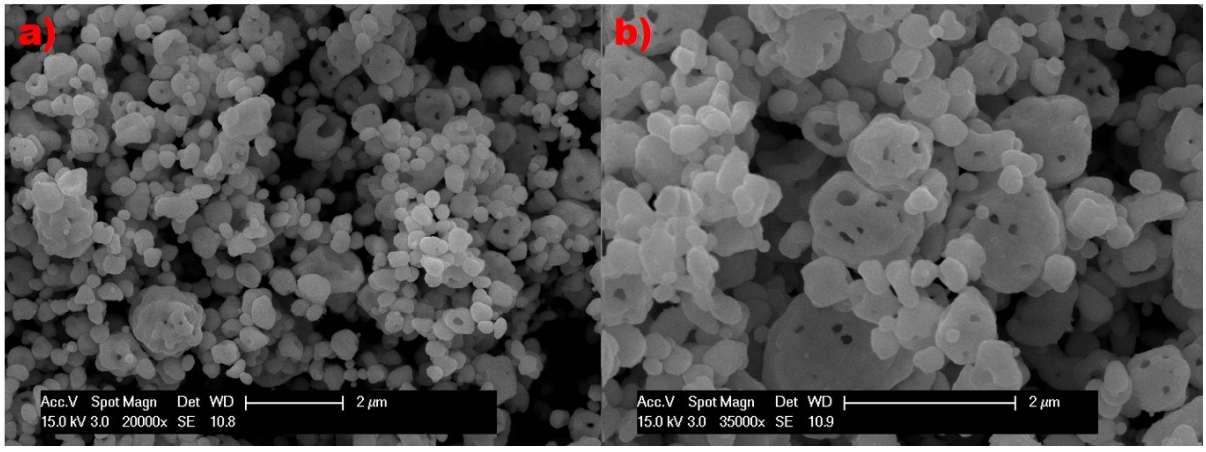

Figure 4.4: SEM micrographs of as-synthesized $BaCoO_{1.80}(OH)_{0.86}$ powder.

For structural analysis, the compound was prepared using deuterium oxide as the solvent, and examined via X-ray and neutron powder diffraction. $BaCoO_{1.80}(OD)_{0.86}$ showed diffraction patterns (see Figure 4.5) with reflection groups significant for the presence of a distorted perovskite type phase with ccp stacking of the BaX_y layers. The patterns showed a clear resemblance to the ones of LW-$BaFeO_{2.33}(OH)_{0.33}$, which is a 6 x $2\sqrt{2}$ x $\sqrt{2}$ superstructure of the cubic aristotype structure (space group *Cmcm*) and was reported previously by our group [37]. Pawley Fits were used to confirm the validity of this symmetry. For LW-$BaFeO_{2.33}(OH)_{0.33}$ [37] the symmetry lowering originates from an ordering of anion vacancies in the anion deficient lattice. The observation of structural similarity for both compounds is chemically plausible, since $BaCoO_{1.80}(OD)_{0.86}$ has a (nearly) identical overall content of anion vacancies. Therefore, the structure of $BaCoO_{1.80}(OD)_{0.86}$ was refined using the structural model of LW-$BaFeO_{2.33}(OH)_{0.33}$ [37] as the starting model.

It was previously shown by V. Jayaraman et. al. that deuterated samples can facilitate the identification of the deuterium positions within a perovskite lattice [223]. In the case of $BaCoO_{1.86}(OD)_{0.86}$, coupled analysis of XRD and NPD data gives the potential to have high scattering contrasts between the different types of atoms, since strong X-ray scatterers (Ba and Co) are present next to weak X-ray scatterers (O), and strong neutron scatterers (Ba, O and D) are present next to weak nuclear scatterers (Co). We attempted to identify potential D

positions by Fourier difference mapping, which were then used as starting positions for the structural analysis. Although scattering contrasts are good, we observed strong correlations between structural parameters when using a very flexible refinement model (e. g., with independent thermal parameters for all oxygen ions), therefore, chemically plausible constraints were used (e. g., identical thermal parameters for same types of atoms). For the location of deuterium, a very strong correlation with the occupancy factor was observed, which we took into account by limiting the thermal parameter to a value of 5 Å² (both parameters increased when refining independently). By this, we obtained a good fit to the pattern (Figure 4.5) based on a chemically plausible structural model (see Table 4.1), with bond distances given in Table 4.2. The D-O bond lengths are in the order of 1.3 - 1.4 Å. This value is too high for a deuterium ion being strongly localized within a covalent D-O bond, which we think could relate to a poor localization of the deuterium between the two neighbouring oxide ions.

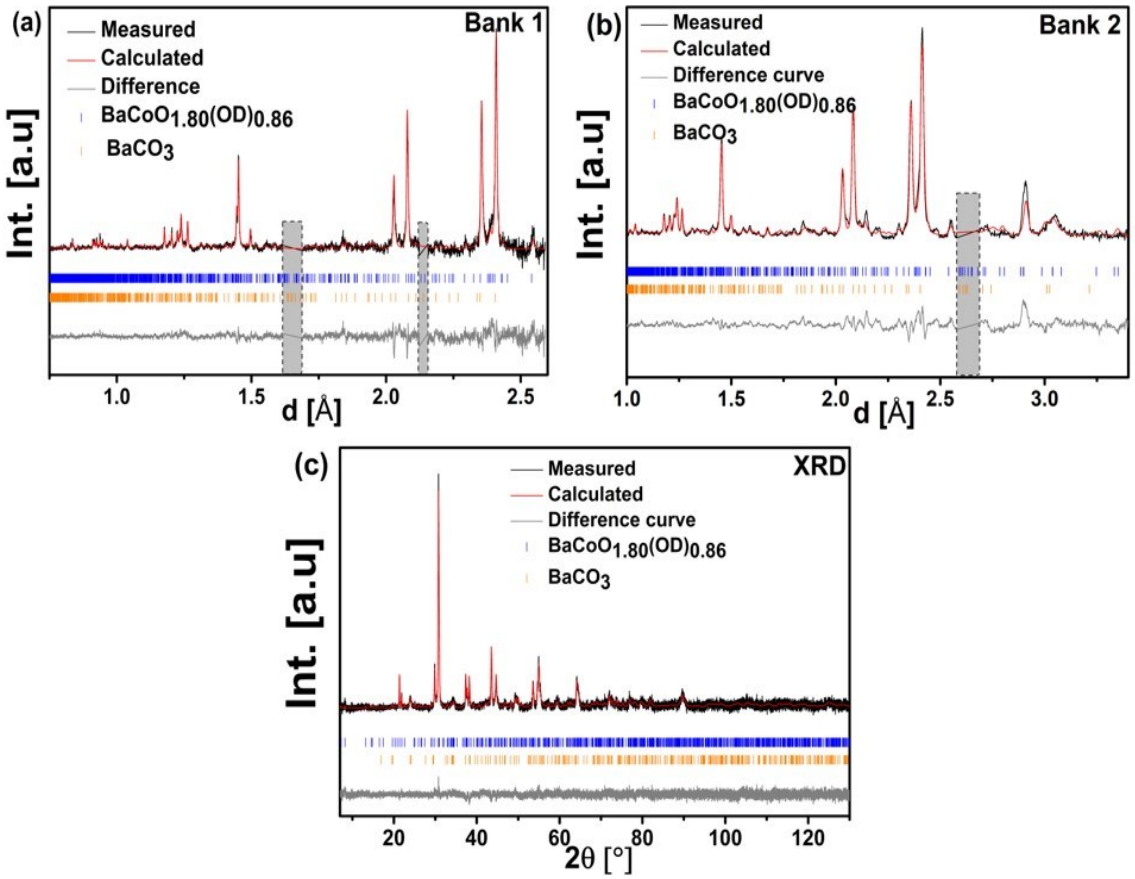

Figure 4.5: Coupled Rietveld analysis of neutron and X-ray powder diffraction patterns of $BaCoO_{1.80}(OD)_{0.86}$. Reflection groups (marked with grey boxes) with strong intensity contributions of $BaCO_3$ (identified by a different shape) were omitted from the neutron diffraction data due to unfavorable correlation with the structural parameters of the main phase.

A drawing of the structure is provided in Figure 4.6. It is found that strong structural relaxations occur in order to account for the incorporation of a large amount of protons. The Co ions appear to shift away from the oxide ions, which are close to the determined deuterium positions within the structure. In addition, the Ba ions shift strongly around the OD groups, whereas they reside closer to their ideal position when no deuterium is close. This need for structural relaxations on water incorporation is also expressed by the change of cell volume on water uptake. Hydrated phases of Ba-rich perovskites with high water content $BaMO_y(OH)_z$, such as $BaInO_2OH$ [224,225], $BaFeO_{2.33}(OH)_{0.33}$ [37], and $BaFeO_{2.25}(OH)_{0.5}$ [37] are known to have a significantly higher volume per $BaMX_{y+z}$ unit (X = O, OH) than their water free counterparts

$BaMO_{y-0.5z}$. Such differences in the volumes per formula unit can be easily visualized from the calculation of a pseudocubic lattice parameter ($a_{ps.cub} = (V_{f.u.})^{1/3}$) from the cube root of the volume per $BaCoX_{3-y}$ formula unit ($V_{f.u.}$). In agreement with the presence of water in the compound, the pseudocubic lattice parameter of $BaCoO_{1.80}(OH)_{0.86}$ (4.12 Å) was found to be significantly higher than the one of $BaCoO_{2.22}$ (4.08 Å [193, 211, 212], which can be considered as the corresponding water-free oxide). This volume difference is further similar to what was observed for the transformation of $BaFeO_{2.33}(OH)_{0.33}$ (4.14 Å) to $BaFeO_{2.5}$ (4.078 Å) [37].

Table 4.1: Structural parameters for refined $BaCoO_{1.80}(OD)_{0.86}$ presented along with the unit cell parameters, GOF and R_{wp} values. Standard deviations given are numerical standard deviations from the refinement and do not necessarily represent an interval of trust.

Label	Atom	site	x	y	Z	Occ.	Beq.
Ba1	Ba^{2+}	4*c*	**0**	0.6030(8)	¼	1	1.27(4)
Ba2	Ba^{2+}	4*c*	**0**	0.16118(8)	¼	1	
Ba3	Ba^{2+}	8*g*	0.8292(3)	0.1371(6)	¼	1	
Ba4	Ba^{2+}	8*g*	0.3417(3)	0.1317(6)	¼	1	
Co1	Co^{3+}	8*g*	0.7519(6)	0.3956(12)	¼	1	0.80(3)
Co2	Co^{3+}	8*g*	0.5713(5)	0.3364(10)	¼	1	
Co3	Co^{3+}	8*g*	0.0779(6)	0.3764(13)	¼	1	
O1	O^{2-}	4*c*	**0**	0.8620(14)	¼	1	2.24(2)
O2	O^{2-}	4*c*	**0**	0.3808(15)	¼	1	
O3	O^{2-}	8*g*	0.7429(4)	½	¼	1	
O4	O^{2-}	8*g*	0.3343(5)	0.3751(11)	¼	1	
O5	O^{2-}	8*d*	**¼**	**¼**	**0**	1	
O6	O^{2-}	8*e*	0.4147(6)	**0**	**0**	1	
O7	O^{2-}	8*e*	0.9247(4)	**0**	**0**	1	
O8	O^{2-}	16*h*	0.0809(5)	0.2601(6)	0.9887(14	1	
D1	D^{+}	8	0.2740(3)	0.2629(9)	0.293(3)	0.75(2	5
D2	D^{+}	8	0.5507(8)	0.5443(11)	0.700(5)	0.40((	
***a* [Å]**	24.2965(8)	***b***	11.9436(4)	***c* [Å]**	5.7693(2)		
GOF [XRD+NPD]	1.38			***R_{wp}* [%] [XRD+NPD]**	2.55		
R_{Bragg} [%]	1.14 **[XRD]**		3.95 **[NPD bank 1]**				

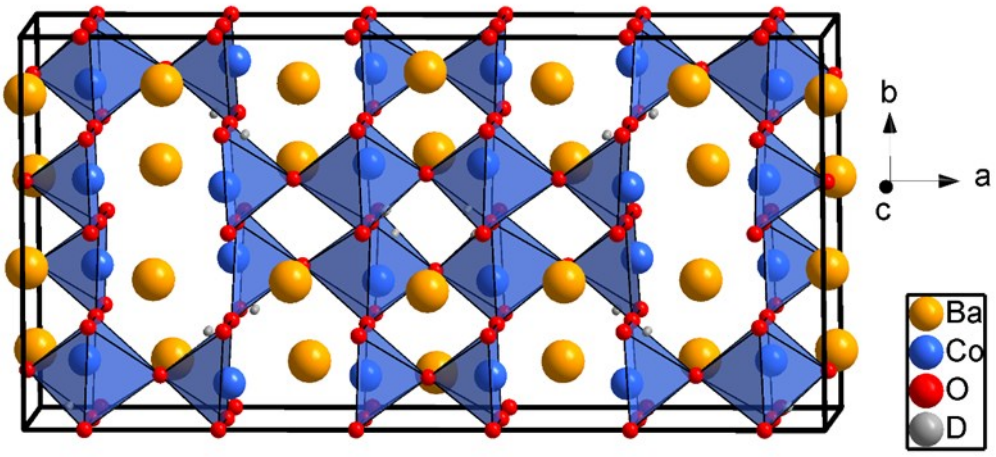

Figure 4.6: Structural representation of $BaCoO_{1.80}(OD)_{0.86}$.

Table 4.2: Refined bond distances between cations and anions for $BaCoO_{1.80}(OD)_{0.86}$

Cation	Distances to anions [Å]	Cation	Distances to anions [Å]	Cation	Distances to anions [Å]
Ba1	2.65(2) (O2 x 1)	**Ba3**	2.76(2) (O5 x 2)	**Co1**	1.92(1) (O3 x 2)
	2.80(2) (O6 x 4)		2.80(1) (O3 x 2)		2.11(2) (O4 x 1)
	2.89(1) (O2 x 2)		2.89(1) (O4 x 2)		2.26(1) (O5 x 2)
	2.90(1) (O8 x 4)		3.03(1) (O8 x 2)		
			3.13(2) (O4 x 1)		
			3.19(1) (O7 x 1)		
Ba2	2.62(2) (O2 x 1)	**Ba4**	2.67(1) (O8 x 2)	**Co2***	1.76(1) (O1 x 1)
	2.75(1) (O8 x 4)		2.78(1) (O6 x 2)		1.81(1) (O8 x 2)
	2.90(2) (O1 x 2)		2.91(2) (O4 x 1)		2.34(2) (O4 x 1)
	3.02(2) (O7 x 4)		3.01(1) (O5 x 2)		2.43(1) (O7 x 2)
			3.21(1) (O3 x 2)		
				Co3	1.89(1) (O2 x 1)
					2.05(1) (O8 x 2)
					2.07(1) (O6 x 2)

4.1.3.2 Temperature stability of $BaCoO_{1.80}(OD)_{0.86}$

The presence of protons within the structure can be monitored by ex-situ FT-IR studies recorded after heating the compound to various temperatures. Within those measurements, a broad band was observed for $BaCoO_{1.80}(OH)_{0.86}$ at 298 K in the spectral range 3300-3500 cm^{-1}, which can be assigned to the OH stretching mode [37,107] (see Figure 4.7). Apart from FT-IR, the incorporation of OH groups is also reflected in distinct valence band features at 9.1 eV and 5.0 eV from XPS studies (see Figure 4.8). Those features have also been observed previously at surfaces of materials with perovskite type structure,[226] as well as on other oxides [227].

FT-IR measurements were also carried out after heating as-synthesized powder of $BaCoO_{1.80}(OH)_{0.86}$ to various temperatures up to 1273 K under the flow of argon. In this respect, we found that the OH stretching mode disappeared when the compound was heated to temperatures above 673 K.

To study the water loss in more detail and to determine the amount of crystalline water, the sample was studied via simultaneous thermal analysis (STA, see Figure 4.9) TGA data show

a steep weight loss between 398 K and 463 K accompanied by an endothermic signal. This indicates a first strong release of water, which is in agreement with the structural changes as found by high temperature XRD (see later in this section). After this first initial step, the weight loss continues until 750 K, at which the TGA shows a clear kink We therefore conclude, that the water release is finished between 693 - 793 K in this more dynamic experiment as compared to the FT-IR studies on heated powder. A total mass loss of ~ 2.8 - 3.2 wt-% was found, accounting for the presence of ~ 0.38 - 0.43 H_2O molecules per $BaCoX_{3-y}$ unit. From this and the average oxidation state of Co, one can determine the approximate composition of the sample to be $BaCoO_{2.22}(H_2O)_{0.43}$ = $BaCoO_{2.66}H_{0.86}$ = $BaCoO_{1.80}(OH)_{0.86}$.

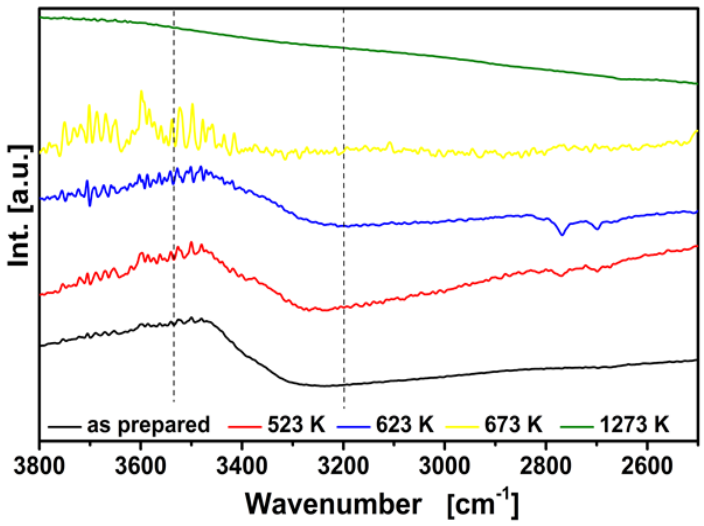

Figure 4.7: FTIR spectra for $BaCoO_{1.80}(OH)_{0.86}$ before and after heating to a variety of temperatures up to 1273 K.The curves are scaled to improve the visibility of the bump corresponding to the OH stretching band.

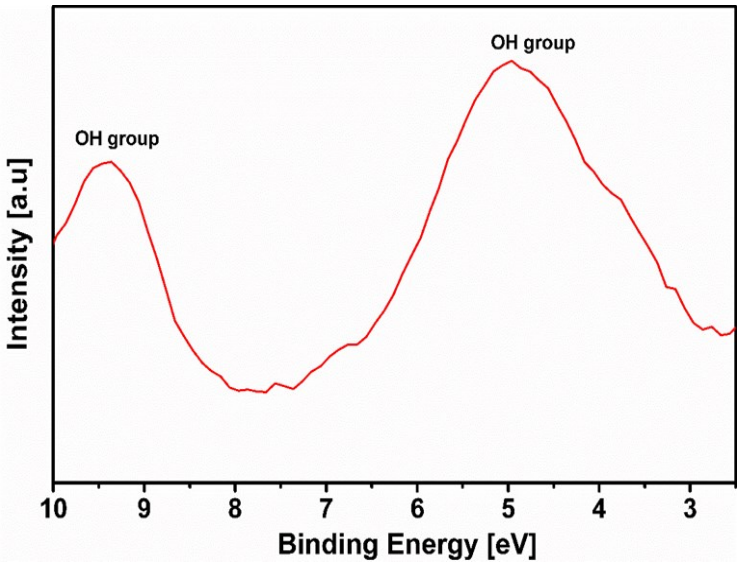

Figure 4.8: XPS of the valence band for $BaCoO_{1.80}(OH)_{0.86}$ powder.

Changes on water loss were further studied by HT-XRD (see Figure 4.10). Although this methodology cannot provide detailed information on changes within the anion sublattice, it is well suited to investigate changes in phase fractions and unit cell volume on variation of temperature. For this analysis, the structural model of $BaCoO_{1.80}(OH)_{0.86}$ was used, without refining any positional parameters. Further, the reader needs to be aware that this study has

different kinetics than the ex-situ FT-IR and in-situ STA measurements. Although a similar heating rate of 10°C min^{-1} was used for HT-XRD, the samples had to be kept at measurement temperature for at least 10 min to record a pattern of sufficient quality, i. e., from which lattice parameters and phase fractions could be determined. This need for longer holding times can shift the water losses to lower temperatures than what was observed for STA.

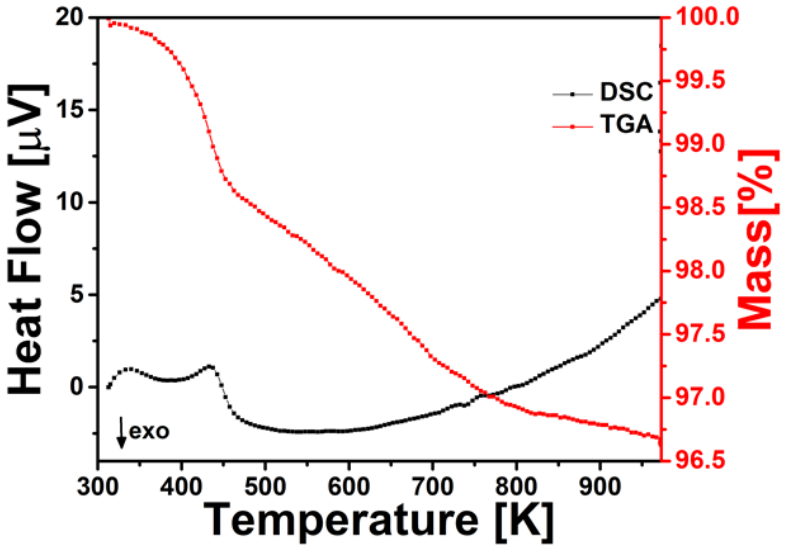

Figure 4.9: TGA/DSC measurement on $BaCoO_{1.80}(OH)_{0.86}$ under a flow of argon.

Strong changes in the XRD pattern were observed above 393 K, which approximately coincides with the steep weight loss on first water release observed in STA. At this temperature, a second perovskite type phase with cubic symmetry (*Pm*-3*m*) can be detected, which coexists with the orthorhombic phase up to 583 K (see Figure 4.10 and Figure 4.11a) and becomes the main phase around 623 K (Figure 4.11b). In addition to the small amount of $BaCO_3$, a small number of further reflections appeared at ~ 27°, 31° and 35° 2θ, which only disappear at the highest temperature of 1023 K. Attempts were made to index those reflections based on *klassengleiche* supergroups of the cubic (or orthorhombic) cell, which was not successful. The reflections were therefore assigned to an unknown impurity phase by ruling out known structures of $Ba_xCo_yO_z$ phases from the ICSD. The assignment to an impurity is also plausible considering that those reflections are still present at 923 K, where only a 2H hexagonal perovskite type phase was observed (see later in this section).

The water loss occurring at 393 K can be easily followed by the changes of the weight-fraction averaged pseudocubic lattice parameter $a_{ps.cub}$(average) (see Figure 4.12a), which is a representative for the average cell volume per unit cell, and shows a sudden drop at this temperature. In addition, an anomaly of $a_{ps.cub.}$(orthorhombic) was observed. On water loss, the orthorhombic phase shows a decrease in cell volume (visually evident from the shifts of the reflections (see Figure 4.10). Surprisingly, the newly formed cubic phase then has a higher value of $a_{ps.cub.}$ than the orthorhombic phase. The weight fraction of the cubic phase increases up to a temperature of 623 K, where it becomes the main perovskite type phase present up to 723 K (see Figure 4.11b and Figure 4.12b).

At a temperature of 623 K, the formation of an additional hexagonal perovskite type phase was observed (2H, $P6_3/mmc$, a = 5.7609(3) Å and c = 4.4613(4), see Figure 4.11c), which has a strongly reduced volume per formula unit as compared to the other phases (see Figure 4.12a). The relative fraction of this phase increases on heating to higher temperatures (see Figure

4.12b), and it becomes the only perovskite type phase at 923 K. Finally, a single phase cubic perovskite type compound is found at a temperature of 1023 K (see Figure 4.11d, a = 4.137 Å), similar to the reports on cubic $BaCoO_{2.22}$ by Mentré et al.[193].

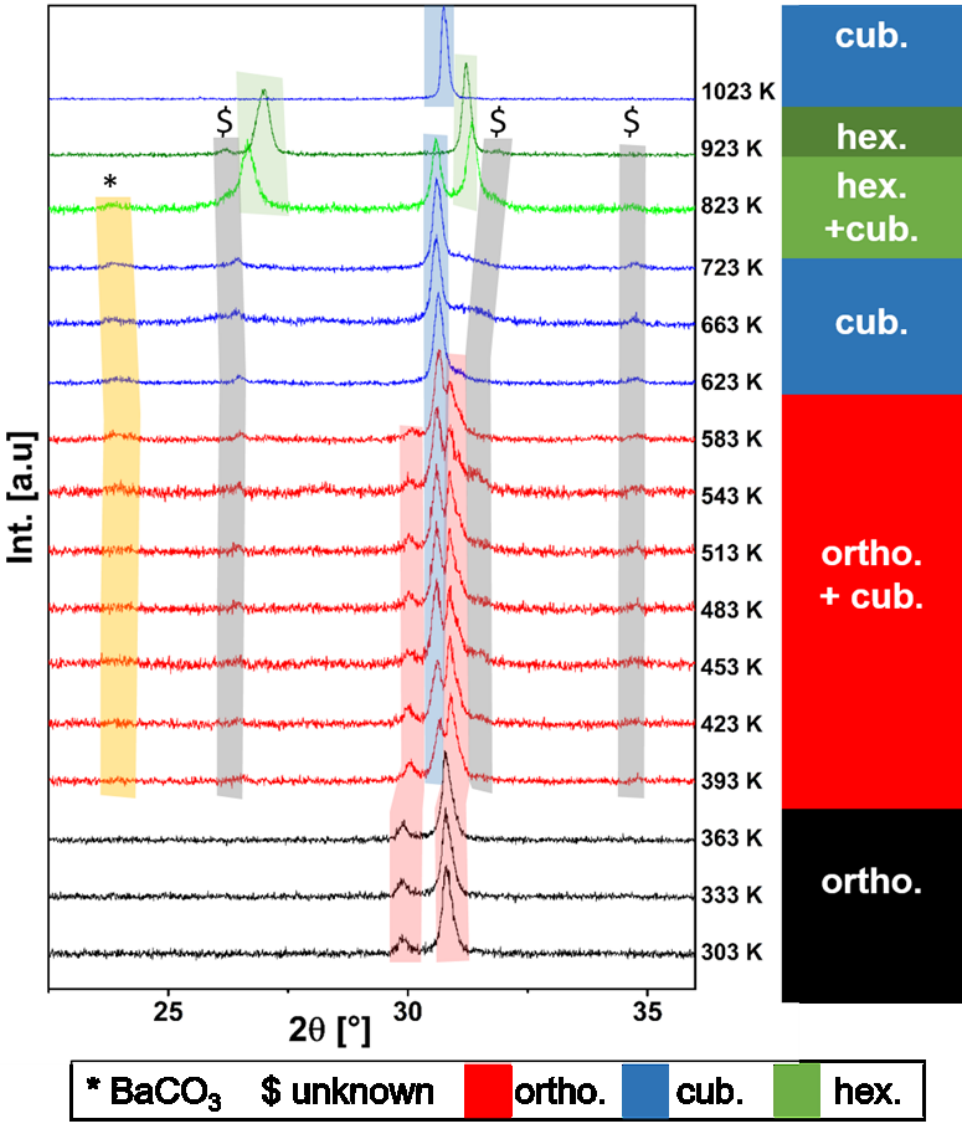

Figure 4.10: XRD patterns of $BaCoO_{1.80}(OH)_{0.86}$ recorded between 303 K and 1023 K under a flow of dry argon. Intensities are normalized to the reflection with maximum intensity.

Further, the observation of the cubic and hexagonal phases at high temperatures are similar to the findings described by Mentré et al. [193] in their high temperature study of $BaCoO_{2.22}$ (which can be considered as the water-free analogous composition to $BaCoO_{1.80}(OH)_{0.86}$). They report [193] a transformation to a hexagonal compound at temperatures above ~523 K, and observed a retransformation to cubic on further heating. However, their temperature range of coexistence of cubic and hexagonal phases [193] is different than what was observed here on studying $BaCoO_{1.80}(OH)_{0.86}$, and this might indicate an influence of residual water on stabilization of the cubic symmetry.

We would also like to point out that the observed changes in phases and cell volumes are different to what we found on heating HW-$BaFeO_{2.25}(OH)_{0.5}$ [37]. For this phase, we found a step-wise transformation to orthorhombic $BaFeO_{2.33}(OH)_{0.33}$ and monoclinic $BaFeO_{2.5}$, with narrow temperature ranges of co-existence of two phases. In future, we will aim to investigate the

unusual phase changes for $BaCoO_{1.80}(OH)_{0.86}$ in more detail via a high temperature neutron diffraction study, for which data recorded at a diffractometer with higher neutron flux will be required.

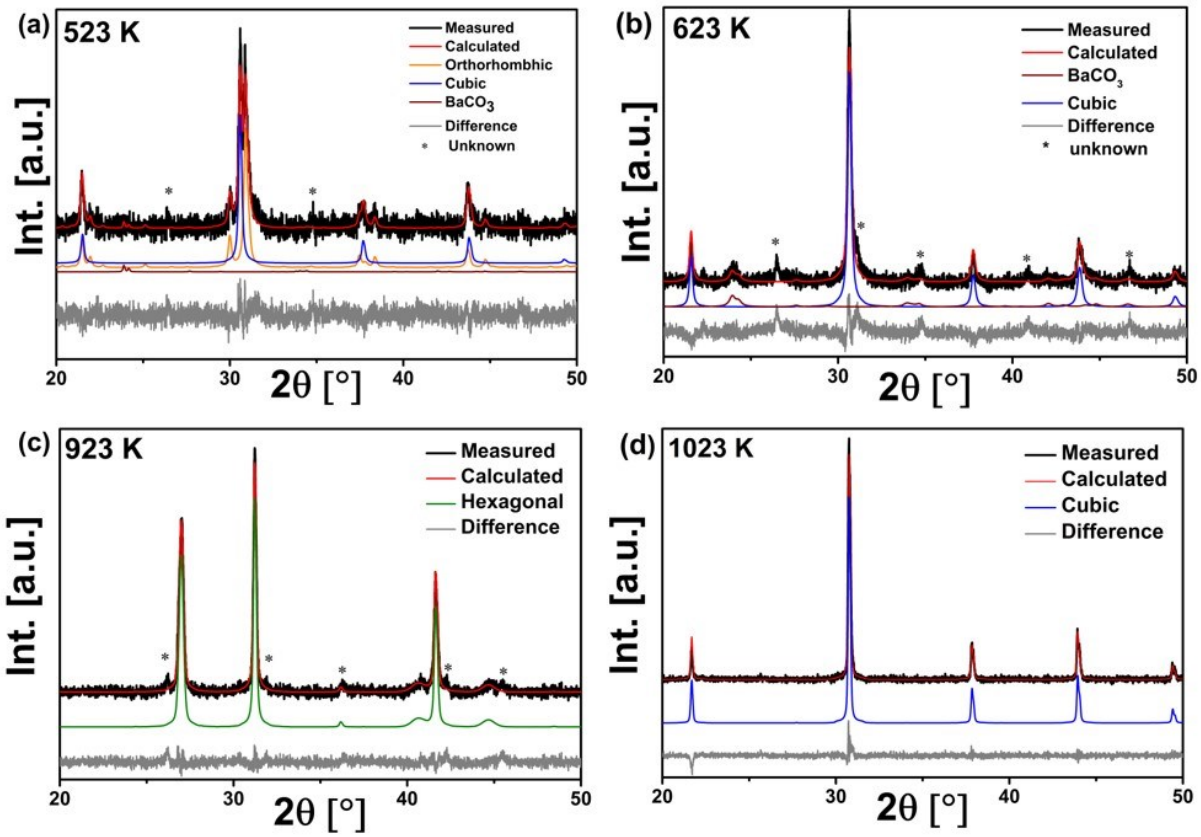

Figure 4.11: Rietveld analyses of high-temperature XRD data at representative temperatures. (a) Phase mixture of a cubic (*Pm*-3*m*) and orthorhombic (*Cmcm*) phase recorded at 523 K. (b) Cubic phase (*Pm*-3*m*) recorded at 623 K. (c) 2H perovskite type phase ($P6_3/mmc$) at 923 K. (d) Cubic phase (*Pm*-3*m*) recorded at 1023 K. Reflections of an unknown impurity phase are marked with an asterisk.

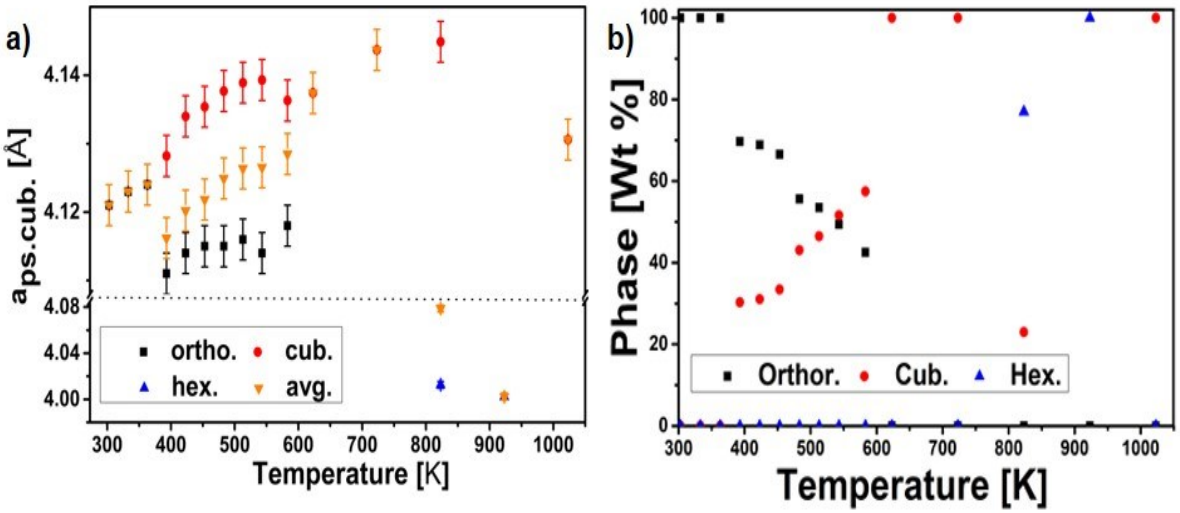

Figure 4.12: Pseudocubic lattice parameters (a) and relative phase fractions (b) of phases with perovskite type structure. Standard deviations are given as the numerical standard deviation of the refinement multiplied by 3. Numerical standard deviations obtained for the phase quantification do not represent a meaningful interval of trust, which is at least in the order of ~ 2 wt-% for such a phase quantification, and have therefore been omitted.

4.1.3.3 Temperature dependent conductivity studies

The conductivity of the title compound was studied by impedance spectroscopy in the temperature range between 298 K and 228 K. As for the ferrites [37], the preparation of sintered pellets of $BaCoO_{1.80}(OH)_{0.86}$ is not possible (explained by strong volume changes on water uptake of water-free sintered pellets, which result in the cracking of pellets); therefore, as-synthesized powder was compacted to form stable pellets by means of isostatic pressing at a pressure of 700 kN, resulting in densities in the order of ~ 85 % relative to the crystallographic density.

Figure 4.13 shows an example of the Nyquist and Bode plots of a typical impedance spectrum. The Nyquist plot can be described as a strongly depressed semicircle, which can be well fitted by an equivalent circuit consisting of a resistance and a constant phase element (CPE) in parallel. In the low frequency range, the impedance is dominated by its real contribution, and no electrode response could be observed independent of the choice of the electrode material (sputter coated Au or Pt). This indicates a strong influence of electronic charge carriers and the compound behaves mainly like a simple resistor at frequencies below ~ 10 kHz. Relative permittivity of 80 – 150 indicate a predominance of grain and/or grain boundary phenomena on the overall conductivity [37].

The overall electrical conductivity of $BaCoO_{1.80}(OH)_{0.86}$ is in the order of ~10^{-4} S cm^{-1} at 298 K. This value is three orders of magnitude higher than what was observed for LW-$BaFeO_{2.5}$ and one order of magnitude higher than found for Y-doped $BaZrO_3$, most likely resulting from a different nature of the charge carrier. Therefore, we conclude that the electrical conductivity of $BaCoO_{1.80}(OH)_{0.86}$ is dominated by electronic charge carriers and that the determination of a protonic contribution to the overall conductivity is not easily possible. To separate those phenomena further techniques, e. g., quasi-elastic neutron scattering will be examined in the future. Significant electronic conductivity is in agreement with cobalt being present in a mixed valent state, which can facilitate electronic charge transport via a hopping mechanism.

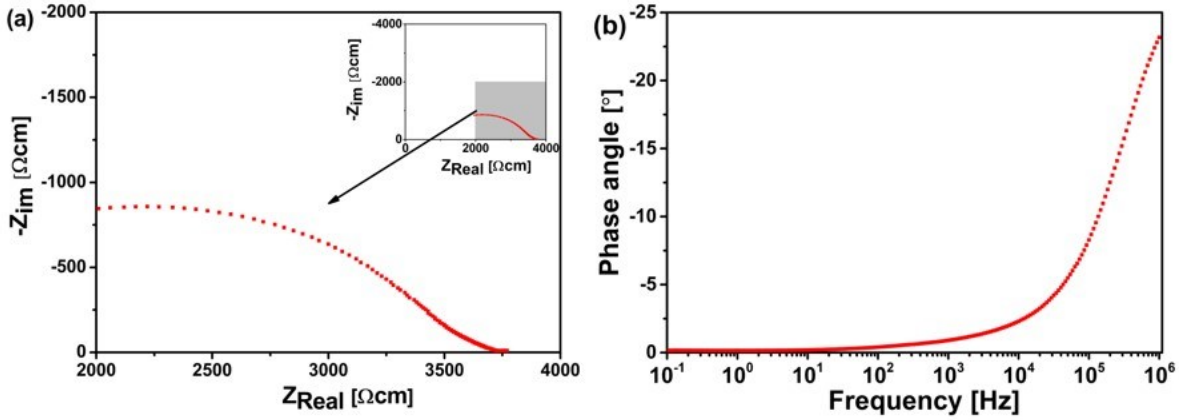

Figure 4.13: (a) Nyquist and (b) Bode plots for the impedance spectroscopical measurement for $BaCoO_{1.80}(OH)_{0.86}$ recorded at 298 K.

The temperature dependency of the conductivity is shown in Figure 4.14 for two different samples in the form of an Arrhenius type plot, from which the activation energy can be calculated to be 0.27(1) eV. Although small differences in total conductivity are found depending on the exact preparation, the overall magnitude of the conductivity is reproducible

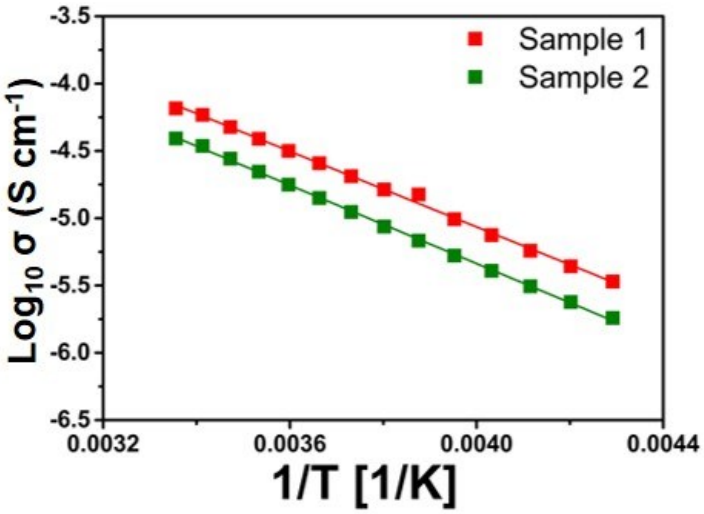

Figure 4.14: Arrhenius plot for temperature dependent total electrical conductivity of two samples of $BaCoO_{1.80}(OH)_{0.86}$ in the temperature range between 240 – 300 K.

4.1.4 Conclusion

Here we have shown that a new phase with composition $BaCoO_{1.80}(OH)_{0.86}$ can be prepared by means of nebulized spray pyrolysis. The compound can be understood as the water rich analogue to $BaCoO_{2.22}$ [193], and was confirmed to be isotypic to LW-$BaFeO_{2.33}(OH)_{0.33}$ [37] by a coupled analysis of X-ray and neutron powder diffraction data. In comparison to $BaFeO_{2.5}$ [37], protons can be stabilized within this compound upto a much higher temperature of ~673 K, in agreement with findings by FT-IR, STA, and HT-XRD studies. Therefore, the results reported here indicate that Ba-rich $Ba(Co,Fe)O_{3-x}$ compounds could be interesting catalysts for the use in PCFCs. Furthermore, the material shows an unusual and complex structural behaviour on heating and water release, which will be investigated in more detail within future studies.

Achknowledgements

O. Clemens acknowledges funding by DFG within CL551/2-1. Neutron diffraction beam time at ISIS was provided by the Science and Technology Facilities Council.

4.2 Synthesis of Bifunctional $BaFe_{1-x}Co_xO_{3-y-\delta}(OH)_y$ Catalysts for the Oxygen Reduction Reaction and Oxygen Evolution Reaction

Aamir Iqbal Waidha [a], Lingmei Ni [b], Jasim Ali [a], Maren Lepple [c,d], Manuel Donzelli [a], Supratik Dasgupta [e], Stephan Wollstadt [a], Lambert Alff [e], U. I. Kramm [b, *], Oliver Clemens [a,f,*]

[a] Technische Universität Darmstadt, Institut für Materialwissenschaft, Fachgebiet Materialdesign durch Synthese, Alarich-Weiss-Straße 2, 64287 Darmstadt, Germany.

[b] Technische Universität Darmstadt, Graduate School of Excellence Energy Science and Engineering, Institut für Materialwissenschaft und Fachbereich Chemie, Fachgebiet Katalysatoren und Elektrokatalysatoren, Otto-Berndt-Str. 3, 64287 Darmstadt, Germany.

[c] Technische Universität Darmstadt, Eduard-Zintl-Institut für Anorganische und Physikalische Chemie, Alarich-Weiss-Straße 12, 64287 Darmstadt, Germany.

[d] DECHEMA-Forschungsinstitut, Theodor-Heuss-Allee 25, 60486 Frankfurt am Main, Germany.

[e] Technische Universität Darmstadt, Institut für Materialwissenschaft, Fachgebiet Dünne Schichten, Alarich-Weiss-Straße 2, 64287 Darmstadt, Germany.

[f] Karlsruher Institut für Technologie, Institut für Nanotechnologie, Hermann-von-Helmholtz-Platz 1, 76344 Eggenstein Leopoldshafen, Germany.

Corresponding author: oliver.clemens@md.tu-darmstadt.de and kramm@ese.tu-darmstadt.de

Abstract

Perovskite oxides with mixed ionic and electronic conductivities are very promising candidates for their application as energy materials related to fuel cell and metal air battery integration. In this article, we report on the systematic characterization of mixed proton and electron conducting compounds of composition $BaFe_{1-x}Co_xO_{3-y-\delta}(OH)_y$ synthesized via nebulized spray pyrolysis. Independent on the value of x, all samples $BaFe_{1-x}Co_xO_{3-y-\delta}(OH)_y$ were found to crystallize in an orthorhombic ordering/distortion variant of the perovskite type structure (space group *Cmcm*) and are isotypic to the border phases (x = 0 or 1) reported previously. A minimum water content was observed for the composition with x = 0.5, which increases steadily for Co or Fe richer compositions. Impedance studies show that the conductivity increases with increasing Co-content, with $BaCo_{0.5}Fe_{0.5}O_{2.07}(OH)_{0.74}$ showing a total electrical conductivity of 10^{-7} S cm^{-1} at 298 K, an order of magnitude higher than found for $BaFeO_{2.33}(OH)_{0.33}$. Further, bifunctional catalytic activity for the oxygen evolution reaction (OER) and oxygen reduction reaction (ORR) was found for the compounds of the series as investigated in 0.1M KOH, with $BaFe_{0.8}Co_{0.2}O_{3-y-\delta}(OH)_y$ possessing the best bifunctional performance parameter of ΔU =1.10 V, which is comparable to that of other non-precious metal catalysts

Keywords

Perovskites, PCFC, bifunctional ORR/OER catalysts, mixed conductors, proton conductors.

4.2.1 Introduction

The next generation electrochemical systems offering clean energy such as metal-air batteries, water electrolysers and low temperature fuel cells are promising technologies due to their capability for storing or converting electrical energy generated from renewable resources. The practical application of these technologies depends on various factors, where a bottleneck can lie in finding suitable catalysts for the oxygen evolution reaction (OER) and the oxygen reduction reaction (ORR). In alkaline medium, (Ni,Fe)OOH is the most active OER catalyst [228, 229], while there are different materials that are active for the ORR. However, catalysts that reveal a good activity for both reactions are rare but could become of crucial interest for the design of compact metal air batteries. Therefore, the preparation of new iron containing oxide hydroxide systems and the determination of their electrocatalytic properties is of general interest within the context of energy research.

Perovskite-based ferrates and cobaltates ($AFe_{1-x}Co_xO_{3-\delta}$) have attracted attentions due to their interesting catalytic properties for the ORR in solid oxide fuel cells (SOFCs) and the OER in solid oxide electrolysis cells (SOECs)[213,83]. The perovskite type structure (with "ideal" ABX_3 composition, A = alkaline earth or lanthanide ion, B = transition metal, X = anion) can be described as a cubic closed packed (*ccp)* arrangement of AX_3 layers with $1/4^{th}$ of the octahedral sites being occupied by the B cation resulting in a corner shared network of BO_6 octahedral. The anion sublattice in the perovskite structure is quite flexible and large amounts of vacancies can be structurally stabilized, which can induce oxide ion conductivity and electronic conductivity for mixed valent compounds, forming the prerequisite for developing catalytic activity for ORR/OER in fuel cell applications [230].

Within the perovskite framework, anion vacancies can often be occupied by water, resulting in the formation of hydroxyl groups [231] according to

$$H_2O + V_O^{\bullet\bullet} + O_O \rightarrow 2\,(OH)^{\bullet}$$

The formed proton conduction can in turn lower the operation temperature of ceramic fuel or electrolysis cells due to the higher mobility of protons as compared to oxide ions. A high content of soft A-site cations such as Ba seems to favor the uptake of larger amounts of water. Therefore, compounds with composition $BaFe_{1-x}Co_xO_{3-y-\delta}(OH)_y$ could become interesting candidates for the use as ORR and OER catalysts in protonic ceramic fuel and electrolysis cells (PCFC, PCEC) [37, 212] or alkaline fuel cells [214].

In previous works, Suga et al. studied the electrochemical oxidation of $BaFeO_{2.5}$ to $BaFeO_3$ in alkaline aqueous media, without considering details of the OER activity further [214]. There are various studies on the catalytic activity of doped $BaCoO_{3-x}$ (either on the A- or the B-site), but only little has been reported about the activity of the non B-site doped compounds, which has been assigned by other reports to the difficulty of preparing it in a *ccp* stacked perovskite type structure [232, 233] via classical synthesis routes. Recently, we have demonstrated that $BaCoO_{1.80}(OH)_{0.86}$ [82] can be easily prepared via nebulized spray pyrolysis (NSP), and is isotypic to $BaFeO_{2.33}(OH)_{0.33}$[37, 212, 211]. Therefore, the use of NSP could provide access for the first preparation of the whole oxide hydroxide series $BaFe_{1-x}Co_xO_{3-y-\delta}(OH)_y$, without the need to dilute the B-sublattice with electrochemically inactive cations such as Zr^{4+}, and a subsequent study of the electrocatalytic properties.

In this article, we present a systematic study on a whole series of $BaFe_{1-x}Co_xO_{3-y-\delta}(OH)_y$, including sample preparation and characterisation, determination of the intrinsic electrical properties and of the structural stability, as well as a characterization of the catalytic activity for

OER/ORR. All compounds with $x \neq 0, 1$ are found to be isotypic to $BaFeO_{2.33}(OH)_{0.33}$ and to $BaCoO_{1.80}(OH)_{0.86}$ with a (distorted) *ccp* stacking of BaX_{3-y} layers, confirmed by Rietveld analysis of the X-ray powder diffraction (XRD) data, and compositional and electrical properties have been determined further. For the first time, this allows us to characterize a morphologically similar series of cubic perovskite related $BaFe_{1-x}Co_xO_{3-y-\delta}(OH)_y$ in the absence of additional dopants for their electrocatalytic activity. For all values $0 < x < 1$, bifunctional activity for ORR and the OER reaction was found, highlighting the importance of the presence of a humid atmosphere during synthesis to obtain dopant free barium cobaltate ferrates with similar catalytic activity as compared to doped counterparts.

4.2.2 Experimental

4.2.2.1 Material Synthesis

Powders with chemical composition $BaFe_{1-x}Co_xO_{3-y-\delta}(OH)_y$ ($0 \leq x \leq 1$) were synthesized using nebulized spray pyrolysis (NSP). To prepare the starting precursor solution, $Ba(NO_3)_2$ (Sigma Aldrich, 99.99%), $Fe(NO_3)_3(H_2O)_9$ (Sigma Aldrich, 99.99%) and $Co(NO_3)_2(H_2O)_6$ (Sigma Aldrich, 99.99%) were dissolved in de-ionized water to obtain an overall cation concentration of 0.06 mol l^{-1}, and the mixture was stirred for 30 minutes in order to obtain a homogenous transparent solution. For the synthesis, a setup as previously described [34] was used. The as-prepared solution was injected into the nebulizer unit using a syringe pump with a flow rate of 1.5 ml min^{-1}, while operating the ultrasonicator to generate the mist at a generator voltage and current of 47.0 V and 0.51 A respectively. The precursor mist formed inside the nebulizer unit was transported by a carrier gas stream of argon at the rate of 2 SLM (standard liter per minute) to the reaction tube, which was maintained at 1323 K, and the compounds were collected on a glass filter collector which was held at 393 K ($0 \leq x \leq 0.5$), and 373 K ($0.6 \leq x \leq 1$) respectively, in order to obtain highest water content compounds and taking into account the lower starting temperature for water release of Co-richer compounds [82].The whole process was carried out at a constant pressure of 900 mbar.

4.2.2.2 Diffraction experiments

Room temperature XRD patterns of the hydrated compounds were recorded on a Bruker D8 diffractometer using Bragg-Brentano geometry with a fine focusing X-ray tube with Cu $K_{\alpha 1,2}$ radiation. A VANTEC detector (3° opening) and a fixed divergence slit (6 mm) were used. The total scan time was set to 2 hours for the angular range between 5° and 80° 2θ at a step size of 0.0075°. High temperature XRD was measured using an Anton Paar HTK1200 sample stage in the temperature range between 303 K and 773 K (heating rate of 5 K s^{-1}) in the angular range between 20° and 60° 2θ at a reduced overall measurement time of 10 min per diffractogram and under a flow of argon. These conditions were chosen as a compromise to obtain sufficient data quality for the determination of lattice parameters and phase composition, but to lower differences to the heating procedure used for simultaneous thermal analysis. Structural refinements and phase analysis were performed on the XRD patterns by the Rietveld method with the program TOPAS 5 (Bruker AXS, Germany) [95]. The instrumental intensity distribution was determined empirically within a fundamental parameters approach [108] using a reference scan of LaB_6 (NIST 660a), and the microstructural parameters were refined to adjust the peak shapes for the XRD data. For the refinements of the compounds with $x > 0$, the structural model of $BaCoO_{1.80}(OH)_{0.86}$ [82] as reported previously was used. Since Fe and Co are basically indistinguishable by means of powder diffractions, a well description of the intensity pattern could already be obtained by only refining the lattice parameters, without refining positional parameters. For $x = 0$, the structural model of HW-$BaFeO_{2.5}$ as reported in [37] was

used, again with only refining the lattice parameters. An overall isotropic parameter was refined, which was constrained to be identical to all atoms of all phases to account for absorption corrections.

4.2.2.3 Simultaneous thermal analysis and elemental analysis

Simultaneous thermal analysis (STA) combining thermogravimetric analysis (TGA) and differential scanning calorimetry (DSC) was conducted on a Netzsch STA 449 F3 Jupiter thermal analyzer. The measurements were performed in the temperature range between 300 K to 973 K using a heating rate of 10 K min^{-1} in corundum crucibles under an argon flow of 50 ml min^{-1}.

Elemental hydrogen analysis was performed on a VarioEL III CHN (Elementar). The samples were burned in Sn boats under oxygen, and the evolving gases were gas chromatographically separated and analyzed quantitatively with a thermal conductivity detector. The proton/water content is given as the mean of three independent measurements.

4.2.2.4 Fourier transform spectroscopy

Fourier-transform infrared spectroscopy measurements were conducted on a Varian spectrometer. Samples were characterized via attenuated total reflection (ATR) by mounting an ATR unit into the sample compartment of the spectrometer. The spectra were recorded in a range between 550 cm^{-1} and 4000 cm^{-1} with a spectral resolution of 0.5 cm^{-1}.

4.2.2.5 ^{57}Fe Mössbauer spectroscopy

The Mössbauer spectrum of $BaFe_{0.5}Co_{0.5}O_{2.07}(OH)_{0.74}$ was measured in transmission mode using a 100 mCi ^{57}Co/Rh source and a proportional detector. Since this sample powder is sensitive to air, 91.4 mg of it was prepared into a closed cylinder sample holder inside a glovebox. The measurement was performed at room temperature and the calibration of the isomer shift was carried out using the sextet signature of an α-Fe foil. The Mößbauer spectrum was fitted with the program Recoil assuming a Lorentzian line shape. In order to obtain a measurement of significant quality, a measurement time of one week within the limited velocity range of ± 5.8 mm s^{-1} was required. It is evident from the spectrum that this range does not provide full spectroscopic information, however based on a comparison to literature on Mössbauer spectroscopy of ferrates still some information can be gained in comparison to that compounds and iron oxidation states.

4.2.2.6 Iodometric titrations

The iodometric titrations were carried out to determine the oxidation state of the series $BaFe_{1-x}Co_xO_{3-y-\delta}(OH)_y$. 0.05 gram of the compound was dissolved in 1M HCl solution and 1 gram of KI was added to the solution. The reduction of Co^{3+} ions by I^- lead to the formation of I_2, leading to the change in colour of solution to light yellow. Few drops of starch solution were added as an indication which further changed the colour of solution to black. The solution was titrated with $Na_2S_2O_3$ till the solution became transparent.

4.2.2.7 SQUID magnetic measurements

Magnetic characterization was performed with a Quantum Design MPMS. Powder samples were encapsulated in gelatin capsules and mounted in a straw. Zero-field cooled (ZFC) and field-cooled (FC) curves were measured from 5 to 350 K in the applied field $\mu_0 H$ = 1 T. All magnetization measurements were corrected by the diamagnetic contributions of the phases and the gelatin capsule and straw used for sample mounting. Field-dependent measurement was performed at 5 K. The magnetic field was scanned from 3 to −3 T.

4.2.2.8 Energy dispersive X-ray spectroscopy

The energy dispersive X-ray spectroscopy (EDX) analysis the EDAX Genesis system was used and an energy resolution of about 140 eV was applied. The mapped area was of the order of 100 µm² and the Ba to Fe to Co ratio was determined from the Ba L, Fe K and Co K lines. The samples were sputtered with approximately 10 nm of Au prior to the measurements.

4.2.2.9 Impedance spectroscopy

Alternating current (AC) electrochemical impedance spectroscopy was carried out to characterize the conductivity of the $BaFe_{1-x}Co_xO_{3-y-\delta}(OH)_y$ pellets (x = 0, 0.3, 0,5 0.7, 1), which were prepared by first uniaxially pressing the powders followed by subsequent isostatic pressing at 700 kN and then sputtered with a thin layer of gold on both sides for electronic contacting A pellet of each sample was placed inside a JANIS STVP-200-XG cryostat, which was operated under a static helium atmosphere of 1 bar pressure. The samples were investigated in the temperature range of 298 K to 348 K. Impedance measurements were recorded using a Solartron 1260 frequency response analyzer, applying an AC signal of 100 mV amplitude with the frequency ranging from 1 MHz to 100 mHz. Fitting of the data was performed using the Z-view program [109].

4.2.2.10 Electrochemical characterization

The electrocatalytic activity of these perovskite-type $BaFe_{1-x}Co_xO_{3-y-\delta}(OH)_y$ catalysts towards OER and ORR was investigated using a conventional three electrode setup with a Hg/HgO reference electrode and glassy carbon rod counter electrode. The ferrate samples were deposited on the glassy carbon disc of a rotating disc electrode (RDE) and connected to an EC4-200 potentiostat (Nordic Electrochemistry). The glassy carbon (GC) electrode was first polished with 1 Fµm diamond on a micro cloth, followed by a 50 nm Al_2O_3 on a master tex polishing cloth, ending by sonicating and rinsing in ethanol and distilled water, respectively. For the preparation of the ink, 3 mg of the sample was mixed with 1 mg of carbon black (P-XP, PentaCarbon GmbH, Germany) as a conductive additive and to enhance the utilization of the perovskite. 25 µl of a Nafion solution (5 wt %, QUINTECH) and 83.3 µl of isopropanol and 142 µl of distilled water were added before the suspension was treated firstly by vortex for several seconds and then in an ultrasonic bath for 60 min, ending with the dispersion by vortex to get a homogeneous ink. Afterwards, 5 µl of the freshly prepared ink was deposited on the surface of the glassy carbon tip of the RDE electrode (geometrical area of 0.1963 cm^2) and the catalyst loading was 0.3 mg cm^{-2} (carbon not considered). Reference measurements of the pure materials (without carbon black addition) were made for reasons of comparison. Ink preparation and catalyst loading were kept the same.

The electrolyte was 0.1M KOH solution (Potassium hydroxide, >99%, Sigma-Aldrich) saturated with N_2 and O_2 for the OER and ORR, respectively. The electrochemical activity of the series $BaFe_{1-x}Co_xO_{3-y-\delta}(OH)_y$ towards OER and ORR was evaluated by cyclic voltammetry (CV) at a rotation speed of 1600 rpm from 1.0 to 1.9 V (OER) and from 0.0 to −1.0 V (ORR) versus reversible hydrogen electrode (RHE) both with a sweep rate of 10 mV s^{-1} [32]. Before the electrochemical tests, an activation step was applied to electrochemically activate the materials and remove the bubbles inside of the catalyst layer by running CV in a range of 1.0 to 0 V_{RHE} for 20 cycles with 100 mV s^{-1} until we could observe a reproducible curve that was not changing anymore [234]. It should be pointed out that all the potential data are reported applying an iR correction ($E_{iR-corrected} = E - iR$) by compensating for the solution resistance.

In case of ORR, the polarisation curve obtained in O_2 saturated electrolyte was capacity corrected by subtracting a CV measurement at 10 mV s^{-1} in N_2 saturated electrolyte. For the iR corrected data, this measured j was used to determine the kinetic current density J_{Kin} by the Koutecky-Levich equation:

$$\frac{1}{j} = \frac{1}{j_{Kin}} + \frac{1}{j_L}$$

In this equation, j_L is the diffusion limiting current density. Tafel plots were obtained for the materials with carbon additive by using the Tafel equation:

$$E - iR = a + b \log j_{Kin}$$

In which, the iR corrected potential E-iR is plotted as a function with logarithm of j_{Kin} kinetic current density.

4.2.2.11 X-ray photoelectron spectroscopy

The valence states were examined by ex-situ X-ray photoelectron spectroscopy (XPS) analysis using a Physical Electronic VersaProbe XPS unit (PHI 5000 spectrometer) with Al K_α radiation (1486.6 eV). All detailed spectra were recorded with 50.6 W, a step size of 0.1 eV and a pass energy of 23.5 eV. The binding energies were calibrated with respect to the carbon 1s (C1s) emission line at 284.8 eV. Neutralizer was used for all the samples to account for the charging effects. For the determination of Cobalt oxidation states, the Co3p emission was selected since the Co2p and the Ba3d emission strongly overlap and a deconvolution of the signals is not possible. In order to ensure a better comparability, the Valence band spectra were normalized to a uniform maximum intensity.

4.2.3 Results and discussion

4.2.3.1 On the intrinsic structural and electrical properties of $BaFe_{1-x}Co_xO_{3-y-\delta}(OH)_y$

4.2.3.1.1 Structural properties of $BaFe_{1-x}Co_xO_{3-y-\delta}(OH)_y$

Figure 4.15a shows the observed X-ray diffraction patterns for $BaFe_{1-x}Co_xO_{3-y-\delta}(OH)_y$ with x varying from 0 to 1 obtained after NSP synthesis. For x = 0, a pattern which is similar to High water $BaFeO_{2.23}(OH)_{0.5}$ [37] (High Water = HW) is found, whereas the patterns for x ≠ 0 were found to be similar to Low water $BaFeO_{2.33}(OH)_{0.33}$ [37] (Low Water = LW) and $BaCoO_{1.80}(OH)_{0.86}$ [82]. A representative fit of the pattern of the compound with x = 0.5 is shown in Figure 4.15b, and such fits can be obtained using either the model of $BaFeO_{2.33}(OH)_{0.33}$ [37] or $BaCoO_{1.80}(OH)_{0.86}$ [82] and refining only the lattice parameters (relating to the fact that the intensities of the XRD patterns are mainly related to the similar position of the Ba / Co,Fe ions and that the oxygen sub lattice plays a minor role here). We also acknowledge the presence of small amounts of $BaCO_3$ in the as-synthesized powders (up to ~ 5 wt-%), which most likely originates from a partial decomposition of the samples in air due to their high basicity resulting in CO_2 uptake, common for Ba-rich perovskites (e. g., $BaInO_{2.5}$ [235]). Since XRD cannot distinguish between Co and Fe, EDX was used to confirm the stoichiometric presence of the heavy metals after synthesis, e. g., a 1 : 0.5 : 0.5 ratio of Ba : Fe : Co for the sample with x = 0.5, in agreement with our previous experience of this method on the preparation of perovskite type samples [36, 82]. The EDX results for the $BaFe_{1-x}Co_xO_{3-y-\delta}(OH)_y$ series are given in Table 4.3.

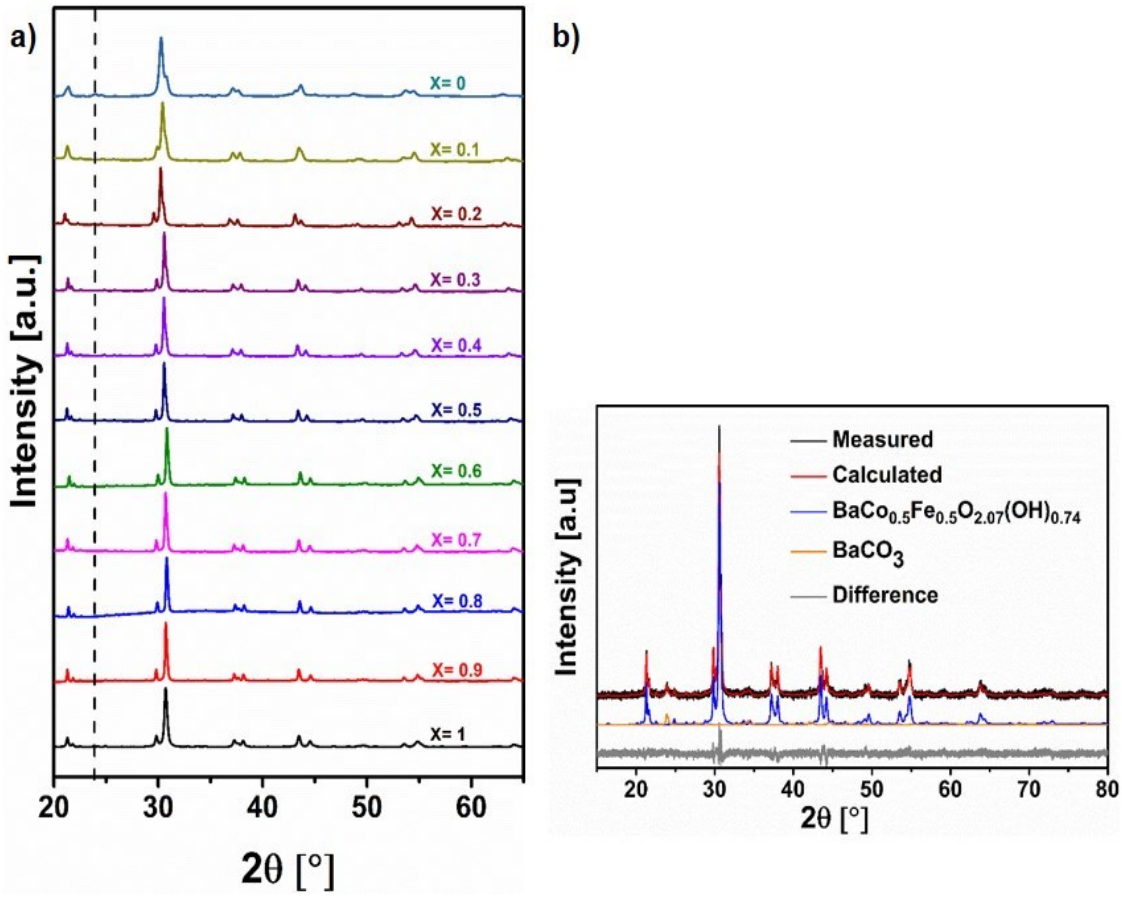

Figure 4.15: (a) X-Ray diffraction pattern for $BaFe_{1-x}Co_xO_{3-y-\delta}(OH)_y$ with x varying from 0 to 1. (b) Rietveld refinement of the X-ray diffraction pattern of $BaFe_{0.5}Co_{0.5}O_{2.07}(OH)_{0.74}$ powder.

Table 4.3: EDX results for the series $BaFe_{1-x}Co_xO_{3-y-\delta}(OH)_y$.

X	A Site	B Site	Fe	Co
0	1	1	0	1
0.1	0.91	1.09	0.12	0.88
0.2	0.91	1.09	0.19	0.81
0.3	0.91	1.09	0.29	0.71
0.4	0.94	1.06	0.40	.60
0.5	1	1	0.49	0.51
0.6	0.91	1.1	0.61	0.39
0.7	0.92	1.08	0.70	0.30
0.8	0.89	1.1	0.85	0.15
0.9	0.95	0.11	0.89	0.11
1	0.90	1.1	1	0

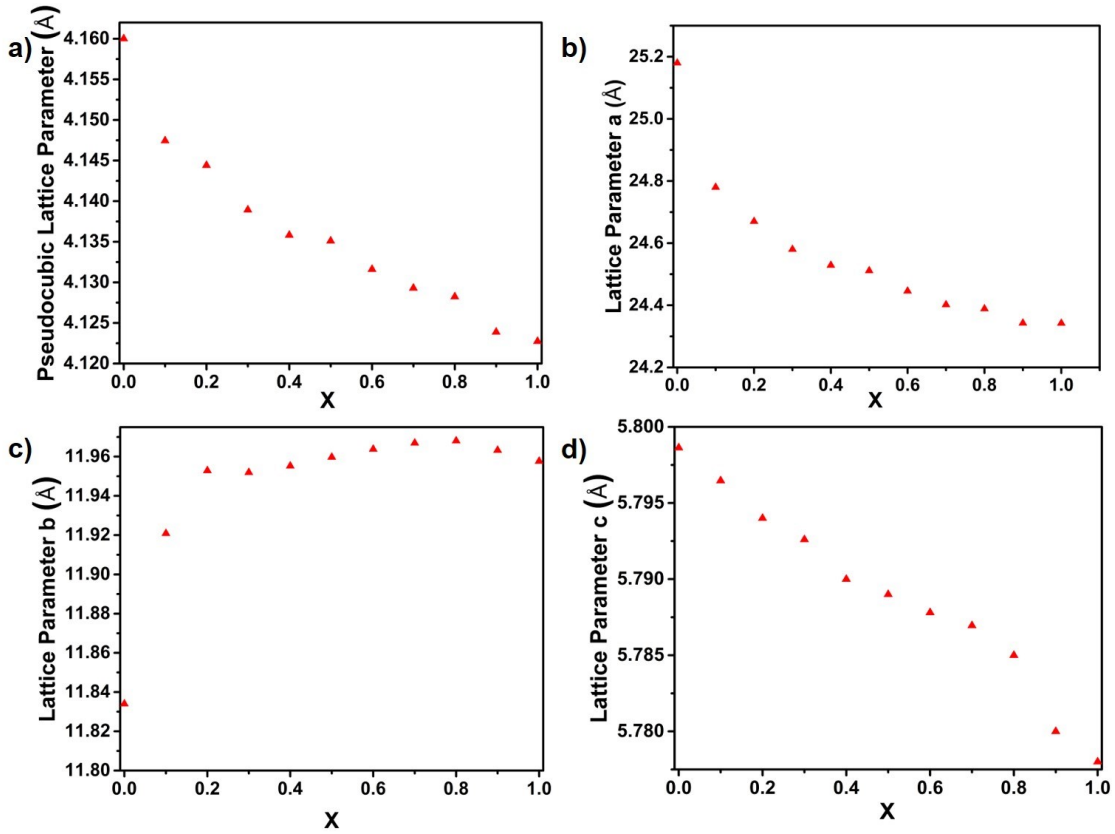

Figure 4.16: Influence of the Co doping on the (a) pseudocubic, (b) a, (c) b and (d) c lattice parameters of $BaFe_{1-x}Co_xO_{3-y-\delta}(OH)_y$ respectively.

The change of the structure of $BaFe_{1-x}Co_xO_{3-y-\delta}(OH)_y$ on changing the value of x can be easily visualized by a representation of the lattice parameters a,b,c and a pseudocubic lattice parameter ($a_{ps.cub} = (V_{f.u.})^{1/3}$) from the cube root of the volume per $BaFe_{1-x}Co_xO_{3-y-\delta}(OH)_y$ formula unit ($V_{f.u.}$). The sample with x = 0 shows an extraordinary high $a_{ps.cub.}$ and does not follow the merely linear trend of the rest of the samples (see Figure 4.16a). This results from a flip of the straining of the a- as compared to the b-axis (see Figure 4.16b-d), and the magnitude of contraction / expansion for those two axes is larger ($\Delta a/a_{x=0}$ = - 3.2 %, $\Delta b/b_{x=0}$ = + 1.2 %) than for the c-axis ($\Delta c/c_{x=0}$ = + 0.3 %). The stability of the length of the c-axis might therefore be

related to the structural role of the incorporated protons in the compound, which are aligned within channels along the c-axis implying additional hydrogen bonds along this direction [82].

From x = 0.1 to 1, the decrease of the volume per formula unit could be explained by two following contributions: (1) the larger size of the iron ion in comparison to the cobalt ion [236] and/or (2) the different amount of crystalline water.

Table 4.4: Tabulation of X dependence on oxygen, water content and composition per formula unit.

X	Oxygen Content per formula unit	Water Content per formula unit	Unit Formula
0	2.50	0.452	$BaFeO_{2.05}(OH)_{0.90}$
0.1	2.50	0.409	$BaFe_{0.9}Co_{0.1}O_{2.09}(OH)_{0.82}$
0.2	2.48	0.39	$BaFe_{0.8}Co_{0.2}O_{2.09}(OH)_{0.78}$
0.3	2.46	0.382	$BaFe_{0.7}Co_{0.3}O_{2.08}(OH)_{0.76}$
0.4	2.45	0.372	$BaFe_{0.6}Co_{0.4}O_{2.08}(OH)_{0.74}$
0.5	2.44	0.37	$BaFe_{0.5}Co_{0.5}O_{2.07}(OH)_{0.74}$
0.6	2.37	0.373	$BaFe_{0.4}Co_{0.6}O_{2.00}(OH)_{0.74}$
0.7	2.35	0.380	$BaFe_{0.3}Co_{0.7}O_{1.97}(OH)_{0.76}$
0.8	2.32	0.394	$BaFe_{0.2}Co_{0.8}O_{1.93}(OH)_{0.78}$
0.9	2.27	0.413	$BaFe_{0.1}Co_{0.9}O_{1.86}(OH)_{0.82}$
1	2.23	0.432	$BaCoO_{1.80}(OH)_{0.86}$

Iodometric titrations were carried out to determine the average oxidation state of the B site (summarized in Table 4.4 and Figure 4.17), which was found to be $B^{2.88+}$ for x=0.5 compound. This would imply a water-free composition of $BaFe_{0.5}Co_{0.5}O_{2.44}$. Mössbauer spectroscopic measurements were used to get deeper insights into the distribution of oxidation states of the transition metals. When the raw data was fitted with two components in the graph shown as D1 and Sext1, the fit curve does not match well with the raw data points especially at a velocity of 2 mm s^{-1} and between 4-6 mm s^{-1}. Besides, the base line is not straight, which indicates there might be some inorganic components at a larger velocity range overlaying with the identified signals. Therefore, some other Fe sites were used for reasons of comparison, that were previously identified in literature for similar ferrates. The detailed parameters can be found in Table 4.5. Under these conditions two different iron states were identified, with chemical shifts of 0.383 mm s^{-1} for the doublet, to 0.074 mms $^{-1}$ for the sextet (see Figure 4.18a updated and Table 4.5). Those values confirm the presence of trivalent iron only located in different coordination environments; lower coordination numbers are known to possess a significantly reduced chemical shift [237] as would be the case for bonding to OH^- instead of to O^{2-} [238] (the latter can even imply asymmetric Mössbauer signals [239], which could not be resolved in the measurement performed here). Remarkably, the presence of a sextet shows that the sample is magnetically ordered: Magnetic ordering at ambient temperature would be implausible for perovskites with tetravalent iron which have lower ordering temperatures (usually around ~ 150 K or lower [240]). Since iron is present in the trivalent state, based on those considerations, the oxidation state of cobalt is fairly close to +3 for samples rich in iron, ($Co^{2.76+}$ for x = 0.5), and decreases steadily for Co-richer compounds with x >> 0.5 (again see Figure 4.17). Co^{3+} is smaller than Fe^{3+} [236] for all of its spin states, whereas Co^{2+} is larger than Fe^{3+}. Therefore, the Co^{3+} content is also reflected in the change of the unit cell volume ($a_{ps.cub.}$), which shows a different slope for 0 < x < 0.5 than for 0.5 < x < 1 (Figure 4.16a). Overall, the experiments

performed here emphasize that the oxidation state stabilized for the Co cations strongly depends on the content of iron within the sample.

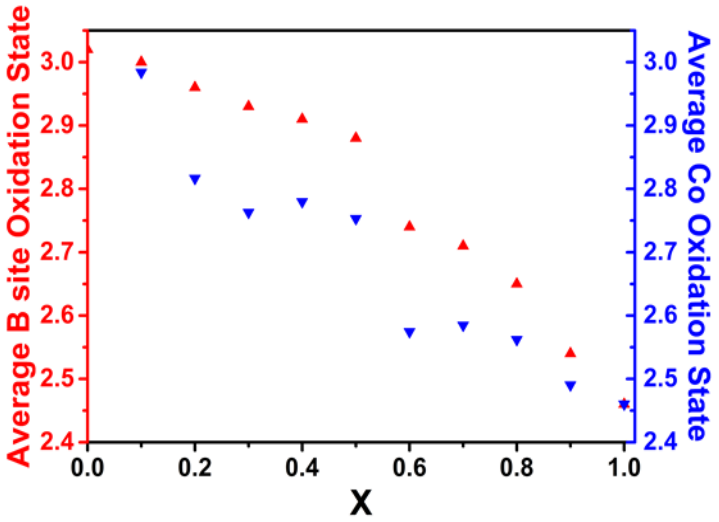

Figure 4.17: Influence of cobalt doping on the average oxidation state of B site and the average oxidation state of cobalt assuming Fe to be present as Fe^{3+} only (as indicated also by Mössbauer measurements).

Since no Curie-Weiss behavior (see Figure 4.18b) can be observed in the temperature range prior to the release of water, it is not possible to trace back the spin state of the Co cations. This observation is also in agreement with the magnetic hyperfine field splitting observed for iron within the Mössbauer spectroscopic measurement (see Figure 4.18a), which to some extent indicates magnetic ordering within the sample. Due to the low moments observed, this ordering is most likely of antiferromagnetic nature, with G-type antiferromagnetic ordering being very common for perovskites rich in Fe^{3+} [34, 201, 241, 242].

Table 4.5: Mössbauer parameters of $BaCo_{0.5}Fe_{0.5}O_{2.07}(OH)_{0.74}$ at room temperature.

Site	δ (mm s^{-1})	ε (mm s^{-1})	BHF (T)
Fit D1	0.383(28)	1.317(48)	
Fit Sext1	0.074(31)	0	20-50(21)
Fe5,CN = 5	0.37(1)	-0.50(2)	49.2(5)
Fe6, CN = 5	-0.33(1)	-0.64(2)	47.3(5)
Fe2-4,b CN = 4	0.15(1)	-0.2	40

No linear dependence of the water content on the value of x was found. The water content decreases in the range between x = 0 - 0.5 from 0.45 to 0.37 H_2O per $BaFe_{1-x}Co_xO_{3-\delta}$, and increases again to 0.43 for x = 0.5 - 1 (see Figure 4.19a). This shows that there is a strong interplay of the vacancy content δ originating from the presence of cation oxidation states lower than +3 and the structural distortion to compensate the presence of such vacancies (see Figure 4.17).

In agreement with the findings of XRD, the structural stabilization of water is also different in the Fe-only sample with x = 0, as indicated from the TG curves shown in see Figure 4.19b. Exemplarily, the water loss has also been characterized structurally for the sample with x = 0.5 (see Figure S2 and explanations given there). A transition to a monoclinic, $BaFeO_{2.5}$ related phase is found after heating to 473 K, which appears to stabilize significant amounts of crystalline water up to a temperature of 773 K, after which the structure becomes water free. It is also worth emphasizing that the NSP route not only gives access to the preparation of new

compounds, which cannot be obtained by hydration of oxides, but that also different water contents can be obtained for the nanocrystalline in comparison to the coarse state within the x = 0 sample. On hydrating powder of $BaFeO_{2.5}$ with large crystallite sizes prepared via solid state reaction at the same temperature than used within the particle collector of the spray pyrolysis process, significantly smaller OH contents (y ~ 0.53 [37] vs. y ~ 0.90) can only be obtained.

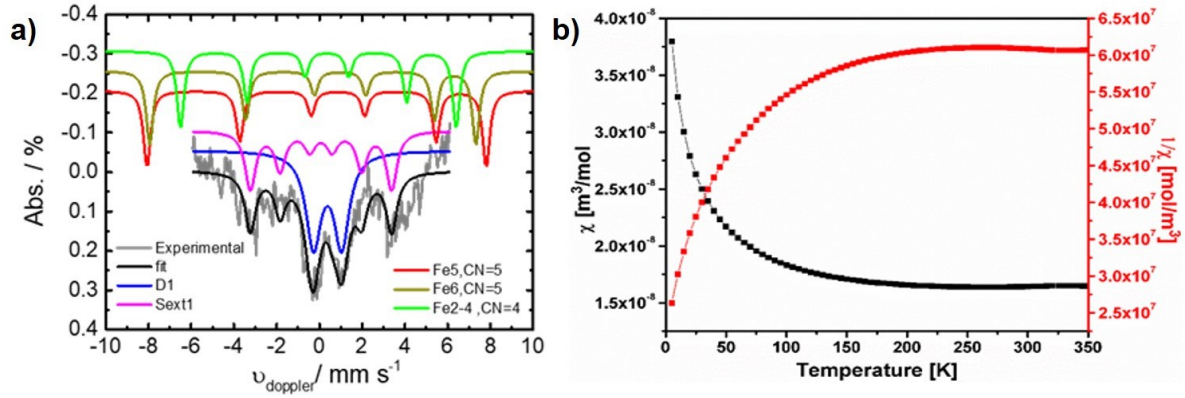

Figure 4.18: (a) ^{57}Fe Mossbauer spectrum recorded for $BaFe_{0.5}Co_{0.5}O_{2.07}(OH)_{0.74}$ at room temperature (b) Susceptibility and inverse susceptibility vs temperature curves recorded for $BaFe_{0.5}Co_{0.5}O_{2.07}(OH)_{0.74}$ in a constant magnetic field of H = 1T.

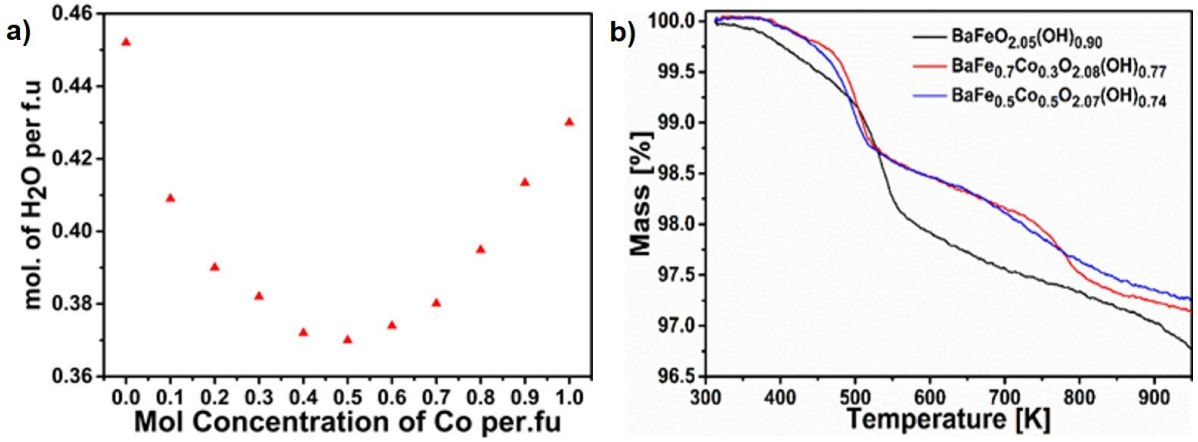

Figure 4.19: (a) Water content per formula unit of $BaFe_{1-x}Co_xO_{3-y-\delta}(OH)_y$ determined by elemental analysis. (b) Comparison of TGA data for three different compositions of $BaFe_{1-x}Co_xO_{3-y-\delta}(OH)_y$.

4.2.3.1.2 A study of the high temperature structural and water loss behavior of $BaFe_{0.5}Co_{0.5}O_{3-y-\delta}(OH)_y$

The temperature dependence of the stabilization is very important for materials to become potential candidates for PCFC electrode catalysts, and we studied this behavior exemplarily by a combination of methods for the compound with x = 0.5. The water loss behaviour and determination of the amount of crystal water could be studied using STA. Figure 4.20a shows the STA measurement of the sample with x = 0.5. TGA data accompanied with the endothermic signal indicated the initial steep weight loss between 400 K and 550 K. This weight loss can be further followed from the elemental hydrogen analysis (Figure 4.20b) carried out on the powder of the same composition heated to different temperatures. Between 400 K and 550 K there is approximately 40 % loss of the crystal water. Above 550 K, the weight loss continues at a lower rate until 800 K, at which a clear kink in the TGA curve is observed. A total mass loss of ~ 2.8 – 3.0 % was found, which corresponding to 0.37 - 0.40 H_2O per formula unit of $BaFe_{0.5}Co_{0.5}O_{3-}$

$_x$, which is in well agreement with the 0.37(2) H_2O per formula unit as obtained from elemental hydrogen analysis. In combination with the result from the iodometric titration, the composition of the sample after synthesis can therefore be approximated to be $BaCo_{0.5}Fe_{0.5}O_{2.44}(H_2O)_{0.37}$ = $BaCo_{0.5}Fe_{0.5}O_{2.81}H_{0.74}$ = $BaCo_{0.5}Fe_{0.5}O_{2.07}(OH)_{0.74}$. The amount of crystalline water is lower than found for the compounds with x = 0 and 1.

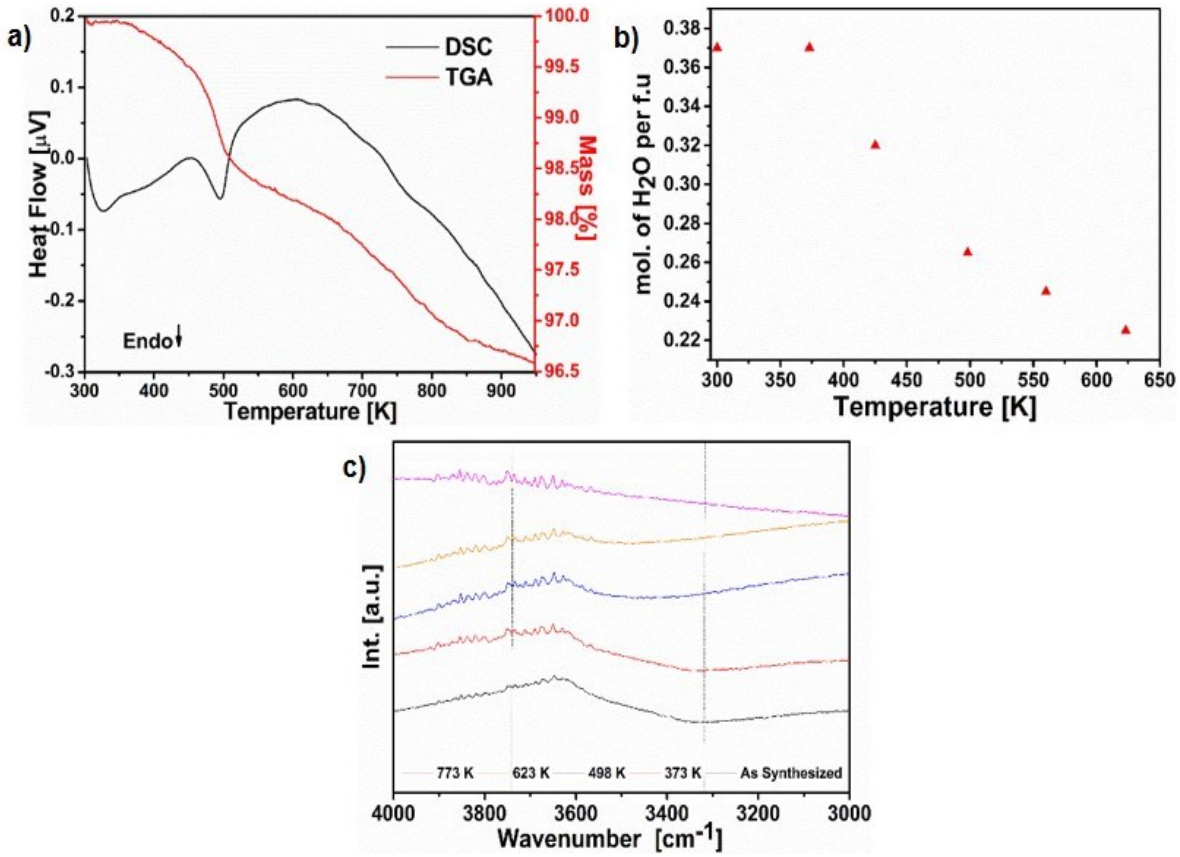

Figure 4.20: (a) TGA/DSC and (b) elemental hydrogen analysis on $BaCo_{0.5}Fe_{0.5}O_{2.07}(OH)_{0.74}$ under a flow of argon. (c) FT-IR spectra recorded for $BaFe_{0.5}Co_{0.5}O_{2.05}(OH)_{0.78}$ up to 773 K. The presence of protons could be confirmed till 623 K.

Ex-situ FT-IR measurements were also carried out for $BaCo_{0.5}Fe_{0.5}O_{2.07}(OH)_{0.74}$ powder heated to various temperature upto 773 K (Figure 4.20c) to confirm the presence of the protons. The presence of protons could be confirmed up to temperature of 623 K, after which the broad band around 3300-3500 cm^{-1} (corresponding to the OH stretching band [82,37])could not be observed further. Again, this is in agreement with the TGA studies as well as the elemental hydrogen analysis performed on the compound (taking into account that longer prevalence times at higher temperatures were used for the samples studied with FT-IR, whereas the TGA is a more dynamic method).

To study the structural changes upon water loss, high temperature X-ray diffraction (Figure 4.21a) was carried out. Consistent with the STA and elemental hydrogen analysis studies, HT-XRD shows significant changes in the diffraction pattern between 373 K and 473 K which is attributed to loss of crystal water. At 473 K, the recorded diffraction pattern shows similarity with that of $BaFeO_{2.5}$ [84], which could be confirmed by Rietveld analysis (Figure 4.21b, monoclinic space group *$P2_1/c$, a= 6.975(4) Å, b= 11.728(6) Å, c= 23.450(5) Å, β= 98.813(5) ° and Z= 28)*. This monoclinic setting is maintained till 773 K and also further down upon cooling to room temperatures. Similar behaviour was observed for $BaFeO_{2.333}(OH)_{0.333}$ [37], for which $BaFeO_{2.5}$ is the water free analog. Water loss can also be followed from the decrease in unit

cell volume, represented by plotting pseudocubic lattice parameter with the temperature as shown in Figure 4.21c. The decrease in the pseudocubic lattice parameter around 473 K is consistent with the water loss and in agreement with the STA and elemental hydrogen analysis. An increased unit cell volume of the hydrated phases is also consistent with the previous reports on similar perovskite oxide compounds which can incorporate large amount of water inside the crystal lattice.eg $BaInO_{2.5}$ to $BaInO_2(OH)$[235] and $BaFeO_{2.5}$ to $BaFeO_{2.33}(OH)_{0.33}$ [37]. Further heating to 773 K causes an increase in the pseudocubic lattice parameters due to thermal expansion. On cooling down, a small difference to the cell volume on heating could be observed, which agrees well with the prevalence of water within the compound during heating. This loss is completed at higher temperatures (773 K), well agreeing with this behavior.

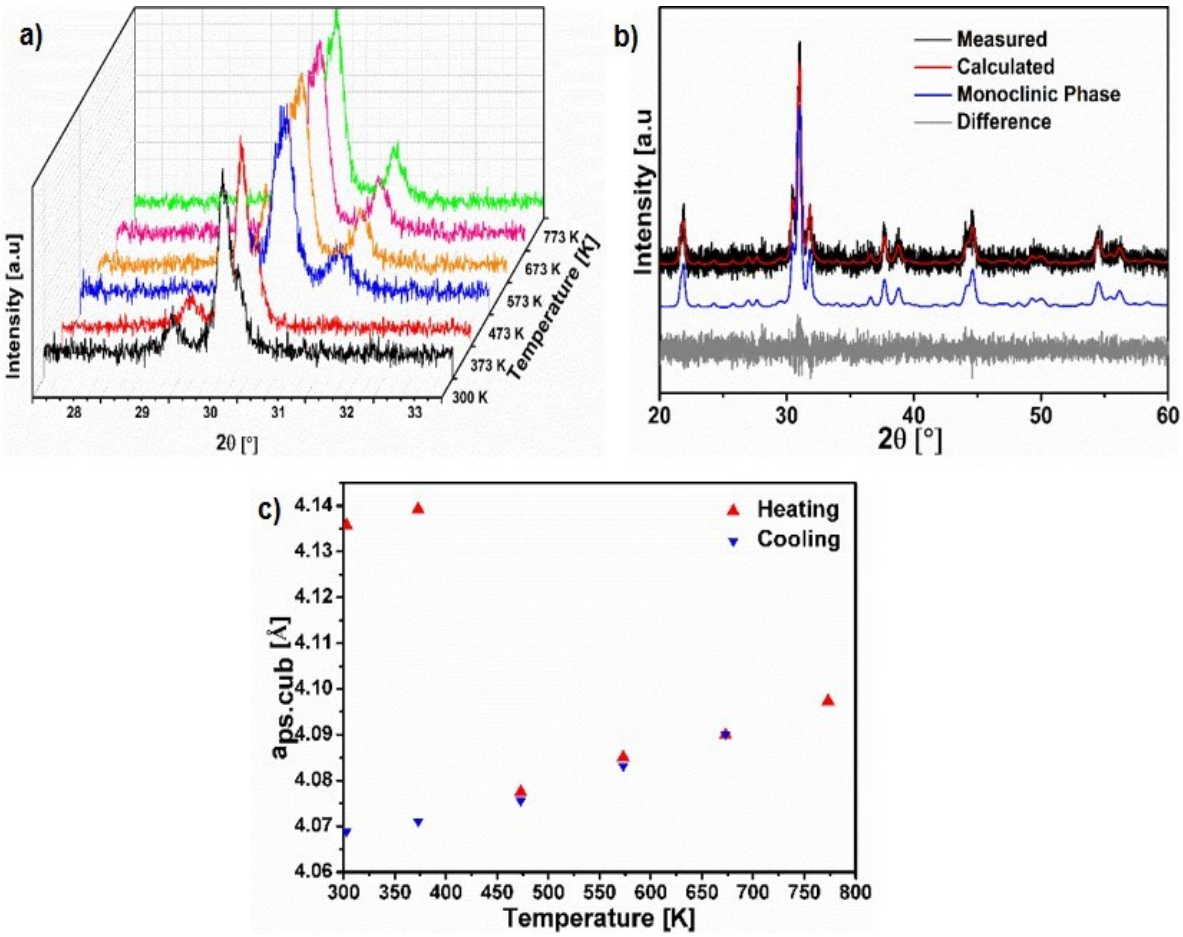

Figure 4.21: (a) High temperature X-ray diffraction patterns for $BaCo_{0.5}Fe_{0.5}O_{2.07}(OH)_{0.74}$ measured under a flow of argon till 773 K. (b) Rietveld fit for th e X-ray diffraction pattern recorded at 473 K under flow of argon. (c) Pseudocubic lattice parameters obtained from the refinement of HT-XRD data of $BaCo_{0.5}Fe_{0.5}O_{2.08}(OH)_{0.74}$.

4.2.3.1.3 Electrical properties of the series $BaFe_{1-x}Co_xO_{3-y-\delta}(OH)_y$

Impedance spectroscopy was carried out to study the conductivity behavior of the compounds in the temperature range between 298 K and 348 K depending on the value of x in $BaFe_{1-x}Co_xO_{3-y-\delta}(OH)_y$. As-synthesized powders were compacted by isostatic pressing (as we described previously for $BaCoO_{1.80}(OH)_{0.86}$ [82] and $BaFeO_{2.333}(OH)_{0.333}$ [37]) for water release ,finally, we obtained pellets with ~ 85 % of the theoretical density.

Figure 4.22a,b shows an example of the Nyquist and Bode plots for $BaCo_{0.5}Fe_{0.5}O_{2.07}(OH)_{0.74}$ recorded at 298 K. The NYQUIST plot shows a typical semicircle which can be fitted with a single equivalent circuit consisting of resistance and a constant phase elements (CPE) in parallel. The intersection of the semi-circle with the real axis at low frequency suggests that the

impedance is dominated by the electronic charge carriers, supported by the absence of any electrode response. The capacitance of the samples is in the order of ~ 10^{-12} F, which points towards a strong influence of the bulk to the overall conductivity [101].

Figure 4.22c shows the Arrhenius plots of the temperature dependent conductivity for $BaFe_{1-x}Co_xO_{3-\delta}(OH)_{2\delta}$. (x =0, 0.3 , 0.5, 0.7, 1). $BaFeO_{2.06}(OH)_{0.92}$ contains trivalent iron only and therefore shows bad electronic conductivity. An increase in cobalt content results in a significant increase of the total electronic conductivity. As observed from the titration experiments mixed valent states of Co^{2+} and Co^{3+} are introduced for x > 0, which can facilitate electron hopping as a conduction mechanism. This influence of the Co oxidation state on the overall conductivity is well expressed by the two jumps in the conductivity found for x = 0 → 0.5 (average Co oxidation of ~ +3 to +2.7) and for 0.5 → 1 (average Co oxidation state of ~ +2.4 to +2.2, again see also Figure 4.22c). The overall conductivity of $BaCo_{0.5}Fe_{0.5}O_{2.07}(OH)_{0.74}$ (as a representative for the intermediate values of x) is in the order 10^{-6} S cm^{-1} at room temperature, which is two orders of magnitude higher than observed for $BaFeO_{2.33}(OH)_{0.33}$ and three orders of magnitude lower than observed for $BaCoO_{1.80}(OH)_{0.86}$ [82]. The activation energy of the samples ranges from 0.33 to 0.39 eV.

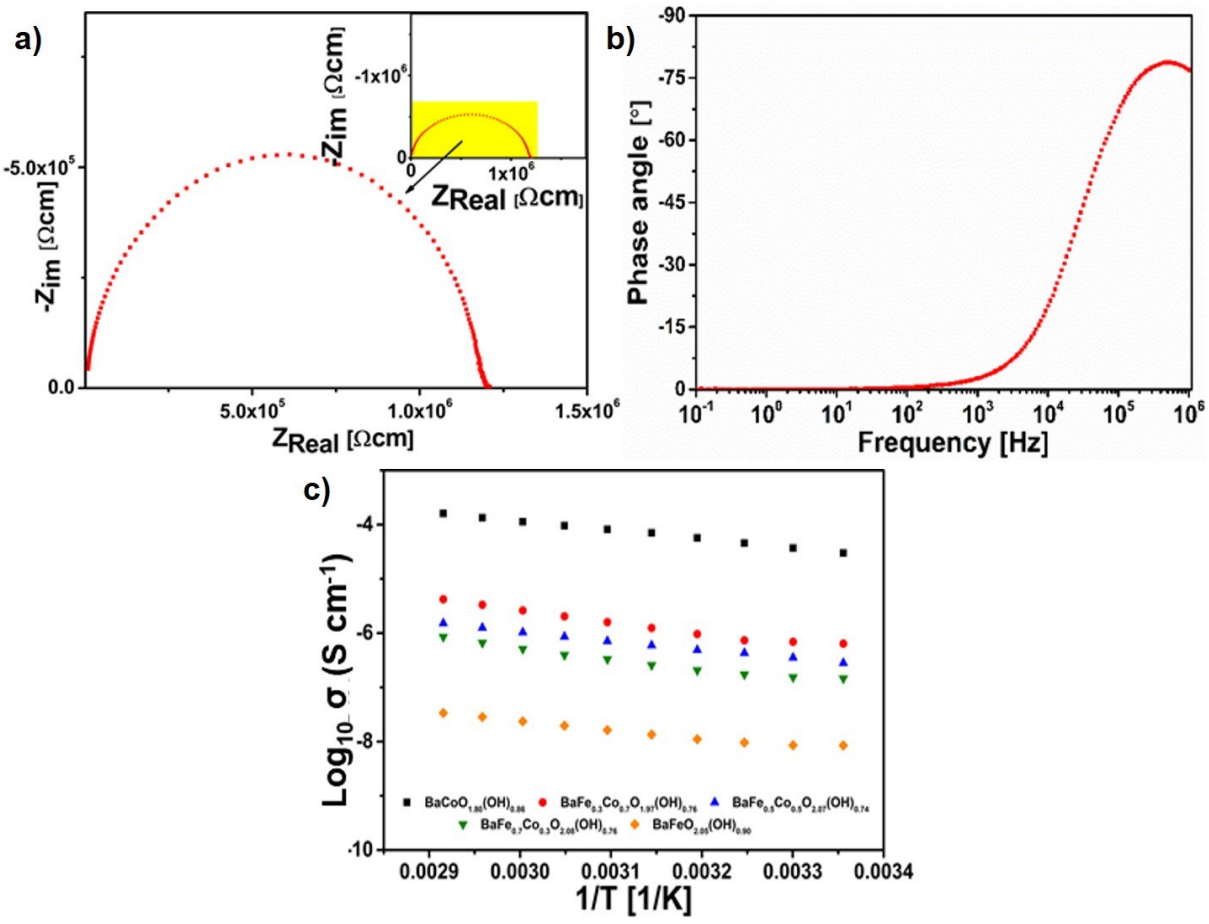

Figure 4.22: (a) Nyquist and (b) Bode plots for the impedance spectroscopical measurement for $BaCo_{0.5}Fe_{0.5}O_{2.07}(OH)_{0.74}$ recorded at 298 K. (c) Arrhenius plot for temperature dependent electrical conductivity of the samples of the series $BaFe_{1-x}Co_xO_{3-y-\delta}(OH)_y$ (x =0, 0.3, 0.5, 0.7, 1) in the temperature range between 298 – 343 K.

4.2.3.1.4 Bifunctional OER/ORR activity

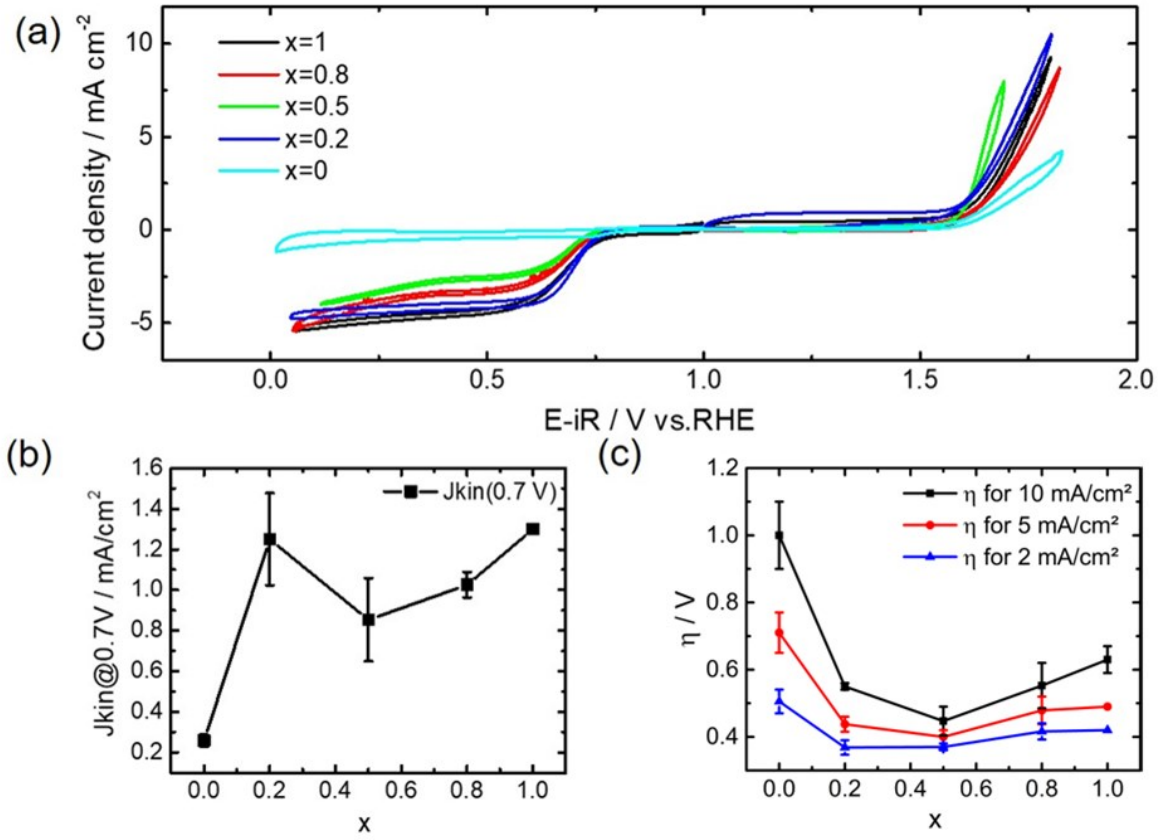

Figure 4.23: (a) ORR and OER activity data obtained in 0.1M KOH for the samples of the series $BaFe_{1-x}Co_xO_{3-y-\delta}(OH)_y$ (x = 0, 0.2, 0.5, 0.8, 1). (b) Kinetic current density as a function of Fe fraction for ORR of the series $BaFe_{1-x}Co_xO_{3-y-\delta}(OH)$. (c) Over potentials for different current densities as a function of Fe fraction for OER of the series $BaFe_{1-x}Co_xO_{3-y-\delta}(OH)$. All data shown were obtained for the catalysts with carbon additive and were corrected for the ohmic electrolyte resistance (iR). Error bars represent standard deviations from two to three independent measurements.

The ORR and OER activities of this $BaFe_{1-x}Co_xO_{3-y-\delta}(OH)_y$ series of catalysts were measured in 0.1 M KOH. The results of ORR and OER were plotted together in Figure 4.23a for reasons of comparison. As it is shown in the graph, the perovskite catalyst with composition of x=0 showed lower activity than all other compositions for both OER and ORR reactions, which could possibly be explained by the low electronic conductivity from Impedance as explained above (Figure 4.23).

From the ORR region, we can see that the potentials needed for achieving a current density of 3 mA/ cm^2 are 0.67 V, 0.65 V,0.59 V and 0.34 V for x=0.2, x=1, x=0.8 and x=0.5, Thus, at x = 0.2 and x = 1 the compounds of the series are most active for the ORR. The onset potentials and current density are comparable to that of recently reported $CaMnO_{3-x}$ [200], $Bi_{0.6}Ca_{0.4}FeO_3$ [243] and $Nd_{1.5}Ba_{1.5}CoFeMnO_{9-\delta}$ [244] . The kinetic current densities (J_{kin}) of the $BaFe_{1-x}Co_xO_{3-y-\delta}(OH)_y$ catalysts at 0.7 V vs RHE were calculated using the Koutecky-Levich equation and are shown in Figure 4.23b. Also in this case, catalysts with x=0.2 / x = 1 have the highest ORR activity of 1.25 mA/cm^2 and of 1.3 mA/cm^2 and lower Tafel slopes of 84 and of 91 mV dec^{-1}, see Figure S3. Nevertheless, the overall activity of all samples is similar and in the order of 1 mA/cm². A simple principle about the electronic configuration of perovskite oxides and the importance for the ORR activity was proposed by Yang Shao-Horn's group, who evidenced that the intrinsic ORR activity has a volcano like relationship with e_g orbital filling, with a one electron filling

having the best activity [31]. Here, the incorporation of d^7 Co^{2+} and d^6 Co^{3+} would lower the occupancy in the e_g orbitals, which is beneficial as compared to the Fe-pure compound, in addition to the increase of the intrinsic electrical conductivity.

As shown in Figure 4.23a for the OER region, the sample with x = 0.5 shows the best OER activity due to its lowest potential for reaching a current density of 10, 5 or 2 mA/cm^2 respectively. This sample also shows the lowest Tafel slope (Figure 4.24), which is further comparable to other well-performing catalysts such as $CaMnO_{3-x}$[200]. However, it must be acknowledged that the OER activity is lower as compared to $Ba_{0.5}Sr_{0.5}Fe_{0.2}Co_{0.8}O_{3-x}$ [32], which might be attributed to a difference in the oxygen vacancy concentration in the sample, that is known to reduce the OER performance [245]. Further, the OER activity follows a volcano type behavior depending on x wherein the onset potential decreases with the cobalt doping (x = 0.5) followed by an increase. The over potential of the sample with x = 0 was found to be the highest within the series; this is most likely related to the overall lowest electronic conductivity for this sample (see section 4.2.3.1.3). Apart from the overall conductivity, it has been predicted for perovskite-based compounds that the OER activity is also directly related to the filling of the e_g band level [32] as well as to the O 2*p*-band center relative to the fermi level [246]. Both are known to depend on the spin and oxidation states of the transition metal ions. As discussed above, to obtain good catalytic activity, an e_g filling level of 1 electron in total would also be favorable in this case, corresponding to a high ratio of ls-Co^{3+} to hs-Fe^{3+} [32], i. e. hs-Fe^{3+} species need to be present within the sample to enhance the catalytic properties. This most likely explains the decrease of catalytic activity for the Co-richer samples with $0.5 < x \leq 1$, for which the overall Fe^{3+} content becomes too low. It is not possible to determine the exact Co spin states within the sample due to the presence of cobalt in different coordination environments [82,246] (octahedral, square pyramidal, tetragonal) and due to the partial magnetic ordering at ambient temperature (even for the Co-pure sample [82]). However, assumed changes in the e_g orbital filling are in principle agreement with XPS measurements of the Co 3p signal (see Figure 4.25a and b), which show an energy shift of ~ 0.5 eV for $BaFe_{0.8}Co_{0.2}O_{2.09}(OH)_{0.78}$ as compared to $BaCoO_{1.80}(OH)_{0.86}$. This confirms that Co^{2+} is the dominant Co-species for Co-rich samples, and that Co^{3+} becomes more dominant for Fe-richer samples. Co^{3+} can be expected to have a reduced e_g orbital filling due to its high stability in IS or LS states [90] This is in good agreement with the titration measurements reported in section 3.1.1, which indicate that Co^{3+} to Fe^{3+} ratios close to unity are found around the x ~ 0.5 composition, and approach values of 1:10 and 5:1 for increasing and decreasing Fe content respectively.

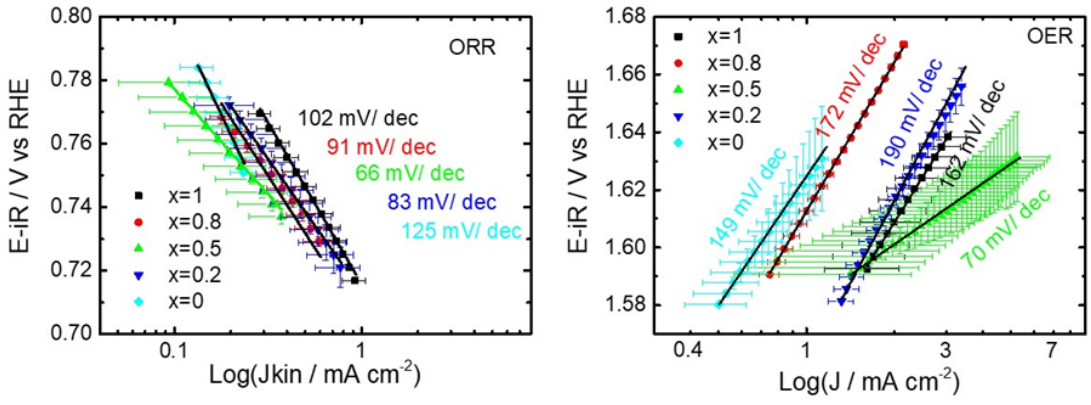

Figure 4.24: Tafel analysis of series $BaFe_{1-x}Co_xO_{3-y-\delta}(OH)_y$ (x = 0, 0.2, 0.5, 0.8, 1) for both the (a) ORR and (b) OER. Tafel plots were obtained for the measurements of the catalysts plus carbon additive.

Further, an increase of the density of states (DOS) near the Fermi level is found with increased cobalt content (Figure 4.25c), agreeing well with the observed increase of electronic conductivity for Co-richer samples. Interestingly, this change of the DOS has also been observed comparing ferrates with HS-Fe^{3+} to cobaltates with LS/IS-Co^{3+}, e. g., $LaFeO_3$ to $LaCoO_3$ [247].

We also evaluated the overall bifunctional performance of the series of compounds reported here, which can be done by calculating the difference between the OER potential at 10 mA cm^{-2} and ORR potential at 2.5 mA cm^{-2} (see Figure 4.26 and Table 4.6). Within the series, the sample with x = 0.2 has the smallest potential difference of δU =1.10 V. This value is comparable to what is found for noble metal catalyst [199] or $CaMnO_{3-x}$ [200] making it of potential interest for metal air battery applications.

We also would like to point out that the obtained electrochemical data for the catalysts without carbon additive and for the pure carbon black are shown in Figure 4.27. For the carbon itself, no significant activity was found. It is interesting to note that in the absence of carbon a diffusion plateau was only reached at low potentials (U < 0.2 V), while on addition of carbon black it was already reached at 0.6 V for the most active catalyst. This might be indicative for a change in ORR mechanism or in general less good utilization of active sites. For the catalysts, the trend was basically the same as with carbon additive (see Figure 4.27b and c), but the overall values were smaller indicating the importance of conductivity for the overall performance.

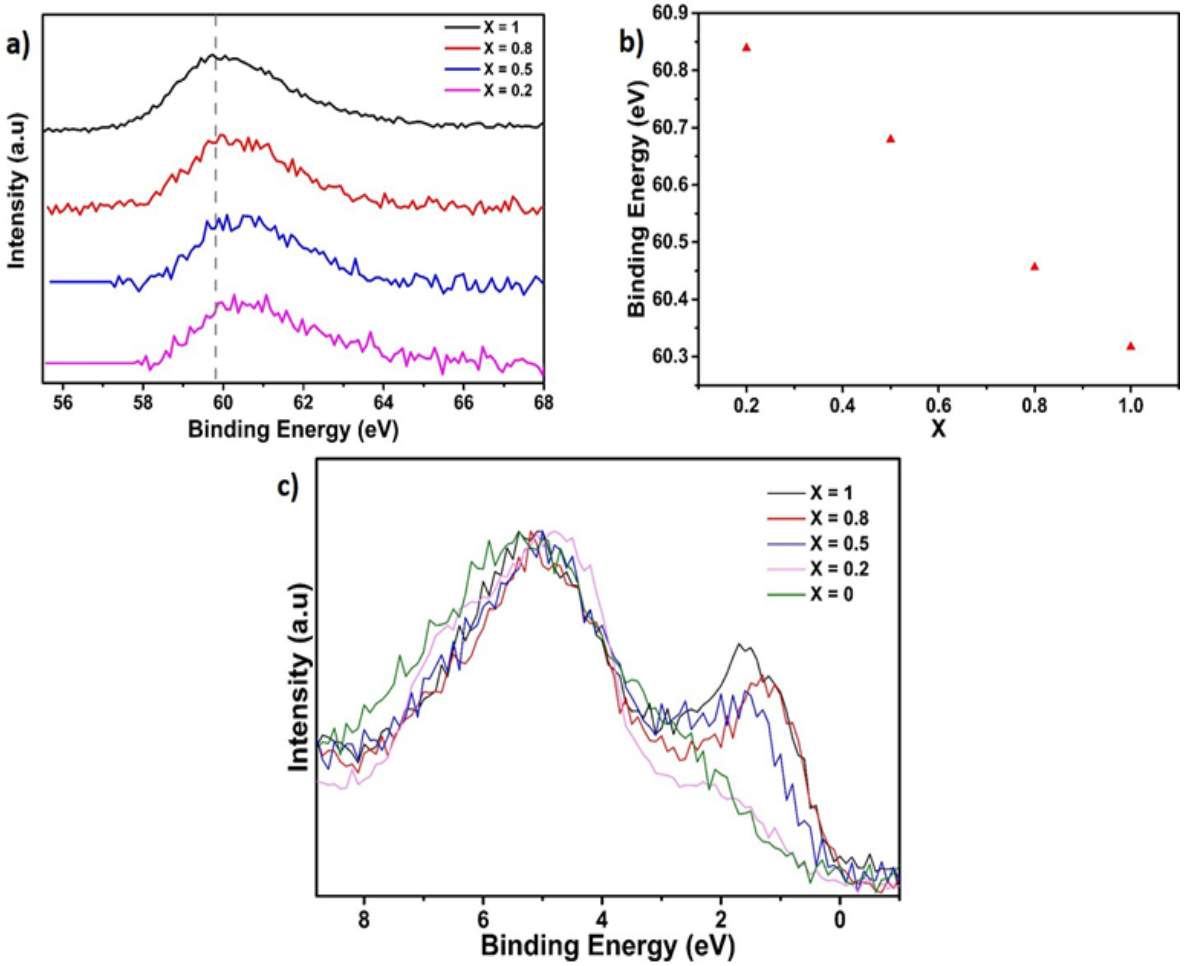

Figure 4.25: (a) & (b) Binding energies of Co3p peaks as a function of X. (c) XPS spectra of the valence band for the series $BaFe_{1-x}Co_xO_{3-y-\delta}(OH)$ (x = 0, 0.2, 0.5, 0.8, 1).

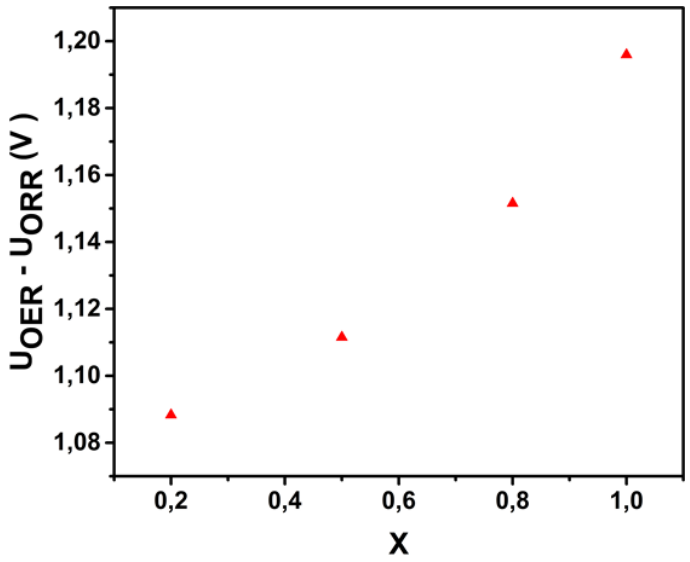

Figure 4.26: Bifunctionality parameter for x= 0, 0.2, 0.5, 0.8, 1 of the series $BaFe_{1-x}Co_xO_{3-y-\delta}(OH)_y$ recorded for U_{OER} at 10 mA cm^{-2} and U_{ORR} at 2.5mA cm^{-2}.

Table 4.6: Tabulated data of electrocatalytic activities for the perovskite-based $BaFe_{1-x}Co_xO_{3-y-\delta}(OH)_y$ catalysts.

* The Uonset of OER were defined as the intercept of the curve on the x-axis

	ORR			OER	
Catalysts	**U_{onset} (V vs RHE)**	**E1/2 (V vs RHE)**	**Tafel slope (mV/dec)**	**U_{onset}* (V vs RHE)**	**Tafel slope (mV/dec)**
X=1	0.788	0.662	102	1.63	162
X=0.8	0.780	0.672	91	1.57	172
X=0.5	0.780	0.660	66	1.57	70
X=0.2	0.798	0.675	84	1.55	190
X=0	0.803	0.251	125	1.58	149

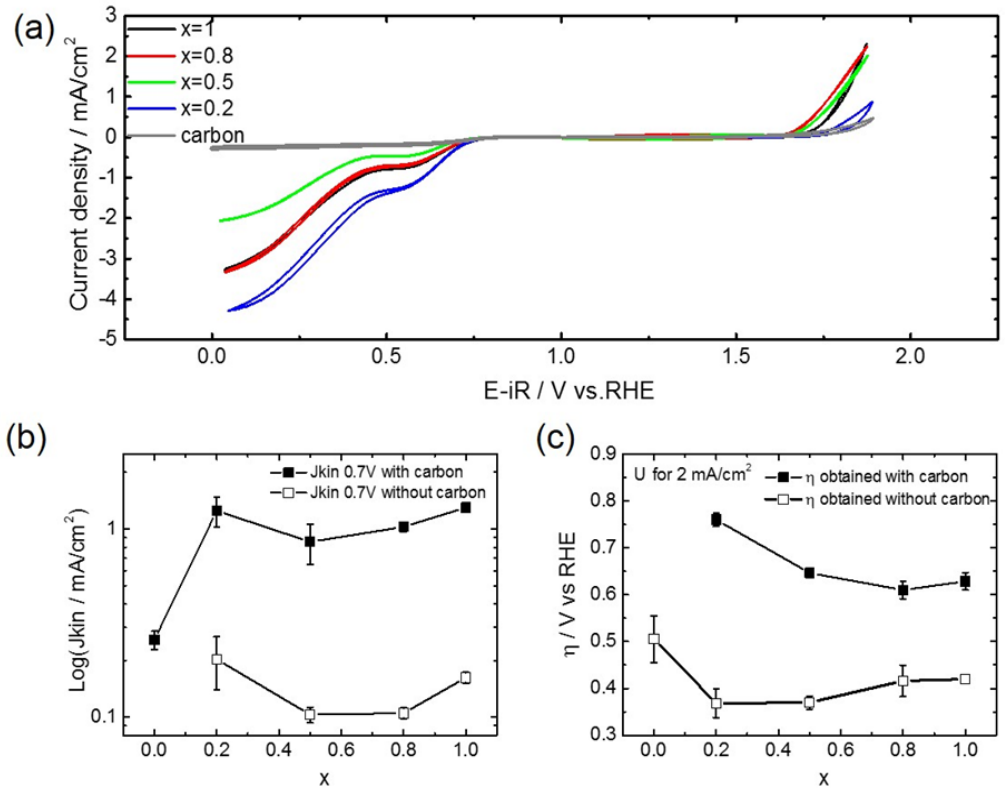

Figure 4.27: (a) ORR and OER activity data obtained in 0.1M KOH for the samples of the series $BaFe_{1-x}Co_xO_{3-y-\delta}(OH)_y$ (x = 0, 0.2, 0.5, 0.8, 1) as measured without carbon additive. (b) Kinetic current density as a function of Fe fraction for ORR of the series $BaFe_{1-x}CoxO_{3-y-\delta}(OH)$ with and without carbon additive. (c) Over potentials for different current densities as a function of Fe fraction for OER of the series $BaFe_{1-x}Co_xO_{3-y-\delta}(OH)_y$. All shown data were e corrected for the ohmic electrolyte resistance (iR). Error bars represent standard deviations from two to three independent measurements.

4.2.4 Conclusion

Here we have highlighted the role of choosing spray pyrolysis as a synthesis-route to be able to prepare and characterize the whole series of oxide hydroxide perovskite compounds with composition $BaFe_{1-x}Co_xO_{3-y-\delta}(OH)_y$ for the first time. This series cannot be obtained by classical routes (e. g., solid state reaction) due to the high stability of hexagonal perovskites for the water free case. We have shown that the transition metal oxidation states and water contents show a complex dependence on x. By this, we have been able to investigate the whole system for its OER / ORR activity for alkaline fuel cells, showing similar performance than other related catalysts. Further, this catalytic performance strongly depends on the detailed value of x. Combining the findings of chemical and structural analysis with the observed intrinsic electrical conductivity as well as catalytic properties, strong indications are given that the catalytic activity depends on the detailed transition metal oxidation states, vacancy as well as water contents found within the samples.

So far this article has addressed the synthesis and principle activity of the system. Future research of our group will also consider the suitability to work as catalysts for ORR/OER in protonic ceramic fuel or electrolysis cells (PCFC, PCEC), which require catalysts being conductive for both, electrons and protons, to obtain large catalytically active areas [248].

Acknowledgements

O. Clemens acknowledges support by the German Research Foundation within the Emmy Noether Programme (grant no. CL551/2-1).

4.3 Structural, Magnetic and Catalytic Properties of a New Vacancy Ordered Perovskite Type Barium Cobaltate $BaCoO_{2.67}$

Aamir Iqbal Waidha, [a] Humera Khatoon Siddiqui, [b] Yuji Ikeda, [c] Maren Lepple, [d] Sami Vasala, [a] Manuel Donzelli, [a] A. D. Fortes, [e] Peter Slater [f] Blazej Grabowski, [c] Ulrike I. Kramm, [b] and Oliver Clemens*[a]

[a] Materials Synthesis Group, Institute of Material Science, University of Stuttgart, Hesisenbergstraße 3, 70569 Stuttgart, Germany.

[b] Catalysts and Electrolcatalyst, Department of Chemistry, Eduard-Zintl Institute for Inorganic and Physical Chemistry Technische Universität Darmstadt, 64287 Darmstadt, Germany.

[c] Department of Materials Design, Institute for Materials Science, University of Stuttgart, Pfaffenwaldring 55, 70569, Stuttgart, Germany.

[d] DECHEMA-Forschungsinstitut, Theodor-Heuss-Allee 25, 60486 Frankfurt am Main, Germany.

[e] Rutherford Appleton Laboratory, Harwell Science and Innovation Campus, ISIS Facility, Didcot, Oxfordshire, OX11 0QX, UK.

[f] University of Birmingham, School of Chemistry, Edgbaston, Birmingham B15 2TT, UK

* Corresponding Author: oliver.clemens@imw.uni-stuttgart.de

Abstract

A new vacancy ordered, anion deficient perovskite modification with composition of $BaCoO_{2.67}$ ($Ba_3Co_3O_8\square_1$) has been prepared via a two-step heating process. Combined Rietveld analysis of neutron and X-ray powder diffraction data shows a novel ordering of oxygen vacancies not known before for barium cobaltates. A combination of neutron powder diffraction, magnetic measurements and density functional theory (DFT) studies confirms G-type antiferromagnetic ordering. From impedance measurements, the electronic conductivity of the order of 10^{-4} S cm^{-1} is determined. Remarkably, the bifunctional catalytic activity for oxygen evolution reaction (OER) and oxygen reduction reaction (ORR) is found to be comparable to that of $Ba_{0.5}Sr_{0.5}Co_{0.8}Fe_{0.2}O_{3-y}$, confirming that charge-ordered anion deficient non-cubic perovskites can be highly efficient catalysts.

4.3.1 Introduction

Perovskite-type ABX_{3-y} compounds have received a lot of attention due to their application in the fields of magnetism, fuel cells, solar cells and batteries [90]. The ideal perovskite structure (ABX_3) can be described as a cubic close packed (*ccp)* arrangement of AX_3 layers with *B* sites occupying ¼ of octahedral voids resulting in a corner sharing octahedral network. The anion sublattice in such a structure is highly flexible and can accommodate a large amount of vacancies (ABX_{3-y}, y = 1 being reported [81]), which can result in enhanced electronic conductivity due to mixed valency of the *B* site cation, which forms an important prerequisite towards developing perovskite catalysts for OER/ORR for fuel cell applications[80]. In this respect, cobalt-containing perovskites have been of particular interest due to their catalytic, magnetic and electronic properties [80, 90, 249].

For $BaCoO_{3-y}$ systems, a variety of compounds have been reported and summarized depending of the value of y by Raveau et al. [90] and Mentré et al.[193] For oxygen rich systems, i.e. for low values of y, hexagonal modifications (2H, 5H, 12H) are known and for higher values of y, the cubic modification or *ccp*-related vacancy-ordered variants are known ($BaCoO_{2.22}$ and $BaCoO_2$) [81, 193, 250], and *ccp*-related arrangements can also be stabilized by the uptake of water ($BaCoO_{1.80}(OH)_{0.86}$)[82]. Such or similar barium cobaltates have attracted a lot of attention for their activitiy for the oxygen evolution reaction (OER).[233, 251]

Herein, we report a new vacancy ordered *ccp*-related modification of barium cobaltate with a composition of $BaCoO_{2.67}$ ($Ba_3Co_3O_8\square_1$, □ = anion vacancy) prepared by a two-step heating process together with its electrocatalytic and magnetic properties. The heating steps, times and temperatures were found to be of significant importance for the successful synthesis of the title compound.

4.3.2 Experimental

4.3.2.1 Material synthesis

Conventional high temperature solid state synthesis was used for the synthesis of the intermediate phase. Precursor powders of $BaCO_3$ (99.99%, Alfa Aesar) and Co_3O_4 (99.99%, Alfa Aesar) were hand milled (with acetone) followed by heating in a tube furnace up to 1273 K for 60 hours with a heating and cooling rate of 2 K per minute under argon atmosphere. The as obtained powder was then hand milled and heated to 473 K under oxygen atmosphere for 2 hours. After the second cycle the desired phase was obtained.

Powders with chemical composition $Ba_{0.5}Sr_{0.5}Co_{0.8}Fe_{0.2}O_{3-\delta}$ (BSCF) were synthesized using nebulized spray pyrolysis (NSP). To prepare the starting precursor solution, $Ba(NO_3)_2$ (Sigma Aldrich, 99.99%), $Sr(NO_3)_2$ (Sigma Aldrich, 99.99%), $Fe(NO_3)_3(H_2O)_9$ (Sigma Aldrich, 99.99%) and $Co(NO_3)_2(H_2O)_6$ (Sigma Aldrich, 99.99%) were dissolved in de-ionized water to obtain an overall cation concentration of 0.06 mol l^{-1}, and the mixture was stirred for 30 minutes in order to obtain a homogenous transparent solution. For the synthesis, a setup as previously described was used [80]. The as-prepared solution was injected into the nebulizer unit using a syringe pump with a flow rate of 1.5 ml min^{-1}, while operating the ultrasonicator to generate the mist at a generator voltage and current of 47.0 V and 0.51 A respectively. The precursor mist formed inside the nebulizer unit was transported by a carrier gas stream of argon at the rate of 2 SLM (standard liter per minute) to the reaction tube, which was maintained at 1323 K, and the compounds were collected on a glass filter collector which was held at 393 K. The whole process was carried out at a constant pressure of 900 mbar.

4.3.2.2 Diffraction experiments

X-ray diffraction (XRD) patterns of the compounds were recorded on a Bruker D8 diffractometer using Bragg-Brentano geometry with a fine focusing X-ray tube with Cu $K_{\alpha 1,}$ radiation. A VANTEC detector (3° opening) and a variable divergence slit (4 mm) were used. The total scan time was set to 10 hours for the angular range between 5° and 130° 2θ at a step size of 0.0075. High temperature XRD was measured using an Anton Paar HTK1200 sample stage in the temperature range between 303 K and 973 K (heating rate of 5 K s^{-1}) in the angular range between 20° and 60° 2θ with the step size of 0.0075° (total counting time of 10 min per scan) under a flow of oxygen. These conditions were chosen as a compromise to obtain sufficient data quality for the determination of lattice parameters and phase composition, while lowering differences to the heating procedure used for simultaneous thermal analysis.

Time-of-flight (TOF) neutron powder diffraction (NPD) data were recorded on the high resolution diffractometer (HRPD) at the ISIS pulsed spallation source (Rutherford Appleton Laboratory, Didcot, U.K.). 2 g of powdered $BaCoO_{2.67}$ was loaded into 6-mm-diameter thin-walled cylindrical vanadium sample can under an inert atmosphere and sealed with indium wire. Data were collected at ambient temperature for 2 h 40 m (120 μAh of integrated proton beam current) using the instrument's 30–130 ms time-of-flight window. Raw data were normalized to the incident spectrum and corrected for instrument efficiency using a V:Nb null-scattering standard with the Mantid suite of diffraction algorithms (http://www.mantidproject.org/).

The analysis of the nuclear structure of $BaCoO_{2.67}$ using both the NPD and XRD data was performed using the Rietveld method with the program TOPAS 5 (Bruker AXS, Karlsruhe, Germany) [95]. For the room temperature XRD data, the whole 2θ-range range was used, while for NPD, data collected from the highest resolution backscattering detector bank (bank 1, 158° < 2θ < 176°) as well as the high intensity bank (bank 2, 80° < 2θ < 100°) and the forward-scattering bank 3 (28° < 2θ < 32°) were used. For better depiction, the fit and measurement curves of the XRD pattern shown in Figure 2d in the manuscript were corrected by the refined background curve.

The instrumental intensity distribution for the X-ray data was determined empirically from a sort of fundamental parameters set [108], using a reference scan of LaB_6 (NIST 660a), and the microstructural parameters were refined to adjust the peak shapes for the XRD data. Calibration of the instrumental contribution to the neutron powder diffraction pattern's peak positions and shapes was done using silicon and ceria standards. The lattice parameters were constrained to be the same for neutron and XRD data, and the same positional parameters were used and refined for both data sets. Independent thermal displacement parameters were refined for each type of atom for neutron data.

4.3.2.3 Simultaneous thermal analysis

Simultaneous thermal analysis combining thermogravimetric analysis (TGA) and differential scanning calorimetry (DSC) were conducted for $BaCoO_{2.67}$ on a Netzsch STA 449 F3 Jupiter thermal analyzer. The measurements were performed in the temperature range between 300 K to 973 K using a heating rate of 10 K min^{-1}. Thermal analysis was performed in corundum crucibles under an oxygen flow of 50 ml min^{-1}.

4.3.2.4 Impedance spectroscopy analysis

Alternating current electrochemical impedance spectroscopy measurements were carried out to record the conductivity of the $BaCoO_{2.67}$ and the BSCF pellet. The pellets were made by

isotatic pressing of the powders of $BaCoO_{2.67}$ at 700 kN. The pellet was placed inside the JANIS STVP-200-XG cryostat, which was operated under static helium atmosphere of 1 bar pressure. The pellet was investigated in the temperature range of 298 K to 228 K. Impedance measurements were recorded using a Solartron 1260 frequency response analyzer while applying an AC signal of 100 mV amplitude with frequency ranging from 1 MHz to 100 mHz. Fitting of the data was performed using the Z-view program [109].

4.3.2.5 SQUID magnetic measurements

Magnetic characterization was performed with a Quantum Design MPMS. Powder samples were encapsulated in gelatin capsules and mounted in a straw. Zero-field cooled (ZFC) and field-cooled (FC) curves were measured from 5 to 350 K in the applied field $\mu_0 H$ = 1 T. All magnetization measurements were corrected by the diamagnetic contributions of the phases and of the gelatin capsule and straw used for sample mounting. Field-dependent measurements were performed at 5 K. The magnetic field was scanned from 5 to −5 T.

4.3.2.6 Scanning electron microscopy and Energy Dispersive X-ray spectroscopy

The scanning electron microscopy (SEM) images were taken using the secondary electron detector of a Philips XL30 FEG scanning electron microscope operating at 10 keV. The energy dispersive spectroscopy (EDAX) analysis was carried out using Phillips XL30 FEG set up operating at 15 keV. An EDAX Genesis system was used and an energy resolution of about 140 eV was applied. The mapped area was of the order of 100 μm² and the Ba to Co to Fe ratio was determined from the Ba L, Fe K and Co K lines. The samples were sputtered with approximately 10 nm of Au prior to the measurements.

4.3.2.7 Iodometric titration

The iodometric titrations were carried out to determine the oxidation state of the Co ions in the intermediate compound $BaCoO_{2.46}$, $BaCoO_{2.67}$. and BSCF. 0.05 g of the compound was dissolved in 1M HCl solution and 1 g of KI was added to the solution. Due to the presence of Co^{2+} ions no formation of I_2 could be observed. A few drops of starch solution were added as an indicator. The solution was titrated with sodium thiosulphate ($Na_2S_2O_3$).

4.3.2.8 X-ray photoelectron spectroscopy

The valence states were examined by ex-situ X-ray photoelectron spectroscopy (XPS) analysis using a Physical Electronic VersaProbe XPS unit (PHI 5000 spectrometer) with Al K_α radiation (1486.6 eV). All detailed spectra were recorded with 50.6 W, a step size of 0.1 eV and a pass energy of 23.5 eV. The binding energies were calibrated with respect to the carbon 1s (C1s) emission line at 284.8 eV. Neutralizer was used for all the samples to account for the charging effects. For the determination of Cobalt oxidation states, the Co3p emission was selected since the Co2p and the Ba3d emission strongly overlap and a deconvolution of the signals is not possible. In order to ensure a better comparability, the valence band spectra were normalized to a uniform maximum intensity.

4.3.2.9 N_2 sorption Measurements

N_2 sorption measurements were performed with an Autosorb 3 instrument (Quantachrome). In a first step samples were degassed at 200 °C overnight to remove possibly adsorbed species. Afterwards the samples were transferred to the measuring station. The nitrogen adsorption and desorption isotherms were recorded and the BET specific surface area determined.

4.3.2.10 Electrochemical Measurements

The electrocatalytic activity of these perovskite-type $BaCoO_{2.67}$ and BSCF catalysts towards OER and ORR was investigated using a conventional three electrode setup with a Hg/HgO reference electrode and glassy carbon rod counter electrode. The samples were deposited on the glassy carbon disc of a rotating disc electrode (RDE, PINE) that was connected to a Parstat 3F potentiostat (Versastat). The glassy carbon (GC) electrode was first polished with 1 Fμm diamond on a micro cloth, followed by a 50 nm Al_2O_3 on a master tex polishing cloth, ending by sonicating and rinsing in ethanol and distilled water, respectively. For the preparation of the ink, 5 mg of the sample was mixed with 1.66 mg of carbon black (P-XP, PentaCarbon GmbH, Germany) as a conductive additive and to enhance the utilization of the perovskite. 25 µl of a Nafion solution (5 wt %, QUINTECH) and 83.3 µl of isopropanol and 142 µl of distilled water were added before the suspension was treated firstly by vortex for several seconds and then in an ultrasonic bath for 60 min, ending with the dispersion by vortex to get a homogeneous ink. Afterwards, 6µl of the freshly prepared ink was deposited on the surface of the glassy carbon tip of the RDE electrode (geometrical area of 0.2375 cm^2) and the catalyst loading was 0.5 mg cm^{-2} (carbon not considered). Reference measurements of the pure materials (without carbon black addition) were made for reasons of comparison. Ink preparation and catalyst loading were kept the same.

The electrolyte was 0.1M KOH solution (Potassium hydroxide, >99%, Sigma-Aldrich) saturated with N_2 and O_2 for the OER and ORR, respectively. The electrochemical activity towards OER and ORR was evaluated by cyclic voltammetry (CV) at a rotation speed of 1600 rpm from 1.0 to 1.9 V (OER) and from 0.0 to 1.0 V (ORR) versus reversible hydrogen electrode (RHE) both with a sweep rate of 10 mV s^{-1}. Before the electrochemical tests, an activation step was applied to electrochemically activate the materials and remove the bubbles inside of the catalyst layer by running CV in a range of 1.0 to 0 V_{RHE} for 20 cycles with 100 mV s^{-1} until the observed current voltage characteristic did not change anymore. It should be pointed out that all the potential data are reported applying an *iR* correction ($E_{iR-\mathrm{corrected}} = E - iR$) by compensating for the solution resistance.

The ORR data were capacity corrected by subtracting the CV data obtained in the same potential window and with the same sweep rate but in N_2 saturated electrolyte. For ORR the cathodic sweep and for OER the anodic sweep are displayed.

For reasons of comparison, onset potentials were determined. As Onset potential for ORR we define the potential where the current density becomes lower than -0.1 mA cm^{-2}. Similarly, the onset potential for OER is defined as that potential where the current density becomes larger than 0.1 mA cm^{-2}.

4.3.2.11 Computational details

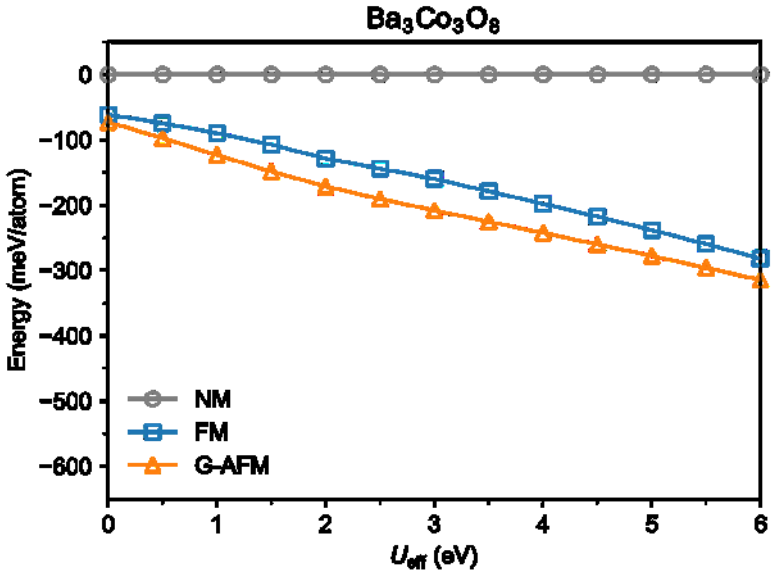

Figure 4.28: *Ab initio* computed energies of $Ba_3Co_3O_8$ = $BaCoO_{2.67}$ as a function of U_{eff}. For each U_{eff}, the energy of the NM state is set as the reference.

The oxygen-vacancy-ordered $P2_1/m$ $Ba_3Co_3O_8$ = $BaCoO_{2.67}$ structure has a 28-atom primitive cell. To be commensurate with the G-type antiferromagnetic (AFM) ordering (in the Wollan–Koehler notation [252]) a 1 × 1 × 2 supercell including 56 atoms was employed as the simulation cell.

We employed the projector augmented wave method [253] and the generalized gradient approximation (GGA) of the Perdew–Burke–Ernzerhof (PBE) form [254] implemented in the VASP code [255, 256] in combination with the provided potentials [257]. The 5s5p6s, 3d4s, and 2s2p orbitals of Ba, Co, and O, respectively, were treated as valence states. The plane-wave cutoff was set to 550 eV. The reciprocal space of the 56-atom supercell was sampled by a Γ-centered 6 × 8 × 4 mesh, and the Methfessel–Paxton scheme [258] with a smearing width of 0.1 eV was employed. Total energies were minimized until they were converged to within 10^{-5} eV per unit cell. Cell volume, cell shape, and internal atomic positions were optimized so that the forces on atoms and the stress components on the supercells are less than 2.5 × 10^{-2} eV/Å and 10^{-3} eV/Å^3, respectively. In addition to the G-AFM state, the nonmagnetic (NM) and the ferromagnetic (FM) states were also computed under the collinear spin-polarized condition. Strong on-site electron correlation was considered for the Co *d* orbitals employing the rotationally invariant DFT+*U* formalism of Dudarev et al.[259] with $U_{eff} \equiv U - J$ varied in a range of 0–6 eV.

As found in Figure 4.28, for the considered U_{eff} range, the G-AFM state is energetically more stable than the FM state, consistently with the experiments in the present study. Following a previous study [260], we focus on $U_{eff} = U - J = 4.5$ eV. The internal atomic positions and lattice parameters are summarized in Table 4.8 and Table 4.9, respectively, which show reasonable agreement with experimental values (Table 4.7).

4.3.3 Results and discussion

4.3.3.1 Structural studies

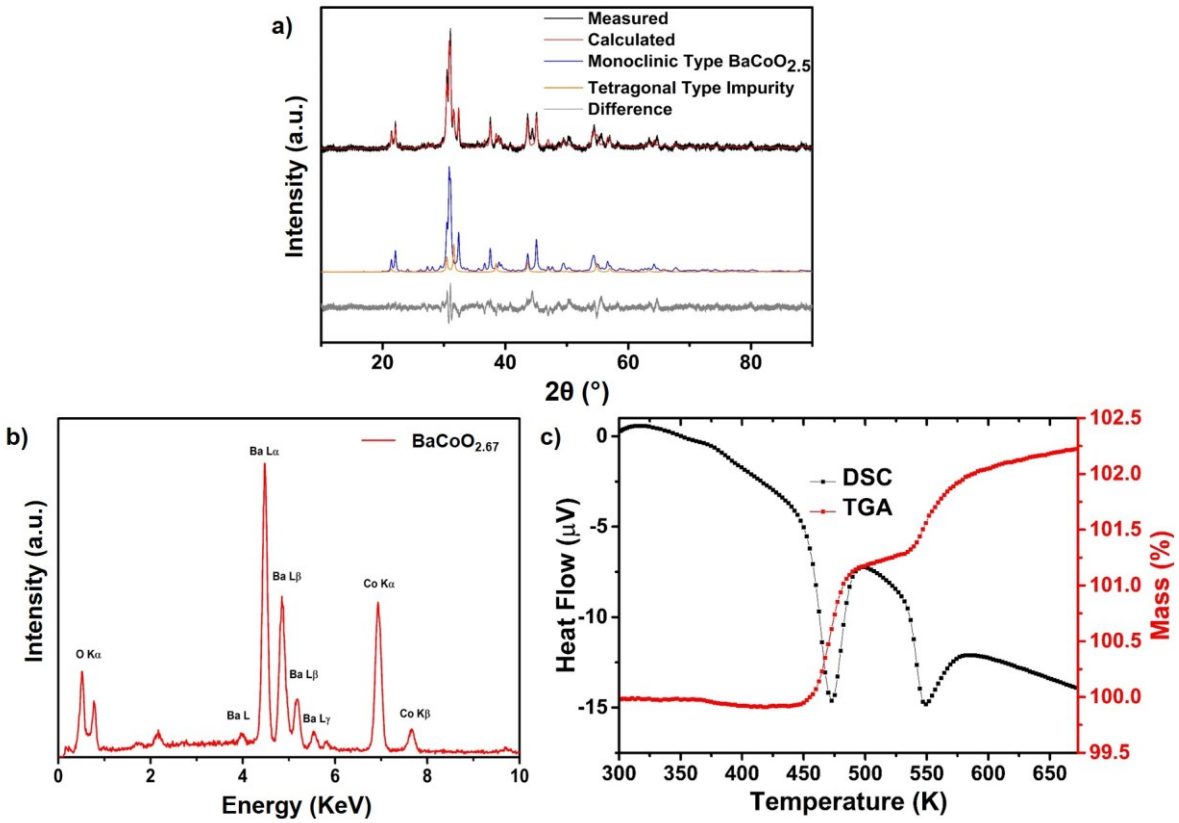

Figure 4.29: (a) Rietveld refinement of intermediate solid state synthesized powder containing a $BaFeO_{2.5}$ type phase and an unknown perovskite related second phase (roughly described here with a tetragonal distorted perovskite phase). (b) EDAX spectra recorded for $BaCoO_{2.67}$ powders using 10 keV electron beam. (c) TGA and DSC curve measured under the flow of O_2 on the intermediate compound $BaCoO_{2.46}$.

After the first heating step at 1273 K for 60 hours under a flow of argon gas, X-ray powder diffraction data indicate the formation of a barium cobaltate phase with a diffraction pattern similar to the vacancy-ordered monoclinic modification of $BaFeO_{2.5}$ [84] together with an additional tetragonal perovskite type phase (see Figure 4.29a). Unfortunately, this phase could not be obtained in a pure form. From the energy dispersive X-ray spectroscopical analysis (EDX), a 1:1 ratio of Ba:Co was confirmed (Figure 4.29b), and iodometric titrations on this phase mixture indicated an average oxidation state of +2.93(1) for cobalt, implying an overall average composition of $BaCoO_{2.46}$. In order to determine the topochemical oxidation behaviour of this compound and suitable reaction conditions for oxygen uptake, simultaneous thermal analysis (STA, Figure 4.29c) was carried out in oxygen atmosphere, which showed an onset of oxygen uptake at 455 K. This mass increase corresponds to an uptake of ~0.21 moles of oxygen, which means an average oxidation state of 3.34 for cobalt and a composition corresponding to ~$BaCoO_{2.67}$. Iodometric titrations confirmed this composition. At 535 K a second mass increase and oxygen uptake is observed, which would lead to a final composition of $BaCoO_{2.80}$. The underlying phase changes were investigated by temperature dependent XRD measurements starting from the phase mixture with composition of $BaCoO_{2.46}$ obtained after the first heating step in oxygen atmosphere. Changes in diffraction pattern are observed starting at 448 K (Figure 4.30a). At 473 K, the X-ray diffractogram shows the appearance of a single phase of the title compound (Figure 4.30b), whereas the patterns recorded at 573 K and above show the presence of a hexagonal type modification (Figure 4.30c), which agrees well

with the further oxygen uptake observed in STA. The appearance of this hexagonal phase is in close agreement to what was reported previously by Raveau et al.[90].

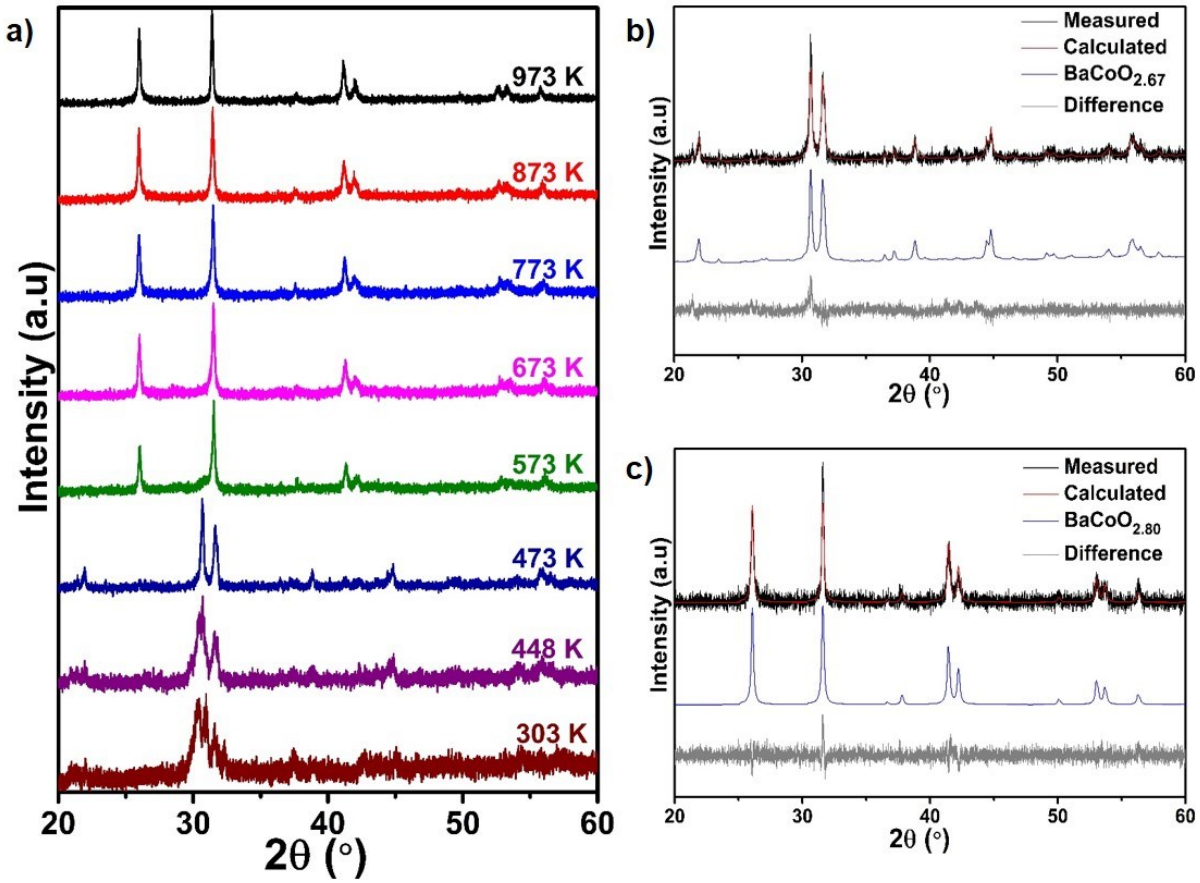

Figure 4.30: (a) High temperature XRD diffractogram for the powder starting from $BaCoO_{2.46}$ powder measured under oxygen atmosphere. (b-c) Rietveld refinement of the diffractogram measured at 473 K and 973 K respectively.

To determine the structure and phase composition of the new modification with composition $BaCoO_{2.67}$, a larger batch of this material was prepared from the as-determined optimized reaction conditions of the second heating step and X-ray diffraction as well as neutron diffraction data were recorded and analysed, see Figure 4.31. The diffraction pattern showed principle similarity to the cubic perovskite modification with apparent splitting of the main reflections and appearance of superstructure reflections. All the reflections could be indexed with a monoclinic unit cell with *a* = 10.1718(3) Å, *b* = 5.6035(2) Å, *c* = 6.9248(2) Å and β = 91.465(4)°, where the lengths of the axes indicate a $\sqrt{6}$ x $\sqrt{2}$ x $\sqrt{3}$ supercell of the cubic aristotype structure (we note that ~3.23(1) wt% of CoO were found as impurity for the larger batch, which indicates close to full homogeneity of the powder). Pawley fits indicated the centrosymmetric monoclinic space group $P2_1/m$ as the most likely symmetry in agreement with the missing (0 1 0) reflection, which is forbidden and could be observed neither in the X-ray nor the neutron diffraction data, further indicating the presence of the 2_1 screw axis (see Figure 4.46 in section 4.5 for the structural relationship). This symmetry had been previously found for the compound $BaFeO_{2.33}F_{0.33}$ [261] [201] with similar overall anion composition by our group for which the symmetry lowering was found to originate from ordering of the anion vacancies. Another member, $BaFeO_{2.67}$, of the $Ba(Fe,Co)(O,F)_{2.67}$ family was recently prepared, and it appears to be isotypic to both $BaFeO_{2.33}F_{0.33}$ and $BaCoO_{2.67}$, which we will report in a separate article. The structural similarity between these compounds is plausible since they contain similar overall anion contents showing that in the setting of a barium-rich anion-deficient

perovskite lattice, only certain anion compositions can give highly favourable structural stabilization and in agreement with our previous finding that hydrated barium ferrates and cobaltates possess close structural similarity [80-82, 262]. Therefore, the structural model of $BaFeO_{2.33}F_{0.33}$ suggested by Clemens et al.[201] was used as the starting model (See Table 4.16 in the section 4.5 for the starting model) for the structural analysis of the X-ray and neutron diffraction data. Relaxation of the model resulted in an excellent fitting of the diffraction data with chemically plausible structural model (see bond distances in Table 4.10). Similar to $BaFeO_{2.33}F_{0.33}$, the 2*a* anion site was found to be vacant which, in combination with smaller structural relaxations, gives rise to cobalt being present in three different coordination environments, i.e., tetrahedral, square pyramidal and octahedral (Table 4.7 and Figure 4.32 structural schematics). Compared to $BaFeO_{2.33}F_{0.33,}$ wherein the Fe cations are only present in the trivalent oxidation state, $BaCoO_{2.67}$ contains mixed valent B site as determined from iodometric titrations corresponding to +3 and +4 oxidation states. From the structural refinements, the average Co-O distances of 2.02 Å, 1.79 Å and 2.01 Å for 6-, 5- and 4-fold coordination were determined for Co1, Co2 and Co3 respectively, which indicates an oxidation state of +3 for Co1 and Co3, as well as +4 for the Co2 site from a consideration of average bond distance [236], and a calculation of bond valence sums (see

Table 4.11). We also would like to acknowledge that we attempted to refine the structure in non-centrosymmetric monoclinic subgroups or within the triclinic subgroup *P*−1. Since these models did not result in any significant improvement of the fit, they were discarded.

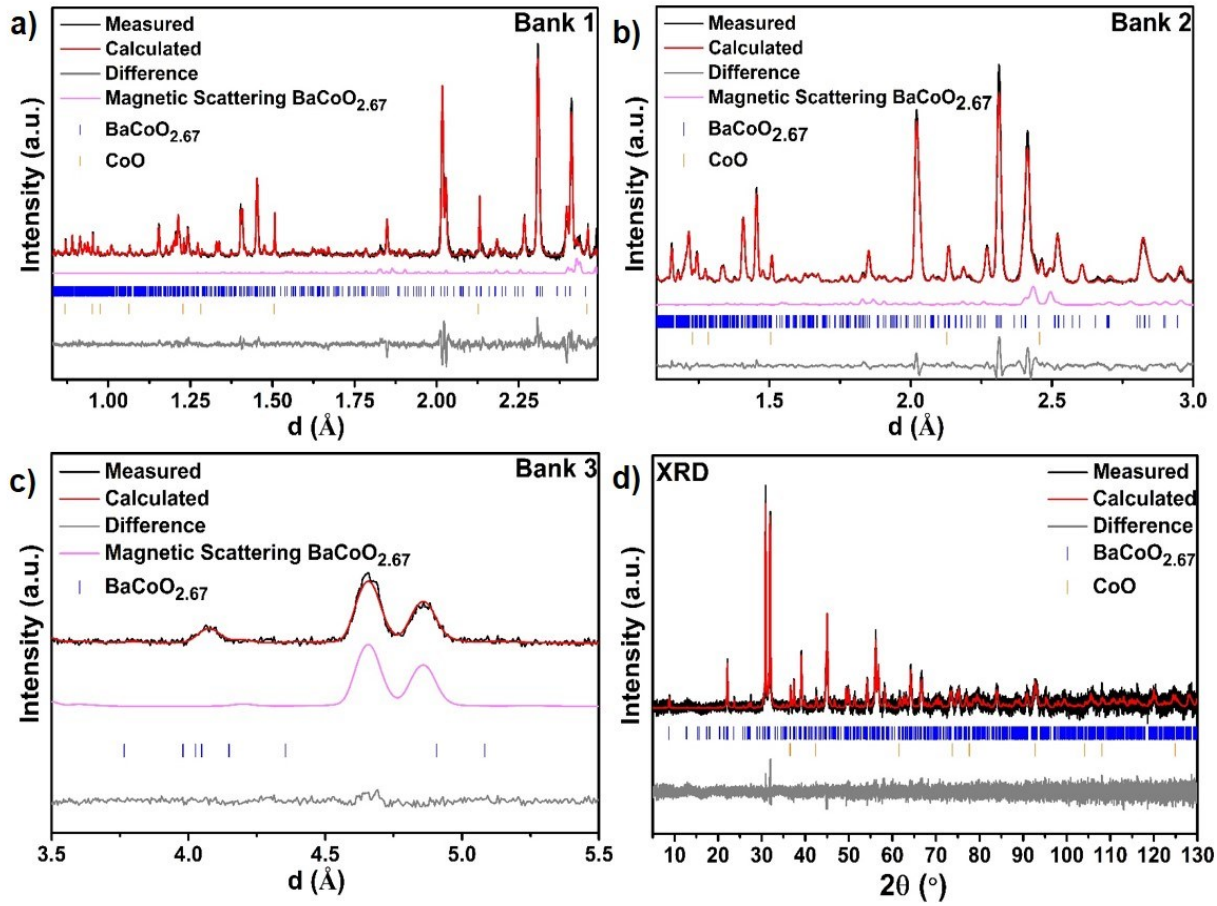

Figure 4.31: Coupled Rietveld analysis of the room temperature neutron (HRPD, bank 1-3,(a-c) and X-ray diffraction (d) patters recorded for $BaCoO_{2.67}$.

Table 4.7: Refined atomic coordinates for $BaCoO_{2.67}$. O7- indicates the O-vacancy position. The red text indicates the coordinates symmetrically restricted. Rietveld refinement of NPD and XRD data were recorded at room temperature. Standard deviations given are numerical standard deviations from the refinements and do not represent interval of trust.

Atom	Wyckoff	*x*	*y*	*z*
Ba1	2*e*	0.2723(7)	¼	−0.0173(10)
Ba2	2*e*	0.9145(6)	¼	0.7191(8)
Ba3	2*e*	0.5683(7)	¼	0.3447(10)
Co1	2*e*	0.2681(16)	¼	0.485(2)
Co2	2*e*	0.8814(12)	¼	0.2200(18)
Co3	2*e*	0.581(2)	¼	0.837(3)
O1	2*e*	0.7541(15)	¼	0.035(3)
O2	2*b*	½	0	0
O3	2*e*	0.4194(17)	¼	0.666(3)
O4	2*e*	0.0362(12)	¼	0.131(2)
O5	4*f*	0.6804(12)	0.022(2)	0.6874(19)
O6	4*f*	0.8478(11)	−0.006(2)	0.3768(15)
O7-vacancy	2*a*	0	0	0

Table 4.8: Ab initio optimized atomic coordinates for BaCoO2.67 with Ueff = 4.5 eV.

Atom	Wyckoff	*x*	*y*	*z*
Ba1	2*e*	0.272	¼	−0.009
Ba2	2*e*	0.912	¼	0.714
Ba3	2*e*	0.569	¼	0.338
Co1	2*e*	0.276	¼	0.501
Co2	2*e*	0.874	¼	0.228
Co3	2*e*	0.586	¼	0.838
O1	2*e*	0.755	¼	0.031
O2	2*b*	½	0	0
O3	2*e*	0.416	¼	0.661
O4	2*e*	0.032	¼	0.144
O5	4*f*	0.674	0.001	0.681
O6	4*f*	0.845	−0.009	0.372
O7-vacancy	2a	0	0	0

Table 4.9: (Experiment) Refined lattice parameters for $BaCoO_{2.67}$ after Rietveld refinements. For the refinements GOF (NPD+XRD) of 1.073 was observed along with the R_{Bragg} value of 7.927 % and 0.664 % for Bank1 and XRD respectively. (Ab initio) Ab initio optimized lattice parameters of G-AFM $P2_1/m$ $Ba_3Co_3O_8$ = $BaCoO_{2.67}$ with U_{eff} = 4.5 eV.

	***a* (Å)**	***b* (Å)**	***c* (Å)**	***β* (°)**
Experiment	10.1717(1)	5.6038(1)	6.9248(1)	91.469(11)
***Ab initio* (U_{eff} = 4.5 eV)**	10.260	5.639	6.999	91.884

Table 4.10: Refined bond distances between cations and anions for $BaCoO_{2.67}$ at room temperature.

Cation	Anion	Distance (Å)	Cation	Anion	Distance (Å)
Ba1	O4 (x 1)	2.596(5)	**Co1**	O3 (x 1)	1.890(8)
	O3 (x 1)	2.721(6)		O6 (x 2)	2.033(6)
	O2 (x 2)	2.739(3)		O5 (x 2)	2.041(6)
	O5 (x 2)	2.805(5)			
	O1 (x 2)	2.8176(6)			
	O6 (x 2)	3.010(5)			
Ba2	O5 (x 2)	2.750(5)	**Co2**	O4 (x 1)	1.733(7)
	O1 (x 1)	2.758(5)		O6 (x 2)	1.801(5)
	O6 (x 2)	2.858(5)		O1 (x 1)	1.824(8)
	O6 (x 2)	2.875(4)			
	O4 (x 2)	3.0209(19)			
	O4 (x 1)	3.077(5)			
Ba3	O3 (x 1)	2.702(7)	**Co3**	O5 (x 2)	1.958(7)
	O3 (x 2)	2.8057(3)		O2 (x 2)	1.971(6)
	O2 (x 2)	2.856(4)		O3 (x 1)	2.038(10)
	O5 (x 2)	2.865(5)		O1 (x 1)	2.234(9)
	O1 (x 1)	2.909(6)			
	O5 (x 2)	2.951(5)			
	O6 (x 2)	3.153(5)			

Table 4.11: Bond valence sum (BVS) for the different crystallographic sites in the monoclinic $BaCoO_{2.67}$ with the global instability index of 0.3125.

Site	BVS	Site	BVS	Site	BVS
Ba1	2.5700	**Co1**	2.3573	**O1**	1.9560
Ba2	2.0711	**Co2**	3.3658	**O2**	2.0302
Ba3	2.3689	**Co3**	2.7675	**O3**	2.1882
				O4	1.8072
				O5	1.8637
				O6	1.8957

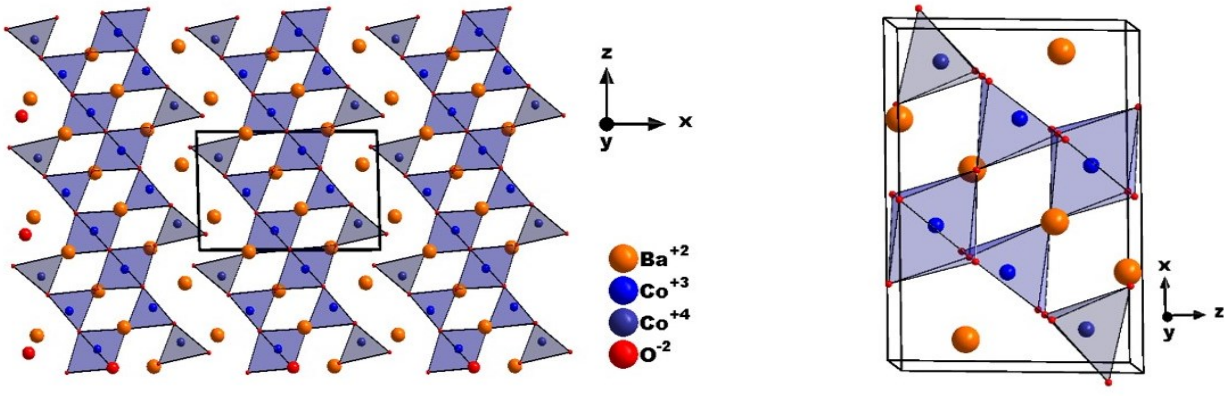

Figure 4.32: Refined crystal structure of $BaCoO_{2.67}$ obtained from the coupled Rietveld fit of neutron and X-ray diffraction data showing the vacancy ordering and three different Co coordination environments.

4.3.3.2 Magnetic studies

Field dependent measurements of magnetization (M-H) were recorded at 10, 80, 250 and 320 K (Figure 4.33a), which mainly indicated an antiferromagnetic behaviour with only a small residual ferromagnetic moment at 10 K (~0.00003 μ_B). This is in agreement with field and zero field cooled measurements (Figure 4.33b) which showed a small but significant difference. This ferromagnetic contribution could be due to the presence of impurity or magnetic canting, which would be undeterminable via powder diffraction techniques. The antiferromagnetic ordering below 350 K is further indicated by the presence of magnetic reflections in the neutron powder diffraction patterns measured at ambient temperatures. These magnetic reflections indicate a magnetic *k*-vector of [0 0 ½]. Thus we attempted to refine the magnetic intensity with different structural models, and found that it can be best described with a G-type antiferromagnetic structure with an average magnetic moment of 2.36(1) μ_B aligned along the *c*-axis. The magnetic moment obtained from the refinements suggests an intermediate spin state for Co with ~1 - 2 unpaired electrons in average. Density functional theory (DFT) based calculations also found consistently that the G-type antiferromagnetically ordered state (G-AFM) is energetically more favourable than the ferromagnetic (FM) state, which nicely supports the experiments above (Figure 4.28).

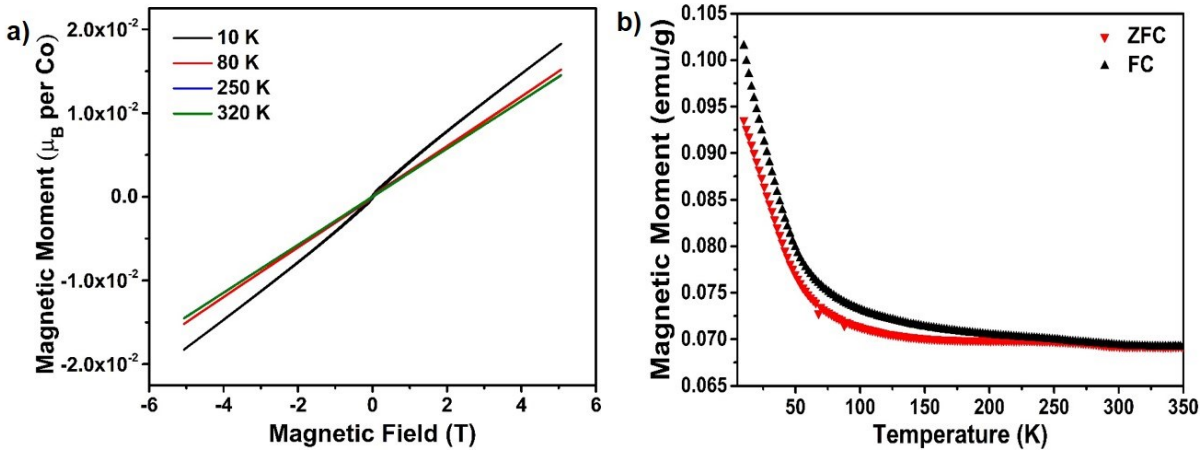

Figure 4.33: (a) Field dependent measurements of magnetization of $BaCoO_{2.67}$. (b) Temperature dependent measurements of magnetization for zero-field cooled and field-cooled sample of $BaCoO_{2.67}$.

4.3.3.3 Electrochemical impedance spectroscopy

Electrochemical impedance spectroscopy measurements (Figure 4.34) were carried out to determine the conductivity of the sample. From the Nyquist plot a single depressed semicircle was observed which was fitted using a single R-CPE (constant phase element). The room temperature conductivity of the sample was determined from the intercept on the X-axis and calculated to be 2.89 x 10^{-4} S cm^{-1} which is of the same order of magnitude as that of $BaCoO_{1.80}(OH)_{0.86}$ [82] and three orders of magnitude higher than that of $BaCoO_{2+\delta}$ [81]. This is in agreement with what is expected from the presence of Co in a mixed oxidation state (+3/+4). An activation energy of 0.21(1) eV was calculated from the slope of the Arrhenius plot (Figure 4.34d) indicating the dominance of electronic contribution to overall conductivity [25, 81].

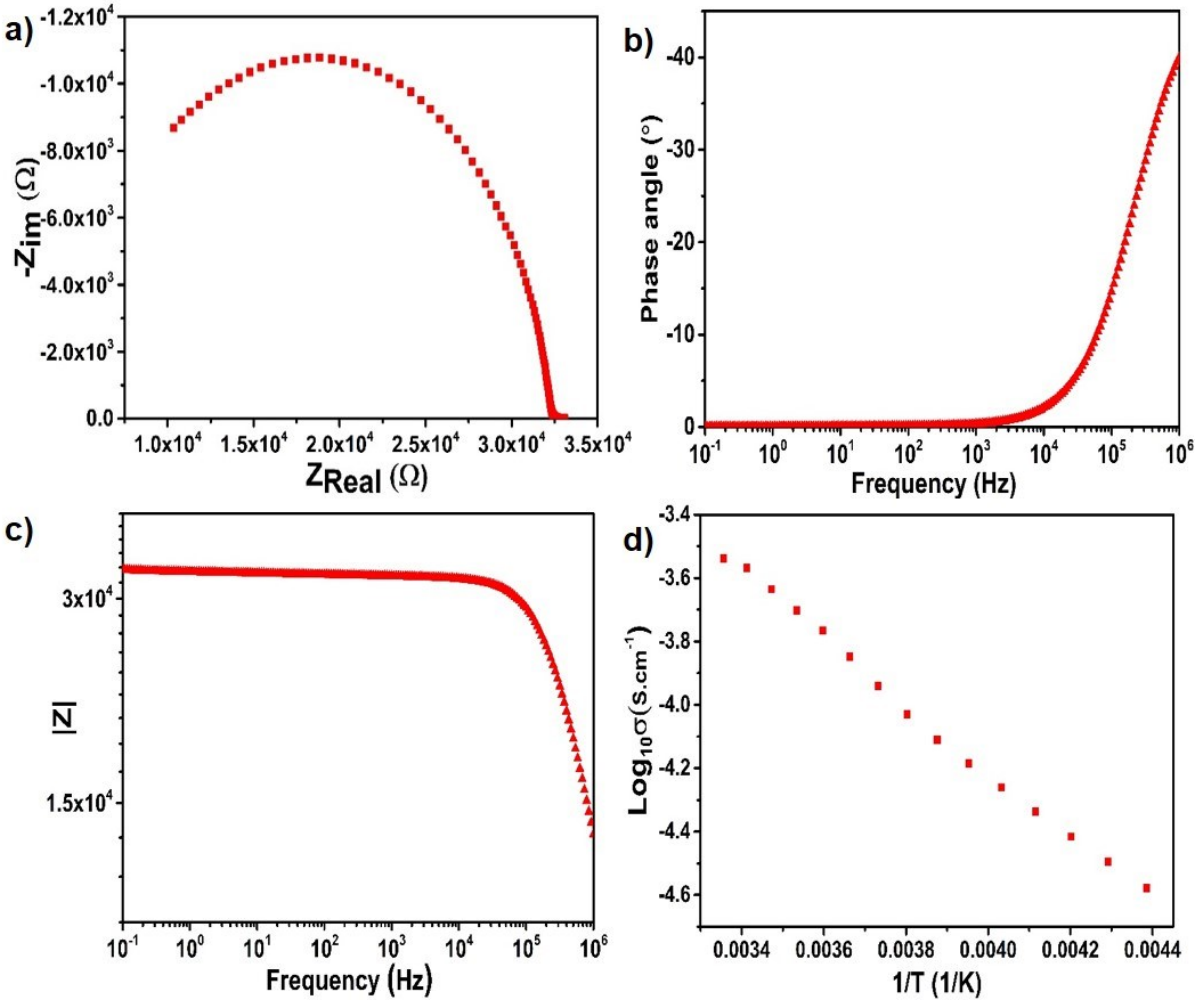

Figure 4.34: (a-c) Nyquist and Bode plots for $BaCoO_{2.67}$ recorded at 228 K. (d) Arrhenius plot for $BaCoO_{2.67}$ measured in the temperature range of 228 to 298 K.

4.3.3.4 Bifunctional catalytic activity

The catalytic activity for OER and ORR was measured for the title compound $BaCoO_{2.67}$ and compared to that of $Ba_{0.5}Sr_{0.5}Co_{0.8}Fe_{0.2}O_{3-y}$ (BSCF) which is the benchmark perovskite catalyst [32] [249] (see 4.5.1 for more details on preparation of reference electrodes and comparative morphological as well as electrochemical characterisation). The catalytic activity in the absence of carbon is low for both compounds (see Figure 4.35). Referencing the activity data to the surface area of the perovskites (Figure 4.35c and d) indicate similar onset of both materials for the ORR while the overall current density (per BET surface area) is larger for $Ba_{0.5}Sr_{0.5}Co_{0.8}Fe_{0.2}O_{3-y}$. The performance towards OER is much better for $Ba_{0.5}Sr_{0.5}Co_{0.8}Fe_{0.2}O_{3-y}$ what might be related to the integration of iron in the system, as it is known for several OER catalysts [229, 263, 264].

Once carbon is added, the catalytic activity of the title compound is very similar to that of the BSCF (for reasons of comparability, the OER and ORR data are plotted together and are shown in Figure 4.36), though the $BaCoO_{2.67}$ particles showed a much coarser crystallinity (see Figure 4.48 in 4.5.1). From the ORR region, we see that at the reference potential of 0.7 V vs RHE (reversible hydrogen electrode) a kinetic current density of 2.305 mA cm^{-2} is achieved and an onset potential of 0.81 V for $BaCoO_{2.67}$. On the other hand, BSCF shows a kinetic current density of 2.105 mA cm^{-2} at 0.7 V with the onset potential of 0.785 V. The positive shift

of the onset potential and larger current density therefore indicate a slightly superior ORR activity for $BaCoO_{2.67}$ as compared to BSCF.

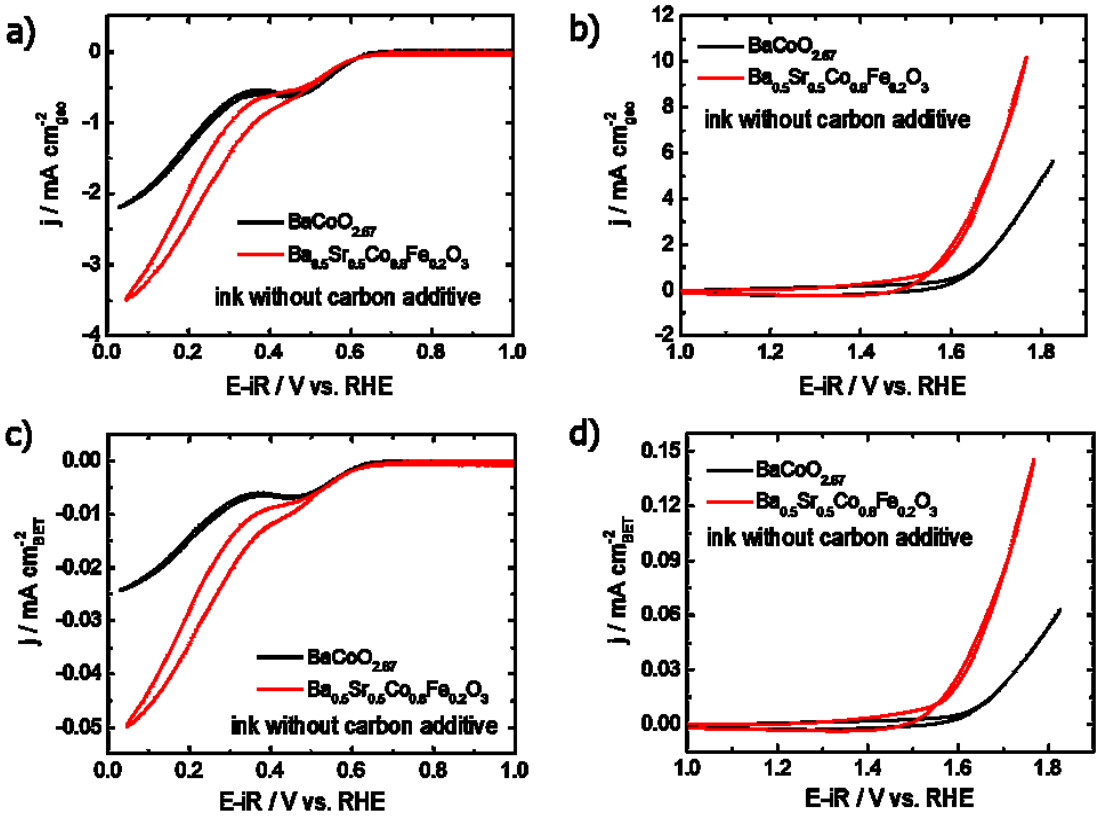

Figure 4.35: Comparison of as-measured geometric current densities towards a) ORR and b) OER and after normalization to the BET specific surface area of the samples c) for ORR and d) OER activity. In all graphs $BaCoO_{2.67}$ and BSCF measured in 0.1M KOH without the addition of conducting carbon are displayed.

In addition to ORR we also investigated the OER characteristics of both $BaCoO_{2.67}$ and BSCF. With the addition of carbon both compounds show almost similar onset potentials and achieve the benchmarking value of 10 mA cm^{-2} at similar potential. The Tafel slopes of both samples are higher in comparison to literature values [234, 265] (see Figure 4.37 and Table 4.12). The origin of this, might be found in smaller conductivity or a larger grain size of our samples in comparison to literature. The bifunctional performance ($\Delta U = U_{OER} - U_{ORR}$) was calculated to be 0.95 V for both $BaCoO_{2.67}$ and BSCF which is much lower compared to the $BaFe_{1-x}Co_xO_{3-y-\delta}(OH)_y$ series [80] and comparable to that of noble metal catalyst [199].

In relation to the suggested dependency of the catalytic activity on electron configuration as provided by Suntivich et al. [31, 32], we aim to provide a qualitative reasoning why similarly high activity can be obtained for $BaCoO_{2.67}$ in comparison to BSCF, though no morphological optimisation of the compound was performed. According to Suntivich et al. [31, 32] both ORR and OER activity are highly dependent on the e_g orbital filling of the transition metal ion with an average occupation of one electron being desirable. For mixed-valent $BaCoO_{2.67}$, all Co ions are located in polyhedra with a local site symmetry of *m*. Such an average filling of e_g states is plausible if Co is present in the intermediate spin state. This would result in the electronic configuration of $t_{2g}^5e_g^1$ for Co^{3+} (and high spin $e_g^3t_{2g}^2$ for Co^{4+}), which could be brought in principle agreement with the local symmetry and thus non-degeneracy within e_g / t_{2g} levels[90], and which might favour such similar catalytic activity. For BSCF, Co has been reported to be present in the intermediate state which would result in the likely electronic configuration of

$t_{2g}^5e_g^{\sim 1.25}$ (average Co oxidation state of +2.75 determined from iodometric titrations) [32]. In addition to the impact of the ordered co-ordination environments and their impact on the electronic configurations, this results in a high density of states (DOS) near the fermi level for both BSCF and $BaCoO_{2.67}$ (Figure 4.38). Although determining the exact spin state of Co in $BaCoO_{2.67}$ on the different crystallographic sites with octahedral, square pyramidal, or tetragonal coordination is hindered experimentally, the catalytic activity observed here in combination with the magnetic moment observed at room temperature by neutron diffraction is plausible in relation to electron configurations found in similar compounds, with an overall occupation of the higher *d*-orbital energy levels by 1.33 electrons for $BaCoO_{2.67}$. Thus, ordering of vacancies can be considered to be the origin for the resulting ordering of charges and electron configurations, which in turn contribute to achieve a high catalytic activity in $BaCoO_{2.67}$.

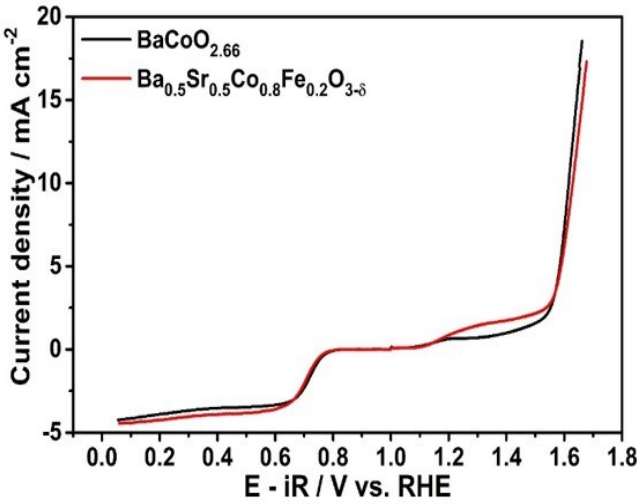

Figure 4.36: Comparison of ORR/OER activity between $BaCoO_{2.67}$ and BSCF in 0.1M KOH. For ORR and OER the cathodic and anodic sweep are displayed.

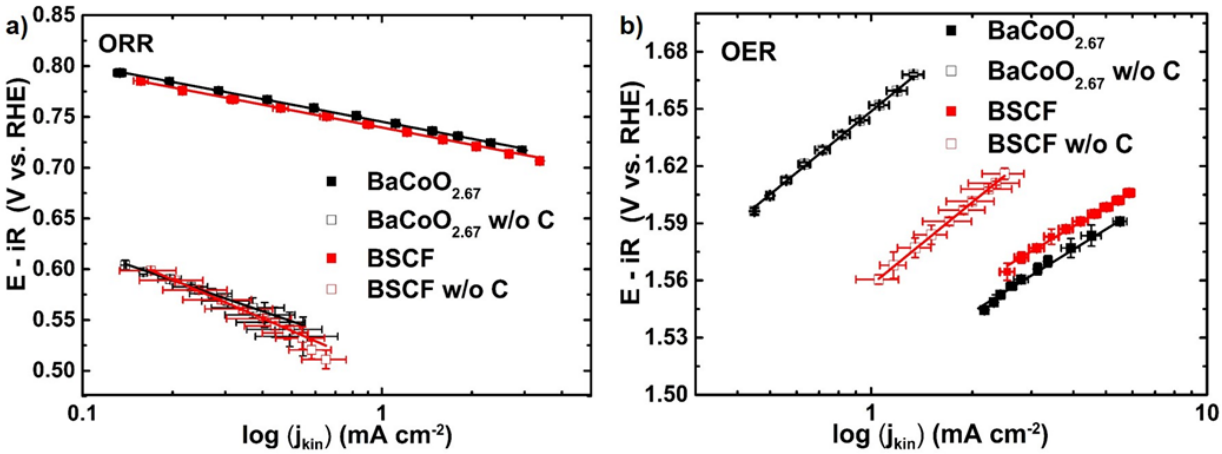

Figure 4.37: Comparison of a) ORR Tafel slopes and b) OER Tafel slopes for $BaCoO_{2.67}$ and BSCF measured with and without carbon.

Table 4.12: Values of Tafel slopes for $BaCoO_{2.67}$ and BSCF.

Sample	OER		ORR	
	With Carbon	Without Carbon	With Carbon	Without Carbon
BSCF	105	144.4	56	126
$BaCoO_{2.67}$	97.8	144.7	55	101

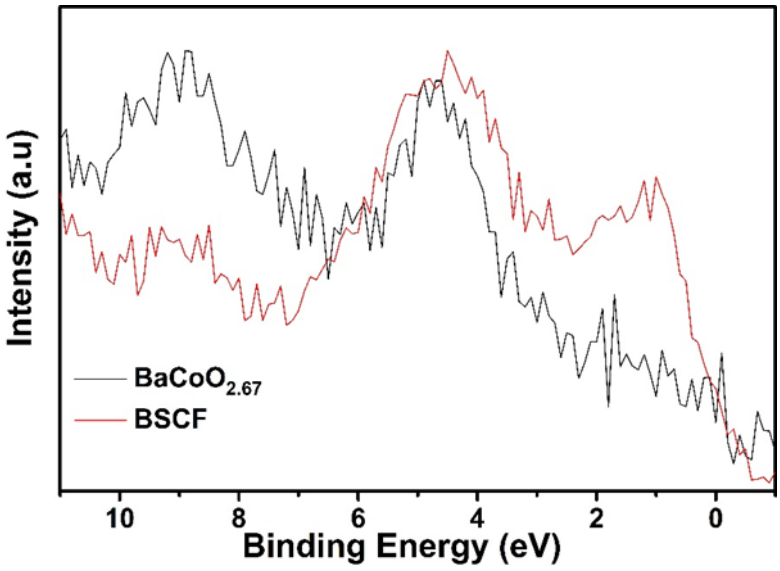

Figure 4.38: Valence band comparison of $BaCoO_{2.67}$ and BSCF.

4.3.4 Conclusion

In summary, a new anion deficient vacancy ordered composition $BaCoO_{2.67}$ synthesized via the topochemical oxidation of an intermediate $BaCoO_{2.46}$ phase. The structure is found to be isotypic to $BaFeO_{2.33}F_{0.33}$ with Co present in 4-,5- and 6-fold coordination. Interestingly, the binfuntional activity of this compound was found to be comparable to that of bench mark perovskite catalyst BSCF possibly due to the mixed valent state of Co along with the favourable anion ordering.

Acknowledgements

We gratefully acknowledge awarding of beam time from the STFC (DOI: 10.5286/ISIS.E.87849379). O. Clemens acknowledges funding by DFG within CL551/2-1. H.K.S. and U.I.K. acknowledge financial support by the Hessian State Ministry for Higher Education, Research and Arts under the LOEWE collaborative project “FLAME”. Open access funding enabled and organized by Project DEAL.

4.4 $BaCoO_{2+\delta}$: A New Highly Oxygen Deficient Perovskite-Related Phase with Unusual Co coordination Obtained by High Temperature Reaction With Short Reaction Times

Aamir Iqbal Waidha,[a] Hongbin Zhang,[b] Maren Lepple,[c] Supratik Dasgupta,[d] Lambert Alff,[d] Peter Slater,[e] A.D. Fortes,[f] and Oliver Clemens[*a,g]

[a] Technische Universität Darmstadt, Institut für Materialwissenschaft, Fachgebiet Materialdesign durch Synthese, Alarich-Weiss-Straße 2, 64287 Darmstadt, Germany.

[b] Institute of Materials Science, TU Darmstadt, 64287 Darmstadt, Germany.

[c] Technische Universität Darmstadt, Eduard-Zintl-Institut für Anorganische und Physikalische Chemie, Alarich-Weiss-Straße 12, 64287 Darmstadt, Germany.

[d] Technische Universität Darmstadt, Institut für Materialwissenschaft, Fachgebiet Dünne Schichten, Alarich-Weiss-Straße 2, 64287 Darmstadt, Germany.

[e] University of Birmingham, School of Chemistry, Edgbaston, Birmingham B15 2TT, UK.

[f] ISIS Facility, Rutherford Appleton Laboratory, Harwell Science and Innovation Campus, Didcot, Oxfordshire OX11 0QX, United Kingdom.

[g] Karlsruher Institut für Technologie, Institut für Nanotechnologie, Hermann-von-Helmholtz-Platz 1, 76344 Eggenstein Leopoldshafen, Germany.

Corresponding Author: oliver.clemens@md.tu-darmstadt.de

Abstract

A new highly oxygen deficient metastable modification of perovskite-related $BaCoO_{2+\delta}$ ($\delta \sim 0.01 – 0.02$) has been prepared using high temperature reactions with short heating times. This defect rich compound has at least partially square planar coordination of the Co^{2+} ions, a highly unusual coordination environment for Co. Low temperature neutron powder diffraction showed a G-type antiferromagnetic ordering, confirmed by SQUID magnetic measurements, which indicates a high Néel temperature of 220 K. This work shows how novel defective phases can be synthesized by exploiting short reaction times in solid state synthesis, thus offering an alternative route for new material synthesis.

4.4.1 Introduction

Perovskite-type or perovskite-related ABX_{3-y} compounds are interesting candidates for a wide range of applications in the field of electronics [206], solid oxide fuel [266] and solar cells [267]. In particular, cobalt based perovskites $ACoO_{3-\delta}$ have drawn a lot of attention due to their interesting electronic, magnetic and catalytic properties [90, 249]. For the latter, especially such compounds with a Co-sublattice, which can be derived from the cubic aristotype structure (i. e. from a close cubic packed (*ccp)* arrangement of AX_3 layers with Co occupying ¼ of octahedral voids), were reported to be of most interest. Within such an atomic arrangement, the structure is highly flexible and can tolerate large amounts of anion vacancies, $ABX_{3-\delta}$ [88, 207, 262] , with values of y up to 1 being known, from which a high mobility of oxygen ions originates.

For non-stoichiometric $BaCoO_{3-y}$ perovskite-related oxides, a broad structural variety of compounds has been found depending on the detailed value of y. Those were summarized by Raveau et al.[90] as well as by Mentré et al.[193] with hexagonal modifications known for oxygen rich systems (2H, 5H, 12H). For large values of y, the most oxygen deficient cubic perovskite phase $BaCoO_{2.22}$[193] as well as trigonal $BaCoO_2$ [215] are known, where the structure of the latter was reported as an ordering variant ($P3_121$) of the cubic aristotype structure with only tetrahedral coordination of the Co ions.

Apart from the thermodynamically stable modifications, highly anion deficient metastable compounds have been previously prepared almost entirely via hydride based reductions [88, 207]. Such reactions are time consuming multi step procedures which require additional washing steps to obtain a phase pure sample. In contrast, direct synthesis of such metastable ABO_2 type perovskite-related phases has not been reported so far.

In this article, we report for the first time the preparation of a highly oxygen deficient tetragonal modification of $BaCoO_{2+\delta}$ synthesized using a simple route, involving high temperature solid state synthesis with considerably short reaction times (twice at 1273 K for 1 h using heating / cooling rates of 2 K/min) of high energy ball milled powders of $BaCO_3$ and Co_3O_4 under pure argon atmosphere. The synthesis conditions show a very narrow sweet spot. Changing the conditions slightly (temperature, flow of argon, heating time, etc.) results either in the formation of the trigonal $BaCoO_2$ modification, or cubic $BaCoO_{2.22}$, or melting of the sample.

4.4.2 Experimental

4.4.2.1 Material synthesis

Conventional high temperature solid state synthesis was used for the synthesis. Precursor powders of $BaCO_3$ (99.99%) and Co_3O_4 (99.99%) were ball milled (with acetone) using vials and balls made of ZrO_2 at the rotation speed of 600 rpm followed by heating in the tube furnace up to 1273 K for 1 hour with a heating and cooling rate of 2 K per minute. The synthesis was carried in a Carbolite STF16180301 tube furnace equipped with an alumina tube (inner diameter of 50 mm) under an argon atmosphere (purity 99.996 %) with constant flow of 0.300 SLM (standard liter per minute). After this cycle, the steps were repeated once again to obtain the desired phase.

4.4.2.2 Diffraction experiments

X- ray diffraction (XRD) patterns of the compound were recorded on a Bruker D8 diffractometer using Bragg-Brentano geometry with a fine focusing X-ray tube with Cu $K_{\alpha 1,}$ radiation. A VANTEC detector (3° opening) and a variable divergence slit (4 mm) were used. The total scan time was set to 10 hours for the angular range between 5° and 130° 2θ at a step size of 0.0075. This 10-hour room temperature XRD pattern must be recorded using an air tight sample holder

to avoid water and CO_2 uptake. This holder causes increased background and reduced signal to noise ratio at the low angle range, which make the superstructure reflection at 10.75 ° 2θ difficult to observe. However, this reflection, which is significant for the 2 x 2 x 1 superstructure, can be clearly observed for measurements taken without airtight conditions in shorter measurement times (see refinement provided in Figure 4.51).

Time-of-flight (TOF) neutron powder diffraction (NPD) data were recorded on the high resolution diffractometer (HRPD) at the ISIS pulsed spallation source (Rutherford Appleton Laboratory, Didcot, U.K.). 2 g of powdered $BaCoO_{2+\delta}$ was loaded into 6-mm-diameter thin-walled cylindrical vanadium sample can under an inert atmosphere and sealed with indium wire. Data were collected at ambient temperature for 2 hr 40 m (120 μAh of integrated proton beam current) using the instrument's 30-130 ms time-of-flight window. The sample was then mounted in a Closed Cycle Refrigerator (CCR) and cooled to 10 K where data were collected for 2 hr (80 μAh) in the 30-130 ms TOF window. Raw data were normalized to the incident spectrum and corrected for instrument efficiency using a V:Nb null-scattering standard with the Mantid suite of diffraction algorithms (http://www.mantidproject.org/).

The analysis of the nuclear structure of $BaCoO_{2+\delta}$ using both the NPD and XRD data was performed using the Rietveld method with the program TOPAS 5 (Bruker AXS, Karlsruhe, Germany) [95]. For the room temperature XRD data, the whole 2θ-range range was used, while for NPD, data collected from the highest resolution backscattering detector bank (bank 1, 158° > 2θ > 176°) as well as the high intensity bank (bank 2, 80° > 2θ > 100°) and the forward-scattering bank 3 (28° > 2θ > 32°) were used. For better depiction, the fit and measurement curves of the XRD pattern shown in Figure 4.51 in the manuscript were corrected by the refined background curve, which contains the high scattering contribution resulting from the air tight sample holder (see Figure 4.51).

The instrumental intensity distribution for the X-ray data was determined empirically from a sort of fundamental parameters set [108], using a reference scan of LaB_6 (NIST 660a), and the microstructural parameters were refined to adjust the peak shapes for the XRD data. Calibration of the instrumental contribution to the neutron powder diffraction pattern's peak positions and shapes was done using silicon and ceria standards. The lattice parameters were constrained to be the same for neutron and XRD data, and the same positional parameters were used and refined for both data sets. Independent thermal displacement parameters were refined for each type of atom for neutron data.

The overall oxygen content of the sample was constrained to a composition of $BaCoO_2$ to avoid correlation with thermal parameters being used. As it has been found previously by Kageyama et al.[262], split sites for the iron or barium ions were found for the disordered structurally similar $Ba_{0.8}Sr_{0.2}FeO_2$. Therefore, we also examined the possibility of split sites for the ions individually, and only included them into the final refinement model, if substantial deviation from the ideal position was indicated.

The misfits in Bank 1 are due to the use of the cryostat to carry out the measurement at 10 K, which causes the appearance of additional sharper reflections. These reflections at 1.24 Å (overlapping with the reflections from $BaCoO_{2+\delta}$), 1.43 Å, 1.50 Å, 2.03 Å and 2.6 Å were not observed in the diffraction pattern recorded at room temperature, for which the cryostat has not been used. Further, we ruled out the possibility of these reflections belonging to the title compound by testing various superstructure models within Pawley type refinements. This is also in agreement with the fact that the FWHM is significantly smaller than observed for the reflections belonging to $BaCoO_{2+\delta}$.

4.4.2.3 Simultaneous thermal analysis

Simultaneous thermal analysis combining thermogravimetric analysis (TGA) and differential scanning calorimetry (DSC) were conducted for $BaCoO_{2+\delta}$ on a Netzsch STA 449 F3 Jupiter thermal analyzer. The measurements were performed in the temperature range between 300 K to 973 K using a heating rate of 10 K min^{-1}. Thermal analysis was performed in corundum crucibles under an oxygen flow of 50 ml min^{-1}.

4.4.2.4 Impedance spectroscopy analysis

Alternating current electrochemical impedance spectroscopy measurements were carried out to record the conductivity of the $BaCoO_{2+\delta}$ pellet. The pellets were made by isotatically pressing the powders of $BaCoO_{2+\delta}$ at 700 kN. The pellet was placed inside the JANIS STVP-200-XG cryostat, which was operated under static helium atmosphere of 1 bar pressure. The pellet was investigated in the temperature range of 298 K to 338 K. Impedance measurements were recorded using a Solartron 1260 frequency response analyzer while applying an AC signal of 100 mV amplitude with frequency ranging from 1 MHz to 100 mHz. Fitting of the data was performed using the Z-view program [109].

4.4.2.5 SQUID Magnetic Measurements

Magnetic characterization was performed with a Quantum Design MPMS. Powder samples were encapsulated in gelatin capsules and mounted in a straw. Zero-field cooled (ZFC) and field-cooled (FC) curves were measured from 5 to 300 K in the applied field $\mu_0 H$ = 2 T. All magnetization measurements were corrected by the diamagnetic contributions of the phases and of the gelatin capsule and straw used for sample mounting. Field-dependent measurements were performed at 5 K. The magnetic field was scanned from 2 to −2 T.

4.4.2.6 Energy Dispersive X-ray Spectroscopy

The energy dispersive spectroscopy (EDAX) analysis was carried out using Phillips XL30 FEG set up operating at 15 keV. An EDAX Genesis system was used and an energy resolution of about 140 eV was applied. The mapped area was of the order of 100 μm² and the Ba to Co to Fe ratio was determined from the Ba L, Fe K and Co K lines. The samples were sputtered with approximately 10 nm of Au prior to the measurements.

4.4.2.7 Iodometric titration

The iodometric titrations were carried out to determine the oxidation state of the Co ions in $BaCoO_{2+\delta}$. 0.05 g of the compound was dissolved in 1M HCl solution and 1 g of KI was added to the solution. Due to the presence of Co^{2+} ions no formation of I_2 could be observed. A few drops of starch solution were added as an indicator. The solution was titrated with sodium thiosulphate ($Na_2S_2O_3$).

4.4.2.8 Raman Spectroscopy

Raman spectra were recorded with a confocal micro-Raman spectrometer (Horiba HR 800, Horiba, Japan), using an Ar-ion laser with a wavelength of 514.5 nm. Spectra were recorded in a Raman shift range from 0 to 4000 cm^{-1}.

4.4.2.9 DFT Studies

The DFT calculations were carried out using the projector augmented wave method as implemented in the VASP code.[254] The exchange-correlation potential is approximated in the generalized gradient approximation (GGA), as parameterized [268]. The energy cutoff was taken to be 500 eV. For the Brillouin zone integration, the number of k-points Nk along each

crystalline axis was determined by Nk×Latt~50, where Latt denotes the lattice constant in Angstrom. The structural optimizations were done with the lattice constants and atomic positions (tolerance for forces being 0.01 eV/Å) fully relaxed. To account for the local Coulomb correlations on the Co sites, GGA+U approximation in the rotational-invariant form [269] was applied with the effective U-J = 4.2 eV. All the calculations have been performed assuming ferromagnetic (FM) configurations, where the antiferromagnetic (AFM) states will lower the energies further but cannot affect the energy difference between the structure models considered. For instance, for model#2, the G-AFM state is about 0.063 eV per formula unit lower in energy than the FM state, confirming also the magnetic ground state (see the main text).

4.4.3 Results and discussion

4.4.3.1 Structural analysis

The composition of the sample was determined from a combination of iodometric titration and energy dispersive X-ray spectroscopy (Figure 4.39a) [82, 193]. The average oxidation state of Co was determined to be $Co^{+2.03(2)}$ with a 1:1 ratio of Ba:Co. This results in an overall composition of the sample close to $BaCoO_{2+\delta}$ with $\delta \sim 0.01 - 0.02$. Since carbonate has been previously reported to be stabilized on the B site within the perovskite structure, the presence of this species was further ruled out by the use of Raman spectroscopy [270] (Figure 4.39b).

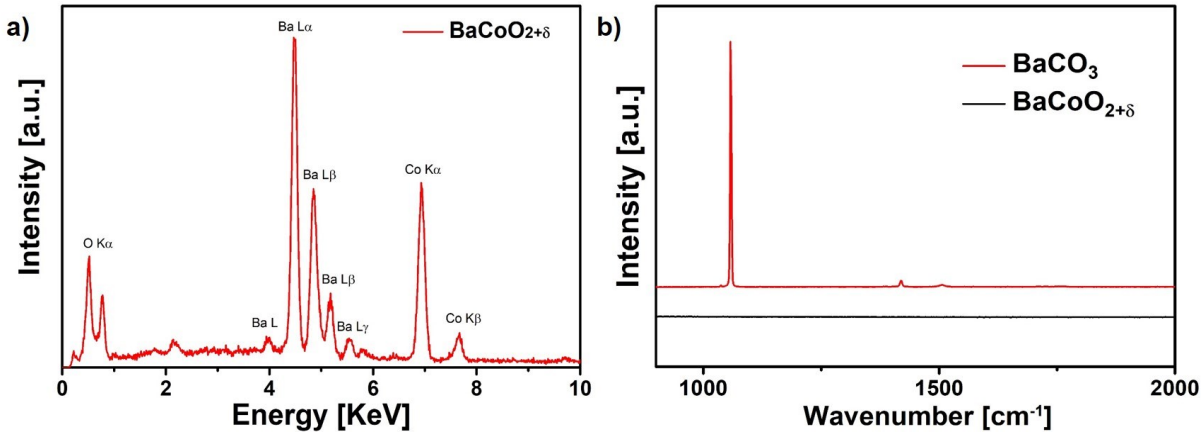

Figure 4.39: (a) EDAX spectra recorded for $BaCoO_{2+\delta}$ powders using 10 keV electron beam. (b) Raman spectra recorded for the $BaCoO_{2+\delta}$ and $BaCO_3$ powders to show the absence of carbonate band around 1200 cm^{-1} for $BaCoO_{2+\delta}$.

The structure and phase composition of the obtained powder was studied via a combined Rietveld analysis of X-ray and neutron powder diffraction data. All of the reflections could be indexed with a 2 x 2 x 1 tetragonally distorted superstructure of the cubic perovskite aristotype (Figure 4.40) with *a* = 8.2201(15) Å and *c* = 3.9181(7) Å, additionally, 8.8(3) wt-% of trigonal $BaCoO_2$ and ~ 3.1(3) wt-% of CoO were identified as impurity phases. Among the maximum subgroups of *Pm*-3*m* with those lattice parameter restrictions, only *P4/mmm* (and its *translationengleiche* subgroups, Figure 4.49 and Figure 4.50 in Section 4.5), allow for the (1 0 0) superstructure reflection observed at 10.74 °(2θ) (Figure 4.51 in section 4.5) in the XRD pattern.

This tetragonal distortion is unusual, since it implies a c/a ratio smaller than 0.5 ($c_{prim}/a_{prim} < 1$), which is often found for compounds with (partial) square planar coordination of the transition metal. Remarkably, only $Ba_{0.8}Sr_{0.2}FeO_2$ was previously reported to crystallize in such a 2 x 2 x 1 primitive superstructure by Kageyama et al. [262], with the B-site cation being located at three independent crystallographic sites (Ba @ 4*k*; Co @ 1*a*, 1*c*, 2*f*). For this compound, square

planar, but also 6-fold coordination of Fe^{2+} and coordination numbers lower than four would have to result from the structural model suggested, originating from an only partial ordering of the anion vacancies, confirmed by Mössbauer spectroscopy. A structural similarity between the phase prepared here to this Fe-based phase is chemically plausible regarding the overall anion content and because barium ferrates / cobaltates are known for their structural similarity [82,37]. However, no tetrahedral coordination is possible from the ideal site symmetries of the Co sites (2x 4/*mmm*, 1x *mmm*). This is surprising with respect to the tetrahedral coordination found for the previously known modification of $BaCoO_2$ [215].Therefore, we also investigated a second structural setting within the same space group, which differs by distribution of the Ba and Co ions on the different crystallographic sites (Ba @ 1*a*, 1*c*, 2*f*; Co @ 4*k*). In this structural setting, a tetrahedral coordination of Co is allowed from its site symmetry (*m*2*m*).

Both, the model suggested by Kageyama et al. [262] (model#1) as well as the alternative model (model#2) were used for the analysis of the neutron (ambient and 10 K) and X-ray diffraction data (see Table 4.17 and Table 4.18 for the starting models in section 4.5 and Table 4.13 and Table 4.14 for the refined structural models and

Table 4.15 for the refined cation to anion bond distances for model #1). Both models result in a good description of the diffraction data, with model#1 resulting in the best goodness of fit / R_{wp} values. Remarkably, no full ordering of oxygen vacancies was found for both models, and this implies that at least some of the Co^{2+} ions must be present in a square planar coordination or in a coordination with even lower coordination numbers (Figure 4.41a and b).

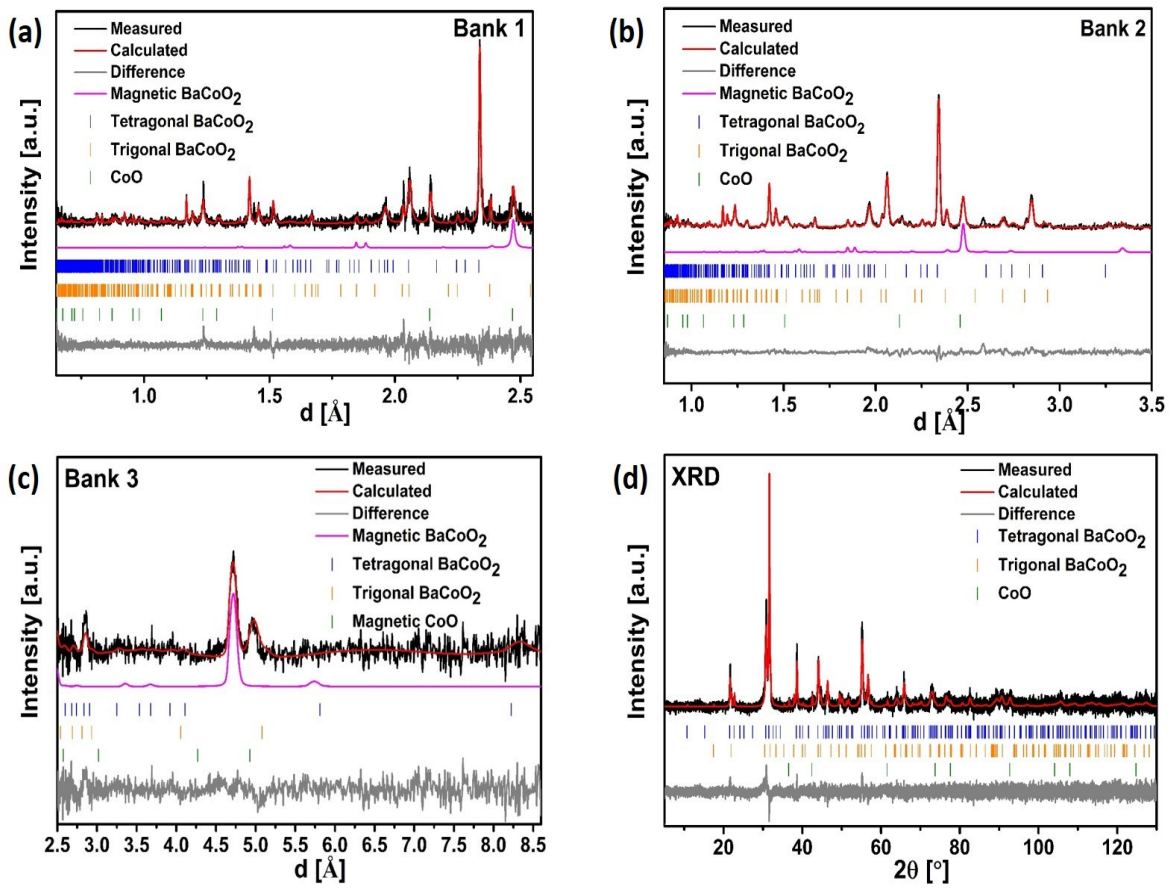

Figure 4.40: Coupled Rietveld refinement of the neutron diffraction data recorded at 10 K and room temperature X-ray diffraction patterns of $BaCoO_{2+\delta}$ using model#1 (see text).

Subsequently, we attempted to refine the structure within the tetragonal *translationengleiche* subgroups of *P*4/*mmm*, which allow for further tilting of the polyhedra. However, such models do not result in a significant improvement of fit with respect to the additional parameters and do not result in an increase of localization of the oxygen ions and anion vacancies. Furthermore, model#2 does not become favourable over model#1. We also would like to emphasize, that the data showed no indication for further symmetry lowering, e. g. from the appearance of superstructure reflections or splitting of the reflections, and using structures within lower symmetry crystal systems did not result in an improved fit. To the best of our knowledge, a planar coordination of Co^{2+} has not been observed so far in anion deficient perovskite structures [193], although it can be found, e. g., in $Sr_2CoO_2Cu_2S_2$ [271].

Table 4.13: Refined structural parameters for $BaCoO_{2+\delta}$ presented along with the unit cell parameters, GOF, R_{wp} values for coupled Rietveld refinement of NPD data recorded at 10 K and room temperature XRD. Standard deviations given are numerical standard deviations from the refinements and do not represent interval of trust.

Atom	Wyck	x	y	z	Occ	B_{eq}
Ba	4k	0.7593(3)	0.7593(3)	½	1	0.18(8)
Co1	1a	**0**	**0**	**0**	1	
Co2	1c	½	½	**0**	1	0.06 (1)
Co3	4l	**0**	0.487(4)	**0**	0.5	
O1	1b	**0**	**0**	½	0.4750(11)	
O2	1d	½	½	½	0.2473(2)	1.15(5)
O3	2e	**0**	½	½	0.2843(13)	

O4	4l	0.2804(6)	**0**	**0**	1	
O5	4n	0.2675(12)	½	**0**	0.5585(12)	
a(Å) (NPD)= 8.2064(4)		**c(Å) (NPD)= 3.9113(3)**			**R_{wp}** = 2.815	
GOF (NPD + XRD)		1.302	**R_{Bragg} (%) =** 1.571 **(NPD Bank 1)**,1.387 **(XRD)**			

Table 4.14: Structural parameters for tetrahedral coordination of Co ion refined $BaCoO_{2+\delta}$ presented along with the unit cell parameters, GOF, R_{wp} values for coupled Rietveld refinement of NPD data recorded at 10 K and room temperature XRD. Standard deviations given are numerical standard deviations from the refinements and do not represent interval of trust.

Atom	Wyck	x	y	z	Occ	Beq
Ba1	1a	0	0	0	1	
Ba2	2f	½	0	0	1	0.81(6)
Ba3	1c	½	½	0	1	
Co1a	4k	0.320(10)	0.320(10)	½	0.136(4)	0.72(4)
Co1b	4k	0.257(12)	0.257(12)	½	0.841(4)	
O1	4j	0.2557(8)	0.2557(8)	0	0.440(9)	
O2	4o	0.2158(8)	½	½	0.885(11)	1.34(5)
O3	4m	0.2302(12)	0	½	0.673(15)	
a(Å)(NPD) = 8.2058(4)			**c(Å)(NPD)= 3.9101(2)**		**R_{wp}** = 3.07	
GOF (NPD + XRD) = 1.455			**R_{Bragg} (%) =** 1.397 **(NPD Bank 1)**,1.209 **(XRD)**			

Table 4.15: Refined bond distances between cations and anions for $BaCoO_{2+\delta}$ at 10K.

Cation	Distance to anions (Å)	Cation	Distance to anions (Å)
Ba1	2.793(3) (O1 x 1) 2.7985(15)(O4 x 4) 2.899(2)(O5 x 4) 2.9034(1) (O3 x 2) 3.010 (3) (O2 x 1)	**Co2**	1.908 (10) (O5 x 4) 1.9555(1) (O2 x 2)
Co1	1.9553(1) (O1 x 2) 2.301 (5) (O4 x 4)	**Co3**	1.91(3) (O4 x 1) 1.9584 (16) (O3 x 2) 2.198 (10) (O5 x 2)

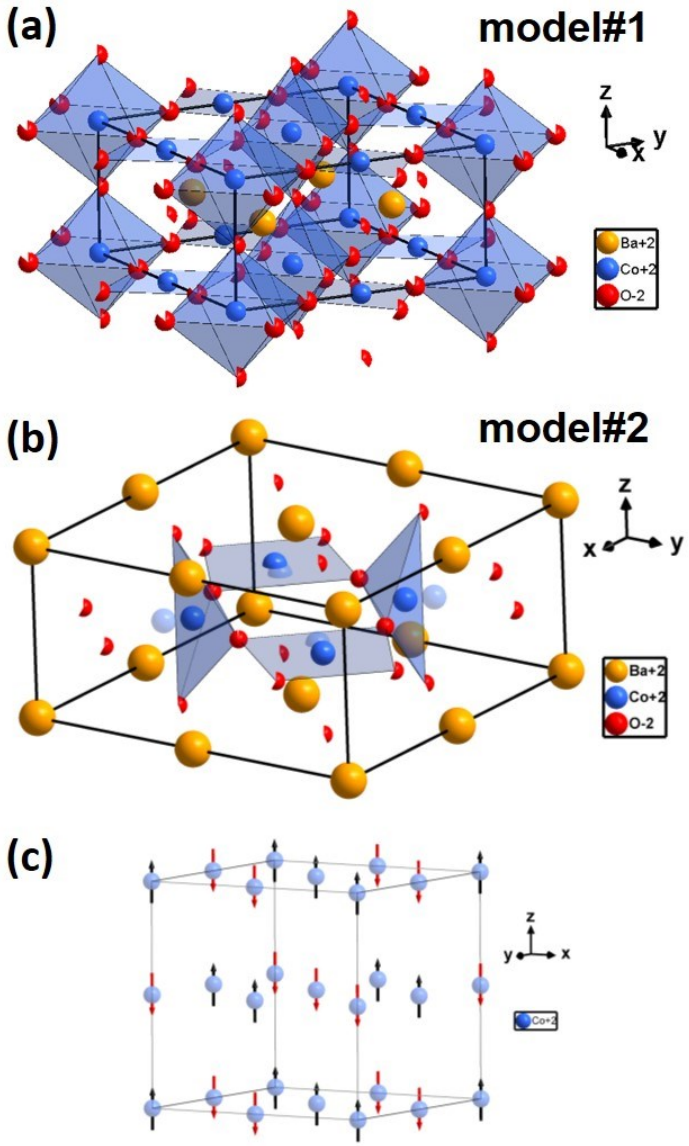

Figure 4.41: Structural representation of $BaCoO_{2+\delta}$: (a) model#1, (b) model#2. Oxygen sites are depicted to indicate their fractional occupancy. For model#2, a split site model was used to refine the position of the Co ion, and most plausible polyhedra are indicated for the different possible coordination scenarios. (c) G-type AFM structure found for the magnetic moments ($c_{magnetic}$ = 2 x $c_{nuclear}$).

To obtain a deeper understanding on the role of coordination geometry around Co on the stability of a phase with ideal composition $BaCoO_2$, we carried out DFT based calculations on fully ordered models #1 and #2, with square planar and tetrahedral coordination of the Co ions, respectively, as well as on the trigonal modification (model #3). The values are summarized in Table 4.19 in section 4.5, showing model #1 to be the least favourable setting and the trigonal modification to be energetically most favourable (E(#3) < E(#2) < E(#1), with differences of Δ(E(#3)-E(#1)) ~ -0.5 eV and Δ(E(#3)-E(#2)) ~ -0.25 eV). Therefore, the disorder generated by the small amount of additional oxygen δ (which are too costly to be calculated) must influence the overall structural stability, making the disordered tetragonal modification more favourable.

4.4.3.2 Magnetic studies

A magnetic phase transition was found to occur at a temperature of approximately 220 K, indicating antiferromagnetic (AFM) ordering (see Figure 4.42a; the magnetic properties are unknown for the trigonal phase of $BaCoO_2$; CoO orders AFM below ~ 290 K [193,272]). This is also in agreement with the presence of only a small residual ferromagnetic moment in the magnetisation curve recorded at 5 K (Figure 4.42b). To determine the magnetic structure of $BaCoO_{2+\delta}$, neutron diffraction data at 10 K were recorded. At this temperature, additional reflections appear as compared to the room temperature data. A part of them arise from the AFM ordering of CoO, and can be described with the magnetic structure of this phase as described previously [272]. The other reflections originate from the magnetic ordering of $BaCoO_{2+\delta}$ and can be indexed based on a magnetic *k*-vector of [0 0 ½]. We tested all models within the maximum magnetic subgroups of *P*4/*mmm*, and found that the magnetic scattering can be best described by the presence of anti-ferromagnetic (AFM) G-type order with the magnetic moment of 2.55(2) μ_B being aligned along the c-axis. This ordering corresponds to the magnetic symmetries P_c4/mcc (124.360) for model#1 or P_C4_2/mmc (131.444) for model#2 respectively, see Figure 4.41c. The refined magnetic moment is in agreement with what would be expected for high-spin Co^{2+} (3.7 μ_B), taking into account that the magnetic moment obtained from neutron diffraction is reduced by covalent contributions.

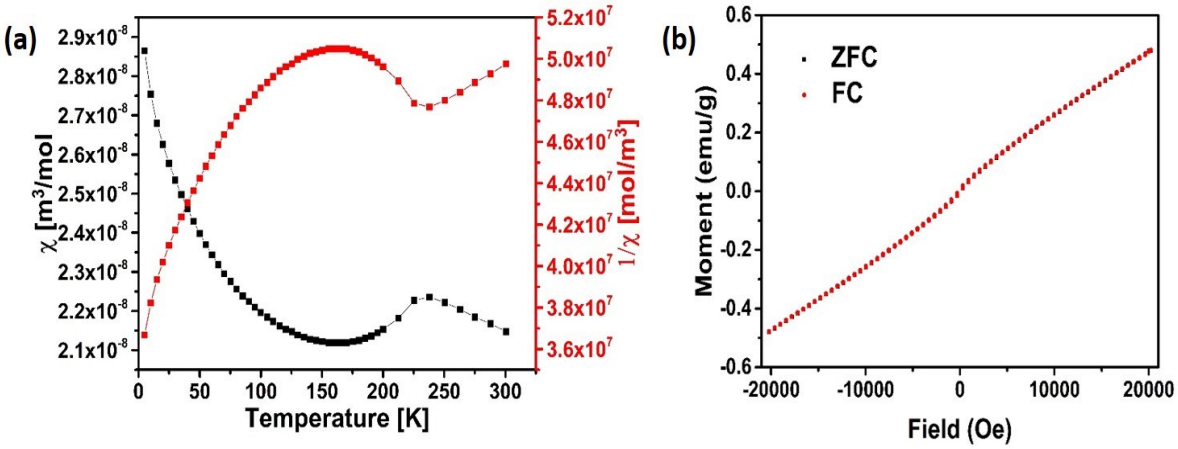

Figure 4.42: (a) Susceptibility vs temperature curve (black) and inverse susceptibility curve (red) for $BaCoO_{2+\delta}$ measured at the field of 2 Tesla.(b) M vs H curve for $BaCoO_2$ measured at 5 K.

4.4.3.3 Electrochemical impedance spectroscopy

We also studied the conductivity of the sample by means of electrochemical impedance spectroscopy (Figure 4.43). The conductivity is of the order 10^{-8} S cm^{-1} at 298 K, which is significantly lower by ~ 3-4 orders of magnitude as compared to, e. g., $BaCoO_{1.80}(OH)_{0.86}$ with Co in a mixed valent +2/+3 oxidation state. The slope of the Arrhenius plot corresponds to an activation energy of 0.30(1) eV, and no blocking behaviour could be observed at low frequencies. Both suggest mainly electronic conductivity of the sample. The relatively low conductivity can be understood from the presence of mainly divalent Co^{2+}, and the similarity of activation energy to mixed valent $BaCoO_{1.80}(OH)_{0.86}$ [82] indicates a similar conduction mechanism by electron hopping due to the presence of Co^{3+}.

We also found that the sample is highly sensitive towards re-oxidation by means of simultaneous thermal analysis (STA) (Figure 4.44a) in pure oxygen. The onset of mass increase due to oxygen uptake upon heating at ~ 425 K is in agreement with the exothermic peak in the DSC profile which is due to the oxygen uptake forming a compound of composition

of $BaCoO_{2.40}$ at this point. XRD measurements showed that the sample is then composed of a cubic perovskite phase (as reported, e.g., for $BaCoO_{2.22}$ [193]) plus a further unknown phase. This is similar to what was observed previously for the dehydration of $BaCoO_{1.80}(OH)_{0.86}$ [82]. On further heating, the mass increase continues up to a temperature of approximately 900 K leading to formation of $BaCoO_{2.66(2)}$, and this oxygen uptake is then accompanied by a complete structural transformation to the 2H modification, as can be seen from the XRD pattern shown in Figure 4.44b.

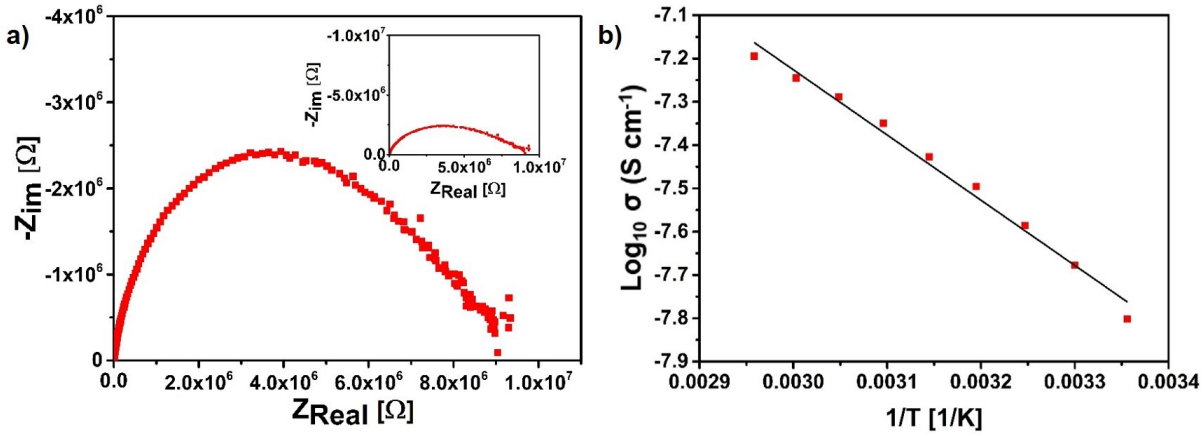

Figure 4.43: (a) Nyquist and (b) Arrhenius plot for temperature dependent total electrical conductivity of $BaCoO_{2+\delta}$ sample.

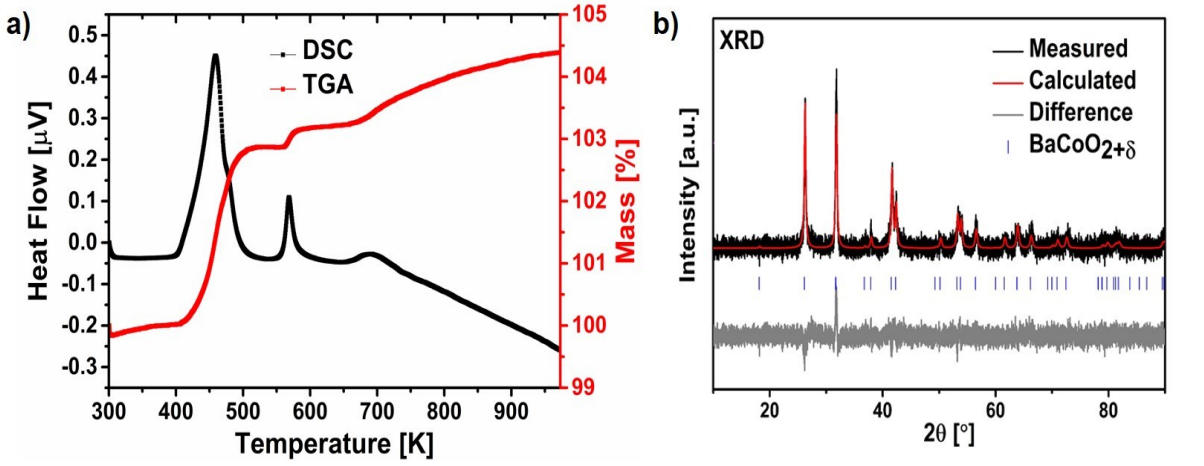

Figure 4.44: (a) TGA and DSC measurements performed on $BaCoO_{2+\delta}$ powders under oxygen atmosphere. (b) Rietveld refinement of X-ray diffraction pattern recorded after carrying out STA measurement.

4.4.4 Conclusion

In summary, a new highly oxygen deficient metastable perovskite-related phase of barium cobaltate with composition of $BaCoO_{2+\delta}$ ($\delta \sim 0.01$ -0.02) is reported in this article. The compound was found to show strong structural similarity to the previously reported Fe based system $Ba_{0.8}Sr_{0.2}FeO_2$ [262], with unusual coordination for Co^{2+} (which is at least partially square planar) and G-type AFM ordering below 220 K.

It is surprising that such a highly oxygen deficient metastable phase could be formed, although the structure of the thermodynamically most stable modification of $BaCoO_2$ can also be derived from the cubic perovskite structure (i. e., shows a nearly identical Ba/Co sublattice). Therefore, the incorporation of small amounts of additional oxygen δ via short reaction times and fine-tuned Ar gas flow, in combination with the milling-based activation of the precursors powders,

are likely to be key to its formation. Thus, the findings presented here highlight the potential impact of small deviations of anion composition on anion ordering within a given cation lattice, and show how control of synthesis parameters can be exploited to produce new defective phases, thus offering an additional avenue for chemists to exploit in the quest for new materials.

Acknowledgements

This work was funded by the German Research Foundation (DFG) within CL551/2-1. We gratefully acknowledge awarding of beam time from the STFC (DOI: 10.5286/ISIS.E.87849379).

4.5 Supplementary information for chapter 4

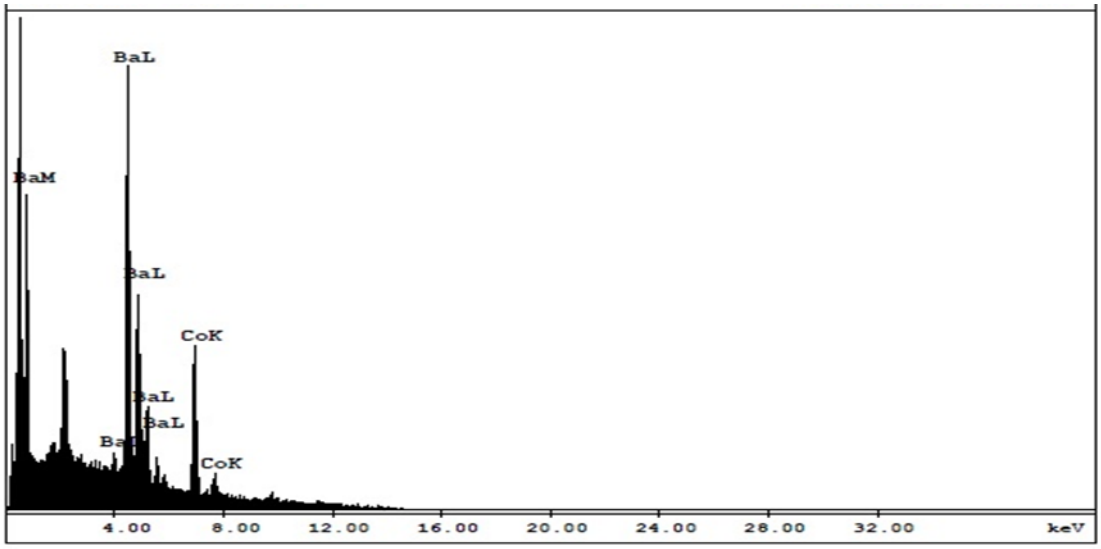

Figure 4.45: EDAX for the as-synthesized $BaCoO_{1.80}(OH)_{0.86}$ powder.

Figure 4.46: Symmetry relationship showing the similarity between the cubic aristotype perovskite structure and the monoclinically distorted of perovskite type $BaCoO_{2.67}$.

Table 4.16: Ideal atomic coordinates for a pseudocubic perovskite within space group $P2_1/m$.

Atom	Wyckoff	*x*	*y*	*z*
Ba1	2*e*	0.250	¼	**0**
Ba2	2*e*	0.917	¼	0.667
Ba3	2*e*	0.583	¼	0.333
Co1	2*e*	0.250	¼	0.500
Co2	2*e*	0.917	¼	0.167
Co3	2*e*	0.583	¼	0.833
O1	2*e*	0.750	¼	**0**
O2	2*b*	½	**0**	**0**
O3	2*e*	0.417	¼	0.667
O4	2*e*	0.083	¼	0.333
O5	4*f*	0.667	**0**	0.667
O6	4*f*	0.833	**0**	0.333
O7	2*a*	**0**	**0**	**0**

4.5.1 Characterization of $Ba_{0.5}Sr_{0.5}Co_{0.8}Fe_{0.2}O_{3-x}$

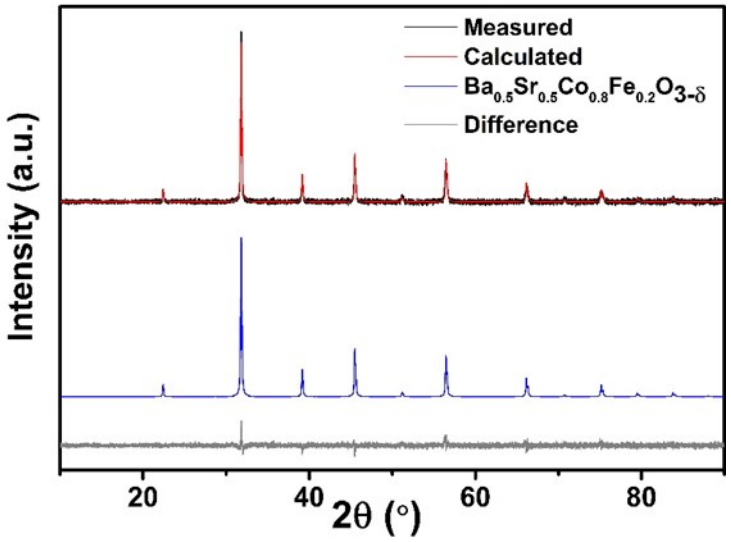

Figure 4.47: Rietveld fit of the BSCF powders synthesized from the nebulized spray pyrolysis technique.

As mentioned previously, BSCF powders were synthesized via the NSP method. The as prepared powders where then heat treated at 1073 K for 6 hours in argon atmosphere. Figure 4.47 shows the Rietveld fit of the room temperature X-ray diffraction pattern recorded for the phase pure BSCF powders. In agreement with the previous reports [273], BSCF was found to crystallize in a cubic structure within the space group *Pm*−3*m* and the lattice parameter of 4.0030(1) Å was determined from the refinements. The powders were then subjected to iodometric titrations to determine the average oxidation state for the *B* site cation (Co/Fe) which was calculated to be +2.75(1). Recently, we have shown for the $BaFe_{1-x}Co_xO_{3-y-\delta}(OH)_y$ [80] series synthesized via NSP method that Fe is mainly present in the +3 oxidation state irrespective of the Fe to Co ratio. In this series Co is mainly present in the mixed valent +2/+3 oxidation state for Co-rich samples [80 82]. This applies also for Fe in BSCF [32]. Herein the Fe is predominantly in the +3 oxidation state whereas Co is present in the mixed oxidation state of +2/+3. To verify this, we have prepared a series of compounds with the composition $Ba_{0.5}Sr_{0.5}Co_{1-x}Fe_xO_{3-\delta}$ and studied them for their oxygen vacancy concentration via iodometric titrations. We observed that for Fe rich composition (x = 1), the average oxidation state of B site was +3, which is similar to what we found for the $BaFe_{1-x}Co_xO_{3-y-\delta}(OH)_y$ [80] series. Therefore, in case of BSCF, our assumption of +3 oxidation state for Fe is valid and changes in the oxidation states would be as a result of lowering of oxidation number for Co. Further, scanning electron micrographs of BSCF, intermediate $BaCoO_{2.46}$ and $BaCoO_{2.67}$ were recorded and are shown in Figure 4.48. It is clear that particle size of the powders synthesized via the NSP route are smaller than the particles synthesized via the solid state route.

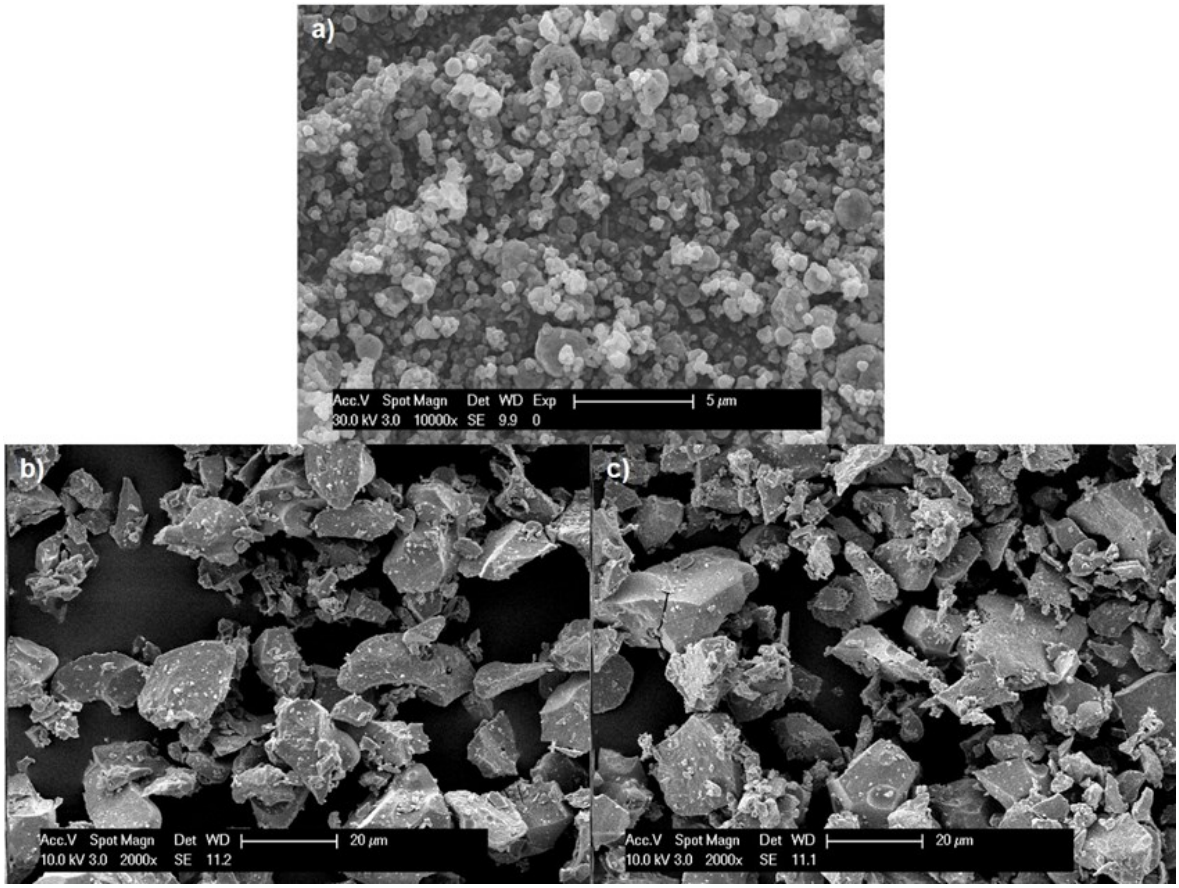

Figure 4.48: SEM micrographs recorded for (a) BSCF synthesized via NSP method (b)intermediate phase $BaCoO_{2.46}$ and (c) $BaCoO_{2.67}$.

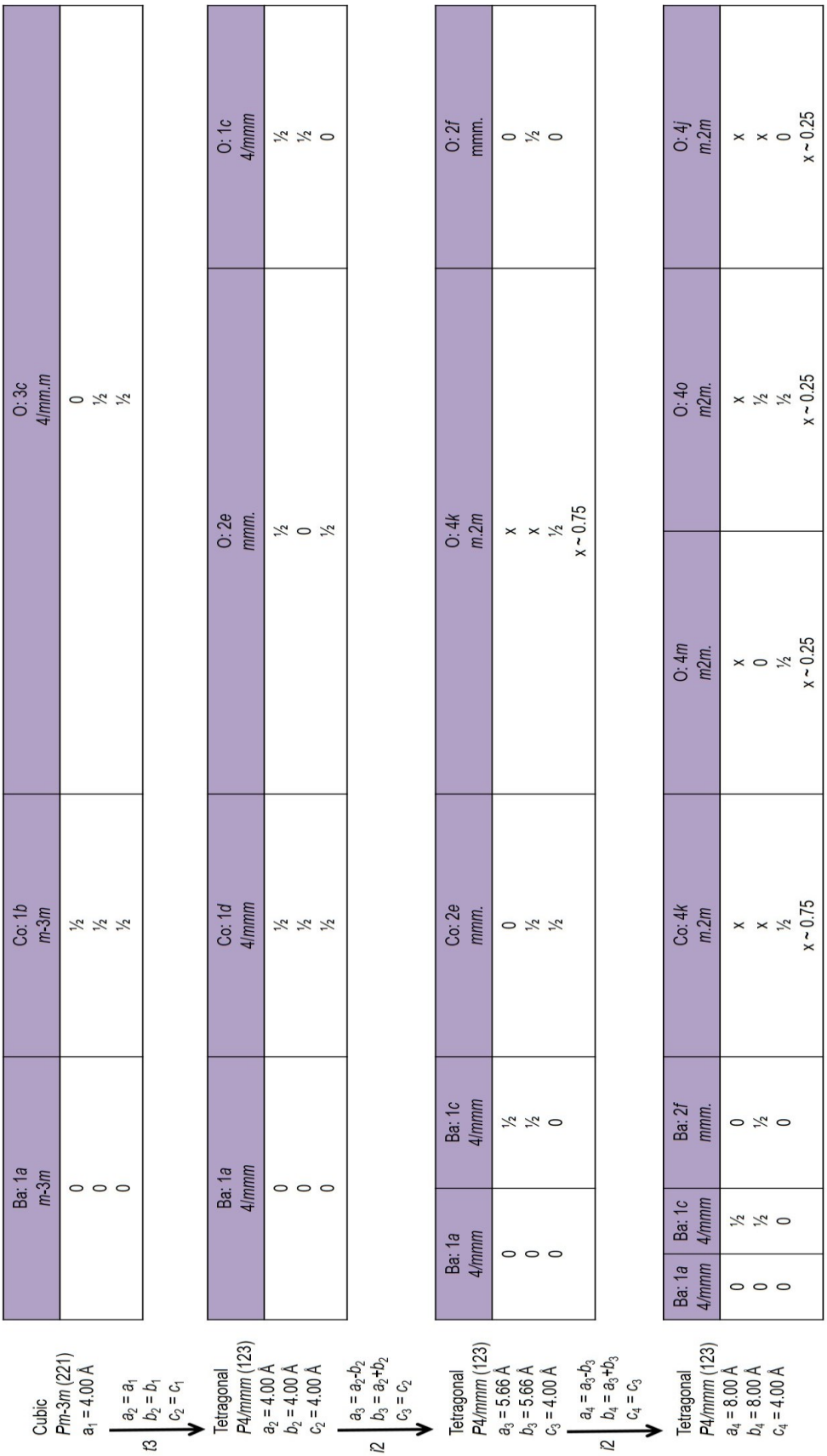

Figure 4.49: Symmetry relationship for model 1, showing the similarity between the cubic aristotype perovskite structure and the tetragonal structure of perovskite-related $BaCoO_{2+\delta}$.

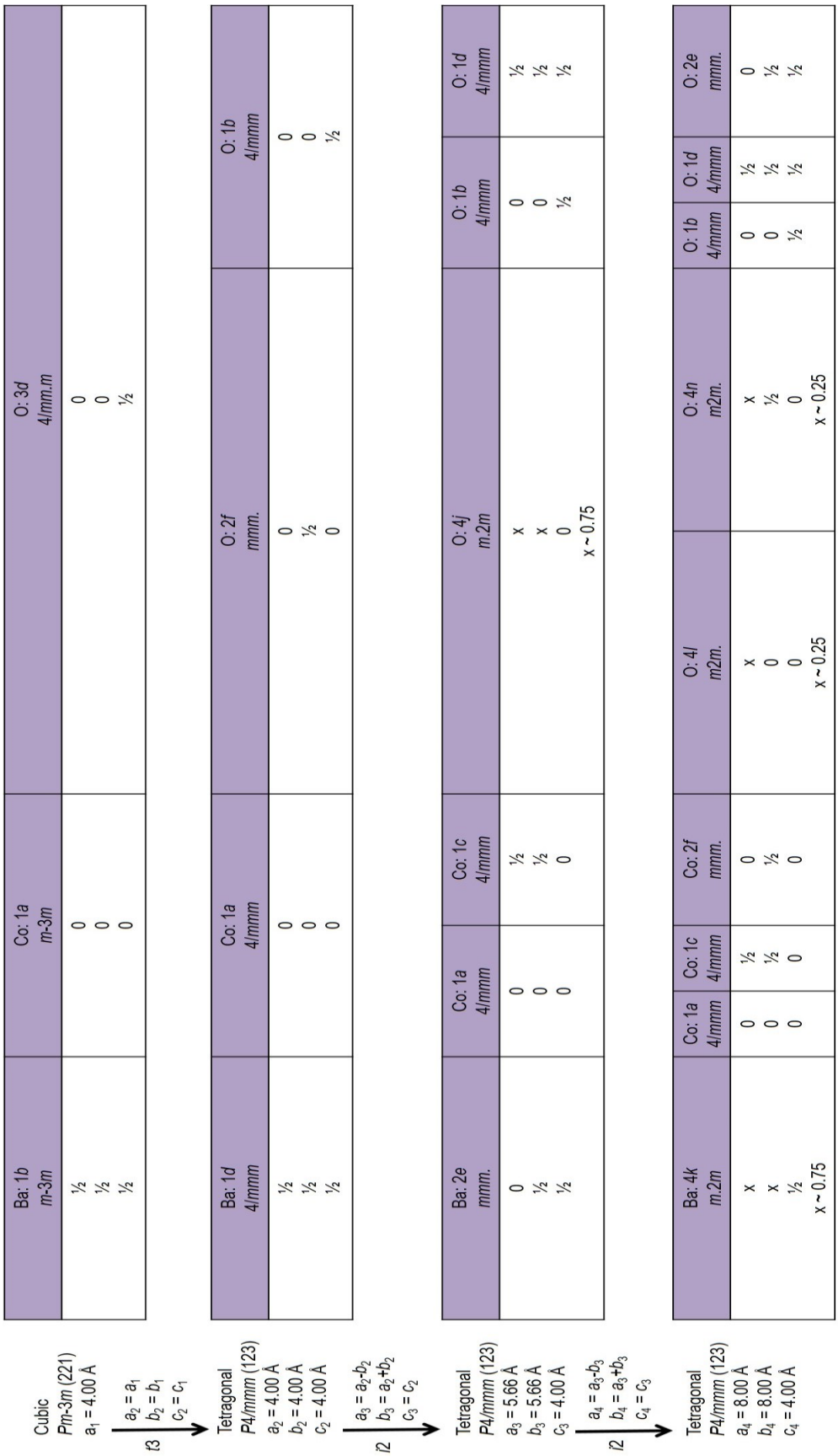

Figure 4.50: Symmetry relationship for model 2, showing the similarity between the cubic aristotype perovskite structure and the tetragonal structure of perovskite-related $BaCoO_{2+\delta}$.

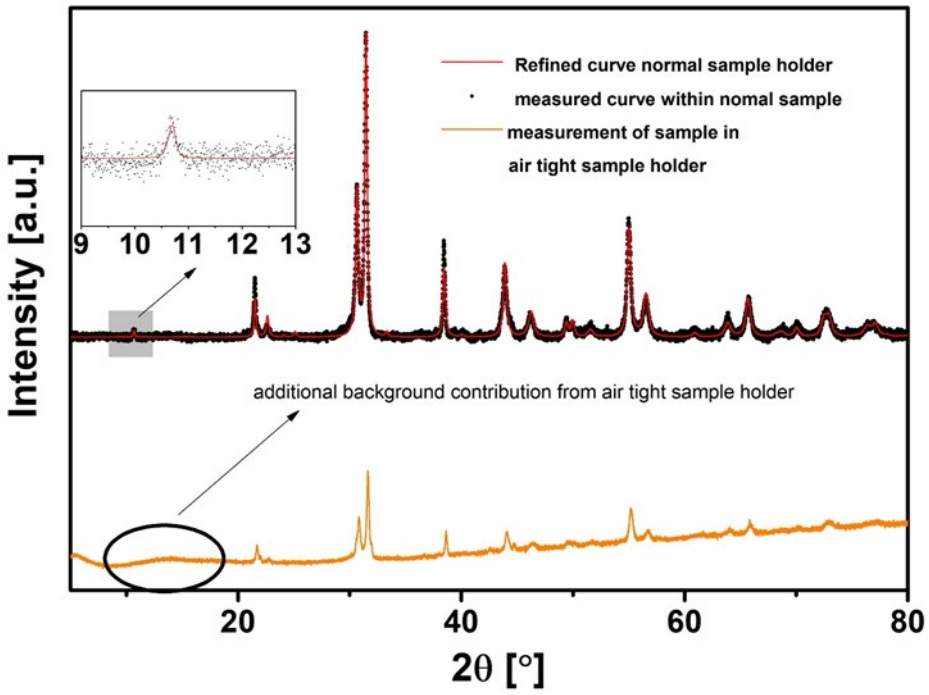

Figure 4.51: Comparison of the X- ray diffraction patterns recorded for $BaCoO_{2+\delta}$ using within an air tight sample holder (red) and within a normal sample holder (black). Inset shows the zoomed view of the reflection at 10.74 ° which is best observed in the scan measured in the normal sample holder (see also experimental details provided in section 1. within this Supplementary Material) and more difficult to be seen in the sample measured in air tight conditions due to the higher signal to noise at lower 2θ angles resulting from the plastic cover.

Table 4.17: Ideal positional parameters for a pseudocubic perovskite within model #1 (Co site splits), with space group P4/mmm with a ▪≈ 8 Å, c ≈ 4 Å.

Atom	Wyck	x	y	z	Occ
Ba	4k	0.75	=x	½	1
Co1	1a	**0**	**0**	**0**	1
Co2	1c	½	½	**0**	1
Co3	2f	**0**	½	**0**	1
O1	1b	**0**	**0**	½	1
O2	1d	½	½	½	1
O3	2e	**0**	½	½	1
O4	4l	0.25	**0**	**0**	1
O5	4n	0.25	½	**0**	1

Table 4.18: Ideal positional parameters for a pseudocubic perovskite within model #2 (Ba site splits), with space group P4/mmm with a ▪≈ 8 Å, c ≈ 4 Å.

Atom	Wyck	x	y	z	Occ
Ba1	1a	**0**	**0**	**0**	1
Ba2	2f	½	**0**	**0**	1
Ba3	1c	½	½	**0**	1
Co1	4k	0.75	=x	½	1
O1	4j	0.25	=x	**0**	1
O2	4o	0.25	½	½	1
O3	4m	0.25	**0**	½	1

Table 4.19: Energies for different models as obtained via DFT+U modifications, given per $BaCoO_{2+\delta}$ formula unit. Energies are given for FM configurations.

model #1	-23.57 eV	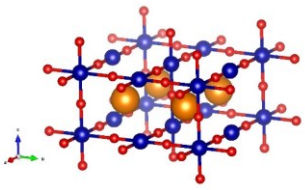
model #2	-23.80 eV	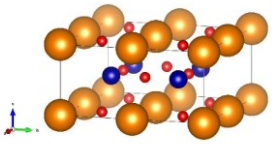
model #3	-24.13 eV	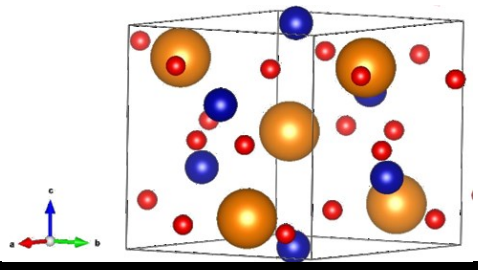

5 Conclusion and Outlook

5.1 Conclusion

Within this dissertation, efforts were devoted towards demonstrating the versatility of NSP towards the synthesis of compositionally different lithium containing garnets and hydrated barium-rich cobaltates and ferrates for their use in energy related applications. NSP as a technique offers advantages like high powder yield, possibility of scalability and synthesis of nanocrystalline powders, all which are crucial for such applications.

- Composite electrolytes for ASSLIBs

For the first time, different garnets synthesized via NSP have been used as ceramic fillers within PEO+LiTSFI matrix for preparing composite electrolyte blends ranging from “ceramic in polymer” to “polymer in ceramic”. Although, the as-obtained nanocrystalline powders from NSP were found to be mixture of Li_2CO_3 and $La_2Zr_2O_7$ and exhibit hollow microstructure, the additional heating step at low temperatures for a short duration resulted in the formation of the desired garnet phase. Due to this post synthesis heat treatment, the resulting garnet powders were found to maintain their nanocrystalline nature and also demonstrate high porosity as a result of necking between the particles, which resulted in particles that exhibit higher surface area compared to the ones synthesized via conventional solid-state routes. The composite electrolytes were prepared via the solvent free cryo-milling method for the first time which limited the subsequent heat treatment for solvent removal usually carried out for the membranes fabricated via conventional solvent based route. The high surface area of the filler particles has already been known to be beneficial for Li-ion transport in polymer-rich composites [76] and within this thesis has allowed for probing the Li-ion pathways within the composite electrolytes as a function of garnet to PEO weight fraction via electrochemical impedance spectroscopy. It was concluded that for polymer-rich composite electrolytes the Li-ion transport mainly takes place via the bulk polymer and along the garnet/PEO interface. For ceramic-rich composite electrolytes with the weight fraction greater than the percolation limit additional transport pathway through the bulk filler were found to become accessible. However, the particle/particle interfacial impedance was found to dominate, resulting in low ionic conductivity within such electrolytes compared to filler free PEO electrolyte.

An important aspect of this thesis was to establish the role of the filler towards the Li-ion transport within the composite electrolytes. In order to probe this, variety of different Li-ion active and inert fillers were used for preparing composite electrolytes with different filler to PEO weight ratios. It was concluded that for polymer-rich composite electrolytes, filler morphology rather than its composition is of importance. For the composite electrolyte containing 10 wt% of SiO_2 nanoparticles, ionic conductivity of 1.1×10^{-5} S cm^{-1} at 298 K was observed, which is an order of magnitude higher than the filler free PEO+LiTSFI electrolyte and several orders of magnitude higher than the compacted micro-sized Al-LLZO garnet powders synthesized via NSP. The intrinsic conductivity of the ceramic filler was found to be of importance only in case of ceramic-rich systems where the filler was found to contribute towards the total Li-ion conductivity of the composite electrolyte. All the Li-ion conducting garnets were found to offer higher conductivity compared to that of inert filler containing composite electrolytes with 90 wt% Ga-doped LLZO demonstrating ionic conductivity of 1.5×10^{-7} S cm^{-1} at 298 K that is significantly higher than the SiO_2 containing composite electrolyte that exhibited Li-ion conductivity of ~4×10^{-8} S cm^{-1} at 298 K. The results again pointed towards the need of reducing the particle/particle interfacial impedances for Li-ion transport.

Further, the high porosity of the garnet powders synthesized via NSP was found to be beneficial in the sense that these pores can be directly accessed by infiltrating them with a Li-ion conducting polymer instead of dispersing the filler into the polymer matrix. Although, these pores could only be accessed on micrometer length scale in thin films, the 3-dimenional backbone resulting from the NSP powders is advantageous since it provides continuous Li-ion transport pathways within the garnet framework as opposed to Li-ion impeding particle/particle interface in particulate based composite electrolytes. In comparison to the pure Al-doped garnet thin film, the PEO infiltrated thin film demonstrated ~6 orders of magnitude higher conductivity, i.e. 5.3 x 10^{-7} S cm^{-1} at 298 K, which is also significantly higher than the composite electrolyte containing dispersed Al-doped LLZO ceramic filler, which demonstrated the ionic conductivity of 8 x 10^{-8} S cm^{-1} with similar garnet to PEO weight fraction.

An important aspect within the composite electrolytes is the stability between its components. Although the Li-ion transport along filler/polymer interface has been known to be beneficial in polymer-rich composite electrolytes, within ceramic-rich composites the Li-ion transport can also take place through this interface. The study of this interface was also crucial since for garnet-rich composite electrolytes the ionic conductivity was found to be orders of magnitude lower than the bulk garnet itself and also pure PEO electrolyte. By making a model hetereostructure comprising of PEO/garnet/PEO, this interface was studied in the through plane mode via electrochemical impedance spectroscopy. The results indicated lower ionic conductivity in garnet/PEO layered structure compared to both the garnet and PEO itself and the origin of this impedance was attributed to garnet/PEO interface. Further increase in impedance was observed upon the application of another layer of PEO leading to PEO/garnet/PEO layered architecture confirming the resistive nature on this interface to Li-ion transport. These observations were complimented by the XPS measurements carried out by project partners, which indicated formation of side products, thus confirming the instability of garnet/PEO interface. The results obtained within this thesis not only show evidence of the role played by the filler composition and morphology on Li-ion transport within composite electrolytes but also highlight the issues related to garnet/PEO interface. Overall the results provide valuable contributions towards the current understanding of the composite electrolyte systems for all state Li-ion batteries.

- Perovskite materials for fuel cell applications

In this thesis, NSP was also used to synthesize the series of oxide hydroxide barium-rich cobaltates and ferrates $BaFe_{1-x}Co_xO_{3-y-\delta}(OH)_y$. Compared to garnet synthesis where the as-synthesized powders require additional heating step in order to obtain the desired garnet phase, the as-synthesized powders obtained via NSP directly show perovskite-type structure with characteristic nanoparticles demonstrating spherical morphology. Interestingly, whole series was found to show *ccp* packing of $AO_{3-\delta}$ layers as opposed to *hcp* packing usually observed for barium and cobalt-rich perovskites, therefore highlighting the role of NSP in stabilizing the *ccp* stacking. Compared to traditional methods of preparing hydrated perovskites, which usually is a two-step process of first synthesizing the precursor perovskite followed by its hydration [37], NSP offered an advantage of mutually doing both the processes simultaneously. The whole $BaFe_{1-x}Co_xO_{3-y-\delta}(OH)_y$ series was found to crystallize in the space group *Cmcm* with x = 0 member up taking higher amount of water compared to previous report [37]. Although the presence of water can result in proton conductivity in such perovskites, this could not be quantified especially for the cobalt-rich systems due to the dominance of electronic transports towards over all conductivity due to the presence of cobalt in mixed 2+/3+ oxidation states. Nevertheless, upon investigation for ORR and OER activity for alkaline fuel cell, the

series demonstrated complex dependence on x with x = 0.2 showing smallest potential difference of δU =1.10 V which is comparable to that of noble metal catalyst [199] and $CaMnO_{3-x}$ [200], therefore making this member of potential interest as air electrode for metal-air battery. Attempts to prepare these compositions via alternative methods did not prove to be successful, therefore highlighting the role of NSP towards synthesizing of these compounds.

In addition, two new oxygen deficient barium cobaltates $BaCoO_{2.67}$ and $BaCoO_{2+\delta}$ were also found in context to above studies. i) $BaCoO_{2.67}$ was synthesized via the topochemical oxidation of an intermediate $BaCoO_{2.46}$ phase and found to be isotypic to previously reported $BaFeO_{2.33}F_{0.33}$ and $BaFeO_{2.67}$ with Co being present in 4-,5- and 6-fold coordination. The results indicate striking structural similarity between barium-rich cobaltates and ferrates which can be attributed to similar overall anion content. Additionally, the bifuntional activity of this compound was found to be comparable to that of bench mark perovskite catalyst BSCF possibly due to the mixed valent state of Co along with the favourable anion ordering. ii) A new metastable modification $BaCoO_{2+\delta}$ (δ ~ 0.01 - 0.02) was also discussed. The compound was found to be structurally similar to $Ba_{0.8}Sr_{0.2}FeO_2$ [262], with Co being present in an unusual partial square planar coordination of Co^{2+}. Although a thermodynamically stable triclinic modification of $BaCoO_2$ is already known, this new modification has its origin tied to short reaction times, Ar flow rate and milling of precursor powders. This was the first report of the synthesis of such highly oxygen deficient composition which so far have been synthesized via two-step hydride reduction method [204]. The findings here highlight the role of anion composition on anion ordering within the perovskite framework, which can be further explored for the synthesis of new defective perovskites for various applications.

Overall, NSP as a synthesis technique has shown to be viable and attractive method not only to obtain oxide but also oxide hydroxide powders for new energy technologies. The powders obtained are suitable for being both in composites and fuel cells. In addition, porous films can also be obtained which is of relevane fo both fuel cell catalyst (metal-air batteries) and solid electrolyte for battery technologies.

5.2 Future research prospects

Although the garnet synthesis via NSP offers an advantage of synthesizing nano-powders with high surface area compared to that of solid state route, the results suggest a need for alternative composite electrolyte membrane preparation strategy. This is important in order to fabricate highly dense membranes which cannot be achieved via simple uniaxial or isostatic pressing used in this thesis. In this respect, hot pressing the composite electrolyte membrane components together may be of interest. Applying pressure and the temperature above the melting temperature of PEO may allow for better filler/filler contact along with the filler/polymer contact within the particulate-based membrane, which can eventually result in higher density of the membranes especially for ceramic-rich composite electrolyte membranes. One of the main advantages of using NSP as the synthesis route for preparing garnets in the resulting high porosity. Although infiltrating this porous network was shown to result in enhanced ionic conductivity by ~6 orders of magnitude compared to that of a porous garnet thin films, the ionic conductivity of the porous garnet framework is still significantly reduced compared to that of a well sintered garnet pellet. This low ionic conductivity can be attributed to the small width of the necks between the particles which is the bottleneck towards achieving high intrinsic conductivity in the 3-dimensional garnet backbone. Therefore, attempts should be made to widen these necks. This can be done via the addition of sintering aids or organic compounds. As recently reported by Bae et al [73], infiltration of porous hydrogel derived perovskite-based

LLTO network with PEO resulted in a membrane that demonstrated ionic conductivity of an order of 10^{-4} S cm^{-1} at room temperatures. A similar approach in combination with NSP could be used for garnets as well, which can result in higher conductivities in the composite electrolyte membranes due to higher intrinsic conductivity of garnets compared to that of LLTO [10]. In addition to engineering the garnet framework, it is also important to look for other polymers which offer higher ionic conductivity along with higher Li-ion transference numbers than PEO. In this respect, single-ion conducting polymer electrolytes would be of interest [274]. These polymers demonstrate ionic conductivity of an order of 10^{-4} S cm^{-1} at 298 K along with the Li-ion transference number of unity [274]. Lastly, the garnet/polymer interface needs to be improved to prevent the formation of resistive decomposition products and allow for the Li-ion exchange through this interface. This can be achieved via garnet coating with LiF, which has been shown to limit the Li_2CO_3 formation on garnet surface but also limit the interfacial resistances [275].

Similarly, for the barium-rich cobaltates and ferrates based perovskites, there is still a need for optimizing the composition in order to find the suitable ORR/OER catalyst. Here, NSP as technique contributes towards the synthesis of nano-powders and therefore offers advantage over solid-state route where particles sizes of the order of micrometers are usually obtained and require subsequent ball milling operation in order to reduce particle size. Lower particle size leads to high surface area that is beneficial towards ORR and OER [276]. As observed in $BaFe_{1-x}Co_xO_{3-y-\delta}(OH)_y$, the doping optimizes not only the electronic conductivity but also bifunctional catalytic activity. Within perovskites, the bifunctional activity descriptor is based on the filling of e_g orbital of the B cation, with e_g occupancy of 1 being most favourable towards ORR and OER. Therefore, doping strategies need to be applied where this electronic configuration for B site atom can be achieved. Since, Fe was found to maintain high spin oxidation state of +3, which implies the e_g occupation of 2, it is therefore of interest of use other transition metal ions whose oxidation states are more flexible within perovskite framework and can be tuned in order to result in e_g occupancy of 1. In this respect Ni and Mn can be of interest. In addition to B site doping, A site doping with can also be used in order to tune the B site spin and oxidation states [28]. Additionally, NSP as a technique can also be applied to investigate other perovskite-related structures like ruddlesden popper type compounds, wherein similar doping strategies may be of interest. Although, high bifunctional activity is of importance for successful implementation of a catalyst in application like metal-air batteries, it will be also of importance to investigate such perovskites for their stability in order to cycle such a battery over larger number of cycles. Since, $BaCoO_{2.67}$ shows catalytic activity similar to that of benchmark perovskite catalyst BSCF, this compound may be of interest in this respect. So far most of studies are mainly focused on cation doping of perovskites in order to optimize their catalytic activities, however anion doping with F^- is also of interest as has been recently shown to improve the performance of perovskites catalysts [198].

Overall the results obtained within this thesis can be used as reference for the future research within both composite electrolytes for ASSLIBs and bifunctional catalysts for fuel cell and metal-air batteries.

Biblography

1. K. Vohra, A. Vodonos, J. Schwartz, E. A. Marais, M. P. Sulprizio and L. J. Mickley, *Environ Res*, 2021, **195**, 110754.
2. P. K. Nayak, S. Mahesh, H. J. Snaith and D. Cahen, *Nature Reviews Materials*, 2019, **4**, 269-285.
3. J. B. Goodenough and K.-S. Park, *J. Am. Chem. Soc.*, 2013, **135**, 1167-1176.
4. S. F. Lux, I. T. Lucas, E. Pollak, S. Passerini, M. Winter and R. Kostecki, *Electrochemistry Communications*, 2012, **14**, 47-50.
5. K. Xu, *Chem Rev*, 2004, **104**, 4303-4417.
6. T. Ohba, K. Kaneko and H. Kanoh, *ISRN Nanotechnology*, 2011, **2011**, 1-5.
7. I. Yoshimatsu, T. Hirai and J. i. Yamaki, *Journal of The Electrochemical Society*, 1988, **135**, 2422-2427.
8. J. Schnell, T. Günther, T. Knoche, C. Vieider, L. Köhler, A. Just, M. Keller, S. Passerini and G. Reinhart, *J. Power Sources*, 2018, **382**, 160-175.
9. F. Yao, D. T. Pham and Y. H. Lee, *Chemsuschem*, 2015, **8**, 2284-2311.
10. Z. Zhang, Y. Shao, B. Lotsch, Y.-S. Hu, H. Li, J. Janek, L. F. Nazar, C.-W. Nan, J. Maier, M. Armand and L. Chen, *Energy & Environmental Science*, 2018, **11**, 1945-1976.
11. Q. Wang, B. Jiang, B. Li and Y. Yan, *Renewable and Sustainable Energy Reviews*, 2016, **64**, 106-128.
12. P. Biensan, B. Simon, J. P. Pérès, A. de Guibert, M. Broussely, J. M. Bodet and F. Perton, *J. Power Sources*, 1999, **81-82**, 906-912.
13. M. Ghiji, V. Novozhilov, K. Moinuddin, P. Joseph, I. Burch, B. Suendermann and G. Gamble, *Energies*, 2020, **13**.
14. Q. Wang, J. Sun and G. Chu, *Fire Safety Science*, 2005, **8**, 375-382.
15. A. Niemczyk, K. Dziubek, B. Sacher-Majewska, K. Czaja, M. Dutkiewicz and B. Marciniec, *Journal of Thermal Analysis and Calorimetry*, 2016, **125**, 1287-1299.
16. S. J. An, J. Li, C. Daniel, D. Mohanty, S. Nagpure and D. L. Wood, *Carbon*, 2016, **105**, 52-76.
17. J. P. Pender, G. Jha, D. H. Youn, J. M. Ziegler, I. Andoni, E. J. Choi, A. Heller, B. S. Dunn, P. S. Weiss, R. M. Penner and C. B. Mullins, *ACS Nano*, 2020, **14**, 1243-1295.
18. C. Zhan, T. Wu, J. Lu and K. Amine, *Energy & Environmental Science*, 2018, **11**, 243-257.
19. C. Sun, J. Liu, Y. Gong, D. P. Wilkinson and J. Zhang, *Nano Energy*, 2017, **33**, 363-386.
20. M. Shoji, E. J. Cheng, T. Kimura and K. Kanamura, *Journal of Physics D: Applied Physics*, 2019, **52**.
21. H. Huo, J. Luo, V. Thangadurai, X. Guo, C.-W. Nan and X. Sun, *ACS Energy Letters*, 2019, DOI: 10.1021/acsenergylett.9b02401, 252-262.
22. S. Qian, H. Chen, Z. Wu, D. Li, X. Liu, Y. Tang and S. Zhang, *Batteries & Supercaps*, 2020, **4**, 39-59.
23. J. Zhang, N. Zhao, M. Zhang, Y. Li, P. K. Chu, X. Guo, Z. Di, X. Wang and H. Li, *Nano Energy*, 2016, **28**, 447-454.
24. Z. Xue, D. He and X. Xie, *J. Mater. Chem. A*, 2015, **3**, 19218-19253.
25. P. Yao, H. Yu, Z. Ding, Y. Liu, J. Lu, M. Lavorgna, J. Wu and X. Liu, *Front Chem*, 2019, **7**, 522.
26. P. Tan, M. Liu, Z. Shao and M. Ni, *Advanced Energy Materials*, 2017, **7**, 1602674.
27. D. U. Lee, P. Xu, Z. P. Cano, A. G. Kashkooli, M. G. Park and Z. Chen, *J. Mater. Chem. A*, 2016, **4**, 7107-7134.
28. C. E. Beall, E. Fabbri and T. J. Schmidt, *ACS Catalysis*, 2021, **11**, 3094-3114.
29. H. F. Kay and P. C. Bailey, *Acta Crystallogr*, 1957, **10**, 219-226.
30. Q. Q. Ji, L. Bi, J. T. Zhang, H. J. Cao and X. S. Zhao, *Energy & Environmental Science*, 2020, **13**, 1408-1428.

31. J. Suntivich, H. A. Gasteiger, N. Yabuuchi, H. Nakanishi, J. B. Goodenough and Y. Shao-Horn, *Nat Chem*, 2011, **3**, 546-550.
32. J. Suntivich, K. J. May, H. A. Gasteiger, J. B. Goodenough and Y. Shao-Horn, *Science*, 2011, **334**, 1383-1385.
33. J. Leng, Z. Wang, J. Wang, H. H. Wu, G. Yan, X. Li, H. Guo, Y. Liu, Q. Zhang and Z. Guo, *Chem Soc Rev*, 2019, **48**, 3015-3072.
34. R. Djenadic, M. Botros, C. Benel, O. Clemens, S. Indris, A. Choudhary, T. Bergfeldt and H. Hahn, *Solid State Ionics*, 2014, **263**, 49-56.
35. M. Botros, R. Djenadic, O. Clemens, M. Möller and H. Hahn, *J. Power Sources*, 2016, **309**, 108-115.
36. C. Benel, A. J. Darbandi, R. Djenadic, A. Evans, R. Tölke, M. Prestat and H. Hahn, *J. Power Sources*, 2013, **229**, 258-264.
37. P. L. Knochel, P. J. Keenan, C. Loho, C. Reitz, R. Witte, K. S. Knight, A. J. Wright, H. Hahn, P. R. Slater and O. Clemens, *J. Mater. Chem. A*, 2016, **4**, 3415-3430.
38. F. Hossain, A. H. Shah, A. Islam, S. Rahman and S. Hossain, *Materials Research Innovations*, 2021, **25**, 300-309.
39. H. Buschmann, S. Berendts, B. Mogwitz and J. Janek, *J. Power Sources*, 2012, **206**, 236-244.
40. B. R. Thomas, *Linden's Handbook of Batteries, Fourth Edition*, McGraw-Hill Education, New York, 4th ed. edn., 2011.
41. Q. Liu, Z. Geng, C. Han, Y. Fu, S. Li, Y.-b. He, F. Kang and B. Li, *J. Power Sources*, 2018, **389**, 120-134.
42. S. M. Rommel, N. Schall, C. Brünig and R. Weihrich, *Monatshefte für Chemie - Chemical Monthly*, 2014, **145**, 385-404.
43. J. B. Bates, N. J. Dudney, G. R. Gruzalski, R. A. Zuhr, A. Choudhury, C. F. Luck and J. D. Robertson, *Solid State Ionics*, 1992, **53**, 647-654.
44. J. B. Bates, N. J. Dudney, D. C. Lubben, G. R. Gruzalski, B. S. Kwak, X. H. Yu and R. A. Zuhr, *J. Power Sources*, 1995, **54**, 58-62.
45. J. B. Bates, N. J. Dudney, G. R. Gruzalski, R. A. Zuhr, A. Choudhury, C. F. Luck and J. D. Robertson, *J. Power Sources*, 1993, **43**, 103-110.
46. R. Kanno, T. Hata, Y. Kawamoto and M. Irie, *Solid State Ionics*, 2000, **130**, 97-104.
47. F. Mizuno, A. Hayashi, K. Tadanaga and M. Tatsumisago, *Advanced Materials*, 2005, **17**, 918-+.
48. N. Kamaya, K. Homma, Y. Yamakawa, M. Hirayama, R. Kanno, M. Yonemura, T. Kamiyama, Y. Kato, S. Hama, K. Kawamoto and A. Mitsui, *Nat Mater*, 2011, **10**, 682-686.
49. B. R. Shin, Y. J. Nam, D. Y. Oh, D. H. Kim, J. W. Kim and Y. S. Jung, *Electrochim Acta*, 2014, **146**, 395-402.
50. Y. Inaguma, L. Q. Chen, M. Itoh, T. Nakamura, T. Uchida, H. Ikuta and M. Wakihara, *Solid State Communications*, 1993, **86**, 689-693.
51. J. A. Alonso, J. Sanz, J. Santamaria, C. Leon, A. Varez and M. T. Fernandez-Diaz, *Angew Chem Int Edit*, 2000, **39**, 619-+.
52. C. Wang, K. Fu, S. P. Kammampata, D. W. McOwen, A. J. Samson, L. Zhang, G. T. Hitz, A. M. Nolan, E. D. Wachsman, Y. Mo, V. Thangadurai and L. Hu, *Chemical Reviews*, 2020, **120**, 4257-4300.
53. V. Thangadurai, S. Narayanan and D. Pinzaru, *Chem. Soc. Rev.*, 2014, **43**, 4714-4727.
54. R. Murugan, V. Thangadurai and W. Weppner, *Angew Chem Int Ed Engl*, 2007, **46**, 7778-7781.
55. H. Huo, J. Luo, V. Thangadurai, X. Guo, C.-W. Nan and X. Sun, *ACS Energy Letters*, 2020, **5**, 252-262.
56. W. Xue, Y. Yang, Q. Yang, Y. Liu, L. Wang, C. Chen and R. Cheng, *RSC Adv.*, 2018, **8**, 13083-13088.
57. B. Karasulu, S. P. Emge, M. F. Groh, C. P. Grey and A. J. Morris, *J. Am. Chem. Soc.*, 2020, **142**, 3132-3148.
58. D. E. Fenton, J. M. Parker and P. V. Wright, *Polymer*, 1973, **14**, 589.

59. Y. Kato, S. Yokoyama, T. Yabe, H. Ikuta, Y. Uchimoto and M. Wakihara, *Electrochim Acta*, 2004, **50**, 281-284.
60. F. Croce, L. Persi, B. Scrosati, F. Serraino-Fiory, E. Plichta and M. A. Hendrickson, *Electrochim Acta*, 2001, **46**, 2457-2461.
61. M. Kumar and S. S. Sekhon, *European Polymer Journal*, 2002, **38**, 1297-1304.
62. J. P. Sharma and V. Singh, *High Performance Polymers*, 2020, **32**, 142-150.
63. S. Zekoll, C. Marriner-Edwards, A. K. O. Hekselman, J. Kasemchainan, C. Kuss, D. E. J. Armstrong, D. Y. Cai, R. J. Wallace, F. H. Richter, J. H. J. Thijssen and P. G. Bruce, *Energy & Environmental Science*, 2018, **11**, 185-201.
64. Z. Shen, Y. Cheng, S. Sun, X. Ke, L. Liu and Z. Shi, *Carbon Energy*, 2021, **n/a**.
65. W. Liu, N. Liu, J. Sun, P. C. Hsu, Y. Z. Li, H. W. Lee and Y. Cui, *Nano Letters*, 2015, **15**, 2740-2745.
66. J. Feng, L. Wang, Y. Chen, P. Wang, H. Zhang and X. He, *Nano Convergence*, 2021, **8**, 2.
67. A. Bunde, W. Dieterich and E. Roman, *Physical Review Letters*, 1985, **55**, 5-8.
68. L. Chen, Y. Li, S.-P. Li, L.-Z. Fan, C.-W. Nan and J. B. Goodenough, *Nano Energy*, 2018, **46**, 176-184.
69. Y. Zhao, C. Wu, G. Peng, X. Chen, X. Yao, Y. Bai, F. Wu, S. Chen and X. Xu, *J. Power Sources*, 2016, **301**, 47-53.
70. J. Zhou and P. S. Fedkiw, *Solid State Ionics*, 2004, **166**, 275-293.
71. J. Zagorski, J. M. L. del Amo, M. J. Cordill, F. Aguesse, L. Buannic and A. Llordes, *Acs Applied Energy Materials*, 2019, **2**, 1734-1746.
72. N. Wu, P.-H. Chien, Y. Qian, Y. Li, H. Xu, N. S. Grundish, B. Xu, H. Jin, Y.-Y. Hu, G. Yu and J. B. Goodenough, *Angew. Chem. Int. Ed.*, 2020, **59**, 4131-4137.
73. J. Bae, Y. Li, J. Zhang, X. Zhou, F. Zhao, Y. Shi, J. B. Goodenough and G. Yu, *Angew Chem Int Ed Engl*, 2018, **57**, 2096-2100.
74. P. Zhu, C. Yan, M. Dirican, J. Zhu, J. Zang, R. K. Selvan, C.-C. Chung, H. Jia, Y. Li, Y. Kiyak, N. Wu and X. Zhang, *J. Mater. Chem. A*, 2018, **6**, 4279-4285.
75. J. Zheng, M. Tang and Y. Y. Hu, *Angew Chem Int Ed Engl*, 2016, **55**, 12538-12542.
76. T. Yang, J. Zheng, Q. Cheng, Y. Y. Hu and C. K. Chan, *ACS Appl Mater Interfaces*, 2017, **9**, 21773-21780.
77. H. Zhai, P. Xu, M. Ning, Q. Cheng, J. Mandal and Y. Yang, *Nano Letters*, 2017, **17**, 3182-3187.
78. J.-F. Wu and X. Guo, *Physical Chemistry Chemical Physics*, 2017, **19**, 5880-5887.
79. T. K.-Y. Wong, B. J. Kennedy, C. J. Howard, B. A. Hunter and T. Vogt, *Journal of Solid State Chemistry*, 2001, **156**, 255-263.
80. A. I. Waidha, L. Ni, J. Ali, M. Lepple, M. Donzelli, S. Dasgupta, S. Wollstadt, L. Alff, U. I. Kramm and O. Clemens, *J. Mater. Chem. A*, 2020, **8**, 616-625.
81. A. I. Waidha, H. Zhang, M. Lepple, S. Dasgupta, L. Alff, P. Slater, A. D. Fortes and O. Clemens, *Chemical Communications*, 2019, **55**, 2920-2923.
82. A. I. Waidha, M. Lepple, K. Wissel, A. Benes, S. Wollstadt, P. R. Slater, A. D. Fortes and O. Clemens, *Dalton Trans.*, 2018, **47**, 11136-11145.
83. Z. Shao and S. M. Haile, *Nature*, 2004, **431**, 170-173.
84. O. Clemens, M. Groting, R. Witte, J. M. Perez-Mato, C. Loho, F. J. Berry, R. Kruk, K. S. Knight, A. J. Wright, H. Hahn and P. R. Slater, *Inorg Chem*, 2014, **53**, 5911-5921.
85. M. A. Hayward, M. A. Green, M. J. Rosseinsky and J. Sloan, *J. Am. Chem. Soc.*, 1999, **121**, 8843-8854.
86. C. Tassel and H. Kageyama, *Chem. Soc. Rev.*, 2012, **41**, 2025-2035.
87. S. W. Strauss, I. Fankuchen and R. Ward, *J. Am. Chem. Soc.*, 1951, **73**, 5084-5086.
88. C. Tassel, J. M. Pruneda, N. Hayashi, T. Watanabe, A. Kitada, Y. Tsujimoto, H. Kageyama, K. Yoshimura, M. Takano, M. Nishi, K. Ohoyama, M. Mizumaki, N. Kawamura, J. Iniguez and E. Canadell, *J. Am. Chem. Soc.*, 2009, **131**, 221-229.
89. R. Sazinas, M. A. Einarsrud and T. Grande, *J. Mater. Chem. A*, 2017, **5**, 5846-5857.
90. B. Raveau and M. Seikh, *Cobalt Oxides: From Crystal Chemistry to Physics*, Wiley VCH, 2012.

91. V. Pecharsky and P. Zavalij, *Fundamentals of Powder Diffraction and Structural Characterization of Materials*, Springer, Boston, MA, 2009.
92. C. Hammond, *The Basics of Crystallography and Diffraction*, 2015.
93. R. A. Young, *The Rietveld method*, International Union of Crystallograhy ; Oxford University Press, [Chester, England]; Oxford; New York, 1993.
94. E. H. Kisi, *Applications of Neutron Powder Diffraction*, Oxford University Press, Oxford, 2008.
95. *Topas V4.2, General profile and structure analysis software for powder diffraction data, User's Manual*, Bruker AXS, Karlsruhe, Germany, 2008.
96. A. Oed, *Nuclear Instruments and Methods in Physics Research Section A: Accelerators, Spectrometers, Detectors and Associated Equipment*, 1988, **263**, 351-359.
97. W. Liu, D. Lin, J. Sun, G. Zhou and Y. Cui, *ACS Nano*, 2016, **10**, 11407-11413.
98. Z. Li, H. M. Huang, J. K. Zhu, J. F. Wu, H. Yang, L. Wei and X. Guo, *ACS Appl Mater Interfaces*, 2019, **11**, 784-791.
99. X. Li, Y. Zhao, L. Cheng, M. Yan, X. Zheng, Z. Gao and Z. Jiang, *Journal of Solid State Electrochemistry*, 2005, **9**, 609-615.
100. J. Zheng and Y. Y. Hu, *ACS Appl Mater Interfaces*, 2018, **10**, 4113-4120.
101. J. T. S. Irvine, D. C. Sinclair and A. R. West, *Advanced Materials*, 1990, **2**, 132-138.
102. I. Yoshimatsu, T. Hirai and J. i. Yamaki, *Journal of The Electrochemical Society*, 2019, **135**, 2422-2427.
103. A. Sharafi, H. M. Meyer, J. Nanda, J. Wolfenstine and J. Sakamoto, *J. Power Sources*, 2016, **302**, 135-139.
104. X. Yu and A. Manthiram, *Energy & Environmental Science*, 2018, **11**, 527-543.
105. J. H. Seo, H. Nakaya, Y. Takeuchi, Z. M. Fan, H. Hikosaka, R. Rajagopalan, E. D. Gomez, M. Iwasaki and C. A. Randall, *J Eur Ceram Soc*, 2020, **40**, 6241-6248.
106. X. C. Chen, X. Liu, A. Samuthira Pandian, K. Lou, F. M. Delnick and N. J. Dudney, *ACS Energy Letters*, 2019, **4**, 1080-1085.
107. L. Truong, M. Howard, O. Clemens, K. S. Knight, P. R. Slater and V. Thangadurai, *Journal of Materials Chemistry A*, 2013, **1**, 13469-13475.
108. R. W. Cheary, A. A. Coelho and J. P. Cline, *J Res Natl Inst Stand Technol*, 2004, **109**, 1-25.
109. D. Johnson, *Inc., Southern Pines, NC*, 2002, **200**.
110. C. Loho, R. Djenadic, P. Mundt, O. Clemens and H. Hahn, *Solid State Ionics*, 2017, **313**, 32-44.
111. G. K. Wertheim, *Journal of Electron Spectroscopy and Related Phenomena*, 1975, **6**, 239-251.
112. M. A. Howard, O. Clemens, E. Kendrick, K. S. Knight, D. C. Apperley, P. A. Anderson and P. R. Slater, *Dalton Trans.*, 2012, **41**, 12048-12053.
113. S. H. Yang, M. Y. Kim, D. H. Kim, H. Y. Jung, H. M. Ryu, J. H. Han, M. S. Lee and H.-S. Kim, *Journal of Industrial and Engineering Chemistry*, 2017, **56**, 422-427.
114. L. Edman, *The Journal of Physical Chemistry B*, 2000, **104**, 7254-7258.
115. H. Suzuki and B. Wunderlich, *Journal of Polymer Science: Polymer Physics Edition*, 1985, **23**, 1671-1679.
116. N. Zhang, J. He, W. Han and Y. Wang, *J Mater Sci*, 2019, **54**, 9603-9612.
117. M. Abreha, A. R. Subrahmanyam and J. Siva Kumar, *Chemical Physics Letters*, 2016, **658**, 240-247.
118. S. K. Chaurasia and A. Chandra, *Solid State Ionics*, 2017, **307**, 35-43.
119. S. K. Chaurasia, R. K. Singh and S. Chandra, *Vibrational Spectroscopy*, 2013, **68**, 190-195.
120. L. Edman, *J Phys Chem B*, 2000, **104**, 7254-7258.
121. I. Rey, J. C. Lassègues, J. Grondin and L. Servant, *Electrochim Acta*, 1998, **43**, 1505-1510.
122. D. Brouillette, D. E. Irish, N. J. Taylor, G. Perron, M. Odziemkowski and J. E. Desnoyers, *Physical Chemistry Chemical Physics*, 2002, **4**, 6063-6071.

123. K. Tadanaga, R. Takano, T. Ichinose, S. Mori, A. Hayashi and M. Tatsumisago, *Electrochemistry Communications*, 2013, **33**, 51-54.
124. J. L. Allen, J. Wolfenstine, E. Rangasamy and J. Sakamoto, *Journal of Power Sources*, 2012, **206**, 315-319.
125. E. Rangasamy, J. Wolfenstine and J. Sakamoto, *Solid State Ionics*, 2012, **206**, 28-32.
126. C. Z. Zhao, X. Q. Zhang, X. B. Cheng, R. Zhang, R. Xu, P. Y. Chen, H. J. Peng, J. Q. Huang and Q. Zhang, *Proc Natl Acad Sci U S A*, 2017, **114**, 11069-11074.
127. S. R. Mohapatra, A. K. Thakur and R. N. P. Choudhary, *J. Power Sources*, 2009, **191**, 601-613.
128. J.-H. Choi, C.-H. Lee, J.-H. Yu, C.-H. Doh and S.-M. Lee, *J. Power Sources*, 2015, **274**, 458-463.
129. F. Langer, M. S. Palagonia, I. Bardenhagen, J. Glenneberg, F. La Mantia and R. Kun, *Journal of The Electrochemical Society*, 2017, **164**, A2298-A2303.
130. M. R. Shoar Abouzari, F. Berkemeier, G. Schmitz and D. Wilmer, *Solid State Ionics*, 2009, **180**, 922-927.
131. W. Wieczorek, Z. Florjanczyk and J. R. Stevens, *Electrochim Acta*, 1995, **40**, 2251-2258.
132. J. Przyluski, M. Siekierski and W. Wieczorek, *Electrochim Acta*, 1995, **40**, 2101-2108.
133. Y. Yamazaki, F. Blanc, Y. Okuyama, L. Buannic, J. C. Lucio-Vega, C. P. Grey and S. M. Haile, *Nat Mater*, 2013, **12**, 647-651.
134. M. F. Sunding, K. Hadidi, S. Diplas, O. M. Løvvik, T. E. Norby and A. E. Gunnæs, *Journal of Electron Spectroscopy and Related Phenomena*, 2011, **184**, 399-409.
135. M. Fingerle, C. Loho, T. Ferber, H. Hahn and R. Hausbrand, *J. Power Sources*, 2017, **366**, 72-79.
136. J. F. Moulder and J. Chastain, *Handbook of x-ray photoelectron spectroscopy : a reference book of standard spectra for identification and interpretation of XPS data*, Physical Electronics, Eden Prairie Minnesota, 1995.
137. K. Kanamura, S. Shiraishi, H. Tamura and Z. i. Takehara, *Journal of The Electrochemical Society*, 2019, **141**, 2379-2385.
138. A. Shchukarev and D. Korolkov, *Open Chemistry*, 2004, **2**, 347-362.
139. S. A. Pervez, B. P. Vinayan, M. A. Cambaz, G. Melinte, T. Diemant, T. Braun, G. Karkera, R. J. Behm and M. Fichtner, *J. Mater. Chem. A*, 2020, **8**, 16451-16462.
140. G. G. Eshetu, T. Diemant, S. Grugeon, R. J. Behm, S. Laruelle, M. Armand and S. Passerini, *ACS Appl Mater Interfaces*, 2016, **8**, 16087-16100.
141. A. Choukourov, A. Grinevich, O. Polonskyi, J. Hanus, J. Kousal, D. Slavinska and H. Biederman, *J Phys Chem B*, 2009, **113**, 2984-2989.
142. É. Kiss, J. Samu, A. Tóth and I. Bertóti, *Langmuir*, 1996, **12**, 1651-1657.
143. N. Schulz, R. Hausbrand, L. Dimesso and W. Jaegermann, *Journal of The Electrochemical Society*, 2018, **165**, A819-A832.
144. K. P. C. Yao, D. G. Kwabi, R. A. Quinlan, A. N. Mansour, A. Grimaud, Y.-L. Lee, Y.-C. Lu and Y. Shao-Horn, *Journal of The Electrochemical Society*, 2013, **160**, A824-A831.
145. A. Sharafi, S. Yu, M. Naguib, M. Lee, C. Ma, H. M. Meyer, J. Nanda, M. Chi, D. J. Siegel and J. Sakamoto, *J. Mater. Chem. A*, 2017, **5**, 13475-13487.
146. L. Cheng, E. J. Crumlin, W. Chen, R. Qiao, H. Hou, S. Franz Lux, V. Zorba, R. Russo, R. Kostecki, Z. Liu, K. Persson, W. Yang, J. Cabana, T. Richardson, G. Chen and M. Doeff, *Phys Chem Chem Phys*, 2014, **16**, 18294-18300.
147. V. Thangadurai, S. Narayanan and D. Pinzaru, *Chem Soc Rev*, 2014, **43**, 4714-4727.
148. C. Xu, B. Sun, T. Gustafsson, K. Edström, D. Brandell and M. Hahlin, *J. Mater. Chem. A*, 2014, **2**, 7256-7264.
149. A. Guéguen, P. Novák and E. J. Berg, *Journal of The Electrochemical Society*, 2016, **163**, A2545-A2550.
150. B. Philippe, R. Dedryvere, M. Gorgoi, H. Rensmo, D. Gonbeau and K. Edstrom, *J Am Chem Soc*, 2013, **135**, 9829-9842.
151. V. Sharova, A. Moretti, T. Diemant, A. Varzi, R. J. Behm and S. Passerini, *J. Power Sources*, 2018, **375**, 43-52.

152. B. S. Parimalam and B. L. Lucht, *Journal of The Electrochemical Society*, 2018, **165**, A251-A255.
153. J. Alvarado, M. A. Schroeder, T. P. Pollard, X. Wang, J. Z. Lee, M. Zhang, T. Wynn, M. Ding, O. Borodin, Y. S. Meng and K. Xu, *Energy & Environmental Science*, 2019, **12**, 780-794.
154. C. C. Nguyen, S.-W. Woo and S.-W. Song, *The Journal of Physical Chemistry C*, 2012, **116**, 14764-14771.
155. X. Shangguan, G. Jia, F. Li, S. Liu, G. Yang, K. Wu and Z. Wu, *Energy Technology*, 2018, **6**, 1667-1674.
156. K. Harrison and L. B. Hazell, *Surface and Interface Analysis*, 1992, **18**, 368-376.
157. K. Takada, *Acta Materialia*, 2013, **61**, 759-770.
158. Y. B. Shen, Y. T. Zhang, S. J. Han, J. W. Wang, Z. Q. Peng and L. W. Chen, *Joule*, 2018, **2**, 1674-1689.
159. J. R. Nair, F. Colò, A. Kazzazi, M. Moreno, D. Bresser, R. Lin, F. Bella, G. Meligrana, S. Fantini, E. Simonetti, G. B. Appetecchi, S. Passerini and C. Gerbaldi, *J. Power Sources*, 2019, **412**, 398-407.
160. E. Quartarone, P. Mustarelli and A. Magistris, *Solid State Ionics*, 1998, **110**, 1-14.
161. C. Brissot, M. Rosso, J. N. Chazalviel, P. Baudry and S. Lascaud, *Electrochim Acta*, 1998, **43**, 1569-1574.
162. P. Barai, K. Higa and V. Srinivasan, *Phys Chem Chem Phys*, 2017, **19**, 20493-20505.
163. M. Falco, C. Simari, C. Ferrara, J. R. Nair, G. Meligrana, F. Bella, I. Nicotera, P. Mustarelli, M. Winter and C. Gerbaldi, *Langmuir*, 2019, **35**, 8210-8219.
164. V. Thangadurai, H. Kaack and W. J. F. Weppner, *Journal of the American Ceramic Society*, 2003, **86**, 437-440.
165. P. Knauth, *Solid State Ionics*, 2009, **180**, 911-916.
166. S. Chen, D. Xie, G. Liu, J. P. Mwizerwa, Q. Zhang, Y. Zhao, X. Xu and X. Yao, *Energy Storage Materials*, 2018, **14**, 58-74.
167. M. Balaish, J. C. Gonzalez-Rosillo, K. J. Kim, Y. Zhu, Z. D. Hood and J. L. M. Rupp, *Nat Energy*, 2021, **6**, 227-239.
168. Y. Li, Z. Wang, C. Li, Y. Cao and X. Guo, *J. Power Sources*, 2014, **248**, 642-646.
169. H. El-Shinawi, E. J. Cussen and S. A. Corr, *Dalton Trans.*, 2017, **46**, 9415-9419.
170. W. Xia, B. Xu, H. Duan, Y. Guo, H. Kang, H. Li and H. Liu, *ACS Appl Mater Interfaces*, 2016, **8**, 5335-5342.
171. C. Galven, J. L. Fourquet, M. P. Crosnier-Lopez and F. Le Berre, *Chem Mater*, 2011, **23**, 1892-1900.
172. S. Zhang, J. Y. Lee and L. Hong, *J. Power Sources*, 2004, **126**, 125-133.
173. B. Kumar and L. G. Scanlon, *J. Power Sources*, 1994, **52**, 261-268.
174. K. K. Fu, Y. Gong, J. Dai, A. Gong, X. Han, Y. Yao, C. Wang, Y. Wang, Y. Chen, C. Yan, Y. Li, E. D. Wachsman and L. Hu, *Proc Natl Acad Sci U S A*, 2016, **113**, 7094-7099.
175. A. I. Waidha, T. Ferber, M. Donzelli, N. Hosseinpourkahvaz, V. Vanita, K. Dirnberger, S. Ludwigs, R. Hausbrand, W. Jaegermann and O. Clemens, *ACS Appl Mater Interfaces*, 2021, **13**, 31111-31128.
176. M. Falco, L. Castro, J. R. Nair, F. Bella, F. Bardé, G. Meligrana and C. Gerbaldi, *ACS Applied Energy Materials*, 2019, **2**, 1600-1607.
177. M. Keller, G. B. Appetecchi, G.-T. Kim, V. Sharova, M. Schneider, J. Schuhmacher, A. Roters and S. Passerini, *J. Power Sources*, 2017, **353**, 287-297.
178. G. T. Hitz, D. W. McOwen, L. Zhang, Z. Ma, Z. Fu, Y. Wen, Y. Gong, J. Dai, T. R. Hamann, L. Hu and E. D. Wachsman, *Materials Today*, 2019, **22**, 50-57.
179. R. J. Chen, M. Huang, W. Z. Huang, Y. Shen, Y. H. Lin and C. W. Nan, *J. Mater. Chem. A*, 2014, **2**, 13277-13282.
180. M. Bitzer, T. Van Gestel, S. Uhlenbruck and B. Hans Peter, *Thin Solid Films*, 2016, **615**, 128-134.
181. S. Wollstadt and O. Clemens, *Materials*, 2020, **13**.

182. M. Huang, T. Liu, Y. Deng, H. Geng, Y. Shen, Y. Lin and C.-W. Nan, *Solid State Ionics*, 2011, **204-205**, 41-45.
183. Y. H. Zhang, F. Chen, R. Tu, Q. Shen and L. M. Zhang, *J. Power Sources*, 2014, **268**, 960-964.
184. J. Sakamoto, E. Rangasamy, H. Kim, Y. Kim and J. Wolfenstine, *Nanotechnology*, 2013, **24**, 424005.
185. H. El Shinawi and J. Janek, *J. Power Sources*, 2013, **225**, 13-19.
186. C. Loho, R. Djenadic, M. Bruns, O. Clemens and H. Hahn, *Journal of The Electrochemical Society*, 2016, **164**, A6131-A6139.
187. J. Wolfenstine, E. Rangasamy, J. L. Allen and J. Sakamoto, *J. Power Sources*, 2012, **208**, 193-196.
188. K. Tadanaga, H. Egawa, A. Hayashi, M. Tatsumisago, J. Mosa, M. Aparicio and A. Duran, *J. Power Sources*, 2015, **273**, 844-847.
189. S. Lobe, C. Dellen, M. Finsterbusch, H. G. Gehrke, D. Sebold, C. L. Tsai, S. Uhlenbruck and O. Guillon, *J. Power Sources*, 2016, **307**, 684-689.
190. N. C. Rosero-Navarro, T. Yamashita, A. Miura, M. Higuchi and K. Tadanaga, *Journal of the American Ceramic Society*, 2017, **100**, 276-285.
191. M. Zanne and C. Gleitzer, *B Soc Chim Fr*, 1971, 1567.
192. A. J. Jacobson and J. L. Hutchison, *Journal of Solid State Chemistry*, 1980, **35**, 334-340.
193. O. Mentre, M. Iorgulescu, M. Huve, H. Kabbour, N. Renaut, S. Daviero-Minaud, S. Colis and P. Roussel, *Dalton Trans.*, 2015, **44**, 10728-10737.
194. H. Taguchi, Y. Takeda, F. Kanamaru, M. Shimada and M. Koizumi, *Acta Crystallographica Section B*, 1977, **33**, 1298-1299.
195. K. Boulahya, M. Parras, J. M. Gonzalez-Calbet, U. Amador, J. L. Martinez, V. Tissen and M. T. Fernandez-Diaz, *Phys Rev B*, 2005, **71**.
196. M. Parras, A. Varela, H. Seehofer and J. M. GonzalezCalbet, *Journal of Solid State Chemistry*, 1995, **120**, 327-331.
197. J. Leng, Z. Wang, J. Wang, H.-H. Wu, G. Yan, X. Li, H. Guo, Y. Liu, Q. Zhang and Z. Guo, *Chem. Soc. Rev.*, 2019, **48**, 3015-3072.
198. C. Sun, J. A. Alonso and J. Bian, *Advanced Energy Materials*, 2020, **11**, 2000459.
199. Y. Gorlin and T. F. Jaramillo, *J. Am. Chem. Soc.*, 2010, **132**, 13612-13614.
200. Y. Q. Lyu and F. Ciucci, *ACS Apl. Mater. Inter.*, 2017, **9**, 35829-35836.
201. O. Clemens, C. Reitz, R. Witte, R. Kruk and R. I. Smith, *Journal of Solid State Chemistry*, 2016, **243**, 31-37.
202. A. Iqbal Waidha, H. Khatoon Siddiqui, Y. Ikeda, M. Lepple, S. Vasala, M. Donzelli, A. D. Fortes, P. Slater, B. Grabowski, U. I. Kramm and O. Clemens, *Chemistry*, 2021, **27**, 9763-9767.
203. T. Yamamoto and H. Kageyama, *Chemistry Letters*, 2013, **42**, 946-953.
204. Y. Tsujimoto, C. Tassel, N. Hayashi, T. Watanabe, H. Kageyama, K. Yoshimura, M. Takano, M. Ceretti, C. Ritter and W. Paulus, *Nature*, 2007, **450**, 1062-1065.
205. G. H. Jonker, *Journal of Applied Physics*, 1966, **37**, 1424-1430.
206. M. L. Medarde, *Journal of Physics: Condensed Matter*, 1997, **9**, 1679-1707.
207. Y. Tsujimoto, C. Tassel, N. Hayashi, T. Watanabe, H. Kageyama, K. Yoshimura, M. Takano, M. Ceretti, C. Ritter and W. Paulus, *Nature*, 2007, **450**, 1062-1065.
208. O. Clemens and P. R. Slater, *Reviews in Inorganic Chemistry*, 2013, **33**, 105-117.
209. S. M. Haile, D. L. West and J. Campbell, *J Mater Res*, 1998, **13**, 1576-1595.
210. Y. Yamazaki, R. Hernandez-Sanchez and S. M. Haile, *Chem Mater*, 2009, **21**, 2755-2762.
211. P. A. Sukkurji, A. Molinari, A. Benes, C. Loho, V. S. K. Chakravadhanula, S. K. Garlapati, R. Kruk and O. Clemens, *Journal of Physics D-Applied Physics*, 2017, **50**.
212. A. Benes, A. Molinari, R. Witte, R. Kruk, J. Brotz, R. Chellali, H. Hahn and O. Clemens, *Materials*, 2017, **11**.
213. H. J. Hwang, M. B. Ji-Woong, L. A. Seunghun and E. A. Lee, *J. Power Sources*, 2005, **145**, 243-248.

214. E. Fabbri, R. Mohamed, P. Levecque, O. Conrad, R. Kötz and T. J. Schmidt, *ACS Catalysis*, 2014, **4**, 1061-1070.
215. U. Spitsbergen, *Acta Crystallogr*, 1960, **13**, 197-198.
216. A. J. Jacobson and J. L. Hutchison, *J Chem Soc Chem Comm*, 1976, **0**, 116-117.
217. N. Raghu, V. Ravi and T. R. N. Kutty, *Materials Research Bulletin*, 1991, **26**, 261-268.
218. Z. H. Hu, H. M. Zhang, J. H. Wang, L. Chen, X. X. Xie, X. Liu, J. C. Yao and A. M. Chang, *J Mater Sci-Mater El*, 2017, **28**, 6239-6244.
219. P. M. Botta, V. Pardo, C. de la Calle, D. Baldomir, J. A. Alonso and J. Rivas, *J Magn Magn Mater*, 2007, **316**, E670-E673.
220. J. L. Cacheiro, M. Iglesias, V. Pardo, D. Baldomir and J. E. Arias, *Int J Quantum Chem*, 2003, **91**, 252-256.
221. T. Inoue, T. Matsui, N. Fujimura, H. Tsuda and K. Morii, *Ieee T Magn*, 2005, **41**, 3496-3498.
222. A. Sarkar, R. Djenadic, D. Wang, C. Hein, R. Kautenburger, O. Clemens and H. Hahn, *J Eur Ceram Soc*, 2018, **38**, 2318-2327.
223. V. Jayaraman, A. Magrez, M. Caldes, O. Joubert, F. Taulelle, J. Rodriguezcarvajal, Y. Piffard and L. Brohan, *Solid State Ionics*, 2004, **170**, 25-32.
224. J. Bielecki, S. F. Parker, L. Mazzei, L. Borjesson and M. Karlsson, *J. Mater. Chem. A*, 2016, **4**, 1224-1232.
225. W. Fischer, G. Reck and T. Schober, *Solid State Ionics*, 1999, **116**, 211-215.
226. V. E. H. Richard L. Kurtz, Roger Stockbauer, Theodore E. Madey, Donald Mueller, Arnold Shih, Louis Toth, *Phys Rev B*, 1988, **37**, 7936-7939.
227. R. L. Kurtz and V. E. Henrich, *Phys Rev B*, 1982, **26**, 6682-6689.
228. C. C. McCrory, S. Jung, J. C. Peters and T. F. Jaramillo, *J Am Chem Soc*, 2013, **135**, 16977-16987.
229. D. Friebel, M. W. Louie, M. Bajdich, K. E. Sanwald, Y. Cai, A. M. Wise, M. J. Cheng, D. Sokaras, T. C. Weng, R. Alonso-Mori, R. C. Davis, J. R. Bargar, J. K. Norskov, A. Nilsson and A. T. Bell, *J Am Chem Soc*, 2015, **137**, 1305-1313.
230. M. A. Kirsanova, V. D. Okatenko, D. A. Aksyonov, R. P. Forslund, J. T. Mefford, K. J. Stevenson and A. M. Abakumov, *J. Mater. Chem. A*, 2019, **7**, 330-341.
231. K. D. Kreuer, *Annual Review of Materials Research*, 2003, **33**, 333-359.
232. K. Li, M. Yin, Z. Wang, X. Chen, T. Zhu, J. Wang, N. Dewangan, Y. Yu, Q. Zhong and S. Kawi, *ChemistrySelect*, 2018, **3**, 12424-12429.
233. X. Xu, C. Su, W. Zhou, Y. Zhu, Y. Chen and Z. Shao, *Adv. Sci.*, 2016, **3**, 1500187.
234. Y. Zhu, W. Zhou, J. Yu, Y. Chen, M. Liu and Z. Shao, *Chem Mater*, 2016, **28**, 1691-1697.
235. V. Jayaraman, A. Magrez, M. Caldes, O. Joubert, F. Taulelle, J. Rodriguez-Carvajal, Y. Piffard and L. Brohan, *Solid State Ionics*, 2004, **170**, 25-32.
236. R. D. Shannon, *Acta Crystallographica, Section A: Foundations of Crystallography*, 1976, **A32**, 751-767.
237. P. K. Gallagher, J. B. MacChesney and D. N. E. Buchanan, *J. Chem. Phys.*, 1964, **41**, 2429-2434.
238. E. Kuzmann, S. Nagy and A. Vértes, *Pure and Applied Chemistry*, 2003, **75**, 801-858.
239. D. F. Valezi, M. T. Piccinato, P. W. C. Sarvezuk, F. F. Ivashita, A. Paesano, J. Varalda, D. H. Mosca, A. Urbano, C. L. B. Guedes and E. Di Mauro, *Mater. Chem. Phys.*, 2016, **173**, 179-185.
240. N. Hayashi, T. Yamamoto, H. Kageyama, M. Nishi, Y. Watanabe, T. Kawakami, Y. Matsushita, A. Fujimori and M. Takano, *Angew. Chem. Int. Ed.*, 2011, **50**, 12547-12550.
241. O. Clemens, F. J. Berry, A. J. Wright, K. S. Knight, J. M. Perez-Mato, J. M. Igartua and P. R. Slater, *Journal of Solid State Chemistry*, 2013, **206**, 158-169.
242. O. Clemens, R. Kruk, E. A. Patterson, C. Loho, C. Reitz, A. J. Wright, K. S. Knight, H. Hahn and P. R. Slater, *Inorg. Chem.*, 2014, **53**, 12572-12583.
243. R. A. Afzal, K. Y. Park, S. H. Cho, N. I. Kim, S. R. Choi, J. H. Kim, H. T. Lim and J. Y. Park, *RSC Adv.*, 2017, **7**, 47643-47653.

244. N. I. Kim, Y. J. Sa, T. S. Yoo, S. R. Choi, R. A. Afzal, T. Choi, Y. S. Seo, K. S. Lee, J. Y. Hwang, W. S. Choi, S. H. Joo and J. Y. Park, *Sci Adv*, 2018, **4**, 9360−9367.
245. X. Miao, L. Wu, Y. Lin, X. Yuan, J. Zhao, W. Yan, S. Zhou and L. Shi, *Chem. Commun.*, 2019, **55**, 1442-1445.
246. A. Grimaud, K. J. May, C. E. Carlton, Y. L. Lee, M. Risch, W. T. Hong, J. Zhou and Y. Shao-Horn, *Nat. Commun.*, 2013, **4**, 2439.
247. W. T. Hong, K. A. Stoerzinger, Y. L. Lee, L. Giordano, A. Grimaud, A. M. Johnson, J. Hwang, E. J. Crumlin, W. L. Yang and Y. Shao-Horn, *Energy & Environmental Science*, 2017, **10**, 2190-2200.
248. L. Bi, S. Boulfrad and E. Traversa, *Chem. Soc. Rev.*, 2014, **43**, 8255-8270.
249. G. Chen, W. Zhou, D. Guan, J. Sunarso, Y. Zhu, X. Hu, W. Zhang and Z. Shao, *Sci. Adv.*, 2017, **3**, e1603206.
250. U. Spitsbergen, *Acta Crystal.*, 1960, **13**, 197-198.
251. X. Xu, W. Wang, W. Zhou and Z. Shao, *Small Methods*, 2018, **2**.
252. E. O. Wollan and W. C. Koehler, *Physical Review*, 1955, **100**, 545-563.
253. P. E. Blochl, *Phys Rev B Condens Matter*, 1994, **50**, 17953-17979.
254. J. P. Perdew, K. Burke and M. Ernzerhof, *Phys Rev Lett*, 1996, **77**, 3865-3868.
255. G. Kresse and J. Furthmuller, *Computational Materials Science*, 1996, **6**, 15-50.
256. G. Kresse and J. Furthmuller, *Phys Rev B Condens Matter*, 1996, **54**, 11169-11186.
257. G. Kresse and D. Joubert, *Phys Rev B*, 1999, **59**, 1758-1775.
258. M. Methfessel and A. T. Paxton, *Phys Rev B Condens Matter*, 1989, **40**, 3616-3621.
259. S. L. Dudarev, G. A. Botton, S. Y. Savrasov, C. J. Humphreys and A. P. Sutton, *Phys Rev B*, 1998, **57**, 1505-1509.
260. V. Pardo, P. Blaha, M. Iglesias, K. Schwarz, D. Baldomir and J. E. Arias, *Phys Rev B*, 2004, **70**, 144422.
261. O. Clemens, *Journal of Solid State Chemistry*, 2015, **225**, 261-270.
262. T. Yamamoto, Y. Kobayashi, N. Hayashi, C. Tassel, T. Saito, S. Yamanaka, M. Takano, K. Ohoyama, Y. Shimakawa, K. Yoshimura and H. Kageyama, *J Am Chem Soc*, 2012, **134**, 11444-11454.
263. N. Weidler, S. Paulus, J. Schuch, J. Klett, S. Hoch, P. Stenner, A. Maljusch, J. Brotz, C. Wittich, B. Kaiser and W. Jaegermann, *Phys Chem Chem Phys*, 2016, **18**, 10708-10718.
264. J. Schuch, S. Klemenz, P. Schuldt, A. M. Zieschang, S. Dolique, P. Connor, B. Kaiser, U. I. Kramm, B. Albert and W. Jaegermann, *ChemCatChem*, 2021, DOI: 10.1002/cctc.202002030.
265. R. Mohamed, X. Cheng, E. Fabbri, P. Levecque, R. Kötz, O. Conrad and T. J. Schmidt, *Journal of The Electrochemical Society*, 2015, **162**, F579-F586.
266. S. J. Skinner, *Int. J. Inorg. Mater.*, 2001, **3**, 113-121.
267. M. M. Lee, J. Teuscher, T. Miyasaka, T. N. Murakami and H. J. Snaith, *Science*, 2012, **338**, 643-647.
268. http://www.vasp.at.
269. A. I. Liechtenstein, V. V. Anisimov and J. Zaanen, *Phys Rev B Condens Matter*, 1995, **52**, R5467-R5470.
270. J. Deakin, I. Trussov, A. Gibbs, E. Kendrick and P. R. Slater, *Dalton. Trans.*, 2018, **47**, 12901-12906.
271. C. F. Smura, D. R. Parker, M. Zbiri, M. R. Johnson, Z. A. Gal and S. J. Clarke, *J. Am. Chem. Soc.*, 2011, **133**, 2691-2705.
272. K. Tomiyasu, T. Inami and N. Ikeda, *Phys Rev B*, 2004, **70**.
273. M. G. Sahini, J. R. Tolchard, K. Wiik and T. Grande, *Dalton Trans.*, 2015, **44**, 10875-10881.
274. L. Porcarelli, A. S. Shaplov, F. Bella, J. R. Nair, D. Mecerreyes and C. Gerbaldi, *Acs Energy Letters*, 2016, **1**, 678-682.
275. Y. Li, B. Xu, H. Xu, H. Duan, X. Lu, S. Xin, W. Zhou, L. Xue, G. Fu, A. Manthiram and J. B. Goodenough, *Angew Chem Int Ed Engl*, 2017, **56**, 753-756.

276. D. Lyu, Y. B. Mollamahale, S. Huang, P. Zhu, X. Zhang, Y. Du, S. Wang, M. Qing, Z. Q. Tian and P. K. Shen, *Journal of Catalysis*, 2018, **368**, 279-290.

List of figures

List of tables

Acknowledgements

The end of a journey is just a beginning of a new one. I would like to express my gratitude to everyone who made last four years of my doctorate journey a beautiful one.

First and foremost, I would like to thank Prof. Dr. Oliver Clemens for giving me an opportunity to carry out this dissertation in his group and taking me under his wing. His endless support during the last 4 years is highly appreciated. I thank him immensely for being available and pushing me to become a good scientist. A role model indeed for me.

I would also like to take this opportunity to thank Prof. Wolfgang Ensinger for accepting to being a co-examiner for this thesis. Further, I appreciate both Prof. Wolfgang Donner and Prof. Ulrike Kramm for accepting to being the members on the examination committee.

I thank the members of my research group Materialdesign durch Synthese for exciting scientific discussions that helped me gain understanding on topics outside the scope of my research. I thank Dr. Stephan Wollstadt for in depth discussions on barium ferrates and giving me his perspective of this system. These discussions have been both joyful and educational. Dr. Kerstin Wissel is thanked for giving me an overview of fluoride ion battery technology and for being my go to person in the group. Dr. Ali Nowroozi, a person from whom I have learned to remain calm irrespective of the research output. Manuel Donzelli is thanked for being a role model for maintaining work-life balance. I would like to thank all the hard working students Jasim Ali, Vanita and Niloofar Hosseinpourkahvaz, who did their advanced research lab and master thesis within the framework of this thesis. Maria Walker is thanked for being an awesome secretary of the research group.

I would also like to thank all the people who have collaborated with me over the last 4 years within the scope of this thesis. Dr. Sami Vasala, Supratik Das Gupta and Prof. Lambert Alff (SQUID measurements), Dr. Maren Lepple, Dr. Klaus Dirnberger and Prof. Sabine Ludwigs (DSC measurements), Lingmei Ni, Humera Siddiqi and Prof. Ulrike Kramm (ORR/OER and Mössbauer measurements), Dr. Alexander Benes and Manuel Donzelli (XPS measurements), A.D. Fortes (neutron measurements), Dr. Yuji Ikeda, Prof. Hongbin Zhang and Prof. Blazej Grabowski (DFT studies).

I also would like to express my gratitude towards the Deutsche Forschungsgemeinschaft (CL551/3-1) for proving the funding to make this work possible. Science and Technology Facilities Council (DOI: 10.5286/ISIS.E.87849379) is thanked for providing the neutron beam time at HRPD ISIS facility.

Last but not the least, my deepest gratitude goes to my parents, brother and especially my sister. Without their love, affection and support, none of this would have been possible. To my friends/family, Ali Malik and Vanita, thanks for your support. This has been a journey to cherish.